Functional Pulmonary MRI Using Hyperpolarised ^{3}He

by

Iain Ball, BSc (Hons)

Thesis submitted to The University of Nottingham

for the degree of Doctor of Philosophy

July 2011

Abstract

The microstructure of the lung is complex, containing many branching airways and alveolar sacs for optimal gas exchange. Lung diseases such as cystic fibrosis (CF), asthma, and emphysema lead to a destruction of this microstructure. As such, there is a growing interest in the early identification and assessment of lung disease using non invasive imaging techniques. Pulmonary function tests such as spirometry and plethysmography are currently used for this purpose but can only provide quantitative lung function measurements rather than direct measurements of lung physiology and disease. Computed tomography (CT) has also been used but due to risk of cell damage and mutation from the ionising radiation, long term monitoring of the lungs is severely constrained.

Recently, new methods based on magnetic resonance imaging (MRI) have been developed to provide diagnostic imaging of the lung. Conventional MRI is not very well suited for lung imaging due to the very low proton density of the pulmonary airspaces. This problem can be overcome by making the patient inspire noble gases such as ^{3}He whose polarisations have been vastly increased through optical pumping. Therefore ^{3}He MRI permits a non-invasive determination of lung function.

The high diffusion coefficient of ^{3}He can be exploited to probe the microstructure of the lung. By measuring how fast ^{3}He diffuses within the

lung, the size of the lung microstructure can be assessed. Normally, the airspace walls impede the diffusion of the gas but for diseased lungs where microstructure has been destroyed, diffusion is less restricted and a higher apparent diffusion coefficient (ADC) is observed.

The research conducted for this thesis focused on the measurement of ADC using three different MRI pulse sequences with each sequence being designed to assess the peripheral airspaces over different length scales. These sequences were then implemented on three different subject study groups.

The largest study group, referred to as the Leicester study group, looked at alveolar development in children and young adults. The measured diffusion results were correlated with age and lung size and demonstrated a significant level of invariance despite a four fold increase in lung volume between subjects. The findings from the study were interpreted as evidence that alveolisation continues beyond early life, a controversial result that is against the current paradigm.

The asthmatic study was a preliminary study involving severe asthmatic adult subjects and aged matched healthy control subjects. An assessment of the disorder was accomplished by correlating diffusion measurements with clinical measurements of asthma severity determined through spirometry. The study demonstrated the potential of ^{3}He MRI for detecting changes in the peripheral airways of asthmatics and assessed which spirometry indices were best for evaluating asthma severity.

The CF preliminary study involved 10 children aged between 6-11 years with early stage disease progression. Like the asthmatic study, an assessment was made by comparing diffusion measurements obtained on CF subjects to aged matched control subjects as well as correlating them to several spirometric indices. Although the results did demonstrate significant differences

between CF and control subjects, significant correlations with measures of spirometry were mostly absent. The conclusions drawn from the study were that the diffusion measurements acquired on the CF subjects, whist being indicative of the disease, were not sensitive enough to be used as biomarkers for disease severity or progression.

Acknowledgements

Although one name is written on the title page of this thesis, the work presented is in reality the result of the combined efforts of a number of people, to all of whom, I owe a great deal.

Firstly, I would like to thank my supervisor Professor John Owers-Bradley whose support, advice, ideas, and accessibility has been invaluable to me throughout my time spent here in Nottingham.

I am indebted to my former colleague Dr Kuldeep Panesar whose friendship and professional support throughout the course of this work I will be forever grateful for. I also thank the other previous members of the research group, Jau-Yi Wang, Marius Mada, and Dr Ruslan Garipov for all their help.

A special thanks must go to Dr Ryan Beardsley for his invaluable help and support in figure making.

Continuing on a professional level, I would like to thank all the technical staff of the School of Physics and Astronomy workshops whose expert craftsmanship allowed a lot of the work presented to be realised.

Many thanks must go to our collaborators at Leicester: Dr Caroline Beardsmore, Dr Manjith Narayanan, Dr Erol Gaillard, and Professor Mike Silverman, all of whom taught this physicist many of the complexities of human anatomy and physiology.

Finally, and most importantly is the appreciation I reserve for my family.

I thank my brother for our Xbox 360 sessions during many an evening when I should have gotten an early night. I am eternally grateful to my mother and my father who have always given me the support and encouragement I have needed throughout my education. I can never repay that to them, but instead, I hope I make them proud.

Dedicated to Mum and Dad

Contents

List of Figures

List of Tables

Chapter 1

Introduction

1.1   The Respiratory System

The human respiratory system consists of the nose, pharynx (the throat), larynx (the voice box), trachea (the windpipe), bronchi, and the lungs. Structurally, the respiratory system is subdivided into the upper and lower respiratory systems. The upper respiratory system consists of the nose, pharynx, and associated structures. The lower respiratory system comprises of the larynx, trachea, bronchi, and lungs.

Functionally, the system also consists of two parts. The conducting zone is a series of interconnecting cavities and tubes both outside and inside in the lungs that filter, warm, and moisten air and conduct it into the lungs. The respiratory zone comprises only airways within the lung where gas exchange occurs.

1.1.1   Lung Anatomy

The lungs are a pair of cone shaped organs situated in the thoracic cavity that are separated from each other by the heart and other intervening structures

in the mediastinum. Each lung is divided into lobes by one or two fissures. Both lungs consist of an oblique fissure whilst the right lung only is further divided by a horizontal fissure. As such, each lung is divided into upper and lower lobes with the right lung also having an additional middle lobe.

At the fifth thoracic vertebra, the trachea divides into the right and left primary bronchi which continue into the right and left lung respectively. Having entered the lungs the primary bronchi divide into smaller secondary bronchi, one for each lobe of the lung. The secondary bronchi then themselves divide into yet smaller tertiary bronchi which further divide into even smaller bronchioles. The bronchioles then undergo repeated branching, getting ever more smaller until the process stops at the terminal bronchioles. The terminal bronchioles then subdivide into the respiratory bronchioles which in turn subdivide further into approximately 2-11 alveolar ducts. Numerous alveolar sacs and alveoli are situated around the circumference of each alveolar duct.

From the trachea to the alveolar sacs there are about 23 orders of branching, referred to as generations (Figure 1.1) [1]. The last 7 generations onward from the respiratory bronchioles constitute a pulmonary acinus. Although airway diameter as a function of generation decreases successively (Figure 1.2) [2], the total cross-sectional area of each successive airway generation increases by virtue of an ever increasing number of airways (Figure 1.3) [3]. It has been estimated that the lungs contain 300 million alveoli providing a total surface area for gas exchange of 70 m^2 [4].
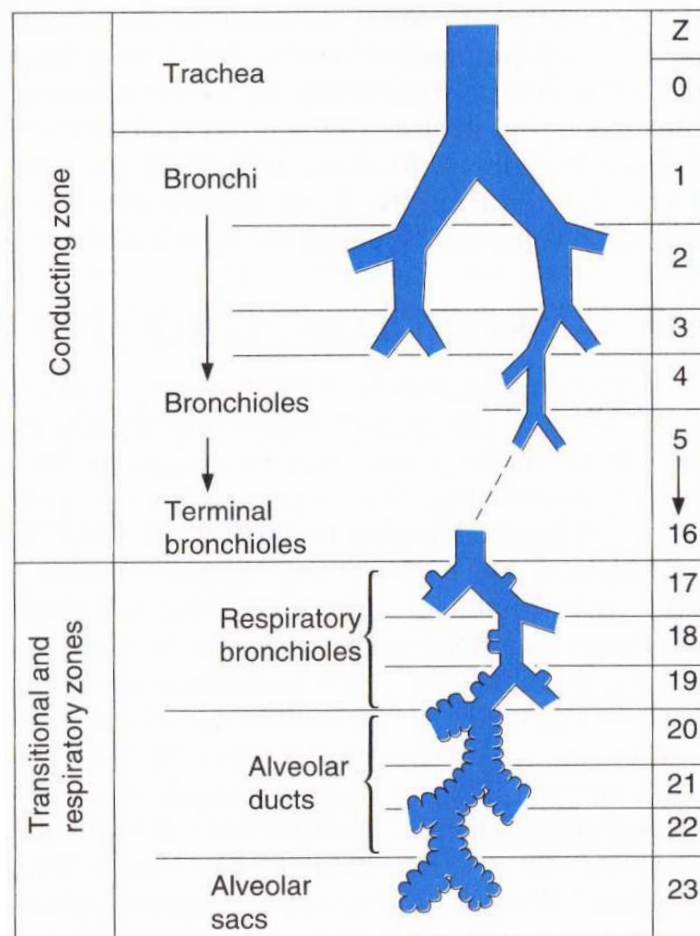
Figure 1.1: Weibel branching diagram (taken from [1]).
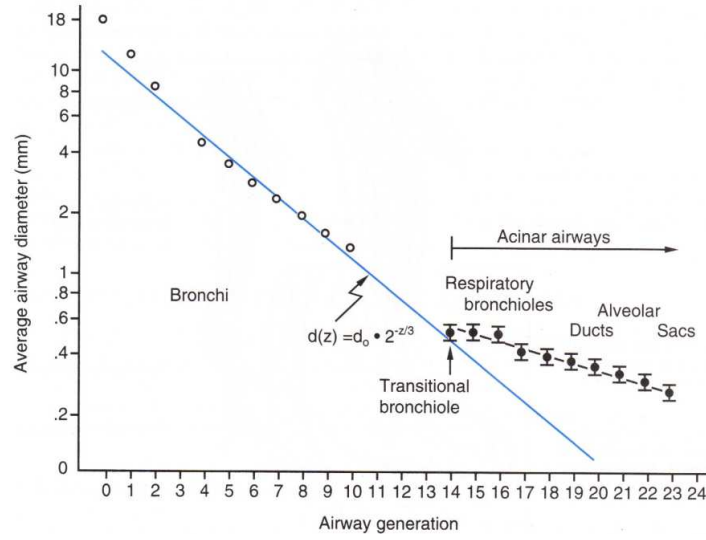
Figure 1.2: Average airway diameter as a function of airway generation (taken from [2]).
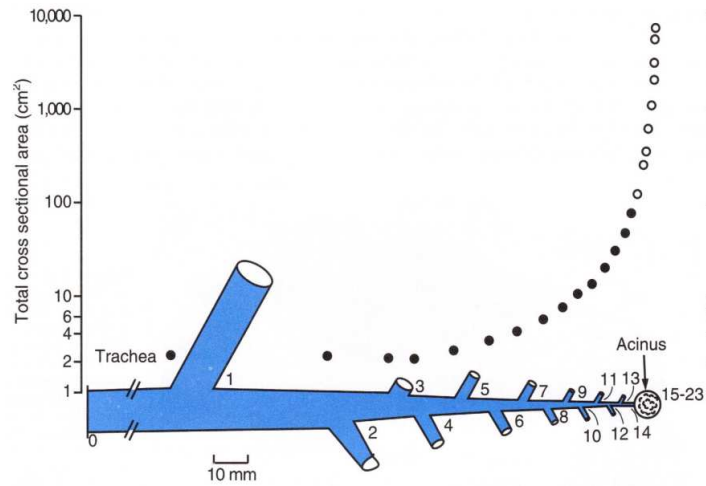
Figure 1.3: Total cross-sectional area of the airways as a function of airway generation (taken from [3]).

1.1.2 Lung Physiology

Pulmonary Ventilation

Ventilation is the inflow and outflow of air between the atmosphere and the alveoli as a result of inhalation and exhalation during breathing. The flow of air is driven by alternating pressure gradients caused by contraction and relaxation of respiratory muscles. There are also three other factors that affect the rate of airflow and thus the ease of pulmonary ventilation. These are: surface tension of the alveolar fluid, airway resistance, and compliance of the lungs. Any impairment of the ventilation process has a subsequent effect on gas exchange which can lead to disruption of homeostasis.

Gas Exchange

Gas exchange between alveolar air and pulmonary blood across the alveolar-capillary membrane is governed by both Dalton's law and Henry's law. Dalton's law is important for understanding how the rate of diffusion through a liquid is dependent on the partial pressure differences between the alveoli and capillary blood. Henry's law demonstrates how the solubility of a gas relates to its diffusion through a liquid [4].

Gas exchange is thereby a two way process of oxygen uptake into the capillary blood and carbon dioxide transfer from the blood into alveolar air whereupon it is expelled through subsequent exhalation. Diffusion of carbon dioxide is 24 times greater than diffusion of oxygen due to its high solubility.

1.1.3 Lung Pathology

Asthma

Asthma is characterised by airway obstruction, chronic airway inflammation, and airway hyperresponsiveness.

Airway obstruction is believed to be caused by damage to airway epithelium, increased mucous secretion, edema of the mucosa of the airways, and/or smooth muscle spasms in the walls of the bronchioles. It is partially reversible through treatment by administration of an inhaled agonist such as albuterol which opens up the airways by relaxing bronchiole smooth muscle.

Individuals with asthma respond to various stimuli with greater sensitivity than people without the disorder. Occassionally, the stimulus that triggers an attack is an allergen such as pollen, molds, dust mites, or a certain foodstuff. Other triggers of an asthma attack are cigarette smoke, breathing cold air, aspirin, sulfiting agents, and emotional upset. The symptoms of such an attack include coughing, wheezing, anxiety, difficulty breathing, chest tightness, tachycardia, and fatigue.

Acute asthma is attributed to bronchiolar smooth muscle spasms and mucous plugging. More severe asthma is characterised by chronic inflammation which leads to necrosis of bronchial epithelial cells, fibrosis, and edema. These structural changes are mediated through chemicals including histamine, prostaglandins, leukotrienes, and thromboxane. Long term therapy of asthma is therefore focused on treating the underlying inflammation with anti-inflammatory drugs such as inhaled corticosteroids and leukotriene.

Cystic Fibrosis

Cystic fibrosis (CF) is an inherited disease that affects the lungs, liver, pancreas, small intestine, and sweat glands. The disease is the result of a genetic mutation that affects a transporter protein responsible for carrying chloride ions across the plasma membranes of epithelial cells. A common index for diagnosing CF is therefore to measure the excess of chloride found in perspiration caused by dysfunction of the sweat glands.

The mutation also causes thick mucous secretions which obstruct the ducts of several organs and ultimately disrupts their normal functioning. Inflammation and replacement of injured cells by connective tissue that further causes obstruction are consequences of a buildup of these mucous secretions. Lung disease accounts for the most deaths from CF. Infection, inflammation, and obstruction of the airways leads to difficulty in breathing and eventual destruction of lung tissue.

Emphysema

Emphysema is a disorder characterised by a permanent enlargement of the airspaces distal to the terminal bronchioles as a result of alveolar wall destruction. Larger airspaces provide less suface area for gas exchange therefore oxygen diffusion across the damaged alveolar-capillary membrane is reduced. As more alveolar wall destruction occurs, lung elastic recoil decreases owing to loss of elastic fibres, and an increase in air trapping at the end of exhalation.

Emphysema is caused by long term irritation usually the result of either smoking, air pollution, or occupational exposure to industrial dust.

1.2 Preamble

There is currently a lack of safe imaging techniques for monitoring lung development and assessing lung physiology. Existing modalities such as CT and radionucleide imaging carry a high ionising radiation burden which limits longitudinal monitoring of lung development as well as intensive monitoring of early stage disease progression. Radionucleide imaging has poor spatial resolution as does CT which can not detect airways below the 10th generation and thus probe the small airways where gas exchange is taking place.

The most widely used clinical techniques to monitor lung growth and assess lung physiology are spirometry and plethysmography. These techniques provide quantitative measurements of lung function but cannot provide direct measurements with regional specificity.

Hyperpolarised ^{3}He MRI offers a non invasive direct measurement of the small airways and therefore overcomes the limitations associated with CT and spirometry and plethysmography. There are several applications of ^{3}He MRI which can be utilised in the assessment of lung physiology and pathology. These applications are; detection of ventilation defects from static images, assessment of ventilation/perfusion mismatch via detection of changes in local partial pressure of oxygen, and changes in ^{3}He diffusion caused by changes in lung morphology. The research conducted in this thesis focussed on ^{3}He diffusion through the peripheral airways of the lung and how this could be exploited to provide functional information.

1.3 Overview of the Thesis

This thesis is divided into six main chapters as follows:

Chapter 1 - Introduction; provides an overview of the thesis as well as describing important aspects of lung anatomy, physiology, and pathology.

Chapter 2 - NMR and MRI; covers the fundamental physics of nuclear magnetic resonance (NMR) and its application in magnetic resonance imaging (MRI). Differences between ^{1}H and ^{3}He MRI are also explained.

Chapter 3 - Diffusion MRI; the theoretical principles of diffusion are presented followed by the challenges it poses to MRI. Specific imaging techniques are then described along with various models of lung geometry that are used to relate magnetic resonance measurements to lung physiological parameters. Lastly, imaging artefacts pertinent to low field diffusion weighted MRI are considered.

Chapter 4 - Radio Frequency Receiver Coil Design; explains the principles of receiver coil design and displays all the custom built coils used throughout this thesis. In particular, it details the process involved in designing and constructing a receiver coil dedicated to parallel imaging, the software that was written and used, and the results obtained from imaging.

Chapter 5 - Methods for Studying Diffusion; starts by describing the three diffusion MRI sequences employed in this research and the data analysis software used for each technique. Measurement protocols are then defined as are scaling of subsequent measurements to account for various experimental parameters such as ^{3}He concentration and bolus size.

Chapter 6 - Results and Discussions; presents the results that were obtained for each of the different study groups (healthy children, severe ashthmatic adults, and children with CF) and discusses their implications.

Chapter 7 - Conclusions; summarises the research that has been presented in this thesis and states the conclusions that can be drawn from the work.

Chapter 2

NMR and MRI

2.1 NMR

The basis of the NMR phenomenon relies on the magnetic properties of the protons and neutrons within the atomic nucleus. The most commonly used nucleus is that of Hydrogen (i.e. the proton, ^{1}H) due to its abundance in the human body (98.98%) and its high NMR sensitivity. The principles of NMR can be described by a combination of quantum mechanical and classical models. From quantum mechanics, atomic nuclei possess a property called spin, which is analogous to angular momentum for a classical model.

2.1.1 Intrinsic Spin and Spin Angular Momentum

There are many nuclei which exhibit what is known as intrinsic spin, which is a fundamental property of nature like charge and mass. Individual nucleons have a spin of 1/2. The spins from the interacting nucleons couple together in the nucleus to form an entity with spin angular momentum $\hbar I$ where I is either an integer or half integer.

The proton and the neutron have the same spin angular momentum as

the electron, $\hbar/2$ but their magnetic moments (also referred to as spins) are much smaller because of their far greater masses.

According to classical theory, and considering the dominant nucleus in MRI (the proton), the magnetic moment of the nucleus, $\vec{\mu}$, can be described as follows. A proton possesses a positive charge $+e$, which rotates about its central axis due to its spin. This rotation generates an angular momentum which in turn gives rise to a magnetic moment $\vec{\mu}$. This process can be compared to a circulating charge through a coil of wire, which has the effect of producing a magnetic flux.

The magnetic moment associated with the total spin angular momentum $\hbar I$ can be written as;

$$\vec{\mu} = \frac{ge\hbar I}{2m_p} \tag{2.1}$$

where g is the Lande factor and is given as 5.586 for the neutron and -3.826 for the proton, e is the charge of an electron, m_p is the mass of the proton, and $\hbar = h/2\pi$. By defining the gyro-magnetic ratio γ as;

$$\gamma = \frac{ge}{2m_p} \tag{2.2}$$

the magnetic moment can be re-written to;

$$\vec{\mu} = \gamma\hbar I \tag{2.3}$$

in which $\gamma = 2.675 \times 10^{10}$ rad s^{-1} T^{-1} for protons.

Since the magnetic moment is a vector quantity, its magnitude and orientation need to be defined. The magnitude of $\vec{\mu}$ denoted by μ is;

$$\mu = \gamma\hbar\sqrt{I(I+1)} \tag{2.4}$$

Although the magnitude of $\vec{\mu}$ is certain under any conditions (with or without an external magnetic field), its orientation is random in the absence of an external magnetic field due to random thermal motion.

2.1.2   Interaction with a Magnetic Field

In the presence of a magnetic field $\vec{B_0}$, which by convention is assumed to be applied in the z-direction ($\vec{B_0} = B_0 \hat{z}$), the randomly orientated magnetic moments will align with the magnetic field. As a consequence of the quantum model, the magnetic moment vectors do not line up exactly with the external magnetic field but instead assume one of a discrete set of orientations.

The z-component of $\vec{\mu}$ is now certain due to the $\vec{B_0}$ field and is defined for all possible orientations by;

$$\mu_z = \gamma m_I \hbar \tag{2.5}$$

where m_I is the magnetic quantum number having $2I+1$ values representing the number of degenerate states for the atom:

$$m_I = -I, -I + 1, ...I \tag{2.6}$$

which in turn correspond to $2I+1$ possible orientations for $\vec{\mu}$ with respect to the direction of the external field. The angle θ between the magnetic moment and the applied magnetic field can be calculated using the following formula:

$$\cos \theta = \frac{\mu_z}{\mu} = \frac{m_I}{\sqrt{I(I+1)}} \tag{2.7}$$

For a spin 1/2 system, $I = 1/2$ and $m_I = \pm 1/2$ making $\theta = \pm 54° \, 44'$. These two possible orientations are commonly referred to as parallel (spin up) and

anti-parallel (spin down) states and are shown in Figure 2.1.
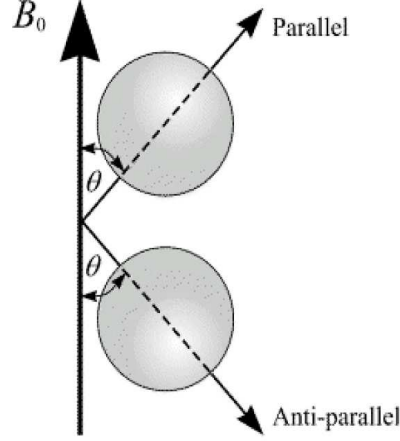
Figure 2.1: Spin 1/2 state orientations.

A magnetic moment in a magnetic field experiences a torque. The equation of motion for $\vec{\mu}$ is;

$$\frac{\mathrm{d}\vec{\mu}}{\mathrm{d}t} = \gamma \vec{\mu} \times \vec{B_0} \tag{2.8}$$

The solution to Eq 2.8 can be expressed by first re-writing the equation in scalar form as;

$$
\begin{aligned}
\frac{\mathrm{d}\mu_x}{\mathrm{d}t} &= \gamma B_0 \mu_y \\
\frac{\mathrm{d}\mu_y}{\mathrm{d}t} &= -\gamma B_0 \mu_x \\
\frac{\mathrm{d}\mu_z}{\mathrm{d}t} &= 0
\end{aligned}
\tag{2.9}
$$

By taking further derivatives with respect to time for the first two equations

decoupling can be achieved. The equations are now given by;

$$
\begin{aligned}
\frac{d^2\mu_x}{dt^2} &= -\gamma^2 B_0 \mu_x \\
\frac{d^2\mu_y}{dt^2} &= -\gamma^2 B_0 \mu_y
\end{aligned}
\tag{2.10}
$$

Setting the initial conditions to be $\mu_x(0)$, $\mu_y(0)$, and $\mu_z(0)$, the solutions to these equations are;

$$
\begin{aligned}
\mu_x(t) &= \mu_x(0)\cos(\gamma B_0 t) + \mu_y(0)\sin(\gamma B_0 t) \\
\mu_y(t) &= -\mu_x(0)\sin(\gamma B_0 t) + \mu_y(0)\cos(\gamma B_0 t) \\
\mu_z(t) &= \mu_z(0)
\end{aligned}
\tag{2.11}
$$

which can be expressed further as;

$$
\begin{aligned}
\mu_{xy}(t) &= \mu_{xy}(0)e^{-i\gamma B_0 t} \\
\mu_z(t) &= \mu_z(0)
\end{aligned}
\tag{2.12}
$$

From these solutions it is evident that the magnetic moment precesses about $\vec{B_0}$ at a frequency;

$$
\omega_0 = \gamma B_0
\tag{2.13}
$$

known as the Larmor frequency (Figure 2.2).

For MRI to be applicable a magnetic moment due to a proton must therefore have to exist resulting in a non zero net spin angular momentum of the nuclei. This is a consequence of the Pauli Exclusion Principle which states that in order to avoid degeneracy no two fermions (protons as applied here) can occupy the same quantum state. Thus nuclei such as ^{16}O cannot be imaged since they possess no net spin angular momentum due to their even
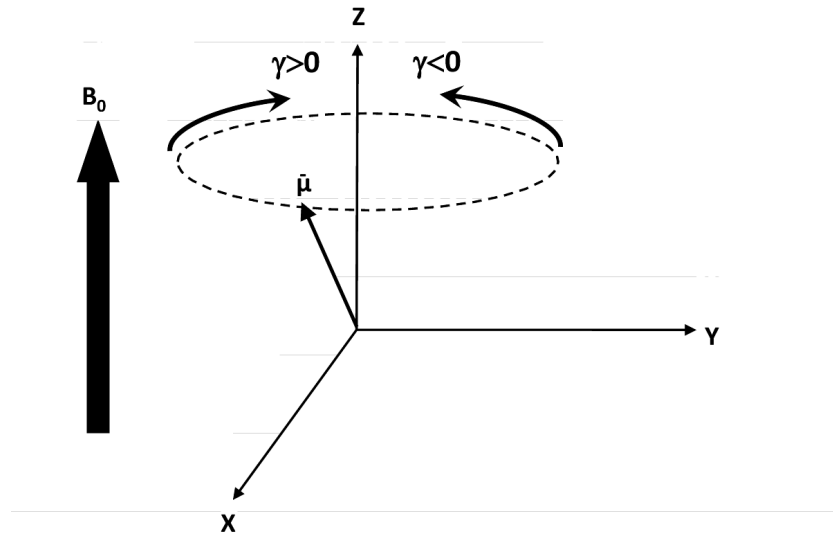
Figure 2.2: Spin precession. A spin, $\vec{\boldsymbol{\mu}}$, precesses around $\vec{\boldsymbol{B_0}}$ at the Larmor frequency. The direction of the precession is determined by the gyromagnetic ratio, γ.

mass and even charge numbers (so called even-even nuclei). Other nuclei including odd-odd and odd-even can be imaged as their net spin are half integers and integers respectively.

2.1.3 Bulk Magnetisation and Polarisation

In 2.1.2 it was shown that an isolated magnetic moment placed in an external uniform magnetic field can assume one of a number of states determined by the value m_I. Generally when involved with NMR imaging it is not just one magnetic moment (i.e. one proton) which is viewed but all the nuclei within the region of interest. To describe the effect of a large number of magnetic moments a bulk (macroscopic) magnetisation vector $\vec{\boldsymbol{M}}$ is introduced, which is the vector sum of all the individual (microscopic) magnetic moments over

the volume being imaged. This summation is expressed by;

$$\vec{M} = \sum_{n=1}^{N} \vec{\mu_n} \tag{2.14}$$

where N is the total number of magnetic moments in the object under scrutiny and $\vec{\mu_n}$ is the magnetic moment of an individual proton.

The equation of motion for $\vec{M}$ is given as;

$$\frac{d\vec{M}}{dt} = \gamma \vec{M} \times \vec{B_0} \tag{2.15}$$

which can be resolved into three coupled linear differential equations which are valid for a homogeneous $\vec{B_0}$ field;

$$\begin{aligned}
\frac{dM_x}{dt} &= \gamma(M_y B_z - M_z B_y) \\
\frac{dM_y}{dt} &= \gamma(M_z B_x - M_x B_z) \\
\frac{dM_z}{dt} &= \gamma(M_x B_y - M_y B_x)
\end{aligned} \tag{2.16}$$

It shall now be considered how every magnetic moment in our ensemble behaves collectively when placed in the $\vec{B_0}$ field.

Magnetic moments occupying the two possible states will have a potential energy given by;

$$\vec{E} = -\vec{\mu} \cdot \vec{B_0} \tag{2.17}$$

Keeping with the convention that the applied magnetic field is taken to lie along the z-direction, Eq 2.17 can be re-written as;

$$E = -\gamma \hbar m_I B_0 \tag{2.18}$$

The energy associated with the spin up state ($m_I = +1/2$) is given by;

$$E_+ = -1/2\gamma\hbar B_0 \tag{2.19}$$

whereas for the spin down state ($m_I = $ -1/2) the potential energy is;

$$E_- = 1/2\gamma\hbar B_0 \tag{2.20}$$

Equations 2.19 and 2.20 indicate that a lower energy level is associated with the spin up state resulting from magnetic moments aligning themselves parallel to the applied magnetic field as opposed to anti-parallel for the spin down state. The difference between the energy states is given by;

$$\Delta E = E_- - E_+ = \gamma\hbar B_0 \tag{2.21}$$

a phenomenon known as the Zeeman effect, shown in Figure 2.3
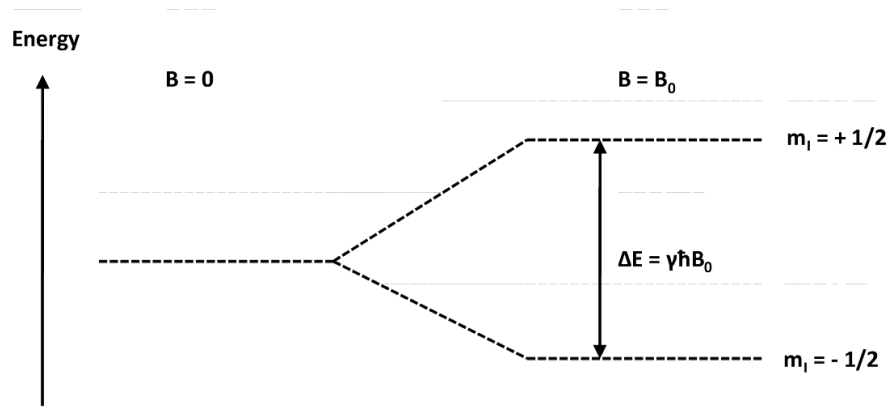
Figure 2.3: The Zeeman effect.

For a transition between the two energy states, quanta of energy equal to $\gamma\hbar B_0$ must be absorbed or emitted. This corresponds to electromagnetic

radiation of angular frequency ω_0 with energy $\hbar\omega_0$. Equating the energy of the electromagnetic radiation with the difference between the energy states the result is the previously defined Larmor equation given by Eq 2.13.

In thermal equilibrium, the population distribution between the two energy states is given by the Maxwell-Boltzmann distribution. The populations of both states are given by;

$$
\begin{aligned}
N_+ &= \frac{N}{Z} e^{\frac{\gamma \hbar B_0}{2k_B T}} \\
N_- &= \frac{N}{Z} e^{-\frac{\gamma \hbar B_0}{2k_B T}}
\end{aligned}
\tag{2.22}
$$

where N is the total number of spins, k_B is the Boltzmann constant, T is the temperature in Kelvin, and Z is the partition function for normalisation of the result:

$$
Z = \sum_{m_I=-I}^{I} e^{\frac{m_I \gamma \hbar B_0}{k_B T}}
\tag{2.23}
$$

For a spin $1/2$ system such as for ^{1}H nuclei, $Z = 2$.

By finding the difference in population of the two energy states under the high temperature approximation;

$$
N_+ - N_- = \frac{N\gamma \hbar B_0}{2k_B T}
\tag{2.24}
$$

it can be seen that there is an excess fraction of spins in the lower energy level spin up state. Thus only a small proportion of the total population of magnetic moments contribute to the bulk magnetisation vector. The bulk magnetisation vector can therefore be expressed as;

$$
\vec{\boldsymbol{M}} = N\vec{\boldsymbol{\mu}}P
\tag{2.25}
$$

where P is the polarisation of the ensemble of spins and is defined as;

$$P = \frac{N_+ - N_-}{N_+ + N_+} \qquad (2.26)$$

The polarisation due to a Maxwell-Boltzmann distribution of spins under the high temperature approximation is given by;

$$P = \tanh\left(\frac{\gamma \hbar B_0}{2k_B T}\right) \approx \frac{\gamma \hbar B_0}{2k_B T} \qquad (2.27)$$

Therefore the magnitude of the magnetisation vector is found to be;

$$M = M_0 = \frac{N\gamma^2 \hbar^2 B_0}{4k_B T} \qquad (2.28)$$

and for a spin-I system M is;

$$M = M_0 = \frac{N\gamma^2 \hbar^2 B_0 I(I+1)}{3k_B T} \qquad (2.29)$$

It can be seen from Eqs 2.28 and 2.29 that M_0 is the equilibrium magnetisation that the spin system establishes with its environment. It is evident from Eq 2.27 that the polarisation increases linearly with frequency and therefore with magnetic field strength. For protons in a 1.5 T field at 300 K, the polarisation is only $5.1 \times 10^{-4}\%$.

2.1.4   The $\vec{B_1}$ Excitation Field

The bulk magnetisation vector, $\vec{M}$, that results from an applied static field, $\vec{B_0}$, cannot be measured with a radio frequency (RF) receiver coil until it is perturbed from the z-axis thereby inducing electromotance that the receiver coil can detect. In order to perturb $\vec{M}$ from its equilibrium position, a second

magnetic field is required which is applied perpendicular to the main static field.

This so called excitation field comes in the form of a time dependent (i.e. oscillating) magnetic field denoted as $\vec{\boldsymbol{B_1}}$. As previously stated in 2.1.3, supplying energy to an ensemble of spins in quanta of $\hbar\omega_0$ causes transitions to occur resulting in emission or absorption of energy. It therefore becomes evident that in order to induce a transition between the energy states, the $\vec{\boldsymbol{B_1}}$ field oscillation frequency, ω_{rf}, must be equal to the Larmor frequency of the spin system which is determined by the applied static field. This is known as the resonance condition.

A typical $\vec{\boldsymbol{B_1}}$ excitation field is linearly polarised and is expressed in the form of;

$$\vec{\boldsymbol{B_1}} = 2B_1^e \cos(\omega_{rf}t + \phi)\hat{x} \tag{2.30}$$

for pulse envelope B_1^e, excitation carrier frequency ω_{rf}, and initial phase angle ϕ. This linearly polarised field can be decomposed into two circularly polarised fields rotating in opposite directions, shown as;

$$\vec{\boldsymbol{B_1}} = \vec{\boldsymbol{B_1}}^+ + \vec{\boldsymbol{B_1}}^- \tag{2.31}$$

$\vec{\boldsymbol{B_1}}^+$ and $\vec{\boldsymbol{B_1}}^-$ are given by;

$$
\begin{aligned}
\vec{\boldsymbol{B_1}}^+ &= B_1^e[\cos(\omega_{rf}t + \phi)\hat{x} - \sin(\omega_{rf}t + \phi)\hat{y}] \\
\vec{\boldsymbol{B_1}}^- &= B_1^e[\cos(\omega_{rf}t + \phi)\hat{x} + \sin(\omega_{rf}t + \phi)\hat{y}]
\end{aligned} \tag{2.32}
$$

where $\vec{\boldsymbol{B_1}}^+$ rotates clockwise and $\vec{\boldsymbol{B_1}}^-$ rotates anti-clockwise (Figure 2.4).

It can be shown that only the component of the $\vec{\boldsymbol{B_1}}$ field that is rotating in the same direction as the bulk magnetisation, represented by the $\vec{\boldsymbol{B_1}}^+$ field in
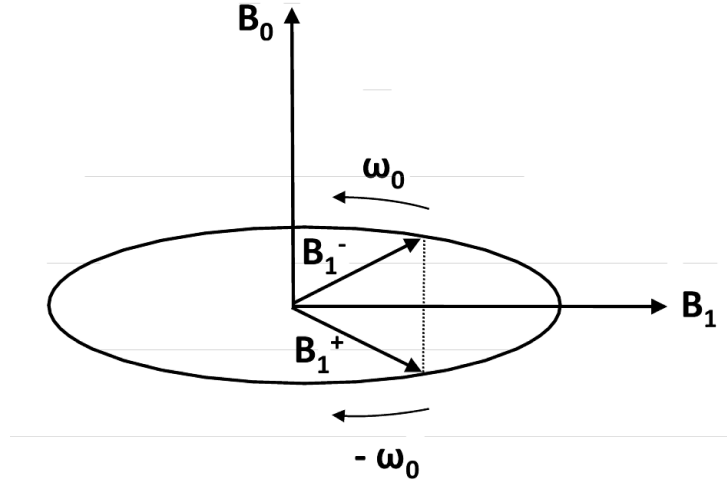
Figure 2.4: Circularly polarised field components of $\vec{B_1}$. If the excitation frequency of the $\vec{B_1}$ field is equal to the Larmor frequency, ω_0, then $\vec{B_1}^-$ can be neglected.

Eq 2.32 has a considerable effect. This is because the circularly polarised field rotating in the opposite direction, represented by the term $\vec{B_1}^-$, is always off resonance and if ω_{rf} is near the Larmor frequency then this term can be neglected since it has a minimal effect on the precessing bulk magnetisation. The $\vec{B_1}^+$ field is thus referred to as the transmit field.

The $\vec{B_1}$ field strength required for a linear polarised field can be seen to be twice that of a circularly polarised field which is why many modern MRI systems use quadrature transmitter coils to generate a circularly polarised field directly, thereby reducing power deposition within the imaged sample.

2.1.5   The Rotating Frame of Reference

The equation of motion for $\vec{M}$ when an RF excitation field is applied in the presence of a static field now becomes;

$$\frac{\mathrm{d}\vec{M}}{\mathrm{d}t} = \gamma\vec{M} \times (\vec{B_0} + \vec{B_1}) \tag{2.33}$$

The resulting precession of the bulk magnetisation is shown in Fig 2.5
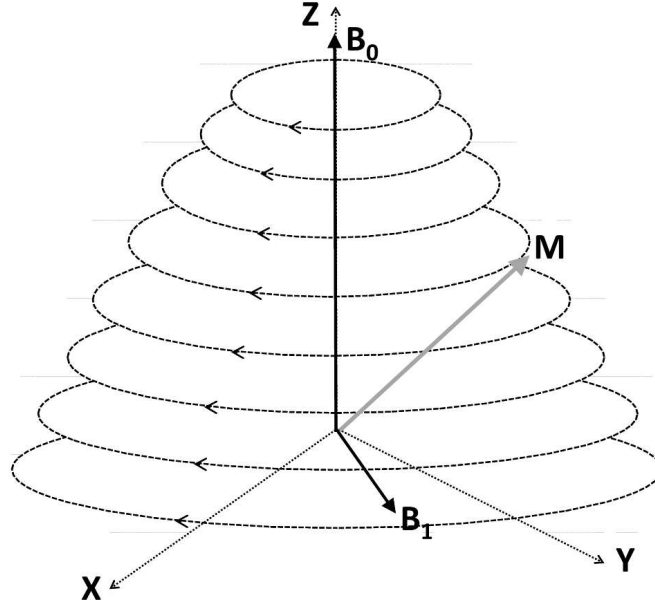
Figure 2.5: Precession of the bulk magnetisation, $\vec{M}$, in the laboratory frame of reference.

Viewed in the laboratory frame of reference, the precession of the bulk magnetisation can be seen to follow a complicated spiral path. If however the bulk magnetisation is viewed from a frame of reference which is rotating at the Larmor frequency the precession can be viewed simply as a tipping motion. The definition of the coordinates of the rotating frame are given as x', y', z' compared to the coordinates of the stationary laboratory frame given by x, y, z. Consider the unit vectors of this coordinate system $\hat{x}$, $\hat{y}$,

and $\hat{z}$ in any of the three dimensions rotating with angular velocity ω_{rf}, then;

$$
\begin{aligned}
\frac{\mathrm{d}\hat{x}}{\mathrm{d}t} &= \omega_{rf} \times \hat{x} \\
\frac{\mathrm{d}\hat{y}}{\mathrm{d}t} &= \omega_{rf} \times \hat{y} \\
\frac{\mathrm{d}\hat{z}}{\mathrm{d}t} &= \omega_{rf} \times \hat{z}
\end{aligned}
\tag{2.34}
$$

Assume a time dependent vector $\vec{A}$ rotating at the same angular velocity whose definition is given by;

$$
\vec{A} = A_x\hat{x} + A_y\hat{y} + A_z\hat{z}
\tag{2.35}
$$

The derivative of $\vec{A}$ is given by;

$$
\frac{\mathrm{d}\vec{A}}{\mathrm{d}t} = \frac{\mathrm{d}A_x}{\mathrm{d}t}\hat{x} + \frac{\mathrm{d}A_y}{\mathrm{d}t}\hat{y} + \frac{\mathrm{d}A_z}{\mathrm{d}t}\hat{z} + A_x\frac{\mathrm{d}\hat{x}}{\mathrm{d}t} + A_y\frac{\mathrm{d}\hat{y}}{\mathrm{d}t} + A_z\frac{\mathrm{d}\hat{z}}{\mathrm{d}t}
\tag{2.36}
$$

Using Eq 2.35 this equation can be re-written as;

$$
\frac{\mathrm{d}\vec{A}}{\mathrm{d}t} = \frac{\mathrm{d}A_x}{\mathrm{d}t}\hat{x} + \frac{\mathrm{d}A_y}{\mathrm{d}t}\hat{y} + \frac{\mathrm{d}A_z}{\mathrm{d}t}\hat{z} + \omega_{rf} \times \vec{A}
\tag{2.37}
$$

which can be simplified further to;

$$
\frac{\mathrm{d}\vec{A}}{\mathrm{d}t} = \frac{\partial\vec{A}}{\partial t} + \omega_{rf} \times \vec{A}
\tag{2.38}
$$

where $\partial\vec{A}/\partial t$ is the rate of change of $\vec{A}$ as observed in the rotating coordinate system. The equation of motion for the bulk magnetisation in the rotating frame of reference can therefore be written as;

$$
\frac{\partial\vec{M}}{\partial t} = \gamma\vec{M} \times \vec{B}_{eff}
\tag{2.39}
$$

where

$$\vec{B}_{eff} = \vec{B_1}\hat{x} + \left(\vec{B_0} - \frac{\omega_{rf}}{\gamma}\right)\hat{z} \qquad (2.40)$$

Equations 2.39 and 2.40 show that the effective field, $\vec{B}_{eff}$, affects the bulk magnetisation and is composed of the $\vec{B_0}$ field plus a fictitious field (ω_{rf}/γ) which is generated by the rotation of the rotating frame. If $\omega_{rf} = \omega_0$ then B_{eff} will be equal to $\vec{B_1}$ and there will be no effective field along the z'-axis meaning there will be no precession in the rotating frame. This is shown in Figure 2.6. When $\omega_{rf} \neq \omega_0$, due to the $\vec{B_1}$ field being off resonance, the bulk magnetisation will precess about $\vec{B}_{eff}$ as illustrated in Figure 2.7.
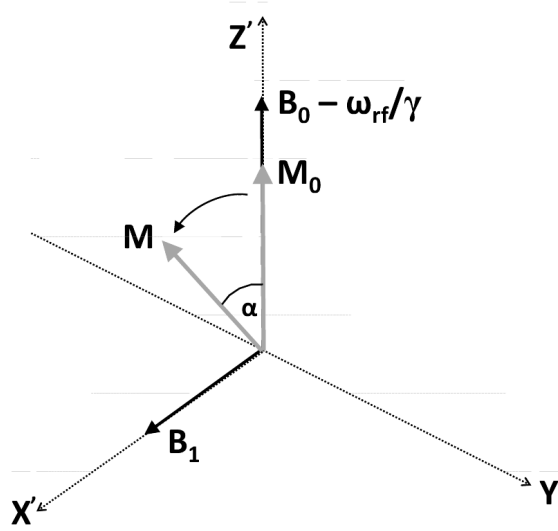
Figure 2.6: Precession of the bulk magnetisation, $\vec{M}$, in the rotating frame of reference. When $\omega_{rf} = \omega_0$, the precession can be viewed simply as a tipping motion.
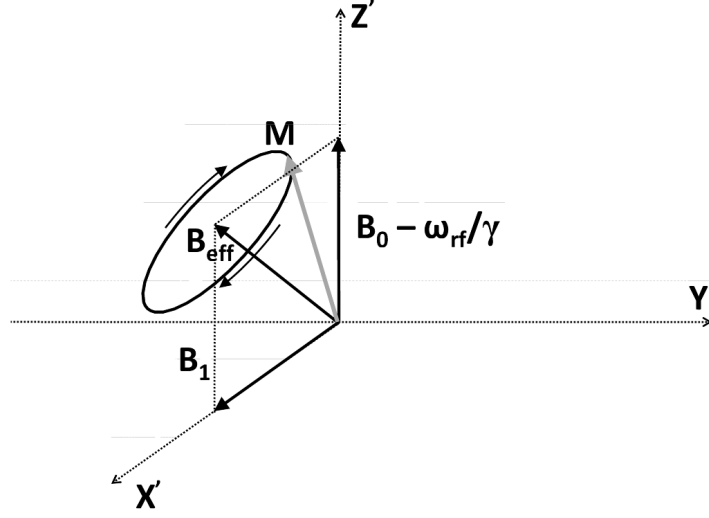
Figure 2.7: Precession of the bulk magnetisation, $\vec{M}$, in the rotating frame of reference. When $\omega_{rf} \neq \omega_0$, precession occurs about $\vec{B}_{eff}$.

2.1.6 The Flip Angle

As a result of applying an RF excitation field in the rotating frame, the bulk magnetisation will tilt away from the z'-axis into the $x'y'$ plane at an angle α. This is known as the flip angle and is given by;

$$\alpha = \gamma \int\limits_0^{T_P} B_1^e dt \tag{2.41}$$

where T_P is the pulse duration. The pulse envelope function B_1^e is commonly referred to as the RF pulse itself. This is because the initial phase angle, ϕ, is kept constant as is the excitation frequency, ω_{rf}, which is determined by the resonance condition meaning both of these parameters have no significant effect on the excitation profile of the RF pulse. Indeed, the excitation profile of an RF pulse can be fully characterised by taking the Fourier transform of

B_1^e using Fourier analysis (this will be discussed in more detail in 2.2.2).

If the envelope of the RF pulse is rectangular then the flip angle is given by;

$$\alpha = \gamma B_1 T_P \tag{2.42}$$

When the duration of the RF pulse is chosen to be $T_P = \pi/2\gamma B_1$ then the bulk magnetisation is tilted through 90° generating maximum transverse magnetisation. This is called a 90° pulse. Should the pulse duration be longer such that $T_P = \pi/\gamma B_1$ then the bulk magnetisation is tilted 180° and said to be inverted. This is known as a 180° pulse.

While the shape and duration of the pulse envelope determines the excitation profile of the RF pulse, they are not important when considering the flip angle providing $\int_0^{T_P} B_1^e dt$ is kept constant. For different envelope functions such as the previously mentioned rectangular pulse and the popular Sinc pulse, the bulk magnetisation will end up in the same location but will traverse a different trajectory during the excitation period.

Once the RF pulse is turned off, $\vec{M}$ will start to realign with the z'-axis and return to its equilibrium value, M_0, through the process of relaxation.

2.1.7 Spin Relaxation

T_1 Relaxation - Spin Lattice Relaxation

The T_1 relaxation process starts to take effect after the RF excitation pulse has ended. It is a measure of the characteristic time it takes the longitudinal component of the bulk magnetisation, M_z, to align with $\vec{B_0}$ and return to its equilibrium state M_0. The rate of change of M_z as it relaxes to M_0 can

be described by first order kinetics and is governed by the equation;

$$\frac{\mathrm{d}M_z}{\mathrm{d}t} = -\frac{M_z - M_0}{T_1} \tag{2.43}$$

This differential equation has the solution;

$$M_z(t) = M_0 + (M_z(0) - M_0)e^{-\left(\frac{t}{T_1}\right)} \tag{2.44}$$

where $M_z(0)$ is the value of M_z at $t = 0$, or immediately after $\vec{B}_1$ is turned off. At $t = T_1$, 63% of the longitudinal magnetisation is recovered and after $5T_1$ the sample is considered to be back to M_0 as shown in Figure 2.8.
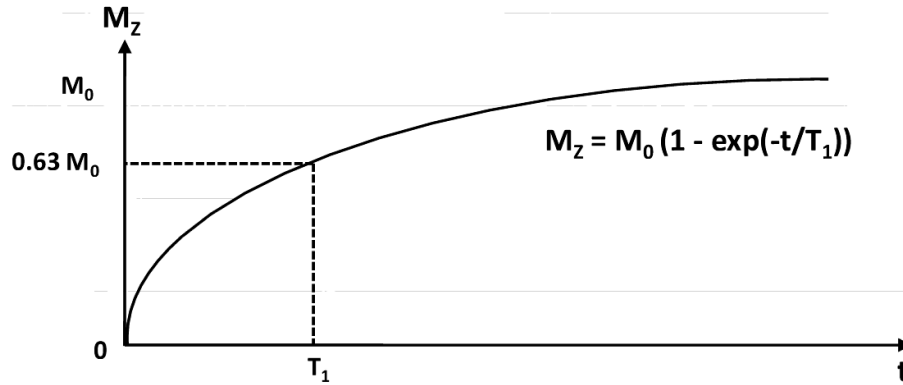
Figure 2.8: T_1 relaxation. At $t = T_1$, 63% of M_z has been recovered.

Spin lattice relaxation is typically induced by magnetic field fluctuations resulting from atomic or molecular motion which serve to transfer energy from the excited spin system to its environment (the 'lattice'). Specifically, this energy exchange occurs due to protons encountering a magnetic field which is fluctuating at the Larmor frequency. The source of this fluctuating field is a proton (or electron) attached to a molecule that is rotating at a rate which is similar to the Larmor frequency.

The molecular motion is characterised by the correlation time, τ_c, with such interactions being referred to as dipole-dipole interactions. For molecules with $\omega_0 \tau_c \sim 1$, then dipole-dipole interactions involving energy exchange are more efficient resulting in shorter T_1 values. Small molecules such as H_2O have short correlation times (faster molecular rotation) and are therefore ineffective at T_1 relaxation. The T_1 of pure water is thus the longest in-vivo (~ 4000 ms at 1.5 T). The protons of hydrogen nuclei in large macromolecules have long correlation times and also have long T_1 values. For H_2O molecules which are transiently bound to proteins and other macromolecules, the correlation times are much closer to $1/\omega_0$ resulting in shorter T_1 values. Free lipid molecules which are larger in size than water molecules also have shorter T_1 values. In general, the T_1 time increases with increased water content and decreases with increased macromolecular content.

The value of T_1 varies between different kinds of tissue and so provides an important source of contrast in MRI. It can be seen that T_1 is dependent on $\vec{B_0}$. By increasing the field strength then ω_0 increases and dipole-dipole interactions become more probable for molecules with shorter correlation times.

T_2 Relaxation - Spin-Spin Relaxation

When $\vec{M}$ relaxes towards it equilibrium state M_0, the transverse components of $\vec{M}$ must decay to zero. Spin-spin relaxation is a measure of the timescale for transverse magnetisation to persist in a uniform $\vec{B_0}$ field. However, due to local inhomogeneities in the $\vec{B_0}$ field, together with energy exchange between magnetic moments within the spin system (spin-spin interactions), phase coherence in the transverse plane will gradually be destroyed.

Loss of phase coherence occurs when protons experience a change in

their local magnetic field due to interactions with neighbouring protons. The amount of interaction is once again dependent on the correlation time. Molecules with long correlation times (slow molecular rotation) produce larger static fields causing greater dephasing which results in efficient T_2 relaxation and thus short T_2 values. Free water molecules have short correlation times hence have long T_2 values. Lipids with an intermediate correlation time also have an intermediate T_2 value relative to other tissues. In tissue, T_2 increases with increasing water content and decreases with increasing macromolecular content.

The T_2 relaxation time reflects both spin-lattice and spin-spin interactions and so is always less than or equal to T_1. Unlike T_1, T_2 is not as susceptible to $\vec{B_0}$ since it is primarily caused by local field imperfections.

The rate of change of transverse magnetisation is given by;

$$\begin{aligned} \frac{\mathrm{d}M_x}{\mathrm{d}t} &= -\frac{M_x}{T_2} \\ \frac{\mathrm{d}M_y}{\mathrm{d}t} &= -\frac{M_y}{T_2} \end{aligned} \tag{2.45}$$

where M_x and M_y are the components of the magnetisation along the x and y axis in the rotating frame of reference. These equations have the solutions;

$$\begin{aligned} M_x(t) &= M_x(0)e^{-\left(\frac{t}{T_2}\right)} \\ M_y(t) &= M_y(0)e^{-\left(\frac{t}{T_2}\right)} \end{aligned} \tag{2.46}$$

where $M_x(0)$ and $M_y(0)$ are the values of M_x and M_y at $t = 0$, immediately after $\vec{B_1}$ is switched off. The elapsed time between the maximum transverse magnetisation and 37% of this value is the T_2 decay constant shown in Figure 2.9.

If there are inhomogeneities in $\vec{B_0}$ then the transverse magnetisation loses phase coherence faster and the T_2 decay constant is replaced by the T_2^* decay constant.
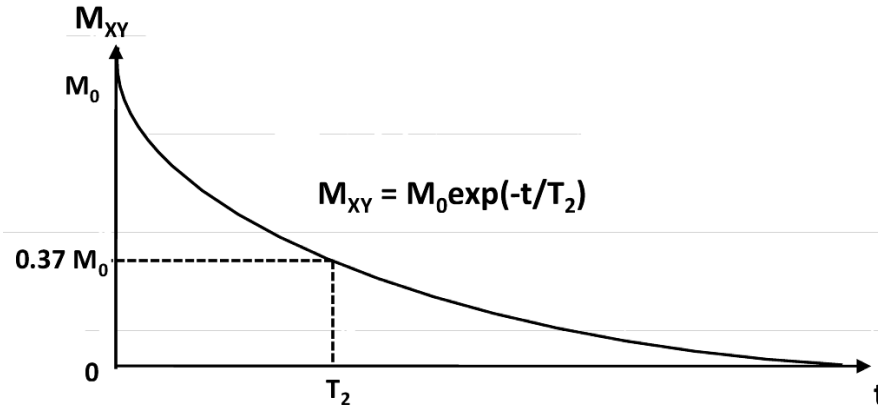
Figure 2.9: T_2 relaxation. At $t = T_2$, M_{xy} has decayed to 37% of its maximum value.

T_2^* Relaxation - Pseudo Relaxation

Pseudo relaxation is another method that contributes to the relaxation phenomenon. The T_2 relaxation process due to spin-spin interactions is a random process and is therefore irreversible. The faster T_2^* decay process is primarily due to an additional loss of phase coherence caused by inhomogeneities in the $\vec{B_0}$ field. These inhomogeneities may be attributed to intrinsic defects in the $\vec{B_0}$ field or may be caused by magnetic susceptibility effects from tissue or other materials placed in the field. Since these inhomogeneities are generally fixed in time and space then this additional loss of phase coherence is reversible.

The time constant for this decay, T_2^*, is related to T_2 by the equation;

$$\frac{1}{T_2^*} = \frac{1}{T_2} + \frac{1}{T_{2INH}} + \frac{1}{T_{2SUS}} + \frac{1}{T_{2OTHER}} \qquad (2.47)$$

where T_{2INH}, T_{2SUS}, and T_{2OTHER} are the transverse magnetisation relaxation constants due to inhomogeneities in the magnetic field, local differences in susceptibility and magnetisation, and other processes.

2.1.8   The Bloch Equations

By combining the equations of motion from section 2.1.3 with the relaxation equations from section 2.1.7 the complete equations of motion for the magnetisation vector in the laboratory frame are obtained;

$$\begin{aligned}
\frac{\mathrm{d}M_x}{\mathrm{d}t} &= \gamma(M_y B_z - M_z B_y) - \frac{M_x}{T_2} \\
\frac{\mathrm{d}M_y}{\mathrm{d}t} &= \gamma(M_z B_x - M_x B_z) - \frac{M_y}{T_2} \\
\frac{\mathrm{d}M_z}{\mathrm{d}t} &= \gamma(M_x B_y - M_y B_x) - \frac{M_z - M_0}{T_1}
\end{aligned} \qquad (2.48)$$

These are the Bloch equations [5] which in vectorial notation can be written as;

$$\frac{\mathrm{d}\vec{\boldsymbol{M}}}{\mathrm{d}t} = \gamma\vec{\boldsymbol{M}} \times \vec{\boldsymbol{B}}_{\boldsymbol{0}} - \frac{M_x\hat{x} + M_y\hat{y}}{T_2} - \frac{M_z - M_0}{T_1}\hat{z} \qquad (2.49)$$

and in the reference frame written as;

$$\frac{\partial\vec{\boldsymbol{M}}}{\partial t} = \gamma\vec{\boldsymbol{M}} \times \vec{\boldsymbol{B}}_{\boldsymbol{eff}} - \frac{M_{x'}\hat{x} + M_{y'}\hat{y}}{T_2} - \frac{M_{z'} - M_0}{T_1}\hat{z} \qquad (2.50)$$

In the presence of an RF pulse, $\vec{B}_1 = B_1\hat{x}$, the Bloch equations in the rotating frame of reference can be written out explicitly;

$$
\begin{aligned}
\frac{\mathrm{d}M_{x'}}{\mathrm{d}t} &= \gamma M_{y'}\left(B_0 - \frac{\omega_{rf}}{\gamma}\right) - \frac{M_{x'}}{T_2} \\
\frac{\mathrm{d}M_{y'}}{\mathrm{d}t} &= \gamma M_{z'}B_1 - \gamma M_{x'}\left(B_0 - \frac{\omega_{rf}}{\gamma}\right) - \frac{M_{y'}}{T_2} \\
\frac{\mathrm{d}M_{z'}}{\mathrm{d}t} &= \gamma M_{y'}B_1 - \frac{M_{z'} - M_0}{T_1}
\end{aligned}
\tag{2.51}
$$

2.1.9 Free Induction Decay and Signal Detection

Once tilted away from the z'-axis, the transverse component of $\vec{M}$ becomes a rotating vector (i.e. it precesses) which generates an oscillating RF field that can be detected using a suitable receiver coil. These coils are tuned and matched with capacitors such that the electronic resonance matches the Larmor frequency. The coils used for the work in this thesis are presented in Chapter 4.

The amplitude of the oscillating RF field decays exponentially with an envelope of $e^{-\left(\frac{t}{T_2}\right)}$. The initial amplitude of this field is determined by how much transverse magnetisation is generated and therefore dependent on the flip angle. The precession of the transverse magnetisation is observed as an induced electromotive force across the receiver coil, this is known as the Free Induction Decay (FID).

The induced voltage in the coil, ignoring relaxation effects is given by;

$$
V(t) = -\omega_0 \int |M_{xy}(\vec{r})||B_1^-(\vec{r})| \sin[\omega_0 t + \Phi_0(\vec{r}) - \Phi_{B_1}(\vec{r})]\mathrm{d}\vec{r}
\tag{2.52}
$$

Equation 2.52 explicitly shows that the detected signal voltage is dependent on the transverse magnetisation in the laboratory frame, $M_{xy}(\vec{r})$, at $t =$

0; the sensitivity of the receiver coil B_1^-, in the transverse plane; and the precession frequency, ω_0, the Larmor frequency in this example. The terms $\Phi_0(\vec{r})$ and $\Phi_{B_1}(\vec{r})$ represent the phase of the transverse magnetisation at $t = 0$ and phase of the receiver coil respectively.

Once detected, the signal is mixed with a reference signal oscillating at ω_{ref} followed by low pass filtering to remove the high frequency component. This process is known as phase sensitive detection (PSD) and is employed to obtain the M_x and M_y components. With normal PSD, only one of these components is being measured. With quadrature detection, two PSD systems that are 90° out of phase are used to measure both components together at the same time.

Assuming that the reference signal is $V_{ref}(t) = 2\cos(\omega_{ref}t)$, after mixing and applying low pass filtering, the output for a single PSD system is;

$$V_{PSD_1} = \omega_0 \int |M_{xy}(\vec{r})||B_1^-(\vec{r})| \cos\left[-\Delta\omega t + \Phi_0(\vec{r}) - \Phi_{B_1}(\vec{r}) + \frac{\pi}{2}\right] \mathrm{d}\vec{r}$$

(2.53)

where $\Delta\omega = \omega_0 - \omega_{ref}$.

With quadrature detection, a second PSD with a reference signal of $V_{ref}(t) = 2\sin(\omega_{ref}t)$ which is 90° phase shifted relative to the first PSD is implemented. The output from this detection system is;

$$V_{PSD_2} = \omega_0 \int |M_{xy}(\vec{r})||B_1^-(\vec{r})| \sin\left[-\Delta\omega t + \Phi_0(\vec{r}) - \Phi_{B_1}(\vec{r}) + \frac{\pi}{2}\right] \mathrm{d}\vec{r}$$

(2.54)

The two outputs can be combined to give a complex demodulated signal, $S(t)$, given by;

$$S(t) = S_R(t) + iS_I(t)$$

(2.55)

where $S_R(t)$ and $S_I(t)$ are the outputs from the first and second PSDs given

in Eqs 2.53 and 2.54. The signal is then recorded using an analogue to digital converter and digitised for subsequent processing.

Interpretation of a time domain response such as the FID becomes difficult when a number of frequencies are contained within it. It is often easier to interpret the complex signal, $S(t)$, once it has been Fourier transformed into the frequency domain, $S(\omega)$ by;

$$S(\omega) = \int_{0}^{\infty} e^{(i\omega t)} \mathrm{d}t \qquad (2.56)$$

The Fourier transform allows each individual frequency contained within the FID to be assigned specific sinusoidal and cosinusoidal components in the frequency domain. The real and imaginary parts of the complex frequency spectrum $S(\omega)$ are called the absorption and dispersion spectra respectively.

In MRI, the magnitude spectrum $|S(\omega)|$ is considered foremost.

2.1.10   The Spin Echo

In 2.1.7 it was shown that the spin-spin interaction which describes T_2 relaxation is an inherent property of the sample which cannot be avoided. However, the signal loss due to T_2^* relaxation can be recovered by the use of a spin echo. An echo signal describes the process of when a spin isochromat that has lost phase coherence reverses its direction. Through time, the set of magnetisation vectors will realign, and then begin to lose their coherence again. The process creates a two sided FID called an echo of the signal.

In order to produce a spin echo a $90°$ pulse is applied along x'-direction to create maximum transverse magnetisation, $M_{x'y'}$, followed by a delay of τ before a $180°$ refocusing pulse along the same axis is implemented. Another delay of τ after the $180°$ pulse results in re-established phase coherence at

time 2τ. The time from the 90° excitation pulse to the centre of the echo (i.e. $t = 2\tau$) is called the echo time (TE).

The amplitude of the echo is smaller than that of the FID due to irreversible T_2 relaxation having decayed by $e^{-\left(\frac{TE}{T_2}\right)}$. Additional 180° pulses will produce similar echoes with further decreasing amplitudes.

Applying the 90° and 180° pulses along the same axis in the rotating frame of reference (i.e. the pulses are in phase) is known as the Carr-Purcell pulse sequence (shown in Figure 2.10). The Carr-Purcell spin echo sequence requires exact 180° pulses with any errors accumulating after each echo. The effect of an error in the 180° pulse can be reduced by using the Carr-Purcell-Meiboom-Gill (CPMG) pulse sequence. The CPMG sequence is identical to the Carr-Purcell sequence except that in this sequence the 180° pulses are phase shifted by 90° with respect to the 90° excitation pulse (shown in Figure 2.11).
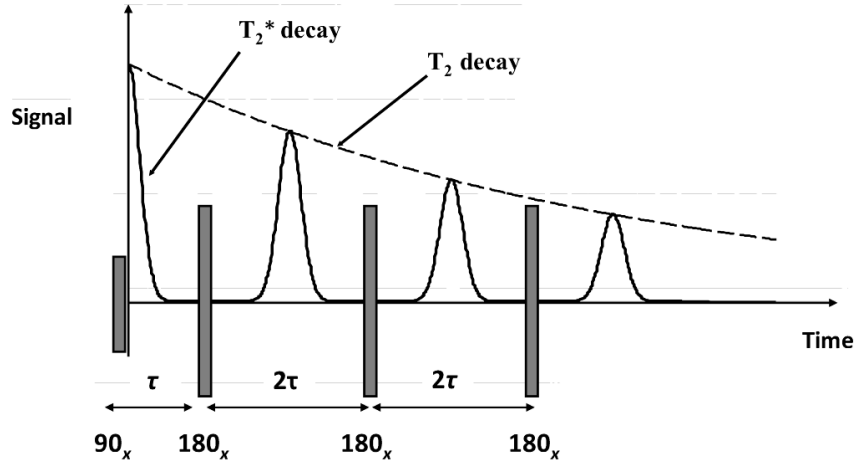
Figure 2.10: Carr-Purcell spin echo sequence. The 90° and 180° pulses are applied along the same axis.
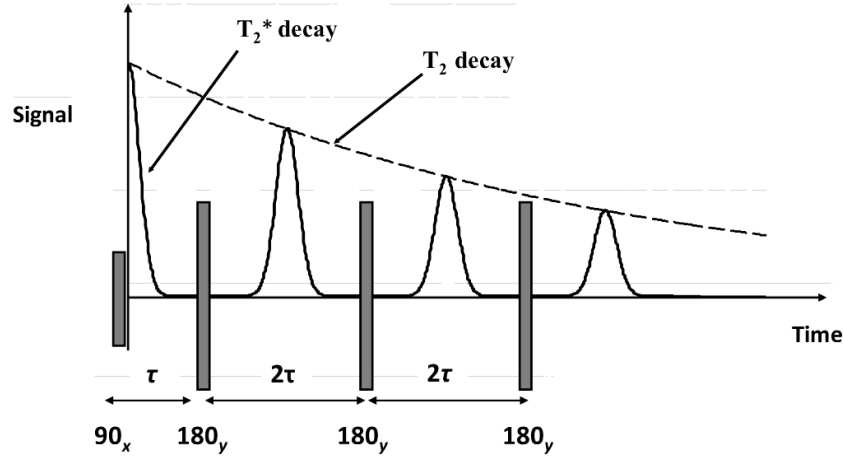
Figure 2.11: Carr-Purcell-Meiboom-Gill spin echo sequence. The 180° pulses are phase shifted by 90° with respect to the 90° excitation pulse.

2.2 MRI

2.2.1 Application of Linear Field Gradients

To reproduce an image, one must be able to derive a method for encoding spatial information on the observed signal, $S(t)$. Such encoding is achieved through the use of field gradients. The field gradient operates in conjunction with the main field $\vec{B_0}$ and also in the same direction (in the z-direction). Therefore it is the z component of the $\vec{B_0}$ field, B_z which is modified and made to vary in the x, y, or z directions. For example, if a gradient G_x is applied in the x-direction, B_z can be written as;

$$B_z(x) = B_0 + G_x x \hat{z} \tag{2.57}$$

The position dependent angular frequency becomes;

$$\omega_z(x) = \omega_0 + \gamma G_x x \hat{z} \tag{2.58}$$

Magnetic resonance imagers have three gradient coils to allow the generation of the field gradients in all three orthogonal directions. The three methods of spatial discrimination used in MRI are referred to as; frequency encoding, phase encoding, and selective excitation. These three independent steps allow a single scalar relationship ($\omega_0 = -\gamma B_0$) to encode a 3D object.

2.2.2 Selective Excitation and Refocusing

In MRI it is often necessary to excite a slice within the sample being imaged. In order to obtain the desired slice of spins that are to be excited a magnetic field gradient is played out concurrently with a shaped RF pulse to select a slice of thickness Δz as shown in Figure 2.12.
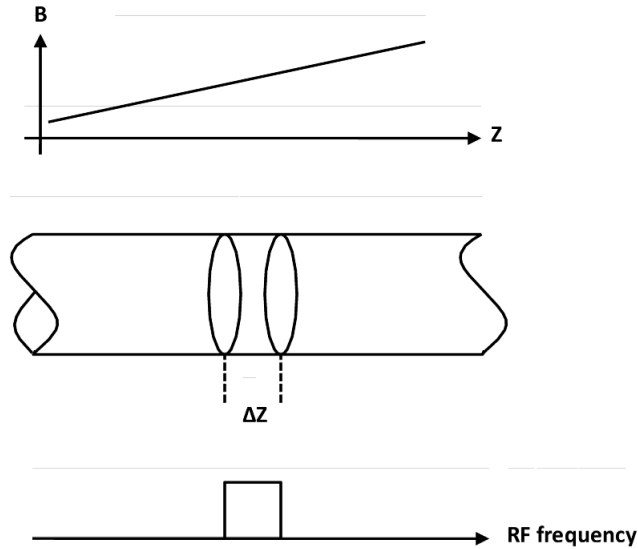
Figure 2.12: Selective excitation. A slice of thickness Δz within a sample is acquired by playing out a slice selective gradient during RF excitation.

As previously mentioned in 2.1.6, the band of frequencies excited by an RF pulse can be determined by taking the Fourier transform of the pulse envelope. For a rectangular pulse envelope of width T, this yields a SINC

distribution of frequencies with first zero crossings at $\pm 1/T$ (top of Figure 2.13).

Ideally, a rectangular frequency spectrum would be used allowing a rectangular profile of spins to be excited. This is achieved through the application of a SINC shaped RF pulse (bottom of Figure 2.13). The bandwidth of the SINC pulse is given by [6];

$$\Delta v = \frac{1}{\tau} \tag{2.59}$$

where τ is the duration from the maximum of the SINC pulse to its first zero crossing.
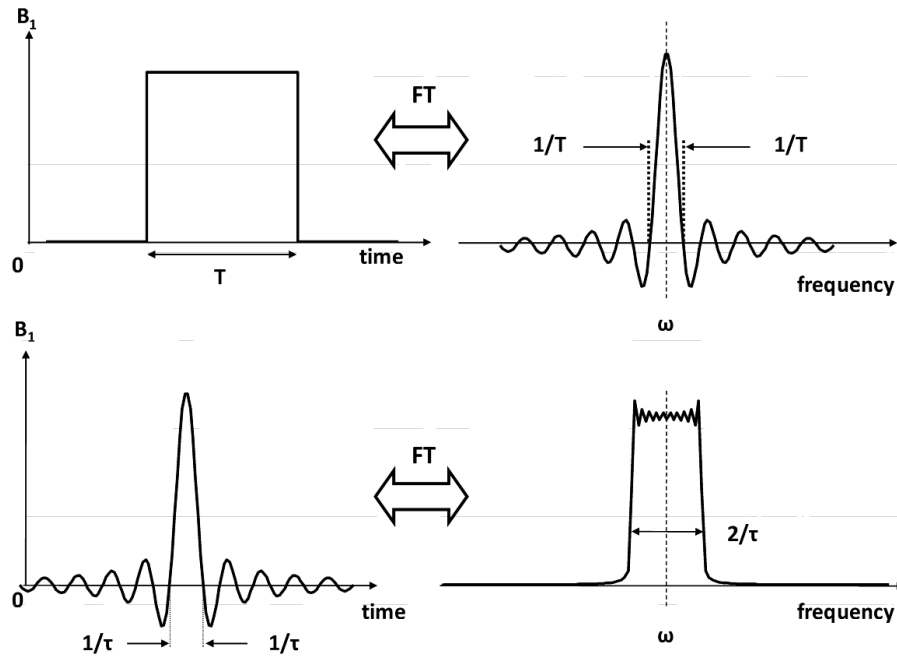
Figure 2.13: Fourier transform of rectangular and SINC RF pulse envelopes and their resulting frequency spectrum profiles.

The combination of a magnetic field gradient and a frequency selective

pulse only excites spins within a region of the sample defined by;

$$\Delta z = \frac{2\pi}{\gamma G_z \tau} \tag{2.60}$$

where G_z is the strength of the magnetic field gradient. The bandwidth of the RF pulse is usually fixed and the thickness of the slice is controlled by changing the amplitude of the gradient.

Since the applied RF pulse is of a finite duration, the SINC pulse envelope must be truncated. Truncating the pulse has the effect of producing ringing at the edges of the rectangular slice profile due to the so called Gibbs' phenomenon. To reduce this effect, the pulse envelope can be weighted by a Gaussian function in the time domain (i.e. an apodised pulse) to give a better approximation to a rectangular slice profile. By minimising pulse truncation effects a more uniform excitation profile is achieved and cross talk between neighbouring slices is reduced.

The slice selection gradient introduces a linear variation of phases across the slice thickness. If this phase dispersion of transverse magnetisation is not compensated for then undesirable signal loss will occur. By applying a slice refocusing gradient which has opposite polarity to the slice selection gradient and lasts half as long, the phase coherence of the transverse magnetisation is restored.

The exact nature of the introduced phase dispersion during the excitation period is determined by the phase properties of the selective excitation RF pulse. Only when the RF pulse has a linear phase is the phase dispersion also linear across the slice. In order to be precise, loss of phase coherence during the excitation period should be calculated from the Bloch equations.

2.2.3 Spatial Encoding

Having selected a slice, the spin ensemble within it must now be localised in two other orthogonal directions. The MR signal from the spins has three components; amplitude, frequency, and phase. Spatial encoding is accomplished by manipulating the frequency and phase of the signal while the amplitude provides greyscale information.

2.2.4 k-space

For MRI, the primary objective is to create a plot of the intensity of detected precessing magnetisation ($S(t)$) as a function of spatial position in image space (i.e. $S(x,y)$). Early in the development of MRI it was recognised that the detected time varying signals could be analysed and understood much more easily by directly mapping them into a domain called k-space. The k-space is the Fourier conjugate to image space. This formalism of acquiring data in k-space and then transforming it into image space is attributed to Likes [7] and Ljunggren [8].

In the presence of an applied field gradient, $\vec{G}$, Eq 2.55 can be written as;

$$S(t) = \omega_0 e^{\left(\frac{i\pi}{2}\right)} \int M_\perp(\vec{r}) B_\perp(\vec{r}) e^{-(i\Delta\omega t)} e^{-\left(i\gamma\vec{G}\cdot\vec{r}t\right)} \mathrm{d}\vec{r} \qquad (2.61)$$

where $M_\perp(\vec{r}) = |M_{xy}(\vec{r})| e^{-i\Phi_0(\vec{r})}$, $B_\perp(\vec{r}) = |B_1^-(\vec{r})| e^{-i\Phi_{B_1}(\vec{r})}$, and $\vec{r}$ is a spatial vector.

Omitting the scaling constant $\omega_0 e^{\left(\frac{i\pi}{2}\right)}$ and mixing out the carrier frequency (i.e. $\Delta\omega = 0$) the MR signal is given by;

$$S(t) = \int M_\perp(\vec{r}) B_\perp(\vec{r}) e^{-\left(i\gamma\vec{G}\cdot\vec{r}t\right)} \mathrm{d}\vec{r} \qquad (2.62)$$

By defining the k-space vector as;

$$\vec{k} = \frac{\gamma \vec{G} t}{2\pi} \tag{2.63}$$

Eq 2.62 can be re-written as;

$$S(t) = \int M_\perp(\vec{r}) B_\perp(\vec{r}) e^{-\left(i2\pi \vec{k} \cdot \vec{r}\right)} \mathrm{d}\vec{r} \tag{2.64}$$

In this form, it becomes evident that the addition of linear field gradients are encoding the MR signal such that received signal is the Fourier transform of the transverse magnetisation weighted by the receiver coil sensitivity.

In order to move through k-space either the duration (t) or amplitude of the field gradient must be varied (usually it is the amplitude of the field gradient). The rate of k-space traversal is determined by the gradient amplitude and also by γ as it is clear from Eq 2.63. As k increases, higher spatial frequencies are sampled which results in higher resolution images. Most pulse sequences are designed to sample k-space symmetrically in order to maximise signal to noise.

2.2.5 Frequency Encoding and the Gradient Echo

Incorporating a field gradient in the x-direction ($\vec{G} = G_x x \hat{z}$) allows a position dependence to be encoded into the precessional frequency as demonstrated in Eq 2.58. The direction in which the received signal is frequency encoded is given by the direction of k, which is also the direction of $\vec{G}$. If one imposes a field gradient on a sample, the MR signal will contain information about the spatial location of the resonating spins. If for example a sample receives an RF pulse of a particular flip angle, followed by a linear gradient in the

x direction, then position is encoded (see Figure 2.14). The position at the centre of the sample is taken as $x = 0$ thus the Larmor frequency defines the centre position within the sample. Any point away from the centre of the sample will have a different precessional frequency.
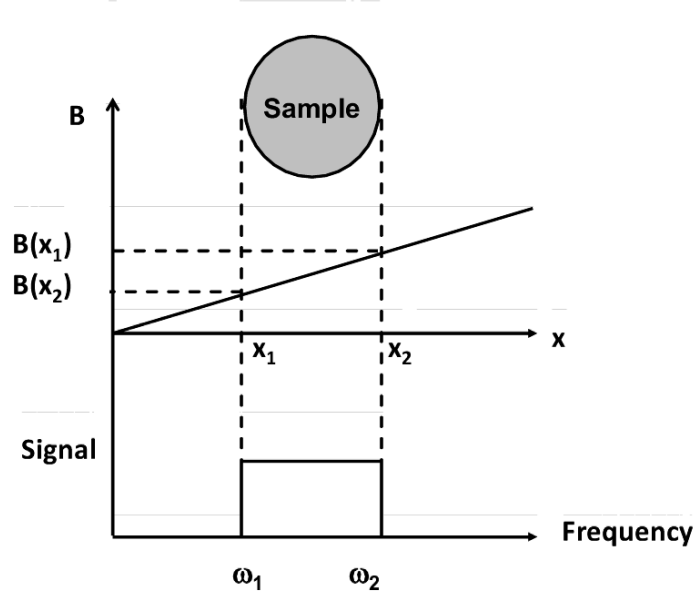
Figure 2.14: A frequency difference is created between two excited areas of the sample (x_1 and x_2) by applying a gradient along the x-direction.

The frequency encoding gradient is commonly referred to as the readout gradient since encoding occurs during signal acquisition. The signal received from the selected slice in the presence of the readout gradient is;

$$S(k_x) = \int_x M_\perp(x) B_\perp(x) e^{-(i2\pi k_x x)} \mathrm{d}x \qquad (2.65)$$

where $M_\perp(x) B_\perp(x)$ is representative of the spin distribution along the x-axis of the imaged sample.

The application of a frequency encoding gradient once again introduces a linear dispersion of phase that is dependent on the position in the direction

of the gradient.

$$\Phi(x) = -\gamma G_x x t_{FE} \tag{2.66}$$

Phase coherence may be restored at $t_{FE} = 0$ by the addition of a prephasing gradient of opposite polarity, $-G_x$, applied for a time $t_{FE}/2$ in a manner similar to that used to refocus a slice selective excitation. When phase coherence is restored at $t_{FE} = 0$ a gradient echo occurs (shown in Figure 2.15).
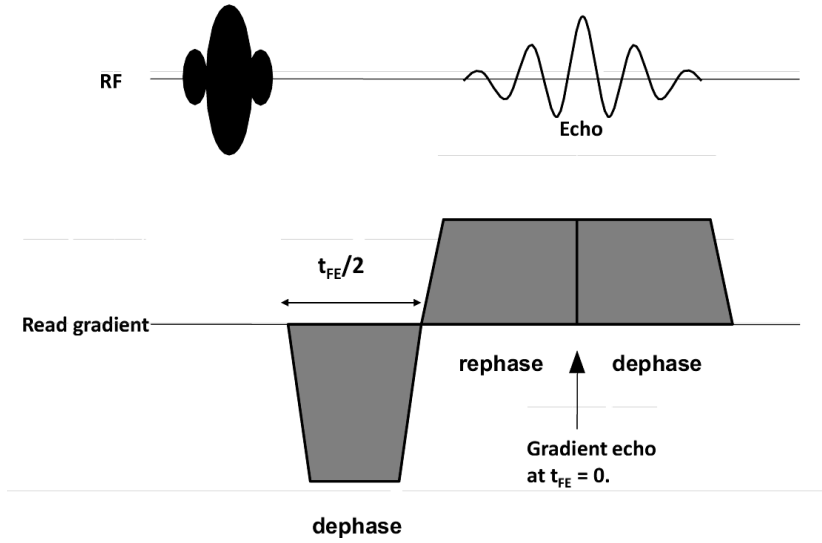
Figure 2.15: The gradient echo. Spins can be brought into phase coherence at $t_{FE} = 0$ by first applying a prephasing gradient for a time $t_{FE}/2$ and then a rephasing gradient of equal duration but opposite polarity.

The gradient echo only provides refocusing of phase shifts created by the applied gradient. Other dephasing mechanisms such as spatial $\vec{B_0}$ inhomogeneity will not be refocused (in contrast to the spin echo). Consequently, the signal decays with a T_2^* relaxation rate, albeit with the addition of spatial encoding. By using both a spin echo and a gradient echo full refocusing of coherent dephasing mechanisms can be achieved whilst providing spatial information.

Utilising the concept of k-space, it can be understood that the prephasing

gradient results in the translation to the negative k_x axis. When phase coherence is restored at $t_{FE} = 0$, this corresponds to both the prephasing gradient and the readout gradient having the same area and being at $k_x = 0$. The readout gradient then remains active for an additional $t_{FE}/2$ time period so that the positive k_x axis is spanned. This process is what produces symmetric k-space coverage.

During digitisation k-space is sampled at N discrete points at intervals Δt in time. Because k-space and image space are related through Fourier transformation, the image field of view (FOV) and resolution are dependent on how k-space is sampled. Using the Nyquist relations, the FOV is inversely proportional to the rate at which k-space is sampled;

$$FOV_x = \frac{2\pi}{\Delta k_x} = \frac{2\pi}{\gamma G_x \Delta t} \qquad (2.67)$$

The spatial resolution of the image is the FOV divided by the number of sampled points;

$$\Delta x = \frac{FOV_x}{N} = \frac{2\pi}{\gamma G_x N \Delta t} = \frac{2\pi}{\gamma G_x T} \qquad (2.68)$$

where $T = N\Delta t$.

If the values of G_x or Δt are not considered appropriately, the FOV will be smaller than the size of the object being imaged. This results in aliasing artefacts and will be discussed further in Chapter 4.

2.2.6 Phase Encoding

The technique of phase encoding involves applying a field gradient to establish a linear phase difference over different positions. If the field gradient G_y along the y-direction is applied ($\vec{G} = G_y y \hat{z}$) spins located at higher fields will precess faster that those at lower fields. When the gradient is turned off

after time T_{PE}, each position will have a different phase angle given by;

$$\Phi(y) = -\gamma G_y y T_{PE} \tag{2.69}$$

Phase encoding can be understood as pre-frequency encoding the signal for a short duration which results in a non-encoded signal with an initial phase angle that is position dependent. The received phase encoded signal can be calculated as;

$$S(k_y) = \int\limits_y M_\perp(y) B_\perp(y) e^{-(i2\pi k_y y)} \mathrm{d}y \tag{2.70}$$

Unlike frequency encoding, phase encoding of the signal takes place before the signal is recorded. The phase associated with the y gradient remains unaltered when data sampling along k_x because $G_y = 0$ when $G_x \neq 0$.

It is not possible to unambiguously identify a position, y, from a single measurement of $S(k_y)$, therefore multiple values of k_y need to be acquired. Repeated excursions in the k_y direction are achieved by altering the amplitude of G_y by ΔG_y and also the gradient polarity to sample both the $-k_y$ and $+k_y$ directions.

Similarly to frequency encoding, the choice of phase encode time, T_{PE}, and step size of the phase encode gradient, ΔG_y, should be chosen appropriately to avoid aliasing. The field of view in this direction is given by;

$$FOV_y = \frac{2\pi}{\Delta k_y} = \frac{2\pi}{\gamma \Delta G_y T_{PE}} \tag{2.71}$$

The spatial resolution in the phase encode direction is given by;

$$\Delta y = \frac{FOV_y}{M} = \frac{2\pi}{\gamma M \Delta G_y T_{PE}} \tag{2.72}$$

In order to acquire all M phase encode steps, it is necessary to repeat the acquisition by M times. The duration of time between successive acquisitions is called the repetition time and is represented by the variable TR.

2.2.7 Spin Warp Imaging

Utilising all the three methods of spatial discrimination in a spin warp pulse sequence, an image can be acquired from anywhere within a 3D object. For a readout gradient in the x-direction and a phase encode gradient in the y-direction, the resultant image is on the axial plane. Combining equations 2.65 and 2.70 gives us the equation for a 2D encoded MR signal;

$$S(k_x, k_y) = \int\limits_x \int\limits_y M_\perp(x, y) B_\perp(x, y) e^{-(i2\pi(k_x x + k_y y))} \mathrm{d}x\mathrm{d}y \qquad (2.73)$$

Figures 2.16 and 2.17 show the spin warp pulse sequence diagram for both spin echo and gradient echo techniques. The echo in both of the figures is sampled N times, with M repetitions each with a different phase encoding gradient amplitude to generate a $N \times M$ matrix of k-space (shown in Figure 2.18). This matrix is then 2D Fourier transformed to produce an image which is the Cartesian representation of the weighted transverse magnetisation, commonly referred to as the spin density.
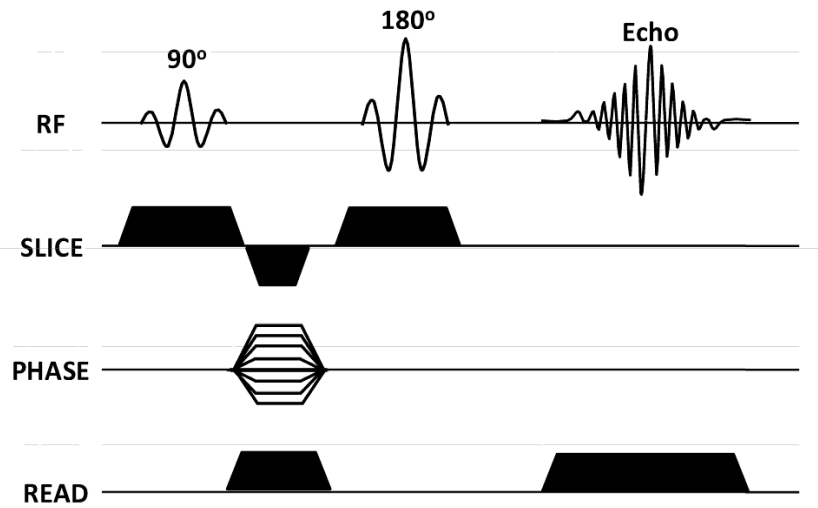
Figure 2.16: 2D spin echo sequence.
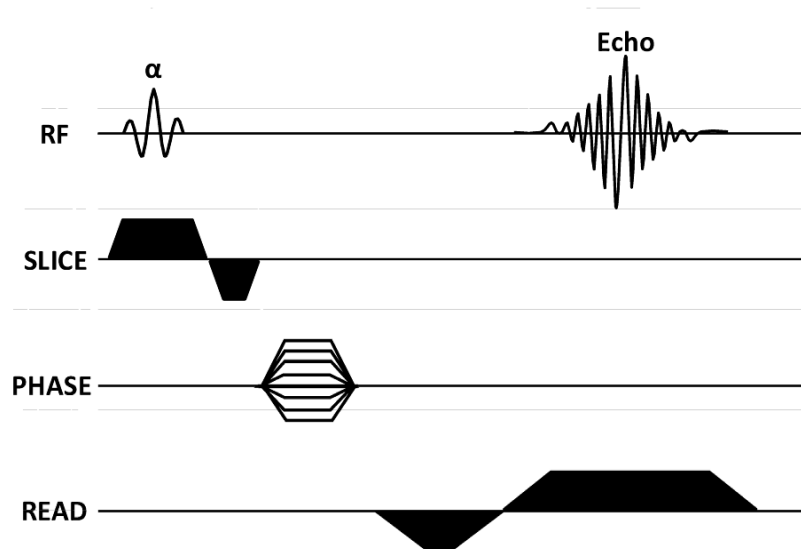
Figure 2.17: 2D gradient echo sequence.
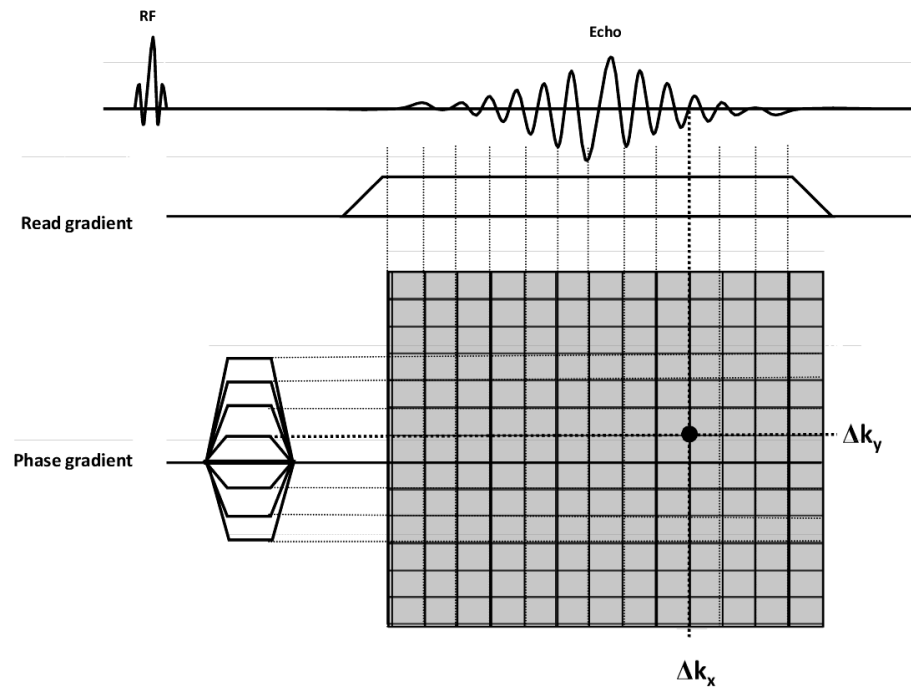
Figure 2.18: k-space acquisition matrix. Once all of k-space has been covered, a 2D Fourier transform is performed to produce an image.

2.2.8 The Signal to Noise Ratio

The measurement of an MR signal includes both the true signal voltage and a background noise voltage which is superimposed on it. The noise voltage is attributed to several sources; the receiver coil, the sample, and noise from background radiation. Each of these noise sources is associated with a resistance and generates a thermal noise voltage governed by Planck's black body radiation law, given as;

$$V_N = \sqrt{4k_B T R \Delta f} \qquad (2.74)$$

where k_B is Boltzmann's constant, T is the temperature, R is the resistance, and Δf is the frequency bandwidth of the receiver.

All the noise sources are assumed to be at an equivalent temperature, and, consistent with quasi-static assumptions, noise from background radiation is usually much less than the other noise sources and is ignored, leaving;

$$V_N = \sqrt{4k_B T \left(R_C + R_S \right) \Delta f} \qquad (2.75)$$

where R_C and R_S are the resistances of the coil and sample.

The magnitude of the noise voltage does not provide much information. Instead, a more useful quantity is the signal to noise ratio (SNR) which characterises the quality of the MR signal. The signal to noise ratio is defined as;

$$SNR = \frac{V_{Sig}}{V_N} \qquad (2.76)$$

The induced signal voltage, V_{Sig}, was given in Eq 2.55 and can be expressed as;

$$V_{Sig} = \omega_0 \int M_\perp(\vec{r}) B_\perp(\vec{r}) \mathrm{d}\vec{r} \qquad (2.77)$$

after mixing out the carrier frequency and omitting the scaling constant $e^{\left(\frac{i\pi}{2}\right)}$.

For a small volume, ΔV, assuming the sample and coil sensitivity are homogeneous; the signal voltage is equal to;

$$V_{Sig} = \omega_0 \left(\frac{N\gamma^2\hbar^2 B_0}{4k_B T} \sin\alpha \right) B_1^- \Delta V \qquad (2.78)$$

Combining Eqs 2.75 and 2.78 into 2.76 gives the SNR of an image voxel;

$$SNR = \frac{V_{Sig}}{V_N} = \left(\frac{N\gamma^3\hbar^2 B_0^2}{\sqrt{24k_B^3 T^3}} \sin\alpha \Delta V \right) \left(\frac{B_1^-}{\sqrt{R_C + R_S}\sqrt{\Delta f}} \right) \qquad (2.79)$$

The signal would ideally be acquired directly at this point (at the terminals of the coil) but must be pre-amplified, combined, filtered, and demodulated before it can be digitised and acquired. All these steps degrade the SNR and are quantified by an overall noise figure. Optimisation of the receiver coil design through maximisation of the second term in Eq 2.79 is addressed in Chapter 4 of this thesis.

2.3 Hyperpolarised Gas MRI

2.3.1 Introduction

Hyperpolarisation is a technique where the polarisation (P) of nuclei can be increased by up to a factor of 10^5 which overcomes the signal loss from the lower gas density which is 3 orders of magnitude smaller than for water protons [9, 10]. Therefore the MR signal from a gas at atmospheric pressure can be more than an order of magnitude greater than that of an equal volume of water.

Optical pumping from polarised laser light to the nuclei of noble gases is

a technique that is able to achieve high nuclear polarisation by a nonequilibrium means. This is done by exploiting the quantum mechanical selection rules of angular momentum. Under such conditions the spin polarisation is determined by factors that are not dependent on the applied magnetic field such as the operating power of the laser and the mixture of the gas.

2.3.2 Literature Review

It was shown by Kastler more than 50 years ago [11–13] that circularly polarised light could be used to optically pump electronic spins of alkali metal vapours into non-Boltzmann population distributions. In the early 1960's Bouchiat [9] and Colegrove [10] developed techniques to hyperpolarise noble gases using laser optical methods.

Noble gases are amenable to high non equilibrium polarisations due their nuclei possessing long spin lattice relaxation times. These long T_1s are the result of electron filled orbitals which produce neither an electric field gradient nor a magnetic field at their nucleus. As noble gases are monatomic there are also no interactions with nearby nuclear moments or molecular moments which occur in polyatomic molecules. It is for these reasons that the spins of noble gases relax much more slowly than the spins of other gases or hydrogen protons in water.

The primary candidates to be used as tracers for void space imaging are ^{3}He and ^{129}Xe because they are the only non radioactive noble gases with spin 1/2. Isotopes with a nuclear spin greater than 1/2 possess an electric quadrupole moment making them sensitive to torque resulting from induced electric field gradients.

It was not until 1994 that Albert *et al* were to demonstrate that hyperpolarised ^{129}Xe could provide sufficient signal to image the lungs of a mouse [14].

Most clinical applications now use hyperpolarised ^{3}He [15, 16] as it can be polarised to a higher degree and provides a much larger NMR signal due to it having a gyromagnetic ratio almost three times that of ^{129}Xe . Such hyperpolarised ^{3}He can be mixed with ^{4}He and N_2 and inhaled by a patient enabling high resolution imaging of the lungs. Ebert *et al* demonstrated this for the first time along with Bachert *et al* in 1996 [17, 18].

^{3}He can be polarised by two established methods which rely on the optical pumping technique: spin exchange optical pumping (SEOP) [19–21], an indirect process of transferring angular momentum from a polarised laser beam to ^{3}He nuclei via alkali metal atoms (usually rubidium), and metastable exchange optical pumping (MEOP) [22, 23], a direct process of transferring angular momentum from laser light to the ^{3}He atoms.

2.3.3 SEOP

Alkali metal spin exchange is capable of achieving moderate to high levels of nuclear spin polarisation in both ^{129}Xe and ^{3}He.

The first step in the SEOP method is the transformation of circularly polarised light with either positive (σ^+) or negative (σ^-) helicity into electronic spin polarisation. The laser light is circularly polarised by a quarter-wave plate before reaching the optical cell to ensure efficient transfer of angular momentum to the electron spins of the alkali metal. The polarised light is tuned to the electric dipole (D_1) transition of the alkali metal vapour (794.7 nm for Rb) resulting in the excitation of the electronic ground state ($nS_{1/2}$) into the excited $nP_{1/2}$ state. For Rb, the principal quantum number n is equal to 5; S and P represent quantum numbers of 0 and 1 respectively, and the subscript 1/2 refers to the total angular momentum quantum number j for both states. Both the ground and excited states have two sublevels

corresponding to the magnetic quantum number $m_j = \pm 1/2$.

Using the example of σ^+ light, the -1/2 ground state sublevel is depopulated which results in an accumulation of population into the +1/2 excited state sublevel (angular momentum is therefore conserved). Once the valence electron has been promoted to the excited state, collisional mixing ensures that the state decays with equal probability back to the two ground state sublevels. Because only one ground state sublevel can absorb light, eventually all the Rb atoms are optically pumped into the nonabsorbing sublevel. An electronic spin polarisation of nearly 100% can thus be achieved within time scales of tens of microseconds. Often, N_2 is added to the gas mixture to quench fluorescence of the excited alkali metal atoms which serves to depolarise the electronic spins.

The second stage of SEOP is to transfer the electronic polarisation to the nuclei of the noble gas. This transfer is achieved by collisions in which spin exchange is permitted via Fermi-contact hyperfine interactions between the electron spins and the noble gas nuclear spins [24]. This interaction is the result of the polarised electron wavefunction of the alkali metal overlapping the noble gas nucleus causing both a nuclear and electronic spin flip (i.e. spin exchange). After the collision, the alkali metal atom is restored to its previous spin orientation by continued optical pumping, ready to collide with another noble gas atom.

The nuclear polarisation therefore grows exponentially as a function of time but is limited by undesirable spin rotation interactions caused by collisions in which electronic spin orientation is lost without a nuclear spin flip. The efficiency of the polarisation process is therefore a balance between these competing physical processes. The SEOP technique is illustrated in Figure 2.19
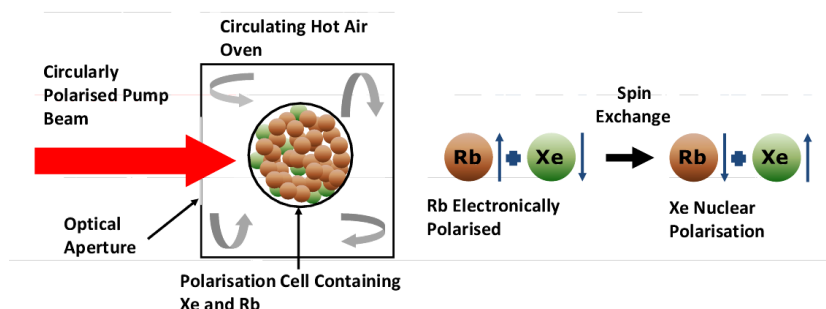
Figure 2.19: The SEOP technique. Circularly polarised laser light creates a large electronic spin polarisation within the Rb atoms. This electronic polarisation is then transfered to the noble gas nuclei (^{129}Xe in this figure) via spin exchange.

2.3.4 MEOP

Developed at about the same time as SEOP, MEOP is a polarisation technique involving only ^{3}He since the only available metastable states for ^{129}Xe interact with radiative states, thereby destroying any polarisation. The main difference from SEOP is that the electron-nuclear coupling takes place in the absence of an alkali vapour intermediary.

Before optical pumping can occur, the sample of ^{3}He is subjected to a weak but continuous plasma discharge so that a fraction of the atoms ($\sim 10^{-6}$) are excited into the metastable 2^3S_1 state. This is done under low pressure in order to preserve the metastable state and to avoid pressure broadening of the optical pumping transitions. The long lived metastable state can then be optically pumped by absorbing circularly polarised light tuned to the C_8/C_9 lines (1083 nm) resulting in the promotion of atoms to the 2^3P excited state.

Nuclear polarisation results from the strong hyperfine coupling between the electronic and nuclear spins of the metastable atoms. Nonetheless, as

with SEOP, collisions are still required to produce laser polarised ^{3}He. During a collision, an orientated metastable ^{3}He atom collides with a ground state ^{3}He atom whose nucleus is unpolarised. The products of such a collision are a ground state ^{3}He atom with a spin polarised nucleus and a depolarised metastable atom. This depolarised metastable atom can then continue the polarisation process by absorbing another photon of circularly polarised light.
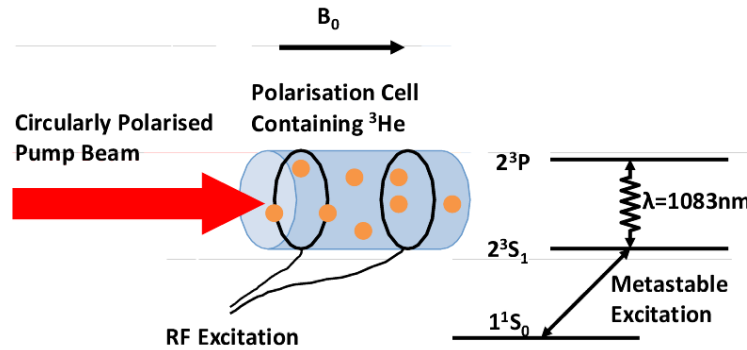
Figure 2.20: The MEOP technique. A weak RF discharge is applied across the polarisation cell in order to excite the ^{3}He atoms into the metastable 2^3S_1 state. This state is then pumped with circularly polarised light resulting in atoms being promoted to the 2^3P state. Collisions between ground state ^{3}He atoms and atoms in the excited metastable state result in nuclear spin polarised ^{3}He.

Other than only being applicable to ^{3}He, the other major disadvantage of MEOP is the need to compress the gas from low pressure to atmospheric pressure in order to create a viable quantity of polarised gas to image with. Such a compressor must not contain any ferromagnetic or other depolarising materials that would otherwise lead to catastrophic relaxation of the polarised ^{3}He. These disadvantages are balanced against the extremely high photon efficiency which is typically near unity, as compared to about 0.05 for Rb-^{3}He SEOP [25]. The characteristic time for polarising ^{3}He is therefore

measured in tens of seconds as opposed to several hours for SEOP.

2.3.5 Imaging Under Non-Equilibrium Conditions

In conventional MRI, after a RF pulse has sampled the longitudinal magnetisation (M_z), said magnetisation is then replenished to thermal equilibrium by T_1 relaxation. For laser polarised gases, the longitudinal magnetisation can only be replenished by a fresh supply of polarised gas. With each sampling of the magnetisation, the RF pulse destroys a portion of the longitudinal magnetisation. As such, employing 90° RF pulses in sequences that require multiple excitations (90° RF pulses can be used in single shot sequences such as RARE) to acquire all lines of k-space will not work because there won't be any residual longitudinal magnetisation after the first view. In order to appropriately sample k-space, the gradient echo sequence using a small flip angle (α) is the most widely used approach.

Since there is no recovery, the repetition time, TR, can be made as short as possible to reduce the scan time. As the gas is sampled during a breath hold period, the signal contribution from the nth view is given by [26]:

$$S(n) = M_z(0)e^{\left[-(n-1)\frac{TR}{T_1}\right]} \cos^{n-1}\alpha \sin\alpha \qquad (2.80)$$

Because T_1 is usually long ($TR \ll T_1$), spin lattice relaxation can be neglected in most cases. The optimal flip angle is therefore a trade off between the generation of transverse magnetisation (maximising $\sin\alpha$) and the rationing of nonrecoverable longitudinal magnetisation given by $M_z(0)\cos^{n-1}\alpha$.

Another consideration which must be taken into account is that of signal depletion over the course of data sampling. Initially, there is a larger amount of magnetisation available for the RF pulses to sample but due to each RF

pulse consuming some of this magnetisation later pulses will have less of it to sample resulting in a steady depletion of signal. This is inherent of the term $e^{\left[-(n-1)\frac{TR}{T_1}\right]}\cos^{n-1}\alpha$. This results in a k-space filter due to different Fourier components of k-space having intensities modified by the exponential decay term. This leads to artefacts such as blurring as each pixel in the image is a convolution of the actual magnetisation with a lorentzian. For flip angles less than $10°$, signal level changes are small so the effects of a k-space filter are negligible.

An alternative to using constant flip angle RF pulses is to employ variable flip angle excitations that yield a more uniform k-space filter [27,28]. Variable flip angle sequences also have better SNR because the magnetisation is more economically sampled. However, the performance of a variable flip angle sequence is very sensitive to deviations from the desired flip angle values [29], as can occur due to $\vec{B_1}$ inhomogeneity or miscalibration of the RF transmitter. In practice, it is difficult to program this sequence and most studies use an optimised constant flip angle acquisition.

2.3.6 Low Field Imaging

Because the nuclear polarisation of laser polarised noble gases is achieved by optical pumping and not by the applied magnetic, the potential of low field imaging has emerged.

There are many advantages that may be gained from MRI at lower fields. The cost of magnets is less, open geometry permanent magnets can provide more friendly scanners (important for paediatrics) and susceptibility gradients in the lung are reduced (see 3.8.3). Durand *et al* [30] have imaged human lungs at 0.1 T using a single shot multiple spin echo sequence [31]. Due to reduced susceptibility effects at low field, T_2 relaxation times are much longer

and so the CPMG echoes could be acquired within the single shot.

Chapter 3

Diffusion MRI

3.1 Introduction

Diffusion weighted imaging (DWI) has become one of the most rapidly evolving techniques in the MRI field due to its numerous clinical and research applications. These applications range from early diagnosis of acute ischaemic stroke [32] to studying white matter degeneration in multiple sclerosis and dementia. Recently, diffusion MRI of laser polarised gases has been used for studying chronic obstructive pulmonary diseases such as emphysema. The possibility of imaging gases directly within the lung offers the potential for assessing pulmonary ventilation, gas exchange, and microstructural changes. Diffusion MRI also provides a quantitative measurement rather than just an image.

3.2 The Diffusion Coefficient

3.2.1 Fick's Law

Diffusion (i.e. Brownian motion) is a term used to describe the motion of molecules due to random thermal motion. The diffusion process depends on temperature, size of the molecules, and their surroundings. The process is driven by differences in concentration, C, and can be described by Fick's second law;

$$\frac{\partial C}{\partial t} = D \frac{\partial^2 C}{\partial x^2} \tag{3.1}$$

where the diffusion coefficient, D, is the proportionality constant that relates the particle flux ($\partial C/\partial t$) to the concentration gradient ($\partial^2 C/\partial x^2$) and reflects the mobility of the molecules in their micro environment. Equation 3.1 is one dimensional but can be extended to three dimensions;

$$\frac{\partial C}{\partial t} = D \left(\frac{\partial^2 C}{\partial x^2} + \frac{\partial^2 C}{\partial y^2} + \frac{\partial^2 C}{\partial z^2} \right) = D \nabla^2 C \tag{3.2}$$

The above equation only holds true for isotropic diffusion, if diffusion is anisotropic (which will be discussed further later) then a tensor is invoked to describe this case and is defined as;

$$\mathbf{D} = \begin{pmatrix} D_{xx} & D_{xy} & D_{xz} \\ D_{yx} & D_{yy} & D_{yz} \\ D_{zx} & D_{zy} & D_{zz} \end{pmatrix} \tag{3.3}$$

with Fick's second law becoming;

$$\frac{\partial C}{\partial t} = \sum_{i,j} D_{ij} \frac{\partial^2 C}{\partial i \partial j} \tag{3.4}$$

For water molecules and other uncharged molecules $D_{ij} = D_{ji}$ hence the diffusion tensor can be defined by six coefficients instead of nine.

From basic kinetic gas theory, the diffusion coefficient is proportional to;

$$D \propto \sqrt{\frac{T^3}{M}} \frac{1}{P\sigma} \qquad (3.5)$$

where T is absolute temperature and P is the pressure of the system. The diffusion coefficient can be reduced by mixing inert buffer gases of high molecular mass, M, and/or large collision cross sections, σ, both of which act as spatial restrictions on ^{3}He in the gas phase (this will be discussed further in 3.2.4).

3.2.2 Free Diffusion

The random displacement of atoms due to Brownian motion makes it impossible to predict the behaviour of an individual atom by deterministic dynamics. The averaged characteristics of the whole ensemble of atoms then become of interest and are described by probability theory.

For the simple case of 1D diffusion, the atoms can move in either a -ve or +ve direction with the same probability with respect to a central position of $x = 0$ (i.e. the origin). The mean displacement is therefore not a useful characteristic when estimating how far the atoms have moved because the average will be zero. Instead, the mean square displacement from the origin is calculated which will always be positive and over time assumes a Gaussian probability distribution. The mean square displacement for unrestricted diffusion can be calculated as;

$$|X^2| = 2n_d D_0 t \qquad (3.6)$$

where n_d is the number of dimensions, t is the diffusion time, and D_0 represents the free diffusion coefficient. The root mean square displacement is defined as;

$$X_{rms} = \sqrt{2n_d D_0 t} \tag{3.7}$$

3.2.3 Restricted Diffusion

In experiments where D_0 is large and the sample size (L) is small, the translational motion of atoms becomes restricted. To characterise the restricted diffusion a dimensionless ratio is defined as;

$$\xi = \frac{D_0 t}{L^2} \tag{3.8}$$

For $\xi \ll 1$ the atoms will still appear to be freely diffusing whereas for $\xi > 1$ diffusion becomes restricted. The diffusion coefficients of gases are three to four orders of magnitude higher than those of liquids making them particularly appropriate for probing porous media such as the lung microstructure.

The restricted diffusion from the small length scales of the lung airspaces is characterised by a time and scale dependent apparent diffusion coefficient (ADC).

Restricted diffusion of ^{3}He in the parenchyma of healthy guinea pig and human lungs has been reported by Chen *et al* and Saam *et al* [33, 34]. An average ADC value of 0.19 ± 0.06 cm^2 s^{-1} was observed by Chen *et al* while a distribution between 0.17 and 0.25 cm^2 s^{-1} was reported by Saam *et al*. The report by Saam *et al* also included results from five patients with severe emphysema and found the ADC to be approximately 2.5 times that of healthy lungs. Salerno *et al* [35] found the mean ADC for a group of 12 healthy volunteers to be 0.23 cm^2 s^{-1} which is in the same range as

that observed by Chen *et al* and Saam *et al.* Their study also included patients with emphysema of varying severity and found the overall mean ADC was a factor of 2 greater then that of the volunteers. A more recent study by Morbach *et al* [36] reported ADC values of 0.173 ± 0.045 and 0.276 ± 0.075 cm^2 s^{-1} (mean value $\pm$ 1 standard deviation) in healthy volunteers and patients with pulmonary emphysema respectively.

It has been found that the ADC appears to be sensitive to gravitational effects that result in variations of alveolar size [37]. The reason for this is not clear but may be a result of sleeping positions. Fichele *et al* examined posture dependent gravitational effects and found a difference of 9% between dependent and non dependent regions in a healthy lung. The study reported that the ADC was higher in the uppermost regions of the lung compared to the lowermost regions.

3.2.4 Diffusion Coefficients in Gas Mixtures

The self diffusion coefficient of ^{3}He, defined as D_3, is the diffusion of the substance through itself and is $D_3 = 1.8 \pm 0.2$ cm^{-2} s^{-1} [38]. Mutual diffusion is the diffusion of an isotopic species at infinite dilution through a second species and is also referred to as binary diffusion. The diffusion coefficient of ^{3}He in a binary mixture of N_2 is $D_{3N2} = 0.798 \pm 0.018$ cm^2 s^{-1} at 324 K and 1 atmosphere [39]. Using classical theory for transport in dilute gases [40], the binary diffusion coefficient of ^{3}He in a gas containing another component, i, is given by;

$$D_{3i} = \frac{3}{16} \frac{\sqrt{2\pi k_B^3 T^3}}{P \pi \sigma^2 \Omega^{(1,1)*}} \sqrt{\frac{M_3 + M_i}{M_3 M_i}} \qquad (3.9)$$

where k_B is the Boltzmann constant; M_3 and M_i are the atomic mass of ^{3}He and the binary component respectively; $\pi \sigma^2$ is the collision cross section in

a rigid sphere model; T is the temperature of the gas in units of Kelvin; P is the total pressure of the binary mixture in units of atmospheres; and $\Omega^{(1,1)*}$ a T-dependent factor depending on the actual inter-atomic potential.

The self diffusion coefficient of a gas can be obtained from Eq 3.9 by observing that for a one gas system $M_3 = M_i$ and $P = P_{3He}$ thus;

$$D_3 = \frac{3}{16} \frac{\sqrt{2\pi k_B^3 T^3}}{P_{3He} \pi \sigma^2 \Omega^{(1,1)*}} \sqrt{\frac{2}{M_3}} \qquad (3.10)$$

The free diffusion coefficient of a gas mixture is usually written as function of reduced diffusion coefficients that account for the partial pressures in the mixture. Using the example of a binary mixture of ^{3}He and N_2, the observed diffusion of ^{3}He (the signal carrying isotope) in the mixture is;

$$\begin{aligned}
\frac{1}{D} &= \frac{P_{3He}}{D_3(P=1)} + \frac{P_{N2}}{D_{3N2}(P=1)} \\
&= \frac{1}{D_3(P=P_{3He})} + \frac{1}{D_{3N2}(P=P_{N2})}
\end{aligned} \qquad (3.11)$$

where $D_3(P=1)$ and $D_{3N2}(P=1)$ are the pressure independent reduced diffusion coefficients and simply represent the self and binary diffusion coefficients evaluated at a pressure of one atmosphere. Equation 3.11 demonstrates that the diffusion of ^{3}He through the mixture of gases is equivalent to the diffusion of one atom of ^{3}He through the rest of the atoms of ^{3}He in addition to the diffusion of one atom of ^{3}He through the atoms of N_2.

Several authors [41, 42] have published empirical formulae to calculate reduced diffusion coefficients as a function of temperature ($\mathcal{D}(T)$) for a wide range of gas mixtures. For mixtures containing helium, the experimental data were obtained for ^{4}He, and the faster diffusion of ^{3}He can be calculated by taking into account the ratio of the relevant reduced masses. The numerical

formulae and reduced mass ratios for ^{3}He in the three most pertinent gases to this thesis are collected in Table 3.1.

$D_3/D_4 = \sqrt{4/3}$
$D_{34}/D_4 = \sqrt{7/6}$
$D_{3N2}/D_{4N2} = \sqrt{31/24}$
$D_{3O2}/D_{4O2} = \sqrt{35/27}$
$\mathcal{D}_3 = P_3 D_3 = 1.997(T/300)^{1.71}$
$\mathcal{D}_{34} = P_4 D_{34} = 1.868(T/300)^{1.71}$
$\mathcal{D}_{3N2} = P_{N2} D_{3N2} = 0.811(T/300)^{1.65}$
$\mathcal{D}_{3O2} = P_{O2} D_{3O2} = 0.857(T/300)^{1.65}$

Table 3.1: A table showing the reduced mass ratios (first 4 lines) and reduced diffusion coefficients (last 4 lines) at a given temperature (Kelvins) and pressure (atmospheres).

For a typical in vivo experiment in which the inhaled bolus (^{3}He mixed with ^{4}He) mixes with a subject's lung contents, Eq 3.11 can be extended further;

$$\frac{1}{D} = \frac{P_{3He}}{\mathcal{D}_3(T)} + \frac{P_{4He}}{\mathcal{D}_{34}(T)} + \frac{P_{N2}}{\mathcal{D}_{3N2}(T)} + \frac{P_{O2}}{\mathcal{D}_{3O2}(T)} \qquad (3.12)$$

allowing the free diffusion coefficient to be evaluated. The in vivo gas composition will vary due to water vapour saturation and alveolar exchange throughout time. Lastly, it should be noted that this entire discussion only holds for the case of unrestricted diffusion.

3.3   Diffusion Weighted Imaging

NMR was used to measure diffusion long before MRI was first proposed in the early 1970's. The unwanted influence of self diffusion on spin echo amplitudes was first recognised by Hahn in 1950 [43]. Hahn's idea was further extended by Carr and Purcell [44] who used multiple echoes to minimise the attenuation of the spin echo amplitude due to diffusion. Shortly after

these discoveries had been made, Torrey [45] modified the formalism of the
Bloch differential equations by including terms to account for the presence
of diffusion:

$$\frac{\mathrm{d}\vec{M}}{\mathrm{d}t} = \gamma \vec{M} \times \vec{B_0} - \frac{M_x \hat{x} + M_y \hat{y}}{T_2} - \frac{M_z - M_0}{T_1} \hat{z} + D\nabla \vec{M} \qquad (3.13)$$

with the assumption that D is both isotropic and homogeneous.

3.3.1   Pulsed Gradient Technique

Stejskal and Tanner [46] introduced pulsed gradients into the spin echo se-
quence which yielded improved sensitivity to diffusion in comparison to the
continuous gradients used previously. By placing a unipolar gradient wave-
form at either side of a refocusing pulse, the spin isochromat acquires a
diffusion induced phase shift (shown in Figure 3.1).
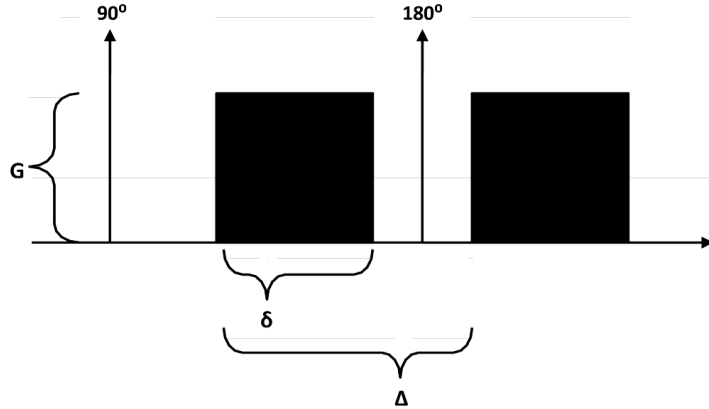
Figure 3.1: Stejskal and Tanner sequence. **G** is the gradient amplitude, Δ is
the separation between gradient pulses, and δ is the duration of a gradient
pulse.

The attenuation of signal intensity due to diffusion was found by solv-
ing the Bloch-Torrey partial differential equations for the symmetric pair of

pulsed gradients and is represented by;

$$S = S_0 e^{-bD} \tag{3.14}$$

where S denotes the signal intensity in the presence of the diffusion sensitising gradient while S_0 is the signal intensity in the absence of the gradient. The diffusion coefficient D will either be equal to D_0 for free diffusion or ADC for restricted diffusion. The b-value represents the amount of diffusion sensitisation and can be expressed as:

$$b = (2\pi)^2 \int_0^{TE} \vec{K}(t)\vec{K}(t)\mathrm{d}t \tag{3.15}$$

$\vec{K}(t)$ is the time dependant position in k-space and is determined by the gradient waveform $\vec{G}(t')$ by:

$$\vec{K}(t) = \frac{\gamma}{2\pi} \int_0^t \vec{G}(t')\mathrm{d}t' \tag{3.16}$$

Therefore the amount of diffusion sensitisation along a single axis is a combination of Eqs 3.15 and 3.16 thus can be simplified to:

$$b = \gamma^2 \int_0^{TE} \left[\int_0^t \vec{G}(t')\mathrm{d}t' \right]^2 \mathrm{d}t \tag{3.17}$$

For a trapezoidal gradient waveform, the b-value is:

$$b = \gamma^2 G^2 \left[\frac{2\delta^3}{3} + \delta^2\xi + \frac{\xi^3}{30} - \frac{\delta\xi^2}{6} \right] \tag{3.18}$$

While for a CPMG spin echo train the b-value is expressed by:

$$b = \gamma^2 G^2 \left[\delta^2 \left(\Delta - \frac{\delta}{3} \right) + \frac{\xi^3}{30} - \frac{\delta \xi^2}{6} \right] \tag{3.19}$$

The parameters δ, Δ, and ξ represent the duration of a lobe, the delay between lobes and the ramp time of the gradient respectively.

Stejskal and Tanner were the first to propose the idea of measuring restricted diffusion of water molecules [47] by varying the separation, Δ, between the gradient pulses. They observed that the attenuation of signal from water molecules in a restricted environment was less than that for freely diffusing molecules and used this method to estimate the diameter of yeast cells.

3.3.2   Diffusion Limited Spatial Resolution

In the basic description of MRI theory in Chapter 2 the effects due to diffusing spins during acquisition were neglected. However, for rapidly diffusing gases these effects are large and place a limit on the attainable spatial resolution. The main problem arises from the fact that the positions and therefore frequencies of the diffusing spins change as k-space is sampled during the readout gradient.

When spins diffuse in the presence of a field gradient they dephase which results in a reduction of T_2^* relaxation. This reduction is the contribution from the previously mentioned attenuation of signal intensity resulting from a net accumulation of phase due to diffusion and can be expressed as;

$$\frac{1}{T_2^*} = \frac{1}{T_{2Diff}} \tag{3.20}$$

where;

$$T_{2Diff} = \frac{T_{CP}}{bD} \qquad (3.21)$$

with T_{CP} being the time interval that transverse magnetisation is refocused.

The accumulation of phase during diffusive motion with no imposing geometrical restriction will assume the same Gaussian probability distribution as that of the Brownian motion itself. A Gaussian phase approximation (GPA) can also be made for restricted diffusion which simplifies the problem of resolving the Bloch-Torrey equation in a confining geometry. The accuracy of the GPA has been investigated numerically [48,49] and experimentally [50,51] and is valid for a wide range of physical parameters. However, the GPA has been discovered to break down under specific circumstances resulting in a non-Gaussian attenuation of signal. The transition to a non-Gaussian regime will be explored in the following subsections.

3.3.3 Diffusion Regimes

The ADC measured in an experiment is intended to be representative of the confining geometry with the reduced value observed a result of restrictive motion only. This simplified interpretation of the ADC is a widely used concept, as is the b-value to which it is directly related.

The b-value defined in Eq 3.17 contains all the information of the applied magnetic field gradient and is the sole parameter used to describe the set up of the experiment. It should be clear that this is an oversimplification since one can obtain the same b-value using different gradient strengths, timing parameters, or gradient waveforms. This means that without an accurate specification of all the relevant physical parameters reported ADC's cannot be compared with other measurements made in the literature.

A full analysis of the restricted diffusion problem requires that three different length scales be considered. The diffusion length scale, L_d, measures the displacement of a diffusing spin along the direction of the gradient during a time t and is a refinement to Eq 3.7;

$$L_d = \sqrt{D_0 t} \qquad (3.22)$$

In order to resolve details of size L_d, the field gradient G must be applied for a time t so that;

$$L_d = \frac{1}{\gamma G t} \qquad (3.23)$$

where γ is the gyromagnetic ratio in units of MHz T^{-1}. From Eq 3.22, $t = L_d^2/D_0$ therefore when substituted into Eq 3.23 the ultimate spatial resolution attainable is limited to [52];

$$L_g = \sqrt[3]{\frac{D_0}{\gamma G}} \qquad (3.24)$$

The length scale L_g is referred to as the dephasing length and is a measure of the characteristic displacement that a spin must diffuse to accumulate a phase shift of 2π relative to its original position. Lastly, the structural length scale L_s is a measure of the displacement a spin must travel before colliding with a physical barrier.

Three different regimes can thus be identified in which the signal attenuation differs; free diffusion, motional averaging, and localised diffusion. In order to determine the relevant regime that the experiment falls under, it is necessary to consider the relative size of the three length scales (see Figure 3.2).

The free diffusion regime occurs when L_d is the smallest length scale. In
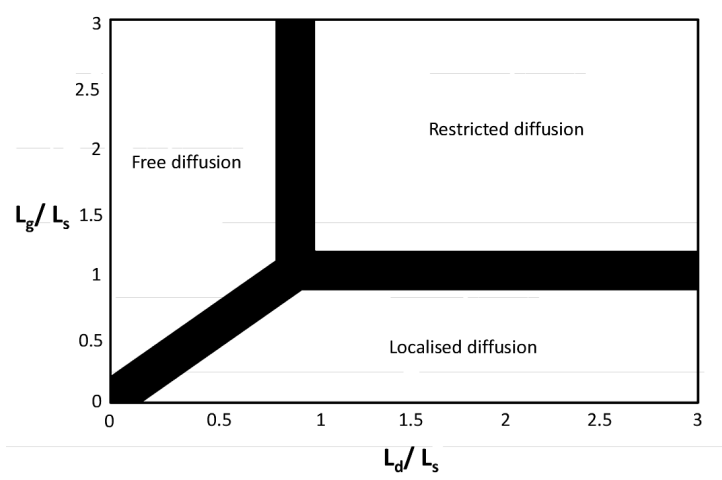
Figure 3.2: Diffusion regimes. The size of each length scale must be considered to ensure the experiment falls under the correct regime.

this regime the majority of the diffusing spins do not come into contact with physical boundaries during the experiment therefore Eq 3.14 remains valid.

The next two regimes both occur under restricted diffusion (when $L_d \gg L_s$).

The motional averaging regime occurs when the dephasing length is much greater than the dimension of the sample ($L_g \gg L_s$). A spin will diffuse throughout the space before dephasing from the gradient can occur. In this regime all spins therefore have the same average frequency which leads to a single resonance line that has been slightly broadened.

Finally, the localisation regime occurs in circumstances where the dephasing length is very much less than the sample length ($L_g \ll L_s$) therefore the effects of diffusion are observed most clearly near the edges (where diffusive motion is restricted). Spins near the edges of the sample are reflected back upon collisions with the boundary, this causes the displacement of these spins to be smaller than those of spins in the middle of the sample during the application of the gradient. Thus, signal decay from spins near the edges is slower

than that for spins in the middle. When the signal is Fourier transformed, narrow spikes are observed at the sample boundaries because of the slower decay in the time domain signal of spins near the edges. In this regime the GPA is invalid and the signal attenuation shows a non-Gaussian behaviour that was predicted theoretically [53] and later observed experimentally [54]. In the localisation regime the ADC or other related concepts do not have any meaning.

3.3.4 Diffusion Anisotropy

The signal decay due to diffusion in the lungs is currently modeled on that of a single exponential with the assumption that the lung is an isotropic porous medium. This assumption only holds in diffusion weighted experiments performed with low *b*-values (≤ 4 cm^{-2} s), in which the accumulated phase distribution can be well approximated by a Gaussian function [55]. At such low *b*-values, signal decay is described by Eq 3.14.

It has been confirmed that the lung is not an isotropic medium and displays anisotropy in such areas as the airway trees. The restriction of diffusion imposed by the lung microstructure will therefore not have spherical symmetry. The restriction in one direction can be much greater than that in other directions, giving rise to a phenomenon known as diffusion anisotropy in which diffusion varies as a function of spatial orientation.

Chen *et al* [33] reported ADC measurements along three orientations (cranio-caudal, left-right, anterior-posterior) in their study involving guinea pigs but did not detect any anisotropy.

Schreiber *et al* [56] also were unable to find any evidence of anisotropy when calculating a full diffusion tensor from six directions.

The assumption of independence of ADC values from anisotropy therefore

seems to be valid for the current spatial resolution available in diffusion experiments in the short time regime.

While anisotropy cannot be directly measured, it can be indirectly inferred when using higher *b*-values. The restriction of diffusion by the lung microstructure results in a signal decay that is non exponential (i.e. the accumulated spin phase is not Gaussian) when imaging with higher and multiple *b*-values. Studying these non-Gaussian effects therefore yields additional information for probing the microstructure of the lung other than the ADC.

Several methods can be employed to analyse non-Gaussian data. These methods are discussed in the following section.

3.4 Diffusion Imaging Techniques

3.4.1 Diffusion Tensor Imaging

Diffusion Tensor Imaging (DTI) is one method to measure diffusion anisotropy. For a heterogeneous media such as the lung containing airways with varying orientation, the diffusion measurement along the axis of the applied diffusion gradient will almost always be oblique to the principal axes of the airway. To accurately find the orientation with the largest ADC, diffusion measurements along thousands of axes would have to be performed which is not practical. To resolve this issue Basser *et al* [57] introduced the concept of the diffusion tensor. To sufficiently estimate the diffusion tensor one must apply diffusion gradients along at least six non collinear, non coplanar directions which provides enough information to estimate the elements of the tensor given in Eq 3.3.

An intuitive description of the quantitative parameters provided by the diffusion tensor such as the size, shape, and orientation of the root mean

square displacement profiles can be made using diffusion ellipsoids. The length of the longest, middle, and shortest axes of the ellipsoid are the eigenvalues and their orientations are the eigenvectors. As already stated, the ellipsoid represents the average diffusion displacement in each direction, not the ADC which would provide a prolate ellipsoid (i.e. a peanut shape).

The diffusion tensor elements are defined in the laboratory frame so are patient orientation dependent. To eliminate this dependency the diffusion tensor matrix in Eq 3.3 can be diagonalised to give a new tensor;

$$\mathbf{D}' = \begin{pmatrix} \lambda_1 & 0 & 0 \\ 0 & \lambda_2 & 0 \\ 0 & 0 & \lambda_3 \end{pmatrix} \begin{pmatrix} v_1 \\ v_2 \\ v_3 \end{pmatrix} \tag{3.25}$$

that is aligned along the three axes of the diffusion ellipsoid. The elements λ_1, λ_2, and λ_3 are the eigenvalues and v_1, v_2, and v_3 their corresponding eigenvectors. If the diffusion is isotropic, the three eigenvalues are equal and when multiplied with their eigenvectors span a sphere. For anisotropic diffusion, the largest eigenvalue is referred to as the principal diffusion coefficient and its eigenvector is aligned along the principal diffusion direction which is assumed to represent the orientation of the airway (Figure 3.3).

The degree of diffusion anisotropy can be measured using one of several scalar anisotropy indices such as relative anisotropy, fractional anisotropy, or volume ratio. The most widely used of these indices is the fractional anisotropy given by;

$$FA = \sqrt{\frac{1}{2}} \sqrt{\frac{(\lambda_1 - \lambda_2)^2 + (\lambda_2 - \lambda_3)^2 + (\lambda_3 - \lambda_1)^2}{\lambda_1^2 + \lambda_2^2 + \lambda_3^2}} \tag{3.26}$$

which has values ranging from 0 to 1 and characterises the eccentricity of the
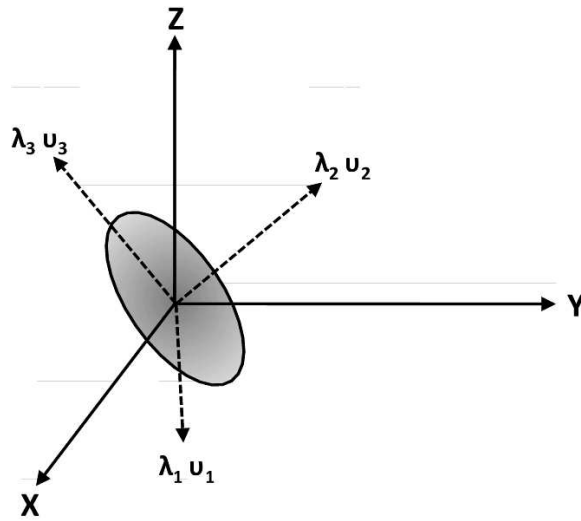
Figure 3.3: Diffusion ellipsoid. The eigenvalues (λ) and eigenvectors (v) determine the level of diffusion anisotropy. A sphere corresponds to isotropic diffusion.

diffusion ellipsoid.

3.4.2   Diffusional Kurtosis Imaging

A method that has been used only recently is that of diffusional kurtosis imaging (DKI). Originally introduced by Jensen *et al* [58] for brain water imaging, the method has subsequently been applied to lung imaging by Trampel *et al* [59].

In DKI, the degree to which diffusion in a biological tissue deviates from a Gaussian function is quantified (Figure 3.4). The quantification is made using a dimensionless metric called the excess kurtosis or apparent diffusional kurtosis (ADK). This deviation or excess kurtosis of the diffusion displacement probability distribution can therefore be attributed to diffusion inhibiting structures and so provides a measure of a tissue's complexity.
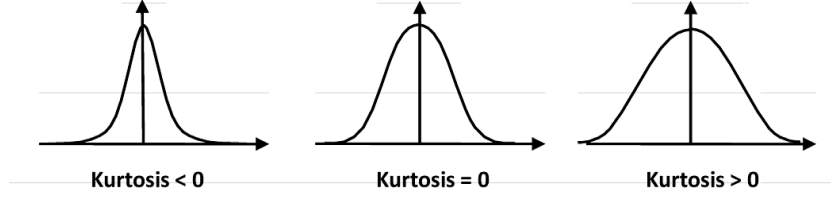
Figure 3.4: Excess kurtosis. The deviation from a Gaussian function (Kurtosis = 0) is illustrated.

The non Gaussian signal decay can be described using [58];

$$S = S_0 e^{\left[-bADC + \frac{ADK}{6}(bADC)^2\right]} \tag{3.27}$$

where ADK is the apparent diffusional kurtosis.

In the paper by Trampel *et al*, it is suggested that DKI is particularly sensitive to diffusion over longer distances. They hypothesized that the ADC would be sensitive to short range diffusion whereas the ADK would be more sensitive to long range diffusion in the bronchi and bronchioles. The findings they reported were consistent with this hypothesis. Whilst it was shown in their paper that Eq 3.27 described the signal decay more accurately than Eq 3.14, the ADK was not related to any specific physiological parameters.

In Jacob *et al* [60], it was shown that the ADK is in fact related to diffusion anisotropy and therefore should be sensitive to changes in tissue organisation.

Both the authors of these papers also demonstrate that Eq 3.27 will only describe the signal decay over a limited range of *b*-values and beyond some critical *b*-value the results are no longer physically meaningful.

3.4.3 q-space Imaging

The q-space imaging technique bears many resemblances to DKI and estimates of diffusional kurtosis have been made using the q-space imaging method. The q-space technique however estimates the full diffusion displacement probability rather than just the kurtosis. This makes q-space imaging more demanding on hardware requirements, post processing methods, and imaging time.

q-space imaging is a diffusion NMR technique that can be used to provide structural information which surpasses the spatial resolution of conventional MRI by several orders of magnitude [61,62]. This made q-space imaging very attractive for microscopic studies and is the reason why a lot of the early work on the q-space technique found applications in material science obtaining structural information on porous materials [63, 64]. Recently, q-space imaging has been applied to biological systems. By extending the technique to MR spectroscopy many studies have been made which include characterising water and metabolite diffusion in neuronal tissues [65] to measuring red blood cell size and shape [66]. The q-space technique is now starting to be applied to lung morphometry using hyperpolarised ^{3}He imaging [67].

The technique employs the same pulsed field gradient experiment as used to obtain DW images. The main difference between the two approaches is in the manner in which the data are processed. The q-space method measures the displacement probability profile (DPP) arising from molecular diffusion as opposed to the ADC.

By taking the Fourier transformation of the echo intensity, $S(q)$, with respect to the q-space variable known as the reciprocal spatial vector, q, the size of the molecular environment can be elucidated. Consider a pair of

rectangular gradient lobes, Eq 3.17 then becomes;

$$b = \gamma^2 G^2 \delta^2 \left(\Delta - \frac{\delta}{3} \right) \tag{3.28}$$

The reciprocal spatial vector is defined as;

$$q = \frac{\gamma \delta G}{2\pi} \tag{3.29}$$

With this definition and Eq 3.28, Eq 3.14 becomes;

$$S(q) = S_0 e^{\left[-4\pi^2 q^2 D \left(\Delta - \frac{\delta}{3} \right) \right]} \tag{3.30}$$

where $S(q)$ is measured at several q-values. A Fourier transform of $S(q)$ gives the DPP $F(r)$;

$$F(r) = \alpha e^{\beta r^2} \tag{3.31}$$

where r is the Fourier conjugate of q, and α and β are parameters of the environment. The DPP is a convolution of the initial spin density and the probability of the displacement in relation to some initial position and resolved along the gradient direction. The elegance of q-space imaging is therefore its ability to fully describe the diffusion properties of a fluid in an arbitrary constraining geometry (unlike diffusion tensor imaging that assumes an ellipsoid geometry) by only performing a Fourier transformation.

The full width at half maximum ($FWHM$) of the DPP is related to the root mean square displacement from Eq 3.7 by;

$$X_{rms} = \sqrt{2n_d D_0 t} = 0.425 FWHM \tag{3.32}$$

and is illustrated in Figure 3.5.
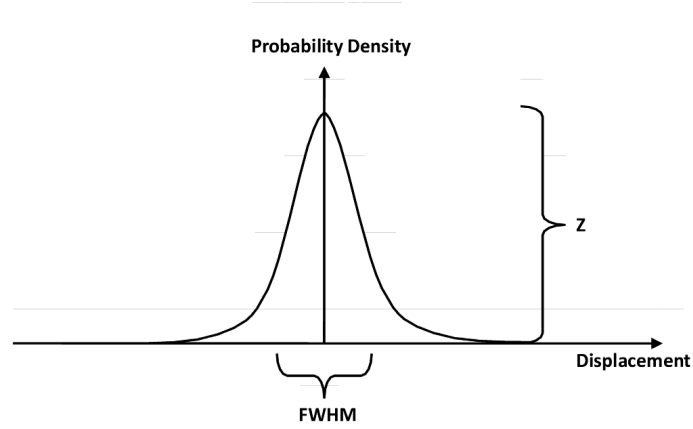
Figure 3.5: Displacement probability profile. The FWHM and probability for zero displacement (**Z**) are shown.

The q-space experiment places two key conditions on the manner in which the data are acquired in order for the Fourier relationship between echo intensity in q-space, $S(q)$, and displacement in conjugate space, $F(r)$, to apply. The first is that the diffusion gradient pulse width, δ, is considered to be infinitesimally narrow. The gradient pulse waveform, $\vec{G}(t)$, can then be described as a delta function with an area $G\delta$ making q no longer a function of time but only a function of δ - the duration of the diffusion encoding gradient.

The second condition is that any molecular displacements that arise during the application of these short diffusion gradient pulses can be assumed negligible when compared to the displacements that occur during the diffusion time, Δ, between the pulses. When this condition - $\delta \ll \Delta$ is met, the probability of a molecule accumulating a net displacement over Δ is straight forward to calculate.

These conditions therefore highlight why q-space imaging is so demanding on hardware. To obtain data over a wide range of q-space in which the signal

has a significant amplitude one has to use large gradient amplitudes in the region of zero to some upper limit that is determined by the need for complete signal attenuation to avoid artefacts such as windowing and truncation.

In human MRI experiments, gradient amplitudes are limited and so in order to compensate, δ is increased. Under these conditions the measured displacement probability profiles are miscalculated and the interpretation of the actual diffusion time at which the probability distribution was measured is complicated. Several methods have been provided by different authors for addressing q-space data where the condition $\delta \ll \Delta$ is not met [68–70].

3.5 Models of Lung Geometry

The q-space method and DKI have the advantage of not assuming any specific model of lung geometry. While this lung model independence in each of the techniques is deemed desirable for its practicality and the flexibility it affords in their applications, the measured variables are difficult to relate to physiological parameters pertaining to the microstructure of the lung.

A different approach for describing non-Gaussian diffusion effects is to use mathematical models of the structure of the lung to derive the diffusion attenuated signal decay. In order for computational models of the lung to be built, various simplifications in geometry have been adopted in the literature. In Haefeli-Bleuer & Weibel (1988) [3], airways were represented as branches covered with alveoli. This model was adopted by Yablonskiy *et al* [71] who for the first time derived a relationship between airway geometry and the measured ADC.

3.6 The Yablonskiy Model

Yablonskiy *et al* modeled the acinar airways as cylinders covered by alveolar sleeves. The cylindrical shape of the airways imposes a non spherical geometry on the diffusion of ^{3}He. Diffusion is less restricted along the airway, and severely restricted by the airway's wall perpendicular to the airway orientation. By taking this anisotropy of the lung microstructure on the acinar level into consideration, Eq 3.14 can be written in the following form;

$$S(b; \alpha) = S_0 e^{-bD(\alpha)} \qquad (3.33)$$

$D(\alpha)$ is given by;

$$D(\alpha) = D_L \cos^2 \alpha + D_T \sin^2 \alpha \qquad (3.34)$$

where α is the angle between the diffusion sensitising gradient and the principal axis of the cylinder, and D_L and D_T are the longitudinal and transverse diffusion coefficients.

It can be seen from Eqs 3.33 and 3.34 that for a single cylinder the signal attenuation with respect to b-value follows a monoexponential decay. The total signal from a voxel which contains hundreds of randomly orientated cylinders can then be calculated by integration under the assumption of uniform distribution of airway orientations;

$$S(b) = S_0 \int\limits_0^\pi g(\theta) \mathrm{d}\theta e^{-b(D_L \cos^2 \alpha + D_T \sin^2 \alpha)} \qquad (3.35)$$

where $g(\theta) = \sin(\theta)/2$ and is the orientation distribution function which is

taken as uniform. Therefore upon integration, Eq 3.35 becomes;

$$S(b) = S_0 e^{(-bD_T)} \sqrt{\frac{\pi}{4bD_{AN}}} \Phi[\sqrt{(bD_{AN})}] \tag{3.36}$$

where $\Phi(x)$ is the error function and $D_{AN} = D_L - D_T$ is the diffusion anisotropy. The non monoexponentiality of the signal decay described by Eq 3.36 can be seen to arise from the superposition of the monoexponential signals of all the individual cylinders.

In their study, Yablonskiy *et al* acquired multiple *b*-value diffusion data in vivo to estimate the cylinder radius R from the value of D_T using the derived theoretical expression;

$$D_T = \frac{16D_0 \xi_R^4 \eta^2}{w(\eta, \epsilon)} \sum_j \frac{\beta_{1j}^{-4}}{(\beta_{1j}^2 - 1)} Q\left(\frac{\beta_{1j}^2}{2\eta\xi_R^2}, \eta, \epsilon\right) \tag{3.37}$$

where β_{1j} is the *j*th (non zero) root of the equation $J_1'(x) = 0$ where J_1' is the first derivative of the first order Bessel function and the functions w and Q are defined in [71]. The parameters ξ_R, η, and ϵ are dimensionless and are defined as;

$$\xi_R = \frac{R}{L_0}$$
$$\eta = \frac{\Delta}{\delta} \tag{3.38}$$
$$\epsilon = \frac{\tau}{\delta}$$

The derivation of Eq 3.37 relies on the Gaussian phase approximation, an assumption that was also made in Eqs 3.33 and 3.34. The relationship between D_T and R as stated by Yablonskiy *et al* is only an approximation and R should be considered as an apparent airway radius only. The Yablon-

skiy model breaks down when dealing with isotropic diffusion, such as in the large airways (i.e. when $D_L \sim D_T$) or with small voxel sizes. The Yablonskiy model is illustrated in Figure 3.6.
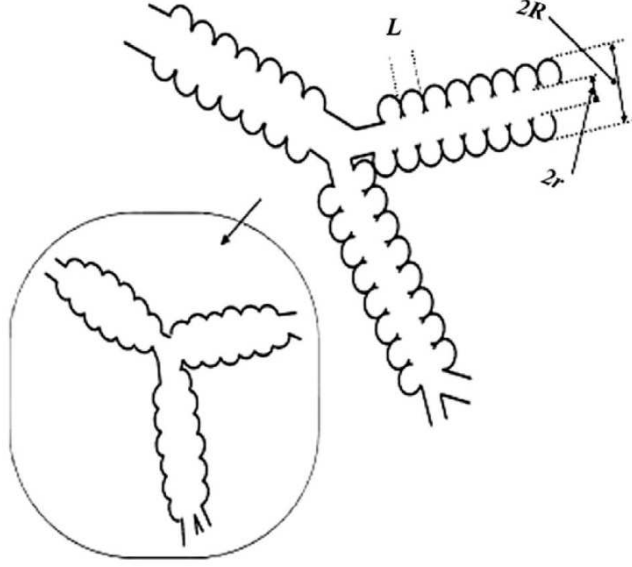
Figure 3.6: Yablonskiy model (taken from [71]). The acinar airways are represented as cylinders with alveolar sleeves. The inner ($\mathbf{r}$) and outer ($\mathbf{R}$) acinar radii along with the alveolar size ($\mathbf{L}$) are shown.

3.6.1   Yablonskiy Updated Cylinder Model

The cylinder model was later updated [72] and empirical relationships between D_L, D_T, and lung geometry were found using Monte Carlo simulations. The effects of non-Gaussian signal behaviour were also taken into account in the simulations which show the dependence of diffusion (D_L and D_T) on

b-values. The results from the simulations are given by;

$$D_L = D_{L0}(1 - \beta_L b D_{L0}) \tag{3.39}$$

$$D_T = D_{T0}(1 - \beta_T b D_{T0})$$

where;

$$\frac{D_{L0}}{D_0} = 1 - \sqrt{\frac{R}{L}} \left[1 - e^{\left(-2.5\left(1-\frac{r}{R}\right)^{1.8}\right)}\right]$$

$$\beta_L = 43.5 \left(\frac{R}{L_{1D}}\right)^2 e^{\left[-4\left(1-\frac{r}{R}\right)^{-\frac{1}{2}}\right]} \tag{3.40}$$

$$\frac{D_{T0}}{D_0} = 0.44 \left(\frac{R}{L_{2D}}\right)^{4\left[1-\left(\frac{R}{L_{2D}}\right)^{0.7}\right]}$$

$$\beta_T = 0.09 \left(\frac{R}{L_{2D}}\right)^{0.1\left[\left(\frac{L_{2D}}{R}\right)^{\frac{3}{2}}\right]}$$

D_0 is the free diffusion coefficient of ^{3}He gas in the lung airspaces; L_{1D} and L_{2D} are the free diffusion lengths for one and two dimensional diffusion; R and r are the external and internal airway radii and L is the alveolar size; D_{L0} and D_{T0} represent D_L and D_T at $b = 0$. The coefficients β_L and β_T reflect the non-Gaussian diffusion effects in each individual airway and are proportional to the kurtosis ($K_L = 6\beta_L$, $K_T = 6\beta_T$). The authors emphasise that the non-monoexponentiality of signal as a function of b-value described by β_L and β_T for individual airways acts in addition to the non-monoexponentiality due to signal averaging from individual airways over a distribution of orientations.

The results are shown to be valid for healthy lungs and lungs with mild emphysema and predict a strong dependence of ADC on the diffusion time (Δ) suggesting caution should be taken when comparing experimental data obtained with different pulse sequence parameters. Tanoli *et al* [73] demon-

strated that the Yablonskiy model gives a very good fit to their multiple b-value data and strongly correlated with quantitative CT values such as local lung density and local lung specific air volume.

3.6.2 Current Yablonskiy Cylinder Model

In the latest iteration of the cylinder model [74], R, r, and L are used to calculate physiological parameters obtained through lung stereology. These parameters include the mean airspace chord length (L_m), lung parenchyma surface to volume ratio (S/V), and number of alveoli per unit lung volume (N_a).

The acquired geometric parameter L is now described as the effective alveolar diameter. This parameter is found by establishing a relationship with the airway radius R through adopting a model of the acinar airway where eight alveoli are distributed along the annular ring [75]. A further assumption that the alveolar size (effective diameter) is the same along the airway and along the circumference is made. By making these assumptions, one can equate L to the chord length corresponding to one eighth of the annular ring;

$$L = 2R\sin\left(\frac{\pi}{8}\right) = 0.765R \tag{3.41}$$

By using the constraint that $L = 0.765R$, the number of parameters in the new cylinder model is reduced to just two: R and the depth of the alveolar sleeve $h = R - r$. These parameters are dependant on the diffusion coefficients D_L and D_T and were found through Monte Carlo simulations similar to the previously updated model. Using the eight alveolar model, the relationships

defined in Eq 3.40 are adapted further and given by;

$$\frac{D_{L0}}{D_0} = e^{\left[-2.89\left(\frac{h}{R}\right)^{1.78}\right]}$$

$$\beta_L = 35.6 \left(\frac{R}{L_{1D}}\right)^{1.5} e^{\left[\frac{-4}{\sqrt{\frac{h}{R}}}\right]}$$

$$\frac{D_{T0}}{D_0} = e^{-0.73\left(\frac{L_{2D}}{R}\right)^{1.4}} \left(1 + e^{-A\left(\frac{h}{R}\right)^2}\right)$$

$$e^{\left(-5\left(\frac{h}{R}\right)^2 + 5\left(\frac{h}{R}\right)^2 - 1\right)}$$

$$A = 1.3 + 0.25e^{14\left(\frac{R}{L_{2D}}\right)^2}$$

(3.42)

The parameter β_T is found to be constant at ~ 0.06 in the range $h/R < 0.7$ with the simulations showing the formulae in Eq 3.42 to be valid to 1-3% within the interval $R/L < 0.7$. The current Yablonskiy model is illustrated in Figure 3.7.
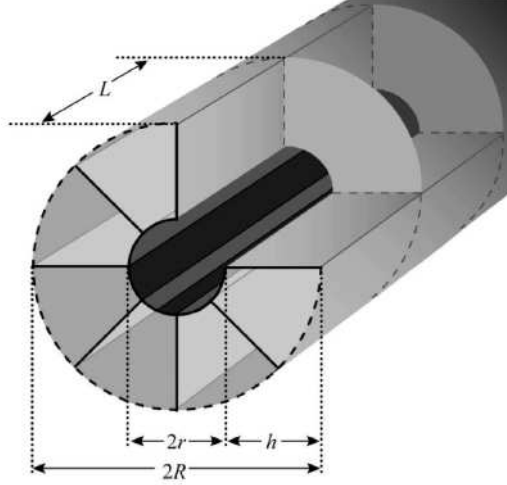

Figure 3.7: Latest iteration of the Yablonskiy model (taken from [74]). The inner ($\mathbf{r}$) and outer ($\mathbf{R}$) acinar radii along with the alveolar sleeve depth ($\mathbf{h}$) and effective alveolar diameter ($\mathbf{L}$) are shown.

Upon calculating the parameters R and h, estimations can be made on the previously stated physiological measurements using;

$$S_a = \frac{\pi}{4}RL + \frac{\pi}{4}h(2R - h) + 2hL$$
$$V_a = \frac{\pi}{8}R^2 L \qquad (3.43)$$
$$N_a = \frac{1}{V_a}$$

with S_a and V_a being the alveolar surface area and volume per alveolus respectively. The mean chord length L_m is found through its relationship to the surface to volume ratio given by:

$$\frac{S}{V} = \frac{S_a}{V_a} = \frac{4}{L_m} \qquad (3.44)$$

The updated model was validated by taking multiple b-value measurements on six excised lungs specimens (two healthy, two with mild emphysema, and two with severe emphysema) and was found to be in good agreement with direct measurements on histological sections of each lung.

In a recent paper by Parra-Robles *et al* [76] the validity of the cylinder model is discussed and tested experimentally on phantoms. The paper highlights two short comings of the model, the first of which is its reliance on the Gaussian phase approximation. The paper argues that even though the model now corrects for the effects of non-Gaussian diffusion, Eq 3.14 which still underpins the Yablonskiy model was obtained under the assumption of Gaussian phase distribution. The model does not account for any angular dependence of non-Gaussian diffusion effects and it is argued this should be incorporated into the cylinder model to better validate it.

The other major shortcoming of the model is concerned around the diffu-

sion regime the experiment is performed in. If the experiment is performed in the localised regime then measurements are more sensitive to the boundaries rather than the volume and shape of the structure [50, 54]. The paper by Parra-Robles *et al* suggests using weaker gradient strengths (below 15 mT m^{-1}) and longer diffusion times although longer diffusion times make branching effects more important. Further work needs to be carried out as only the basic assumptions of the cylinder model were tested whereas other assumptions and approximations included within its framework have yet to be investigated.

3.7   Other Models of Lung Geometry

Although the cylinder model by Yablonskiy, and the updated cylinder model by Sukstanskii *et al* have been shown to produce ADC values in agreement with clinical findings, they are only representative of a single airway. Other geometrical models of the acinar tree have been used and reported in the literature. These models include: the alveolar grape model by Fichele *et al* [77], the labyrinth model by Grebenkov *et al* [78], and the voronoi model by Burrowes *et al* [79]. Each of these will be discussed briefly.

3.7.1   The Grape Model

The alveolar model represents the alveolar ducts as cylinders with spheres attached around them (representing alveoli) (Figure 3.8) and is a finite difference model in which the Bloch-Torrey equations are solved numerically. The improvements of this model of the cylinder model are that the airway and alveoli geometries are more elaborate and no Gaussian phase distribution has been assumed. However, in this model all the ducts are equal in size

and isolated from one another. Difficulties in simulating tissue destruction by creating additional pathways between ducts (as is believed to happen in emphysema) proved too difficult to implement outside of 2D models [80].

3.7.2   The Labyrinth Model

The labyrinth model treats the acinus as a Kitaoka labyrinth [81] and is a random walk model. In this model, a cubic volume of surface area equal to that of a real acinus is spatially filled using a 3D labyrinth with a dichotomic non-symmetric branching structure (Figure 3.8). Grebenkov *et al* simulated emphysema by removing random cell walls that led to air trapping loops. The model improves over the previous models by virtue of the alveolar ducts being connected by dichotomous branching as is the case in real acini. The disadvantages of the model are that the alveolar ducts are once again all the same size and that when a duct bifurcates only parallel and perpendicular orientations are permitted.

3.7.3   The Voronoi Model

The voronoi model is an alternative alveolar model in which the alveolar geometry is simulated using a voronoi meshing technique. The voronoi mesh is implemented using a Delaunay triangulation to create an alveolar sac consisting of 19 adjacent alveoli (Figure 3.8). The surface to volume ratio of the model alveolar sac is within 2.7% of the accepted anatomical value. The voronoi meshing technique in this model is a relatively simple method that can be used to generate complex alveolar geometry. The model can also in theory be extended to simulate larger geometries such as an acinus. Differences in alveolar size and shape were not accounted for because of the

difficulty in prescribing pressure boundary conditions on the capillary model that is developed over the alveolar model.
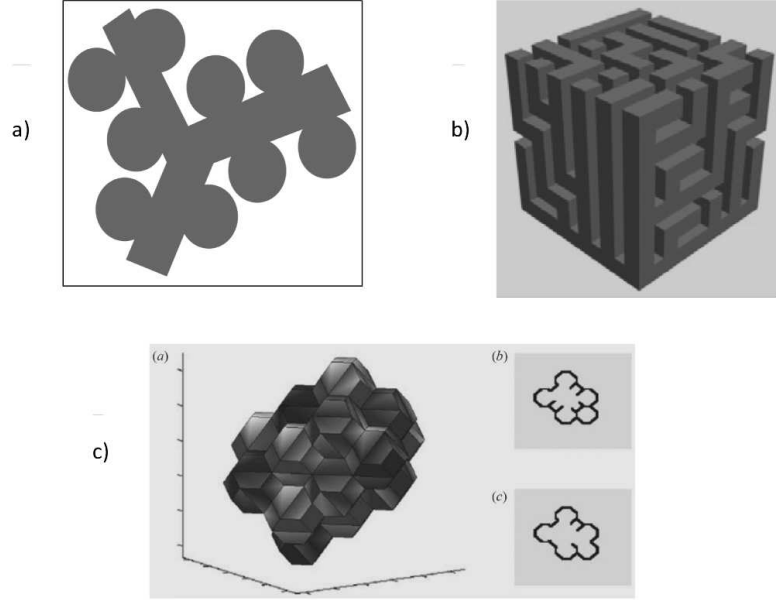
Figure 3.8: Other models of lung geometry. a) The grape model (taken from [77]), b) the labyrinth model (taken from [78]), and c) the voronoi Model (taken from [79]).

3.8   Artefacts in DWI

The DWI experiment is dependent upon the interplay between the diffusion sensitising gradients and the diffusing atomic nuclei. Undesirable field gradients also present during the experiment result in signal attenuation that is not diffusion induced. The sources of these unwanted fields are many and varied and therefore only the most pertinent to this thesis will be briefly discussed in this section.

3.8.1 Eddy Currents

The large, rapidly switched diffusion gradients produced by the gradient coils during the pulse sequence can induce currents in the electrically conductive structures of the magnet, the gradient coils themselves, and the RF coils. These induced currents, which are referred to as eddy currents, are simply a consequence of Faraday's law of induction. The eddy currents in turn produce unwanted rapidly and slowly decaying magnetic fields which oppose the direction of the field generating the eddy currents (Lenz's law). The result of this is two undesirable effects: first, the actual diffusion gradients will differ from their prescribed gradient waveforms causing a miscalculation of the b-value; second, a slowly decaying magnetic field present during the readout gradient will generate an extra contribution to said gradient creating image distortions due to ill defined k-space positions.

Eddy currents can be modelled using a set of exponential functions with various amplitudes and time constants. With this approach several methods have been developed for reducing eddy current induced artefacts in diffusion weighted images [82, 83].

3.8.2 Concomitant Gradients

Whenever a gradient is applied, perpendicular gradients are also created according to Maxwell's equations. Maxwell's equations require that;

$$\nabla \cdot \vec{B} = 0 \tag{3.45}$$

$$\nabla \times \vec{B} = 0 \tag{3.46}$$

for a static magnetic field in free space. Equations 3.45 and 3.46 can be expanded to give four scalar relationships;

$$
\begin{aligned}
\frac{\partial B_x}{\partial x} + \frac{\partial B_y}{\partial y} + \frac{\partial B_z}{\partial z} &= 0 \\
\frac{\partial B_x}{\partial y} &= \frac{\partial B_y}{\partial x} \\
\frac{\partial B_y}{\partial z} &= \frac{\partial B_z}{\partial y} \\
\frac{\partial B_z}{\partial x} &= \frac{\partial B_x}{\partial z}
\end{aligned}
\tag{3.47}
$$

where B_x, B_y, and B_z are the components of the field along the three orthogonal axes. These four relationships imply that only five of the total nine partial derivatives are independent. The strength of these concomitant gradients is proportional to the square of the applied gradient and inversely proportional to the main magnetic field. Concomitant gradients therefore have a substantial effect when imaging at low field. The field strength of the magnet used in this research (0.15 T) is high enough for concomitant gradients to not pose a problem.

In the presence of concomitant gradients spins accumulate a spatially and temporally dependent phase known as the Maxwell phase which results in added signal attenuation. In a spin echo sequence the Maxwell phase can be completely cancelled providing the gradient pulses are applied for the same duration before and after the refocusing pulse. In gradient echo sequences the Maxwell phase cannot be easily cancelled so phase correction techniques must be implemented [84].

3.8.3   Magnetic Susceptibility Effects

Local magnetic field gradients resulting from large inhomogeneities in bulk magnetic susceptibility such as those occurring at tissue-air interfaces in the lung cause image distortion and lower resolution. The change in magnetic field from the susceptibility heterogeneity, $\Delta\chi$, is given by;

$$\Delta B = \Delta\chi B_0 \qquad (3.48)$$

Thus, it is clear that the susceptibility heterogeneity of the sample not only enhances T_2^* relaxation (resulting in loss of spatial resolution), but also provides additional spatially variable gradients to those of the imaging gradients (leading to image distortion).

Equation 3.48 shows that the effects of susceptibility heterogeneity scale with applied field. In lung imaging, the gas filled alveoli give rise to susceptibility gradients of 0.1 T m^{-1} for an applied field of 1 T. Low field imaging clearly minimises susceptibility effects and for heterogeneous samples like the lung should preferentially be used.

Chapter 4

Radio Frequency Receiver Coil Design

4.1 Introduction

The receiver coils used during imaging have all been built in house. There are a wide variety of coil designs employed by MRI, with the design of the coil being dependent on what is being imaged. The majority of coils can be categorised as either surface or volume coils which can be used to transmit, receive, or transmit and receive radiofrequency (RF) signals. Recent advances in MRI have seen the development of parallel acquisition techniques which enable the number of phase encoding steps, and consequently acquisition times to be significantly reduced with no loss of spatial resolution.

4.2 Helmholtz Coils

A common design for a volume coil is the Helmholtz pair coil. A Helmholtz pair consists of two identical circular current loops that lay in parallel planes

to each other, one on either side of the area of interest along a common axis, and separated by a distance equal to the radius of the coil. The two loops carry an equal electric current flowing in the same direction. By setting the separation distance equal to the radius, a cylindrical region extending between the centres of the two loops and approximately 1/5 of their diameter will have an almost uniform magnetic field.

The majority of the receiver coils used within the MRI scanner implements such a design. When imaging a subject's lungs, a single Helmholtz coil pair (a single channel system) of appropriate size is used to enclose the whole chest region. The subject is supine with one loop positioned below their shoulders and the other above their chest.

An important factor when determining the exact geometry of the Helmholtz coil is human anatomy. The volume enclosed by the coil should be similar to that of the volume occupied by the lungs to ensure a good filling factor and thus signal to noise ratio (SNR). The design of a coil is therefore a compromise between the requirements of human anatomy and the necessity to make the coil as close to the optimum Helmholtz geometry as possible to ensure the best possible field uniformity.

4.3   Surface Coils

For many applications in MRI it is not always desirable to receive signal from the whole sample (i.e the patient) as it is to obtain as much signal from a small region of interest (ROI). A surface coil provides a convenient and effective way of obtaining a higher SNR than a volume coil. When sample losses (section 4.5) are dominant, a surface coil adapted in size and shape to the ROI is clearly advantageous because SNR is not only increased through

higher received signal but by noise also being reduced through better filling factor (section 4.6).

The optimised SNR of the surface coil through improved sensitivity comes at the price of B_1^- field homogeneity. The B_1^- field homogeneity of the surface coil decreases significantly with distance from the centre of the coil in all directions, scaling as r^{-3} (r is the coil radius) when sample losses are dominant.

4.4 Receiver Coil Optimisation

The SNR given in Eq 2.79 was shown to be dependent on certain parameters describing the receiver coil. In order to maximise the received signal two important properties of the coil require optimisation. The first is that all loss mechanisms should be minimised to achieve a high sensitivity. This is quantified by the quality factor, Q, and is discussed in 4.8. The second, which has previously been mentioned, is that the geometry of the coil should correspond to the geometry of the sample. This is quantified by the filling factor [85].

4.5 Minimising Losses

The resistances associated with the coil (R_C) and sample (R_S) arise from various loss mechanisms. These mechanisms and how they influence the design of an optimal receiver coil are discussed in the following subsections.

4.5.1 Coil Losses

These losses are caused by ohmic resistance of the copper conductor and are attributed to the random thermal motion of electrons (Johnson noise). The coil resistance may be decreased by lowering the temperature, increasing the conductivity (σ), and optimising the geometry of the conductor (by considering the length of the conductor and the current cross sectional area).

The resistance of the coil is raised as a consequence of the skin effect. As the frequency of the AC carried in the conductor increases there is a greater propensity for current to flow at the surface of the conductor than at the centre due to a higher self inductance at the centre. The thickness of the surface layer that current flows is defined as the skin depth and is given by;

$$\delta = \sqrt{\frac{2}{\mu\omega\sigma}} \tag{4.1}$$

where ω is the frequency of the RF coil and μ is the permeability of the conductor. To sufficiently reduce this effect the thickness of the copper conductor should be at least five times greater than the skin depth.

Coupling between different parts of the coil such as adjacent turns in tightly wound solenoid coils results in an additional force on the current. This proximity effect causes the current density to become more non-uniform, reducing the conductors current carrying cross section and consequently increasing the coil resistance even more. The effect can be easily avoided by placing nearby conductors at least one conductor thickness apart [86, 87].

4.5.2 Sample Losses

Sample losses represent sample-coil interactions and are cauised by two different loss mechanisms: inductive losses and dielectric losses.

4.5.3 Inductive Losses

During transmission of the B_1^+ field, eddy currents will be induced in any electrically conducting material within the field, including the sample, according to Maxwell's laws. Some of this transmitted power is dissipated within the sample causing local sample heating. Through the principle of reciprocity, these eddy currents will in turn induce voltages in the receiver coil causing noise.

The losses in the sample originating from this mechanism are unavoidable because magnetic coupling between the sample and the receiver coil is necessary for signal reception. While unavoidable, the noise due to this sample resistance can be minimised with proper coil design. Optimisation is achieved by improving the filling factor and minimising the axial component of the B_1^+ field which does not contribute to the received signal but may contribute additional noise.

4.5.4 Dielectric Losses

Potential differences across different parts of the receiver coil produce an electric field around the coil that penetrates the sample. The primary sources of the electric field are the capacitors that are used to tune and match (see section 4.7) the receiver coil.

The electric field exerts a force on the electrons within the dielectric sample resulting in a linear movement of electrons parallel to the B_1^+ field. These displacement currents cause energy dissipation within the sample and through capacitive coupling, contribute noise in the receiver coil.

The resistance due to dielectric coupling can be reduced by decreasing the inductance of the coil and distributing the capacitance, thereby reducing

the potential difference across the capacitors and minimising the conservative electric field. The remaining losses due to electric fields located in the sample can be diminished by optimising the filling factor as with inductive losses.

4.6   The Filling Factor

The filling factor, η_f is defined as the magnetic energy in the transverse component of the B_1^- field throughout the sample divided by the total magnetic energy, U, throughout all space [88]. The filling factor is given by;

$$\eta_f = \frac{\int (B_1^-)^2 \mathrm{d}V}{2\mu_0 U} \tag{4.2}$$

where the integration is over the sample volume.

For linear polarisation, half of the energy in the transverse component of B_1^- throughout the sample is used for calculating Eq 4.2 in order for the concept of the filling factor to apply to circular polarisation.

In low field imaging (< 0.3 T) where coil losses dominate, a high filling factor is desired.

4.7   Tuning and Matching the Receiver Coil

The receiver coil should be tuned to the resonant frequency of the appropriate nucleus. If the coil is not correctly tuned there will be a suboptimal transfer of energy from the resonant nuclei in the imaged volume to the receiver which will result in the detected MR signal being reduced. The impedance of the coil must also be matched to the 50 Ω input impedance of the pre-amplifier to minimise reflection of signal. The fraction of signal reflected at the interface between the two circuits can be described by the reflection coefficient, Γ, as

given by the equation:

$$\Gamma = \frac{Z_1 - Z_2}{Z_1 + Z_2} \tag{4.3}$$

Z_1 and Z_2 are the impedances of the coil circuit and the pre-amplifier. When Z_1 and Z_2 are equal, Γ goes to zero and thus the maximum transfer of signal is achieved.

In order to tune and match the designed receiver coils, a Network Analyser was used. This piece of apparatus can transmit a signal over a range of frequencies to the coil and then plot the reflection coefficient as a function of frequency. All the receiver coils in use were tuned to the resonant frequency of ^{3}He at 0.15 T (i.e. the field strength of our magnet).

The resonant frequency is determined from the Larmor equation and therefore the resonant frequency of the RLC circuit must be tuned to this frequency. The resonant frequency of a parallel tuned RLC circuit is defined as:

$$\omega = \sqrt{\frac{1}{LC} - \frac{R^2}{L^2}} \tag{4.4}$$

where L and C are the inductance and capacitance and R is the equivalent parallel resistance of the circuit (including the coil resistance).

Tuning is achieved by soldering high voltage (2 kV) capacitors in parallel with the coil. The first step is to determine the inductance of the coil by observing the resonant frequency of the circuit on the Network Analyser for a capacitance of known value. With the inductance now known, Eq 4.4 was used to calculate a value of capacitance (C_T) that would tune the coil to the Larmor frequency.

The impedance of the coil is matched to 50 Ω by adding larger capacitors in series with the coil. The Network Analyser is used to display a Smith chart to make matching easier. When the impedance contour of the circuit

overlays the 50 Ω contour shown on the display the coil is matched. The better matched the LC circuit, the larger the dip of the resonant frequency as observed in the trace of the Network Analyser.

With the coil matched to 50 Ω, C_T needed to be re-adjusted since the addition of the matching capacitance C_M had changed the resonant frequency of the coil. The required total capacitances for C_T and C_M were thereby found through an iterative process since altering C_T would also alter the impedance and so C_M would need to be adjusted once again. An LC circuit diagram to which all the receiver coils built in this thesis conform to is illustrated in Figure 4.1.
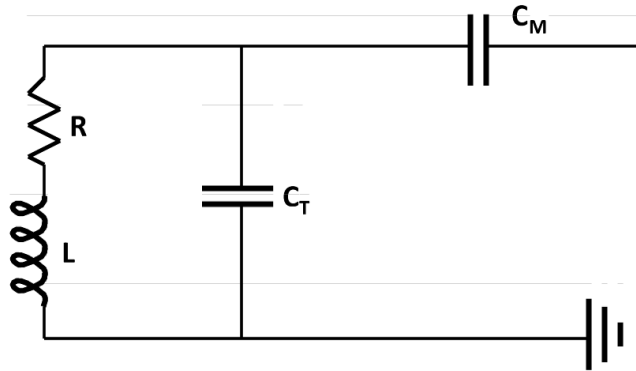

Figure 4.1: LC circuit diagram. Tuning capacitance (C_T) is added in parallel to the coil (L) while matching capacitance (C_T) is added in series. R is total resistance of the coil from all losses.

Once the coil had been tuned to the specific MR nucleus and matched to 50 Ω, crossed diodes were connected in parallel with the coil to protect the preamplifier from large voltages during transmission. Before reaching the receiver input of the MR console, the small voltages picked up by the coil were passed through the preamplifier.

4.8 Q Factor

An ideal inductor will be lossless irrespective of the amount of current flowing through it. However, the metal wire that forms the coils (6 mm and 10 mm diameter copper piping for the different receiver coils) introduces a winding resistance into the inductor. This winding resistance is often called the series resistance as it appears in series with the inductor. The inductor's series resistance causes loss of inductive quality through the conversion of electrical current to heat.

The Q factor (or quality factor) of an inductor is the ratio of its inductive reactance to its resistance at a given frequency, and is a measure of its efficiency. The Q factor is inversely proportional to the range of frequency (i.e. the bandwidth, Δf) which the inductor exhibits resonance (f). The bandwidth represents the frequency range where less than half the received signal power is attenuated. The higher the Q factor of the inductor, the closer it approaches the behaviour of an ideal, lossless, inductor. Increasing the Q factor results in improved SNR.

The Q factor of an inductor can be found through the following formula:

$$Q = \frac{\omega L}{R} \tag{4.5}$$

where R is the internal electrical resistance (the series resistance) and ωL is the inductive reactance at resonance. The Q factor can also be found by:

$$Q = \frac{f}{\Delta f} \tag{4.6}$$

The Q factor of the coil is dependent on the circumstances under which it is measured. When loaded by a patient, the dielectric losses and magnetic

induction inside them result in a shift of the resonance frequency of the coil and a reduction of the Q factor. The receiver coils built by the author are shown in the Figures 4.2 - 4.4 below with their resonant frequencies, bandwidth, Q factor and dimensions.

Figure 4.2: Small receiver coil. $f = 4.73$ MHz, $\Delta f = 0.03$ MHz, $Q = 158$, Dimensions $= 26 \times 17 \times 18$ cm.
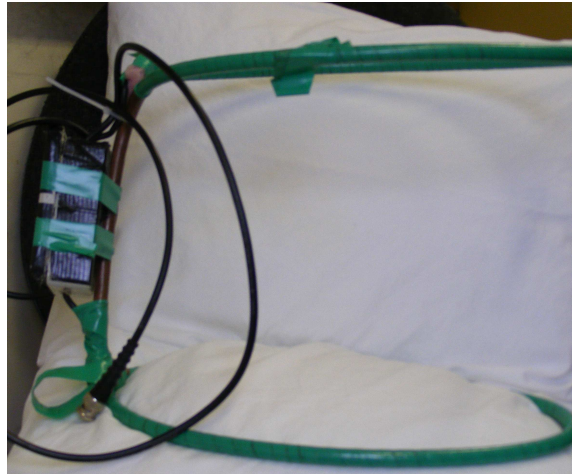

Figure 4.3: Medium receiver coil. $f = 4.75$ MHz, $\Delta f = 0.04$ MHz, $Q = 119$, Dimensions $= 32 \times 21 \times 22$ cm.

Figure 4.4: Large receiver coil. $f = 4.75$ MHz, $\Delta f = 0.06$ MHz, $Q = 79$, Dimensions = 36×26×25 cm.

4.9 Parallel Imaging

4.9.1 Introduction

Faster Imaging results in greater patient throughput and a reduction of movement related artefacts. Instead of reducing the acquisition time by using faster and stronger gradients, knowledge of the spatial sensitivity of the receiver coils can be used to replace the missing spatial encoding steps.

Parallel acquisition methods fall into two catergories - pre-Fourier transform and post-Fourier transform. The pre-Fourier technique is commonly called SMASH (SiMultaneous Acquisition of Spatial Harmonics), and the post-Fourier method is called SENSE (SENSitivity Encoding).

4.9.2 SENSE Theory

The SENSE method suggested by Pruessman *et al* [89] reduces scan time by a reduction factor R by spacing the phase encoded (PE) k-space lines by this factor. This in turn results in the field of view (FOV) of the reconstructed image being reduced by this same factor. The image that is acquired from the array of receive coils is therefore aliased or wrapped. The signal at an aliased pixel is a superposition of signal from that actual location in the object and pixels that are displaced integer multiples of L/R, where L is the unreduced PE FOV.

For each receive coil, one set of wrapped k-space data is produced which can be defined by;

$$M_\gamma(k_x, k_y) = \int \int \rho(x, y) s_\gamma(x, y) \exp(-i(k_x x + k_y y)) dx dy \qquad (4.7)$$

where $\rho(x, y)$ is the spin density of the imaged object and $s_\gamma(x, y)$ is the

sensitivity profile of the γth receive coil. If the acquired data for each receive coil is inverse Fourier transformed then real space images that are wrapped due to undersampling are obtained.

Knowledge of the coil sensitivities over the FOV is used to unwrap the individual images since aliasing occurs with different weighting due to different coil sensitivities. Information about the spatial sensitivity variation of each coil is obtained from a separate measurement that will be discussed later.

Using the sensitivity maps, sensitivity matrices which give the complex coil sensitivities for a certain pixel are extracted. If N_a denotes the number of superimposed pixels due to aliasing at a certain pixel location and N_c is the number of coils, the complex coil sensitivities for for the N_a superimposed positions form an $N_a \times N_c$ sensitivity matrix $\mathbf{S}_{\gamma,\rho}$;

$$\mathbf{S}_{\gamma,\rho} = \begin{bmatrix} s_1(r_1) & \ldots & s_1(r_{N_a}) \\ \vdots & \ddots & \vdots \\ s_{N_c}(r_1) & \ldots & s_{N_c}(r_{N_a}) \end{bmatrix} = s_\gamma(r_\rho) \qquad (4.8)$$

where r_ρ denotes the position of the aliased pixel ρ and s_γ indicates the spatial sensitivity of coil γ.

In order to unwrap the images, the wrapped data from the receive coils (a) must be multiplied by the unfolding matrix $\mathbf{U}$. This matrix has dimensions $N_a \times N_c$ and is calculated from the sensitivity matrix as;

$$\mathbf{U} = (S^H \Psi^{-1} S)^{-1} S^H \Psi^{-1} \qquad (4.9)$$

The matrix is chosen so that it maximises the SNR in a pixel as well as unwraps the pixels. Determination of this matrix is necessary since S is

non invertible. Therefore the pseudo inverse is used and the superscript H indicates the transposed complex conjugate. The matrix Ψ is defined as the noise correlation matrix.

The noise correlation matrix Ψ has dimensions $N_c \times N_c$ in which a diagonal element represents the noise variance and an off diagonal element corresponds to the noise cross correlation between two coils. Scaling and correlation of noise is determined by acquiring data from all the receive coils without RF pulses or gradients [90]. The coils must be loaded as for imaging so that the received noise is that from the object and the coil must also be placed as it would for imaging so that noise correlations due to coupling of the individual coil elements are measured correctly. The bandwidth of the receiver and the receiver gain must also be set as for imaging to ensure noise is scaled correctly. If the coupling between component coils is low, the off diagonal elements of Ψ are negligible and the diagonal elements are nearly equal to one another. In that case, to simplify the calculations the noise correlation matrix can be set to the identity matrix and Eq 4.9 is reduced to;

$$\mathbf{U} = (S^H S)^{-1} S^H \tag{4.10}$$

Hence the unwrapped pixel values v, of length N_a can be calculated by;

$$v = \mathbf{U}a \tag{4.11}$$

This process is repeated for every pixel in the aliased image to obtain a full FOV unwrapped image.

The matrix inversion of Eq 4.10 is only possible as long as the number of aliased pixels does not exceed the number of coils. If $N_c > N_a$ the unfolding matrix is over determined. The extra degrees of freedom are then used with

the noise correlation matrix to optimise the SNR. When $N_c = N_a$ there are no extra degrees of freedom available to improve the SNR. For $N_c = N_a$, S is a square matrix and assuming all inverses exist, Eq 4.11 becomes;

$$
\begin{aligned}
v &= [(S^H \Psi^{-1} S)^{-1} S^H \Psi^{-1}] a \\
&= (S^H)^{-1} \Psi S^{-1} S^H \Psi^{-1} a \\
&= S^{-1} a
\end{aligned}
\tag{4.12}
$$

The SNR of a reconstructed SENSE image decreases as the reduction factor increases since SNR is proportional to the square root of the acquisition time. The SNR can be calculated as;

$$
SNR_{SENSE} = \frac{SNR_{NORMAL}}{g\sqrt{R}}
\tag{4.13}
$$

where SNR_{NORMAL} represents the SNR from an image that has no reduction in the PE direction (i.e. full FOV) and SNR_{SENSE} is the SNR from an image with $R > 1$. The factor $\sqrt{R}$ is the expected SNR loss from reducing the scan time and also sets an upper bound limit on the SNR. The factor g is called the geometry factor.

The g-factor represents the noise amplification that occurs during the unfolding process and combining of the acquired images. It can be thought of as the coil configuration's ability to separate aliased pixels. It is a pixel dependant property that represents a scaling factor for increasing the noise floor level.

The geometry factor is determined by the diagonal elements of the matrix $S^H \Psi^{-1} S$ and its inverse. The g-factor as given by Pruessman *et al* [89] is;

$$
g_p = \sqrt{(S^H \Psi^{-1} S)^{-1}_{pp} (S^H \Psi^{-1} S)_{pp}} \geq 1
\tag{4.14}
$$

The subscript p is the index of the aliased pixel to be separated, S and Ψ are the sensitivity matrix and noise correlation matrix that were defined earlier. Thus it can be seen that in order to obtain high quality reconstructed images the sensitivity difference between aliased pixels should be as large as possible for the slice of interest. This will result in improved g-factor maps. The g-factor is also a function of N_a with values of $g = 1$ to $g \approx 1.5 - 2$ for $N_a = 2$ for typical coil designs.

The sensitivity difference is dependant on the coil conductor placement, the scan plane orientation, the PE direction within the scan plane (coil plane of symmetry should not be parallel to the PE direction), and the pixel location within the scan plane.

The noise amplification described by the g-factor is related to the inverse of the sensitivity matrix S. A poorly conditioned matrix amplifies the noise in the unwrapped SENSE images, but this amplification can be reduced by a process called regularisation.

One such method of regularisation involves the addition of a term proportional to the unit matrix [91]. The unfolding matrix in Eq 4.10 is then re-written as;

$$\mathbf{U} = (S^H S + \lambda I) S^H \qquad (4.15)$$

I represents the unit matrix and λ is a constant that can be adjusted to reduce the noise. This method is a simple estimation of a constant regularisation parameter but there are other techniques [92] where the parameter can be optimised on a pixel by pixel basis to give a more uniform SNR.

The g-factor can be further reduced by excluding pixels which do not contribute significant signal from the SENSE reconstruction [89, 93]. Information about which regions can be excluded are obtained from the sensitivity maps. This region thresholding locally reduces the degree of aliasing since

some aliased components are zero and thus will also lower the g-factor.

4.9.3 2-Channel Chest MRI Coil

In order to exploit the SENSE technique on the newly acquired MR6000 spectrometer from MR Solutions, a SENSE RF coil needed to be designed, constructed, and bench tested. Software also needed to be written to reconstruct the images obtained from the individual coils into one final image.

Design and Construction

The 2-channel chest coil is a localised receive only RF coil that improves upon the design by Barnaby Waters [94]. The design methodology is based on the multi-channel array concept in which multiple receive coils are arranged in an appropriate configuration that closely conforms to the anatomy under scrutiny.

The 2 channel chest coil was developed for imaging both children and adults. The RF coil is spatially configured and geometrically orientated to conform to the shape of the chest, thus increasing its sensitivity (through good B_1 field coverage) and filling factor for maximum SNR gains.

The coil was designed by the author, Dr Ruslan Garipov, and Professor J. Owers-Bradley and constructed by the student workshop in the School of Physics and Astronomy. The coil consists of two Helmholtz pairs that are placed in close proximity to each other with each of the two coil elements being used to image one half of the chest.

Ideally, the coil elements would have been circular loops in order to make them as close to the optimum Helmholtz geometry as possible. However, the design of a coil is a compromise between this ideal geometry and the requirements of human anatomy and so each coil element has an elliptical

geometry with a 10 cm semi-minor axis and a 13 cm semi-major axis. The coils therefore fill a rectangular area of approximately 35×26 cm (depending on the overlap of the coils for decoupling) and enclose a volume of 35×26×20 cm.

The top and bottom plates of the 2 channel chest coil have had recesses milled out to frame the coil loops. This was done so that the person being imaged did not have to lie on the coils but instead on a thin layer of plastic that served as a covering for the plates. The individual coil loops are held into position within the plates by a polythene tube grip that is held firm by a screw that is accessible on each plate. This was a deliberate design consideration as it was fully expected that the position of each of the loops would need to be adjusted in order to reduce inductive coupling between their neighbouring coil loops. The coils are made from 6 mm diameter copper piping and in order to prevent short circuiting have had a layer of insulation covering applied to them around where they overlap.

The entire coil frame was designed to match the dimensions of the scanner's couch and so the need for a projecting railing was not necessary. Unlike the previously constructed 2 channel chest coil, the top and bottom plates that house the coil loops were not separated using four threaded polyphenylenesulphide rods. For our design, the top and bottom plates are attached to each other via two connectors (machined in the Electrical Workshop, School of Physics and Astronomy), each of which are inserted into an 8-way non reversible plug module (RS Components Ltd). The connectors and their associated plug modules are housed in separate modular pieces made from the same 26 mm MDF that the top and bottom plates of the RF coil are made from. These additional pieces (four in total) were specifically fashioned so that when attached to their corresponding RF coil plate, and when each plate

was connected to each other, would result in a 20 cm separation between the top and bottom coil loops.

The two ends of each coil loop were bent and then consequently put through carefully positioned holes that had been drilled out of each of the modular pieces that were now firmly attached to each plate (Figure 4.5). Each of these pieces of MDF had a specific area milled out to form recesses where the bent ends of each coil loop would rest (Figure 4.6). A larger area was milled out for those pieces attached to the bottom plate to make space for the circuit boards. Coverings were made to conceal the milled out areas, these were screwed on and had grips on them to make handling of the coil easier.

The top and bottom loops of each Helmholtz pair were connected using single core 3 amp cable. Care was taken to ensure that they were connected in such a way that the current in each coil pair circulated in the same direction for each loop otherwise the induced current in the loops of each coil pair would act to cancel each other out.

The advantages of this design consideration are that the subject can be easily put into the coil, and that the coil itself conforms a lot better to the anatomy of the chest which results in a better filling factor as previously mentioned. Figure 4.7 shows each plate of the chest coil without the plastic covering on in order to reveal the coil loops for each plate. The completed 2 channel chest coil is shown in Figure 4.8.
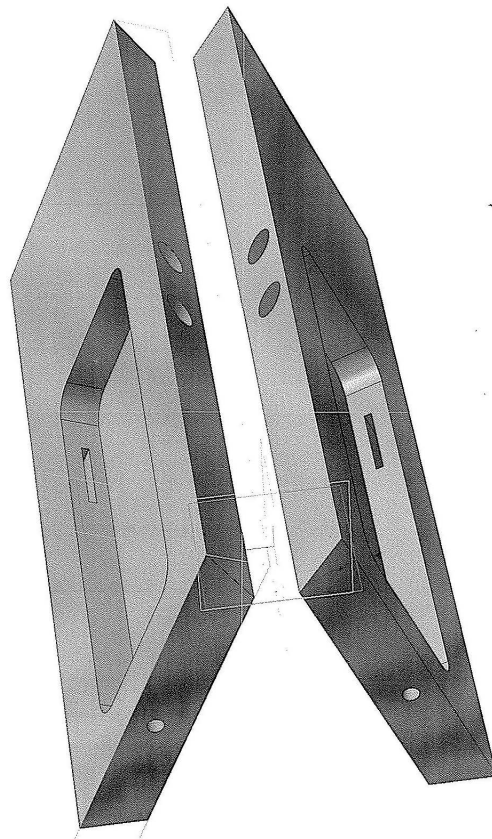
Figure 4.5: Bottom plate modular pieces. The 2 adjacent holes on each module are where the bent ends of one coil loop element are put through. The other hole is for the coaxial cable and the housing for plug module is also shown.
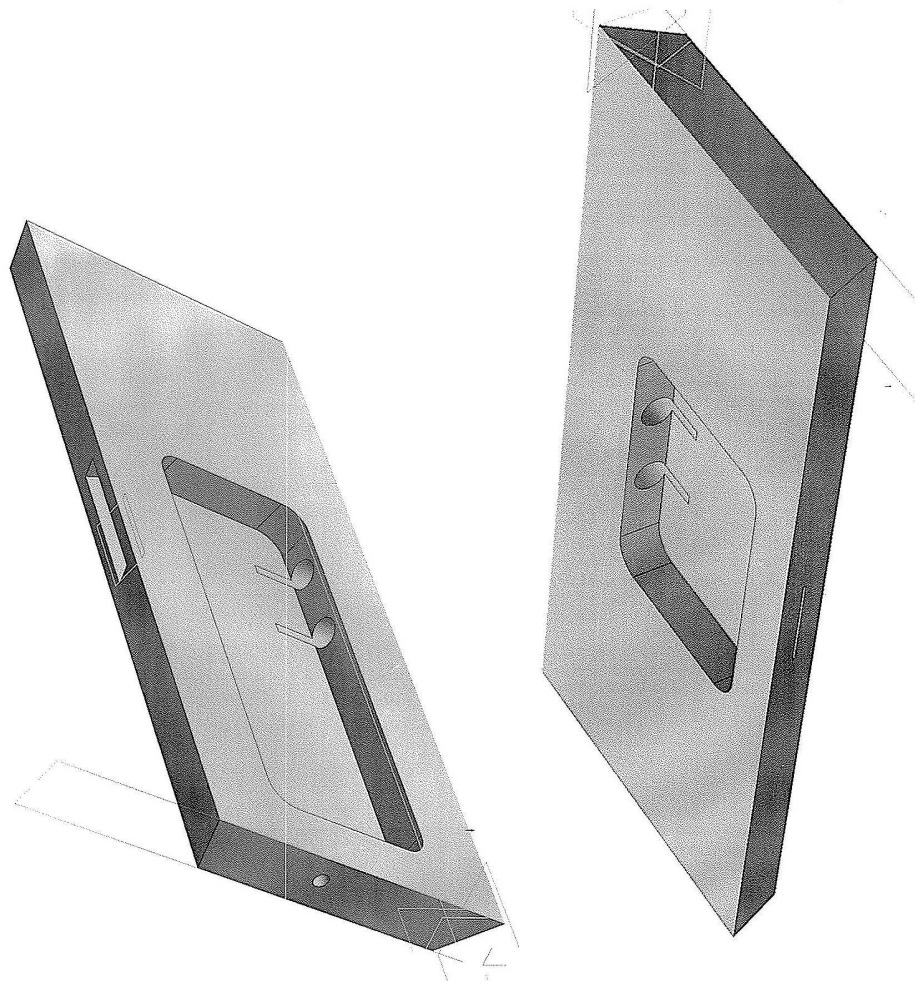
Figure 4.6: Bottom and top plate modular pieces. The design plan on the left is a different view of the previous bottom plate pieces. The recesses for the coil loop ends are shown within a larger milled out area. The circuit boards are housed in the bottom modular pieces.
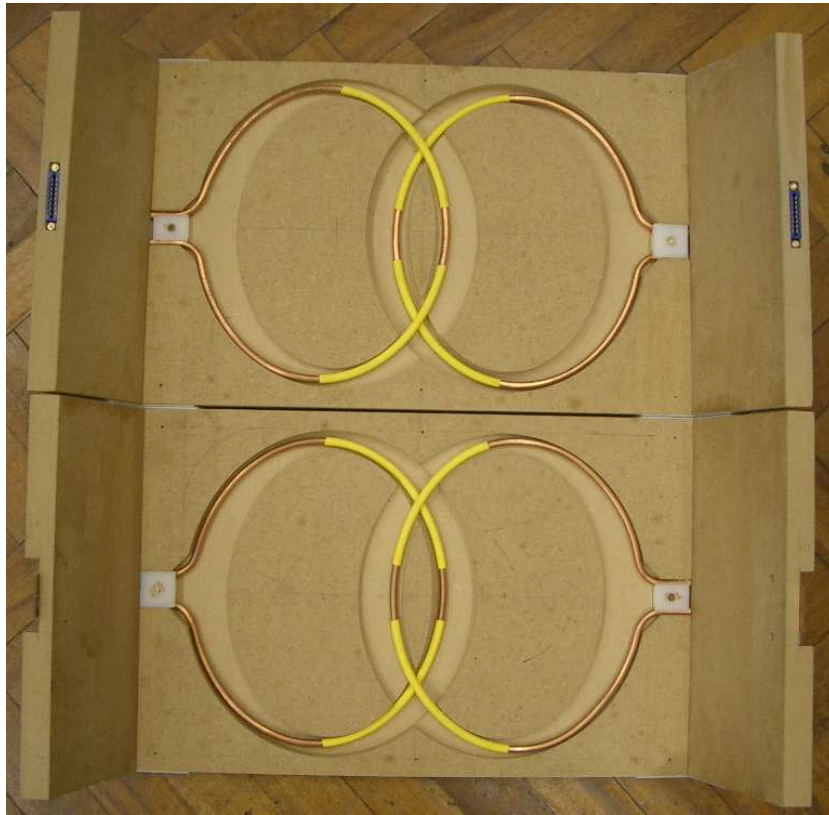
Figure 4.7: Top and bottom plates. The bottom plate is shown at the top of the figure and the top plate is shown below it.
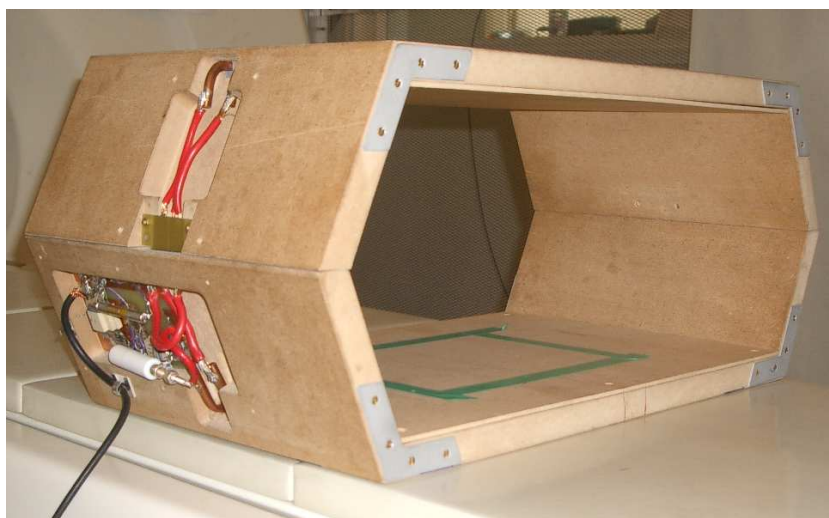
Figure 4.8: Completed 2 channel chest coil.

4.9.4   Design Considerations

The 2-channel chest coil is a receive only RF coil that is to be integrated into our MRI system. Our system features a body resonator coil that generates the required RF transmit pulses. Therefore the 2-channel chest coil must be detuned when the body resonator coil is generating RF transmit pulses. The impedance must also be made large enough during transmission in order to suppress the large circulating currents that will be induced in the coil. Another design concern is the minimisation of coupling between the individual coil loops of the dual channel coil. These issues constitute some of the most important design considerations in the development of the 2-channel chest coil. The implemented solutions that address these issues are discussed in this section.

Detuning

Detuning (or passive detuning) is a simple circuit implementation that utilises various electrical components to detune an RF coil and also create the high impedance that is necessary to reduce circulating current during transmission. To accomplish this a pair of back to back diodes are connected in series with an inductor and a detuning capacitor. The detuning circuit acts as a parallel resonating circuit (tuned to the Larmor frequency of the system) when the transmit coil is active. During transmission, the induced voltages in the receive coil are large enough to forward bias the diodes which results in a parallel resonance at the resonance frequency. This ensures a high impedance in the receiver coil during transmission. During signal reception when the receive coil is active, the induced voltages are too small to forward bias the diodes and so the parallel resonance effect does not occur.

Decoupling

An important design step to ensure good SNR in each coil loop involves minimising the mutual coupling between adjacent coil loops. Mutual inductance causes noise and undesired signal transfer from one loop to the other which is of detriment to the performance of the receive coil. When not adequately decoupled from each other, a splitting of the resonances between coil loops is observed which results in lower sensitivity at the desired resonance frequency.

Inductive coupling is minimised by overlapping the coil loops of concern. The amount of overlap to apply for irregularly shaped loops such as those used in our design had to be determined through experiment. For symmetric loop geometries such as circular and square loops, their centres should be separated by 3/4 and 9/10 of their diameter respectively [95].

Another method of reducing coil interference is by preamplifier decoupling. This is achieved via a circuit interface that connects the receiver coil to the input terminals of the preamplifier. The circuit interface forms a parallel resonating circuit at the input of the receiver coil when the input impedance of the preamplifier is ideally zero. This serves to transform a high impedance to the RF receive coil which suppresses the flow of induced currents caused by mutual coupling. Because the preamplifier is a voltage amplification device, the suppression of induced current flow does not affect signal reception. This results in all the coil loops in the RF receive coil becoming electrically isolated from each other. For coil designs where underlap is applied, preamplifier decoupling is the technique that is used to ensure isolated signals from each coil loop.

The preamplifiers that are used for this research are not low impedance but have the conventional $50\,\Omega$ input impedance. Therefore the main method of decoupling that was implemented was that of overlapping the individual

coil loops. Figure 4.9 gives an illustrative comparison of applying underlap and overlap between two adjacent coil loops [95]. Some coil designers have implemented both overlap and preamplifier decoupling to minimise coupling [95].
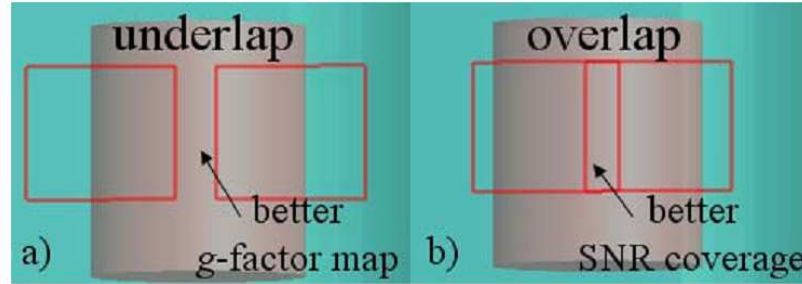

Figure 4.9: Comparison between coil underlap (a) and overlap (b) (taken from [95]).

Coil Simulations

When designing a receiver coil it is desirable to determine the $\vec{\mathbf{B}}$ field distribution. The field distribution can be solved via computational simulation or by physically acquiring the sensitivity distribution by using tested B_1^- mapping techniques (described in 4.9.5). By acquiring full $\vec{\mathbf{B}}$ field and $\vec{\mathbf{E}}$ field knowledge then an analysis of coil performance can be conducted.

There are a number of computational algorithms that already exist that simulate how an induced current affects electric and magnetic fields within a specific volume. The receiver coil sensitivity profile can be calculated by the application of the Biot-Savart law or Coulomb's law. By solving the latter, more accurate electromagnetic conditions can be be determined which will provide more precise results but is much more complicated to do so. Both of these laws can only be used for direct current fields and so an assumption of no time varying currents within the system is made. Coulomb's law and the

Biot-Savart law are given as;

$$\vec{E}(\vec{r}) = \frac{\int \rho_L d\vec{L}}{4\pi\epsilon_0\epsilon_r r^2}\hat{r} \tag{4.16}$$

$$\vec{B}(\vec{r}) = \frac{\mu_0\mu_r\vec{I}}{4\pi}\int\frac{d\vec{L}\times\hat{r}}{|\vec{r}|^3} \tag{4.17}$$

where ρ_L is the charge density for infinitesimal length $d\vec{L}$, $\epsilon_0\epsilon_r$ is the material permitivity, $\vec{r} = |\vec{r}|\hat{r}$ is the distance vector from the current position to the field point, $\mu_0\mu_r$ is the material permeability, and $\vec{I}$ is the current flowing through the space.

When modeling field behaviour under time varying MRI signals, the sample dimension must be much smaller than the signal wavelength. For $B_0 \leq 1.5$ T quasi-static calculations are permitted. If this criterion is not met then the sample can distort the field and thus full wave field solutions are required as the $\vec{E}$ field can no longer be approximated as conservative ($\nabla \times \vec{E} \neq 0$).

A script was developed in MATLAB to simulate the magnetic field of our coil geometry. Each coil loop is approximated to an N sided polygon of elliptical shape with a semi-major and semi minor axis of 10 cm and 13 cm respectively. Each side of this polygon defines one of the $d\vec{L}$ vectors. Once the coordinates of the coil loop have been defined the net field at each $d\vec{L}$ within the volume is calculated by approximating the Biot-Savart integral at each point. The script thus returns three 3D matrices - the resultant $\vec{B}$ vector. The program then repeats the procedure to calculate the field due to the second loop. The net field of the Helmholtz configuration is given by the vector addition of the two fields over the whole volume. From the added 3D matrices the magnitude of the field over the volume can be determined (Figure 4.10). The profile of the field magnitude along the centre of the

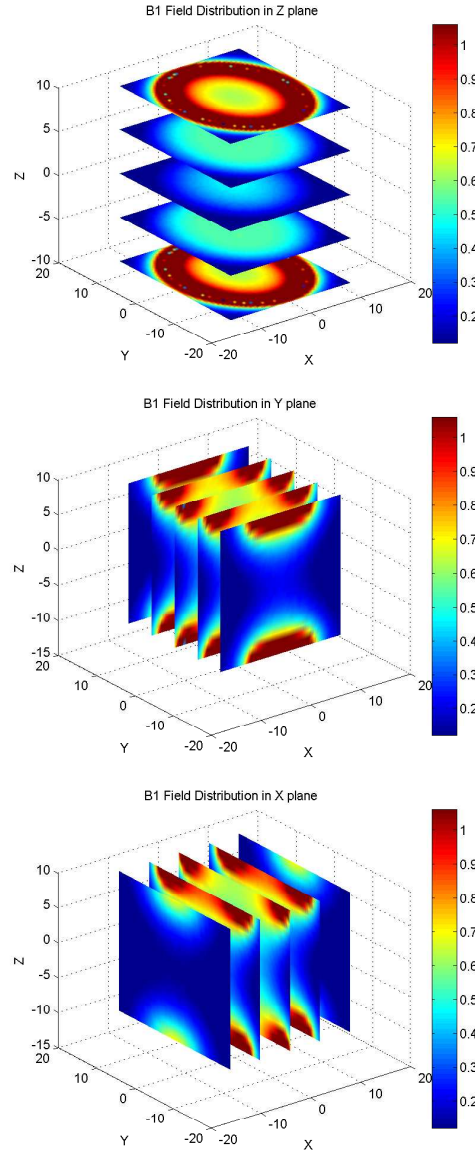vertical axis of the coil was also calculated (Figure 4.11).

Figure 4.10: B_1 field distribution across volume of coil in each plane. The simulated results show ample B_1 field coverage within the region of interest.
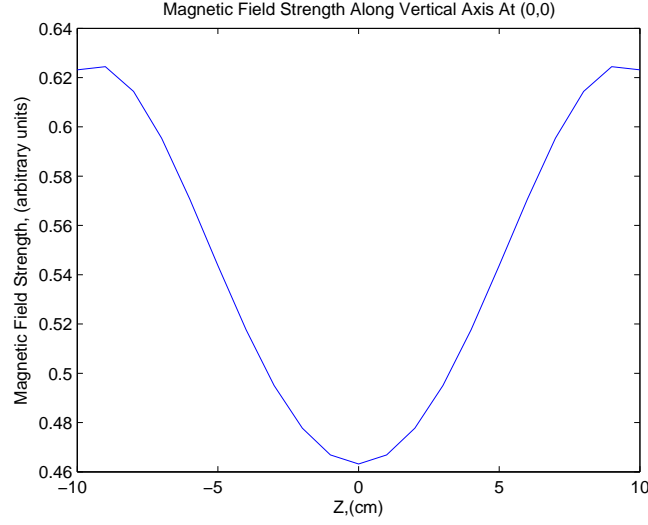
Figure 4.11: Variation in B_1^- field along the central vertical axis. Unlike the ideal circular geometry, there is no flat region of field uniformity which is unfortunate.

Bench Testing

Upon construction of the 2 channel chest coil, each Helmholtz coil element must then be tuned to the desired resonant frequency, impedance matched to 50 Ω, and decoupled from its neighbouring coil.

Changing the load of the coil or the coil position relative to the load results in a shift of the resonance and also changes the impedance match of the coil element being bench tested.

Each Helmholtz coil (i.e. each receiver port channel) was tuned individually with the load present, and whilst being in close proximity to the scanner, and also with the other coil element being open and connected to the 50 Ω preamplifier input. An Agilent 8712ET RF Network Analyser was used to tune both coil elements to 6.227 MHz. Tuning was achieved by soldering high voltage (2 kV) ceramic capacitors in series with the coil while variable

ceramic trim capacitors (range 2-120 pF) were used to make finer frequency tuning adjustments.

Inductively decoupling two neighbouring coil elements was achieved by adjusting their respective overlap whilst loaded and within the scanner. To measure the effect of the coupling, the Network Analyser was used in transmission mode. The transmission from one coil element to the other was measured and a trace of the transmission coefficient plotted. The position of the coils was adjusted until the peak in the transmission coefficient was at a minimum. By using a coil overlap of 6.2 cm for the coil loops in the top plate and 5.9 cm for those in the bottom plate, an overall isolation value of -27 dB was achieved. This indicates that there is a good decoupling between the Helmholtz coil elements. When adjusting the overlap of the coil elements, the resonance frequency and impedance matching of the coil will consequently change.

The impedance of each coil element is matched to 50 Ω by adding a larger capacitance in parallel with the coil element. The Network Analyser is used to display a Smith chart to make impedance matching easier. With each coil element matched to 50 Ω under load conditions and in the imaging environment, the resonant frequency had been shifted once again.

These coil characteristics govern an iterative process of bench testing where each level of complexity requires iteration through all previous levels to make minor adjustments.

Once the coil elements had been tuned to the specific MR nucleus and matched to 50 Ω at the best overlap value for the coil loops, crossed diodes were connected in parallel with the coil to protect the pre-amplifier from the large voltages during transmission.

4.9.5 Acquiring Sensitivity Maps

The sensitivity profiles from receive coils in MRI are normally non uniform which creates problems that can be corrected for once the sensitivity profile is known. The sensitivity map of a receive coil reveals a non uniform signal intensity profile within the coil volume associated with an inhomogeneous transmit field and a non uniform receive sensitivity.

To acquire a full sensitivity map experimentally the receive B_1^- field is measured using an homogeneous phantom. For the purposes of this research, a large $30\times30\times17$ cm perspex tank was filled with water doped with a small quantity of copper sulphate to reduce the T_1 relaxation time. Before connecting the SENSE coil the magnet was shimmed and the proton resonance frequency was found using a quadrature ^{1}H RF receive coil. The SENSE coil was then connected and the perspex tank was placed inside it and then driven to the isocentre of the magnet (Figure 4.12).

Figure 4.12: Sensitivity mapping using the 2 channel chest coil.

The sensitivity maps were produced by imaging the water tank using each

of the 2 channels of the RF coil. By imaging an homogeneous object, any variation in signal intensity throughout the acquired images can be associated with a non uniform coil sensitivity. The `1Se_cl_2_2.ppl` pulse sequence was used with the `1Se_cl_2_2.ppr` parameter file. A spin echo (SE) sequence is normally used for sensitivity mapping when using a volume coil for transmitting RF pulses. This is because the magnitude of the transmitted B_1^+ field varies little with distance meaning the SE signal dependence of $\sin^3 \alpha$ is more appropriate to exploit than that of the $\sin \alpha$ dependence for a gradient echo signal (α represents the flip angle). It should also be noted that the acquired sensitivity maps are sample dependent due to varying transmit field distribution between an in-vivo experiment (i.e. using a human subject and a uniform phantom [96]).

It was observed that the copper sulphate that was added to reduce the T_1 was not completely homogeneous throughout the perspex tank. Higher concentrations of copper sulphate would deposit themselves in the corners of the phantom. To avoid this problem, the water was stirred prior to imaging for a more homogeneous mixture and a longer TR of 3 seconds was used. To improve the SNR of the sensitivity maps, six averages were taken. A FOV of 360 mm was used so that aliasing of the sensitivity maps was avoided. An image matrix of 180×180 was used to give a 2 mm spatial resolution. This image was then cropped to give either a 150×150 sensitivity map (FOV 300 mm), 140×140 (FOV 280 mm), or a 128×128 sensitivity map (FOV 256 mm). Sensitivity maps were taken in several scan orientations which include coronal PE horizontal and vertical and transverse PE horizontal and vertical. A slice thickness of 5 cm was used for all of the sensitivity maps. A coronal PE horizontal map was also acquired with 3 slices separated 3 cm apart to get three sensitivity maps specific to each slice.

The raw sensitivity maps were post processed to remove the DC spot and the horizontal zipper artefact. As suggested by Pruessman *et al* [89], the maps were further refined by polynomial fitting in order to filter out high frequency random noise and also by region thresholding to further prevent the introduction of unwanted noise. All post processing on the acquired sensitivity maps was carried out using the `CreateSMaps.m` program written by the author in MATLAB 7.1. Both the raw and refined sensitivity maps for each coil are shown below in Figure 4.13.
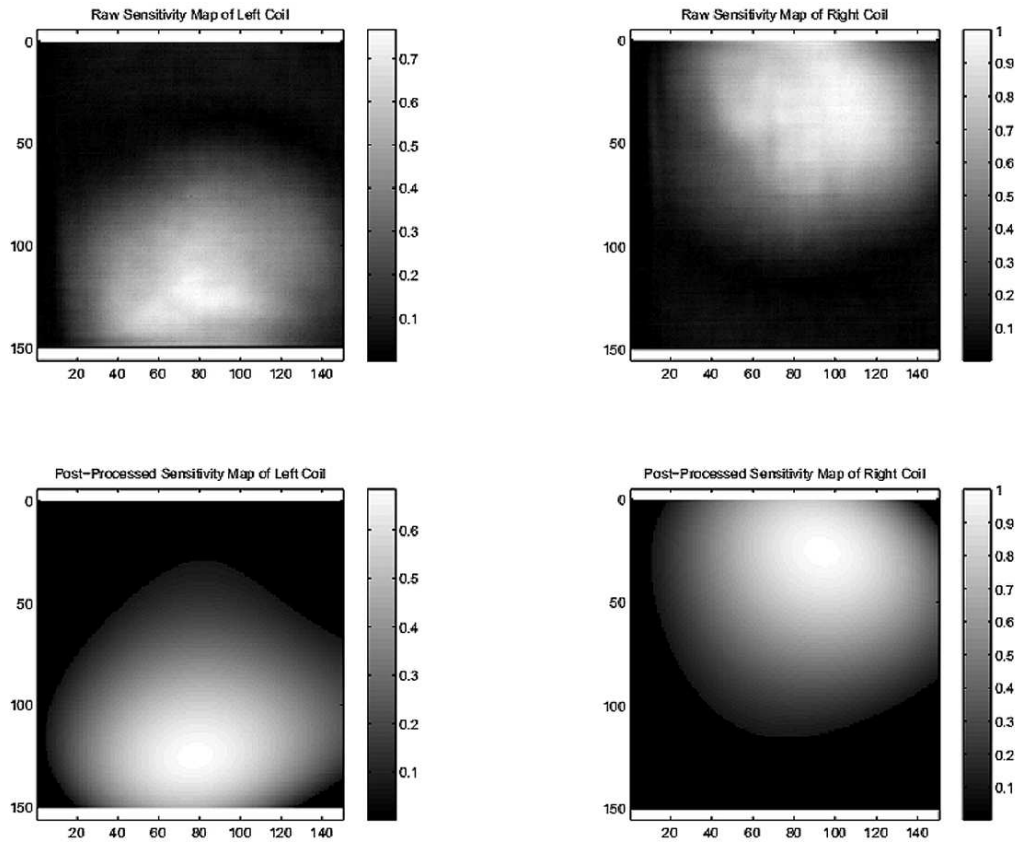
Figure 4.13: Raw and post-processed sensitivity maps. The maps have been scaled and show that the right Helmholtz coil is more sensitive than the left.

4.9.6 Software

This section details the changes that are required in order to make the imaging sequences for the MR6000 compatible for parallel imaging. It also details the MATLAB algorithms written during the research.

Pulse Sequence Modification

In order to acquire aliased images the number of PE lines was halved and the phase undersampling parameter was changed from 0 to -1 in the parameter set up file for that sequence.

For the previous MR spectrometer the `NO_RECEIVERS` command was added to the pulse sequence code in the parameter header list that precedes the main sequence code. The ppl source code was then compiled in order for this change to take effect. Once compiled, the number of receive channels to be used can be stipulated in the parameter file. If more than one receive channel is being used then it is necessary to specify a DSP card for each additional receive channel.

The recently installed MR6000 spectrometer does not require the `NO_RECEIVERS` keyword to select multiple receivers but instead uses the keyword `RECEIVER_MASK`. A detailed description of this keyword can be found in the `Pulse Program Manual.doc` as one of several manuals from MR Solutions. Implementing this new keyword was the only significant change that needed to be made to the imaging sequences that were used.

Image Post Processing Code

Upon acquiring wrapped and unwrapped images it is then necessary to unwrap the wrapped images and correct for the inhomogeneous coil sensitivity profile for the unwrapped images. This imaging processing was implemented

in MATLAB 7.1 and the various algorithms are detailed below.

CreateSMaps.m

This code opens the raw sensitivity maps acquired from each channel of the SENSE coil and removes both the DC spot and the horizontal zipper artefact. The sensitivity maps are then cropped to the desired matrix size and fitted to a 4th order 2D polynomial function. The maps are also region thresholded with signal below 10% being set to zero. The real and imaginary components of the cropped and cleaned sensitivity maps are then saved as two separate .csv files that are used for image reconstruction and sensitivity weighting in other m-files.

Sens2xweight.m

This algorithm uses the saved sensitivity maps to correctly weight unwrapped (full FOV) acquired images by dividing them by the coil sensitivity. A mask is also created from the sum of squares image (each individual unweighted modulus image added together) which is used for the purposes of thresholding noise and is saved as a .csv file for use in other m-files. The two sensitivity corrected images are then combined into a single image. For a more accurate result, the author employed a selective combination method in which the pixel to be included in the final image was determined by which of the sensitivity corrected images had the higher pixel value at that point.

Sens2xrecon.m

This code opens each of the wrapped images and then extends them to the full FOV for the purposes of easier indexing when performing the unwrapping. The code then determines which two pixels are superimposed and

from the loaded sensitivity maps calculates the sensitivity matrix S. The noise correlation matrix N is set to the identity matrix (N = eye(2)). The unfolding matrix is then calculated and multiplied by the extended aliased images to generate a full FOV unwrapped image. This image can be cleaned by applying the previously saved mask.

gfactor.m

Using the processed sensitivity maps this code generates a simple unregularised g-factor map. As before, the noise correlation matrix N is set to the identity matrix.

4.9.7 Results

Imaging

All imaging was performed on a 0.15 T magnet with the MR Solutions MR6000 console. For preliminary imaging, a 3 litre bottle containing water doped with copper sulphate was used. The imaging protocol used for the acquisition of all the phantom datasets was the same (Table 4.1).

Parameter	Dimension
Sample Period (KHz)	50
Slice Thickness (cm)	5
Repetition Time, TR (ms)	1000
Echo Time, TE (ms)	10
Number of Averages	4
Field of View (mm)	300
Acquisition Matrix Size	150×150
Flip Angle (°)	60

Table 4.1: Imaging protocol used for acquiring phantom datasets.

Sensitivity Weighting Unwrapped Images

The first imaging experiments to be conducted were those that acquired unwrapped full FOV images from each channel of the chest coil. These images were then weighted by the sensitivity map data of their respective channel and are shown in Figures 4.14 - 4.15.
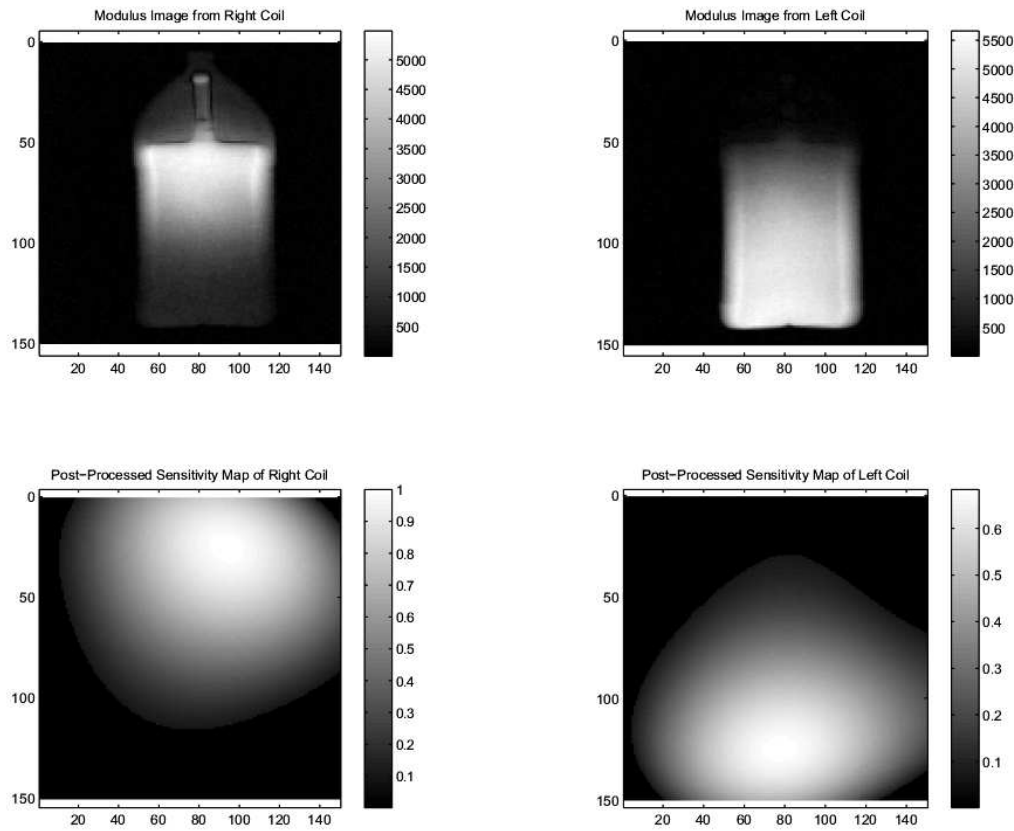

Figure 4.14: Acquired images and the sensitivity maps from each channel of the chest coil.

Once each of the images had been weighted by their respective sensitivity profiles they were then combined into a final single image. This image was cleaned by applying a mask to it. The mask, obtained from the sum of squares image, was used to remove noise by setting all signals below a certain threshold to zero. This threshold depends on the resolution of the sum
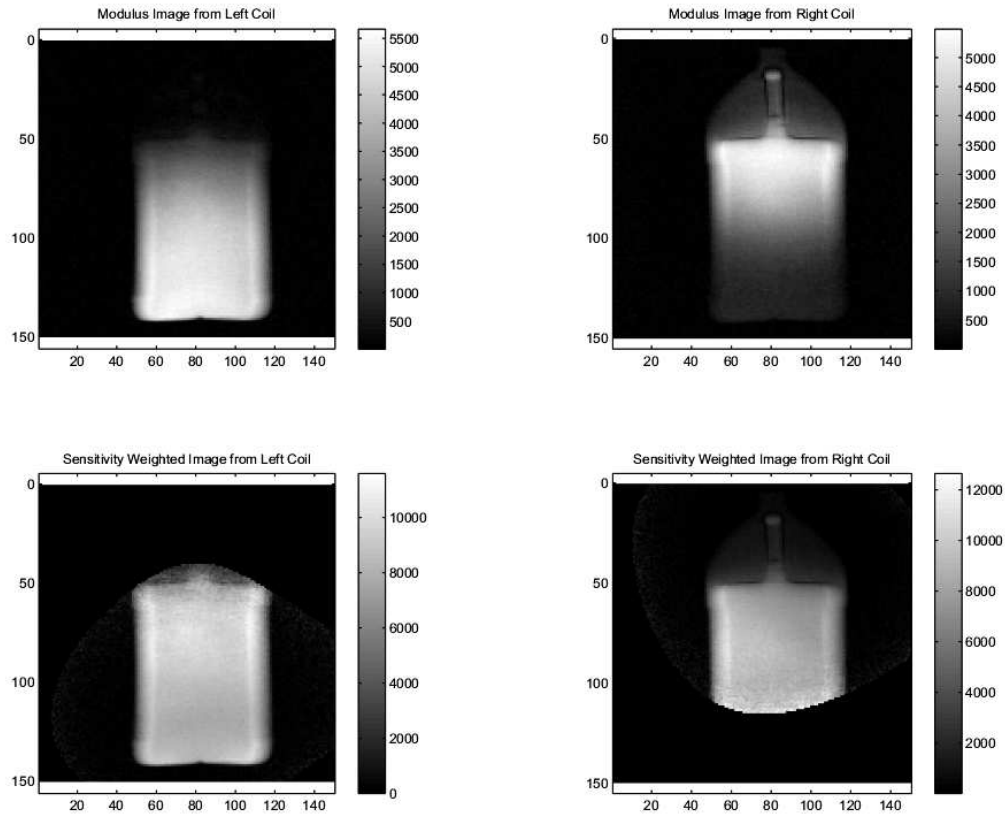
Figure 4.15: Unweighted and sensitivity weighted images from each channel.

of squares image, but for the phantom an approximate value of 5% of the maximum signal intensity was used (Figure 4.16).

Whilst there is no reduction in scan time when acquiring full FOV images, the SNR benefits from weighting the images by sensitivity can be clearly observed. The largest increase in SNR was seen were the sensitivity maps overlap (i.e. coil overlap) which is to be expected. When weighting the individual coil images the signal level was seen to increase by a factor of 2 for each coil. For the final selectively combined image, the maximum signal intensity was 50% greater than the standard combined modulus image.
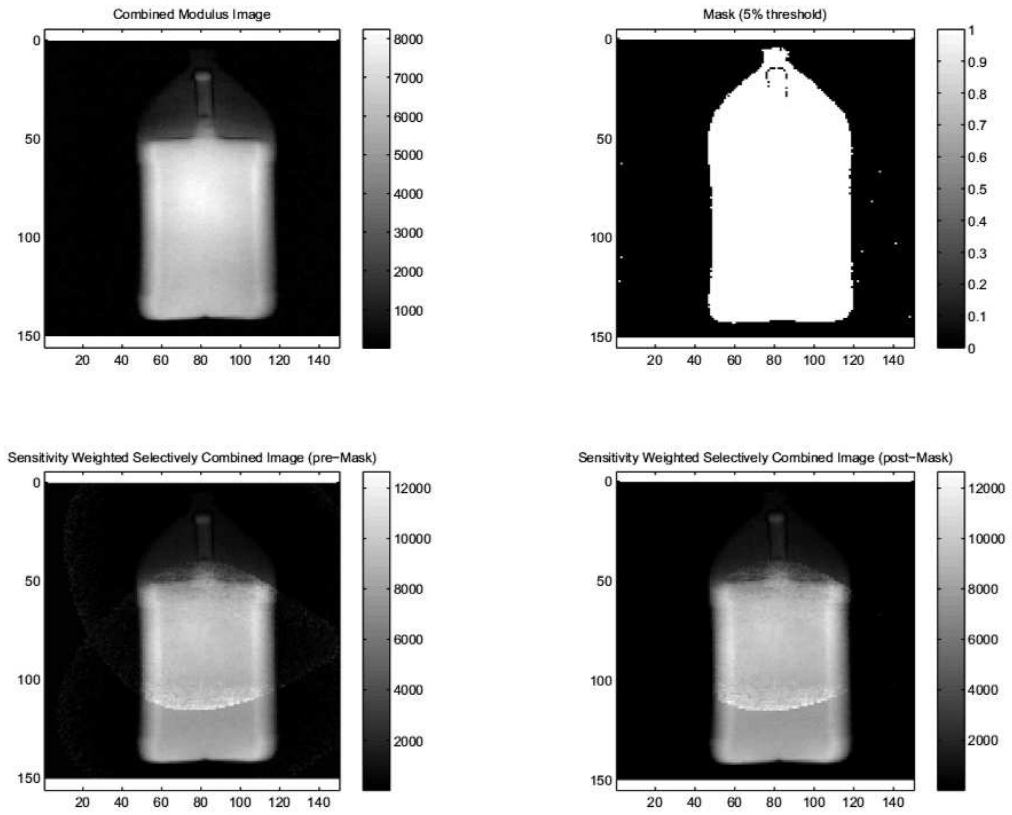
Figure 4.16: Unweighted and selectively weighted combined images.

SENSE Reconstruction of Wrapped Images

Upon acquiring unwrapped full FOV images the appropriate parameter settings were then changed in order to acquire wrapped images. Figure 4.17 shows the acquired wrapped images from each channel of the chest coil.

These wrapped images were then unwrapped using the raw sensitivity maps, synthetic sensitivity maps consisting of one half with a value of 1 and the other half with a value of zero, and the 4th order polynomial fitted sensitivity map. These reconstructed images were then further refined by applying the mask. The results of the reconstruction are shown in Figures 4.18 - 4.20.
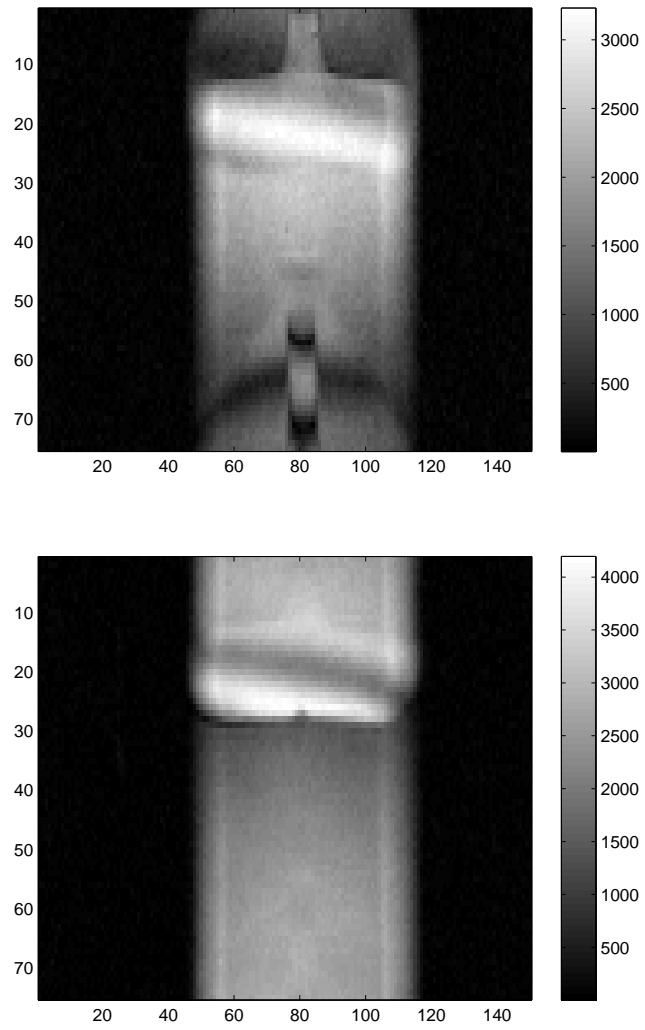
Figure 4.17: Wrapped images from each channel.
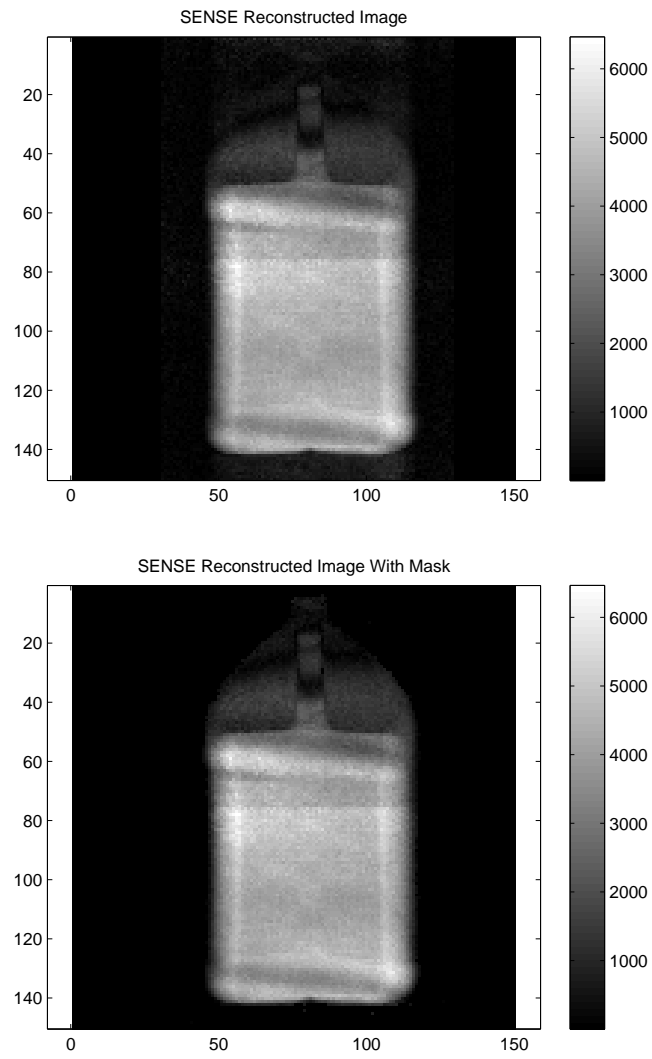
Figure 4.18: Unwrapped image using raw sensitivity maps.
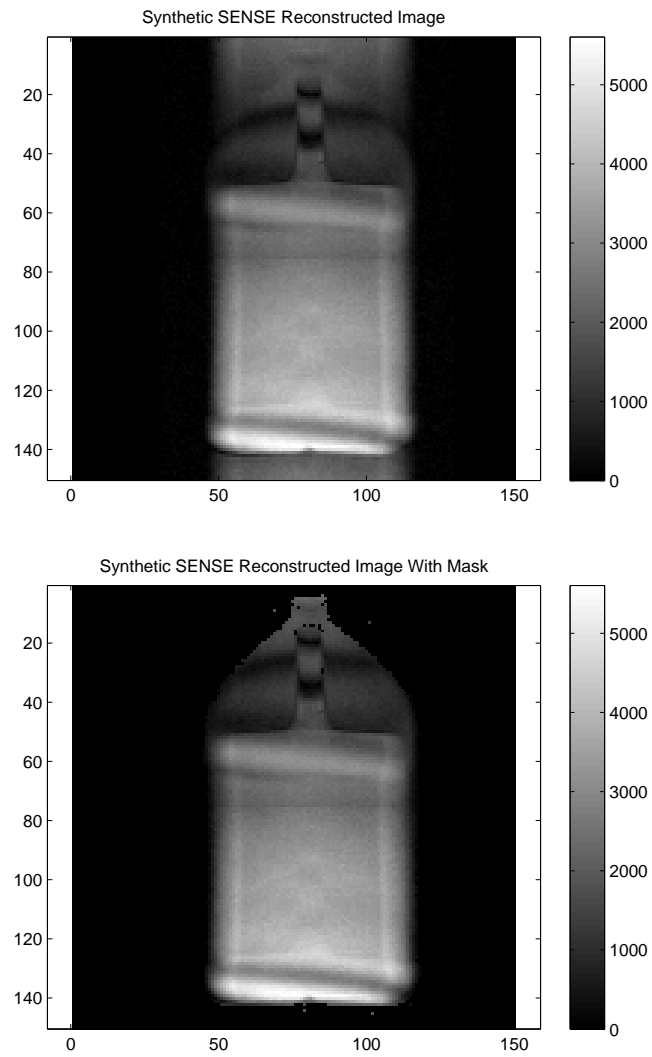
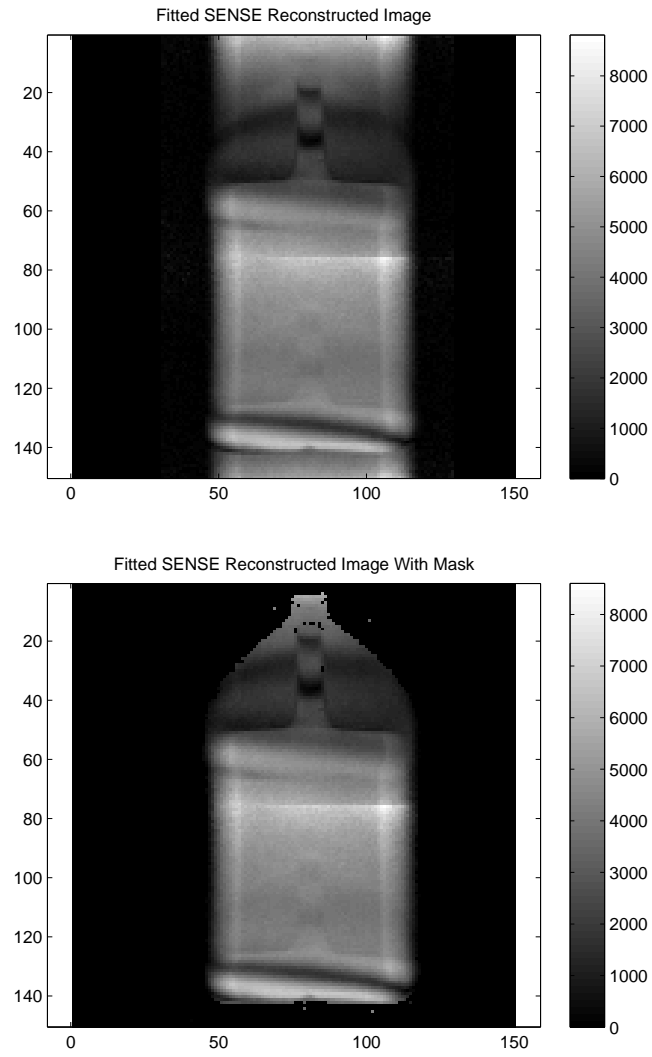Figure 4.19: Unwrapped image using synthetic sensitivity maps.

Figure 4.20: Unwrapped image using polynomial fitted sensitivity maps.

As is evident from the reconstructed images, the main problems of the reconstruction were the presence of ghost images and the amplification of random noise which leads to a reduced SNR. The ghosting observed in the images (most clearly for the synthetic and fitted reconstructions) is most likely caused by coupling of signal between the receive coil elements. The imaging phantom volume is less than the perspex tank on which the sensitivity maps were acquired and so the load characteristics are very different. One way of correcting for this problem would be to use full FOV images for each channel as the sensitivity maps since the same coupling would be present.

The noise amplification is determined by the g-factor, the noise due to coupling will thus be further amplified for an area in which the g-factor is high which confounds the problem even more. Upon acquiring the sensitivity maps, a g-factor map was calculated and is shown in Figure 4.21.
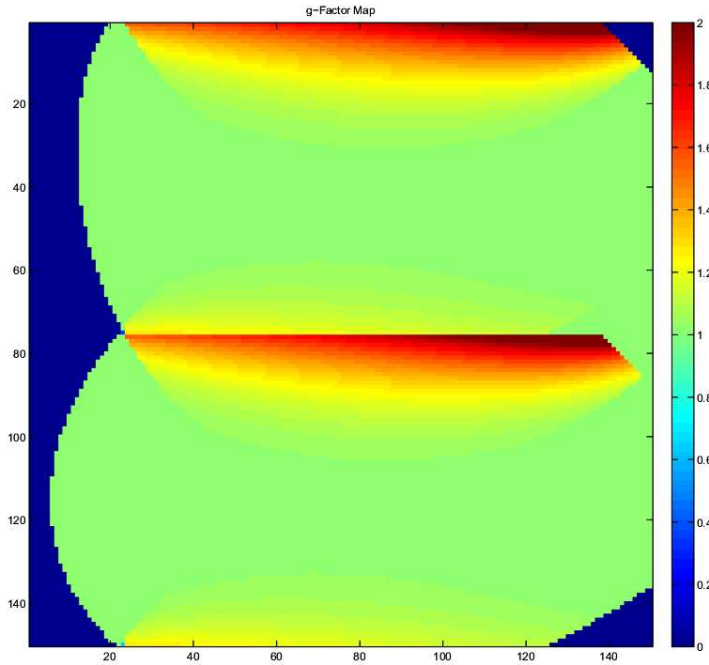

Figure 4.21: g-factor map.

The g-factor map shows that there is amplification of noise around the

edges of the image and at the centre. Even though this map was calculated using the sensitivity map data from imaging of the perspex tank, it does explain the bright ghosting artefact. If the full FOV images of the phantom were used as sensitivity maps then a more accurate g-factor map could be determined because the noise correlation matrix can no longer be set to the identity matrix as the coupling between the coils is more severe.

4.9.8   Summary

The parallel imaging section has introduced the technique and hopefully shown how images can be unwrapped and combined using knowledge of receive coil sensitivities to reduce scan time or increase signal to noise.

The results showed that sensitivity weighting unwrapped full FOV images increased the observed signal level by a factor of two for each coil. Combining these images into one modulus image resulted in an improvement of signal level of over 50% compared to the standard combined modulus image.

Reconstruction of wrapped images demonstrated that unfitted sensitivity maps were best at minimising ghosting artefacts whilst sensitivity maps fitted to 4th order polynomial functions optimised signal to noise.

The next step for the 2 channel chest coil is to get some images on a human subject. The greater SNR of images when sensitivity weighted would be of great benefit for taking images of the chest. A human subject will also load the coil more similarly to the perspex tank than a 3 litre bottle phantom which should lead to reduced ghosting artefacts in the reconstructed image.

Reconstruction of wrapped images using full FOV reference scans of the object being imaged is also an area of further work. This should be a more reliable way of correcting for ghosting artefacts and the issue of load characteristics is only important when determining g-factor maps.

Chapter 5

Methods for Studying Diffusion

5.1   Introduction

In spite of the limitations imposed on the spatial resolution with ^{3}He MRI, restricted diffusion from the small length scales of the lung airspaces as compared to the diffusion length of the gas can provide relevant information on the microstructure of the lung. This restricted diffusion is characterised by a time and scale dependent apparent diffusion coefficient (ADC).

Several NMR techniques can be used to measure ADCs, the most common being the pulsed field gradient experiment by Stejskal and Tanner described in Chapter 2. This chapter details the three methods employed in this research for studying diffusion and the data analysis software used for each technique. The chapter also outlines the protocol for taking diffusion measurements and how the measurements were scaled so that values could be compared with one another.

5.2 Fast Spin Echo (RARE) Sequence

5.2.1 Implementation

The Stejskal and Tanner [46] technique employs employs a bipolar gradient which results in a diffusion induced phase shift of the spin isochromat. For spin echo sequences a pair of unipolar gradient waveforms are implemented at either side of a refocusing pulse. The net phase shift of diffusing spins within a voxel leads to an attenuation of signal intensity according to:

$$\frac{S}{S_0} = e^{-bD_{msec}} e^{\left(\frac{TE}{T_2}\right)} \tag{5.1}$$

where S denotes the signal intensity in the presence of the diffusion sensitising gradient while S_0 is the signal intensity in the absence of the gradient. The b-value represents the amount of diffusion sensitisation and for a CPMG spin echo train as used in RARE imaging, and assuming negligible ramp times (τ), the b-value is expressed by:

$$b = \gamma^2 G^2 \left[\delta^2 \left(\Delta - \frac{\delta}{3} \right) \right] \tag{5.2}$$

where δ is the duration of a gradient lobe and Δ is the delay between the lobes which for this sequence is equivalent to the echo time (TE). The term D_{msec} represents the ADC measured over the short timescale (milliseconds) that the RARE sequence operates under.

The RARE sequence implemented for this research (64×64 matrix, TE = 14 ms, TR = 4000 ms, and $b = 0.3$ cm^{-2}s) has been adapted for measuring global ADCs and global ADC lung profiles. By acquiring a 1D image from only using the readout gradient, the readout lobes on either side of a 180° refocusing pulse serve to sensitise the sequence to diffusion. Each

readout gradient throughout the echo train increases the diffusion weighting
and results in the echo peaks exponentially decaying as described by Eq 5.1
(Fig 5.1). The T_2 relaxation of ^{3}He in the lung at 0.15 T has been mea-
sured [94] and found to be 5 seconds. The signal loss due to diffusion is
therefore much greater (an order of magnitude) than that of T_2 decay and so
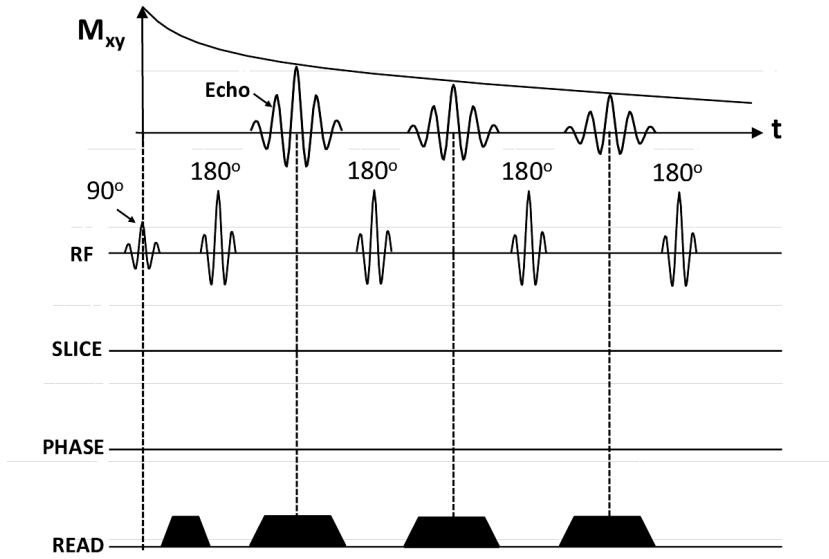the T_2 term in Eq 5.1 was ignored for the data analysis.

Figure 5.1: RARE pulse sequence diagram. Slice and phase gradients are
switched off therefore the read gradient acts as the diffusion weighting gradi-
ent. Loss of transverse magnetisation (M_{xy}) is dominated by diffusion since
T_2 at 0.15 T is long.

5.2.2   Data Analysis

Three RARE diffusion weighted (DW) scans are acquired for every subject.
These measurements consume a single batch of hyperpolarised ^{3}He gas. Un-
like the other two experimental methods a smaller quantity of polarised gas
can be used while still ensuring a high SNR. A batch can be made in 10-15

minutes.

The raw data is post processed using an updated version of a MAT-LAB m-file originally developed by Waters [94]. The program designated `DWGlobalHe.m` calculates the global ADC value, D_{msec}, for each dataset that has been selected. This is achieved by taking the peak value of each of the 64 exponentially decaying echoes (Fig 5.2).
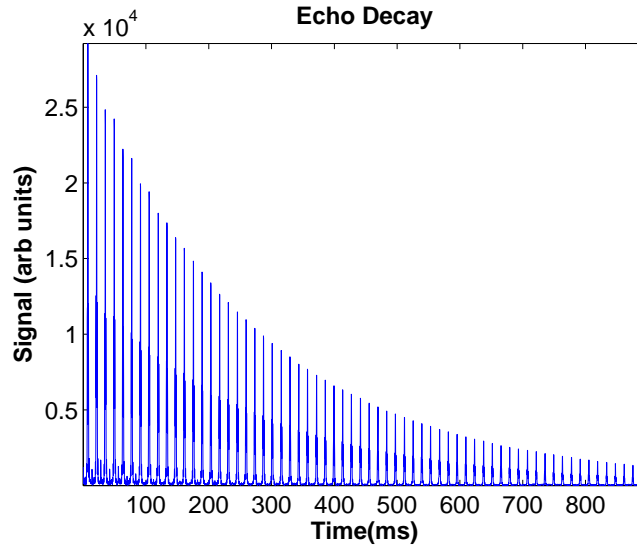

Figure 5.2: Diffusion induced signal decay.

The peak value is determined by finding which sample point from $k_x = 23$ - 41 (i.e $k_x = 32\pm9$) returns the highest value. A range of sample points over the echo are used for the determination of the peak value to account for the fact that the echo is not perfectly centred at $k_x = 32$.

Natural logarithms were then performed to give a straight line of which the gradient is proportional to D_{msec}. The gradient was found by applying a least squares linear fit to the data of which the range of fitting could be controlled by the user. Figure 5.3 shows the output of the analysis software.

An updated version of the MATLAB script written to determine ADC lung profiles was created by the author called `DWRegionalHe.m`. The pro-

gram creates signal weighted ADC histograms for the right lung, left lung, and entire lung profile. Two metrics are also calculated in the script, the fractional width of the histogram and the width of the histogram.

The script Fourier transforms each of the acquired echoes to get 64 1D profiles across the lung. Each profile is sampled 64 times and so it is possible to determine the ADC across the lung by measuring the signal decay of each sample point throughout the 64 profiles. The range of profiles to be used for the purposes of calculating ADC can be adjusted by the user with the default settings starting on 5 and finishing on 60. Not all of the 64 sample points are chosen, those points < 20% of the maximum signal of the starting profile are discarded (Fig 5.4). Using the remaining sample points the lung is divided into left and right and the values of D_{msec} are calculated. The D_{msec} values are then weighted by signal and histograms are generated (Fig 5.5).

The script corrects for the DC offset prior to the analysis. This is done by taking the first and last 3 points in k-space for each echo and averaging them together. This value is then subtracted from the raw data.

The program can also read in lots of datasets as a .txt file and return values in another .txt file for easy import into Excel or Origin.
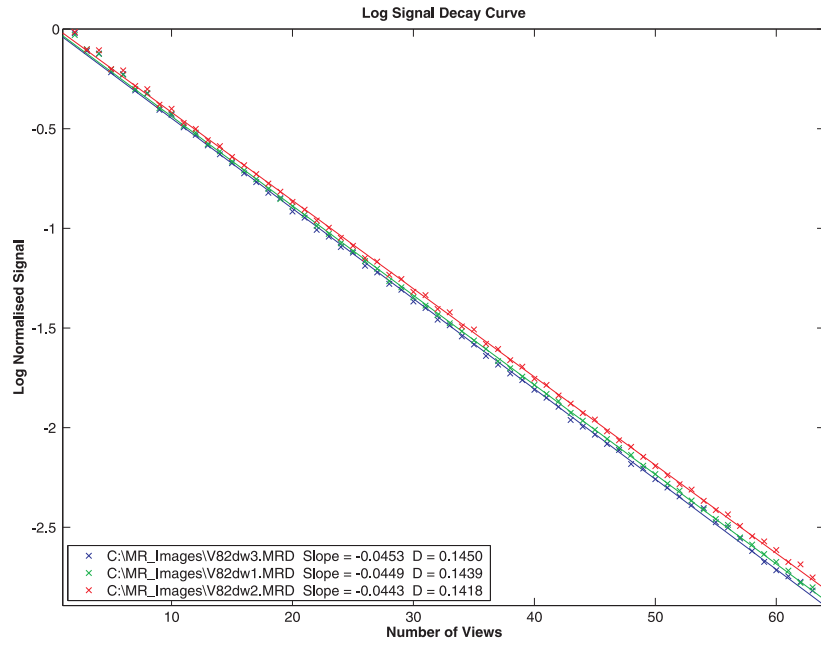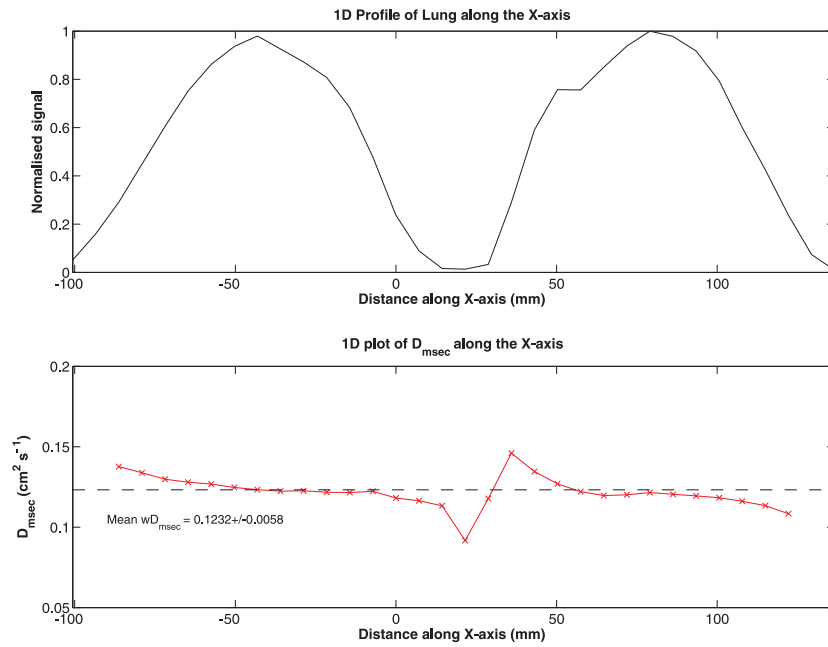
Figure 5.3: D_{msec} for each of the 3 DW scans performed on a subject.
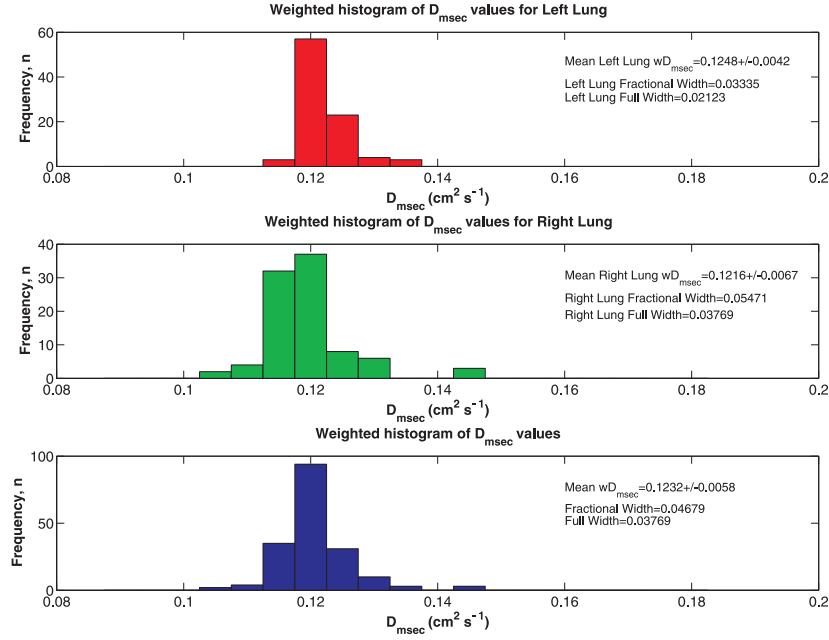

Figure 5.4: 1D Lung Profiles.

Figure 5.5: Weighted ADC Histograms.

5.3 Global Pulsed Field Gradient Sequence

5.3.1 Implementation

The latest sequence developed in this research (Fig 5.6) is analogous to that of an unpublished paper by Shanbhag *et al* [97]. The sequence is a simple pulse and acquire free induction decay (FID) that is interrupted by a bipolar gradient - i.e. the pulsed field gradient technique from Stejskal and Tanner ($gADC$).

The sequence uses a non-selective 900 μs Gaussian RF pulse for each spin excitation. During the acquisition a total of 50 FIDs are taken of which 40 are diffusion weighted and 10 have $b = 0$ cm^{-2}s. The sequence is segmented into
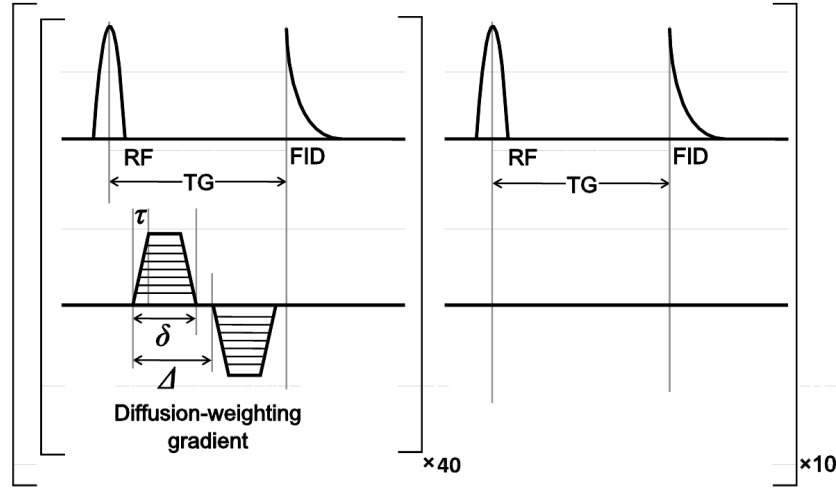
Figure 5.6: *gADC* pulse sequence diagram. By varying the strength of each diffusion gradient, multiple *b*-values could be acquired. Interleaved with the 40 diffusion weighted FIDs are 10 non-weighted acquisitions, which are used to correct for RF depletion and T_1 relaxation. TG = 10.4 ms.

blocks with each block consisting of 4 diffusion weighted acquisitions followed by a single non-diffusion weighted acquisition. The *b* value was varied by using different diffusion sensitising gradient strengths with a maximum value of $b = 56$ cm^{-2}s. Since our maximum gradient amplitude is only 16.2 mT m^{-1} for a coronal orientation, in order to achieve the *b* values published by Shanbhag *et al* we use larger δ and Δ parameters ($\Delta = 5200$ μs, $\delta = 4700$ μs). Ramp times of 150 μs are used and there is a 500 μs separation between each diffusion sensitising gradient.

In order to maximise the SNR the *b*-values are acquired from highest to lowest. The reason for doing this is because the hyperpolarised longitudinal magnetisation is non recoverable. The 10 FIDs which are not diffusion weighted are used to correct for T_1 relaxation and RF depletion. The correction is also applied to the SPAMM tagging sequence (next section) as the scan directly follows this sequence with the subject in the same position and

the receive coil under identical load conditions.

A repetition time of 200 ms is used with a spectral bandwidth of 12.5 KHz (80 μs), $\alpha = 14°$, and 2048 sample points. At the end of the acquisition crusher gradients (11 mT m^{-1} amplitude, 5 ms duration) are applied on all axes to destroy any residual transverse magnetisation.

The sequence was later adapted to sample a lower range of b-values in order to maximise SNR even further. The maximum b-value was adjusted to 15 cm^{-2}s with all other aspects of the sequence remaining the same. By implementing this change it was no longer possible to perform q-space analysis on the measurements.

5.3.2 Data Analysis

The T_1 and flip angle corrected diffusion weighted data were fitted to the geometric model proposed by Yablonskiy [71] and analysed using the q-space technique.

Yablonskiy Geometric Model

In the Yablonskiy model the diffusion induced signal decay is characterised by D_L and D_T and expressed as;

$$S(b) = S_0 e^{-b\overline{D}} \left(\frac{\pi}{4bD_{AN}} \right)^{1/2} e^{\left(\frac{bD_{AN}}{3} \right)} \Phi[(bD_{AN})^{1/2}] \qquad (5.3)$$

where $\Phi(x)$ is the error function, and the terms $\overline{D}$ and D_{AN} represent the mean ADC and anisotropy of ADC respectively. These two terms are defined below as;

$$\overline{D} = \frac{1}{3}D_L + \frac{2}{3}D_T \qquad (5.4)$$

$$D_{AN} = D_L - D_T \qquad (5.5)$$

The acquired 50 FIDs are post processed using the MATLAB program `gADC_bspace_qspace.m`. Any noise spikes present in the FIDs (caused by persisting eddy currents when going to high b-values) were identified and removed with the missing points of the FID being interpolated. The data was then zero padded to 4096 points and then Fourier transformed. An integration over a small window centred on the peak of the resulting Lorentzian was performed to obtain values of the signal intensity of each FID. These values were then fitted to Eq 5.3 (over the range of $b = 0$ -15 cm^{-2}s) which had been re-written with the relationships of D_L and D_T to the geometrical parameters R and h substituted in (see 3.6.2). After the sequence had been changed, all 40 diffusion weighted FIDs were now within the $b = 0$-15 cm^{-2}s range resulting in a more robust fit. The outputs of the analysis software are shown in Figures 5.7 - 5.9.
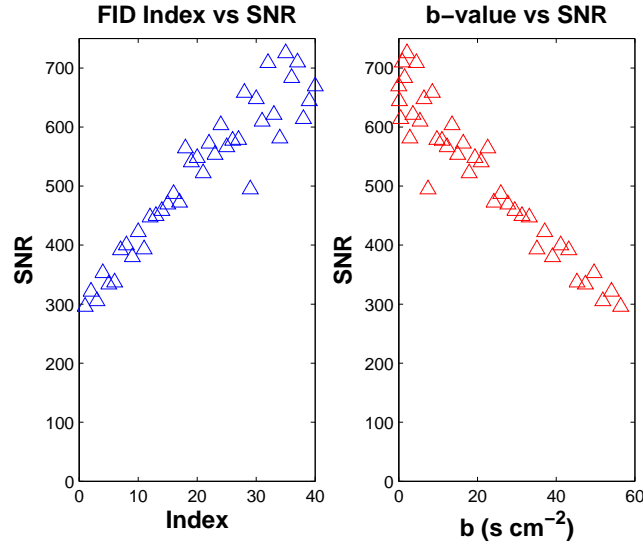

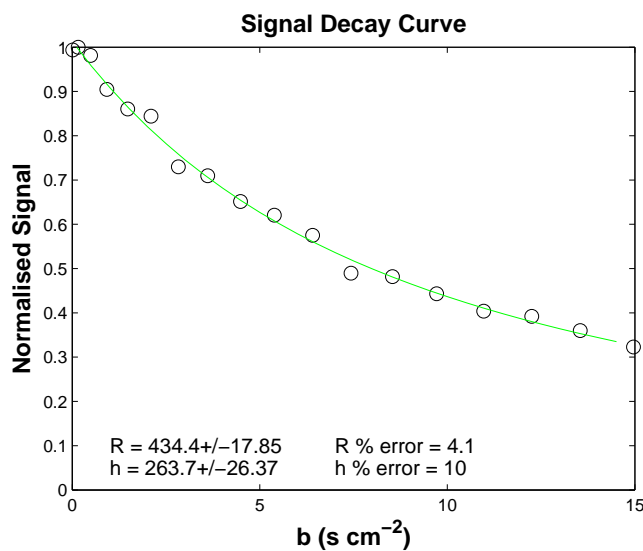Figure 5.7: Signal to noise ratio throughout data acquisition.

Figure 5.8: Diffusion induced signal decay with Yablonskiy model fitted over data. The derived values for the geometric parameters R and h are shown.
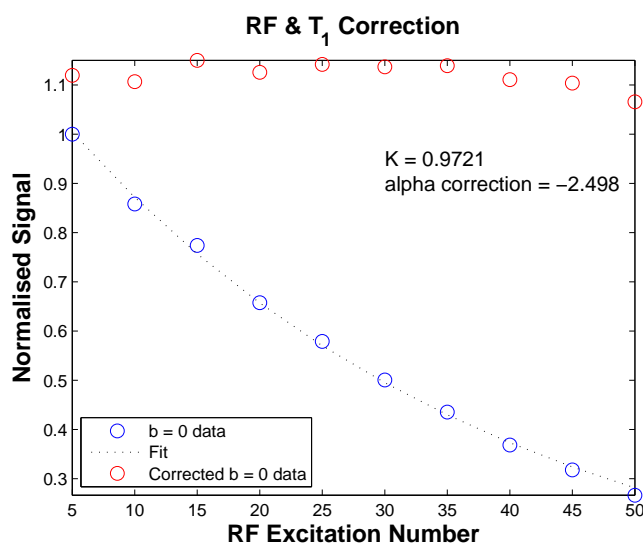

Figure 5.9: RF and T_1 correction curve. The value K is derived from the fit applied to the $b = 0$ data and is used to obtain the actual flip angle during the measurement. By knowing the actual flip angle, a correction can then be applied to the data. A T_1 of 25 seconds is assumed.

q-Space Analysis

Linear dimensions of the lung microstructure were also probed by using q-space analysis on the acquired data. The 40 diffusion weighted FIDs correspond to a range of q-values between 0.02 and 1.23 mm^{-1} where q is given by;

$$q = \frac{\gamma \delta G}{2\pi} \sqrt{\frac{\Delta - \delta/3}{\Delta + \delta}} \qquad (5.6)$$

The expression for q as written in Eq 5.6 takes into account the effect of the finite width of the diffusion-weighting gradient lobes, and the actual experimental diffusion time given by $t_{exp} = \Delta + \delta$.

The signal intensity values of the 40 diffusion weighted FIDs obtained from the analysis software were normalised and plotted as a function of q. The q-space curve needed to be interpolated since q had not been sampled linearly and was then zero padded to four times its original length. The curve was then Fourier transformed to give the displacement probability profile (DPP). The DPP is a probability density function of the average displacement of the ^{3}He atoms during t_{exp}. The DPP was fitted to a mono-Gaussian model;

$$DPP(x) = Z \exp\left(\frac{x^2}{2X_{rms}}\right) \qquad (5.7)$$

where the width of the Gaussian function is determined by X_{rms}, the root mean square displacement of the ^{3}He atoms. This gives a measure of the mean peripheral airspace dimension which restricts diffusion. The parameter Z is interpreted as the zero displacement probability. Originally, the DPP was fitted to a bi-Gaussian model and two values of X_{rms} were obtained ($X_{rms}1$ and $X_{rms}2$) corresponding to two different length scales. However, $X_{rms}2$ did not comfortably satisfy the required restricted diffusion regime criteria and so the mono-Gaussian model was adopted instead. Figure 5.10
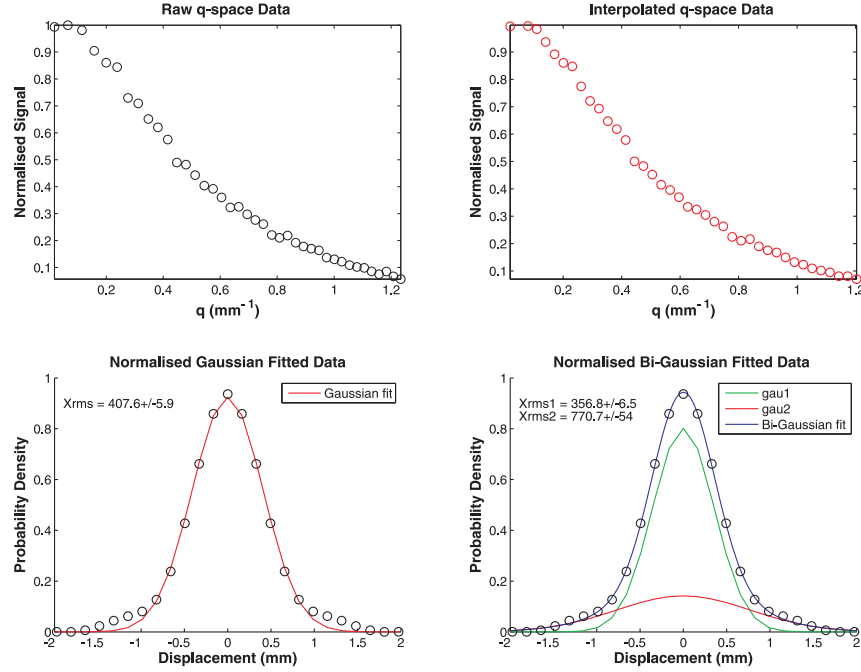
shows a typical q-space analysis output.

Figure 5.10: q-space output screen.

5.4 SPAMM Tagging Sequence

5.4.1 Introduction

The previous methods discussed so far are based upon the diffusion induced decay of transverse spin magnetisation. This occurs over times of a few milliseconds which correspond to diffusion lengths of tenths of a millimetre. The diffusion time for the previous experimental methods is limited by T_2^* (for the pulsed field gradient sequence) and T_2 (in the case for the RARE sequence) relaxation, which makes it impossible to probe the microstructure of the lung at long distances with transverse magnetisation.

Diffusion at long length scales is important to study as it provides a useful assessment of the airway interconnections, particularly collateral ventilation pathways (connections between distant parts of the lung tree).

One method for measuring diffusion at long length scales is to tag the longitudinal magnetisation whose decay is governed by the longer T_1 relaxation constant (~ 25 seconds for ^{3}He in healthy lungs *in vivo*). This ADC, measured over times of seconds and distances of centimetres is represented by D_{sec}. Measurements of ADC at long length scales by Nottingham and others have found a value of $D_{sec} \sim 0.02$ cm^2 s^{-1} for explanted healthy human lungs and *in vivo* dog lungs [98–100].

5.4.2 Implementation

The most common tagging technique is that of spatial modulation of longitudinal magnetisation (SPAMM) and was originally used to evaluate cardiac motion but has also been used to track thoracic motion. SPAMM, in its simplest form consists of two non selective RF pulses (θ_1, and θ_2) with a gradient lobe in between which introduces a spatially dependant phase $\phi(r)$. This results in a sinusoidal spatial modulation with wavelength:

$$\lambda = \frac{2\pi}{\gamma G t} \tag{5.8}$$

in which G is the gradient amplitude and t is the duration for which it is applied for. The longitudinal magnetisation after the second RF pulse is obtained from Bloch's equations:

$$M_z(r) = -M_0 \left[\sin\theta_1 \sin\theta_2 \cos\phi(r) - \cos\theta_1 \cos\theta_2 \right] \tag{5.9}$$

If both tagging pulses are 45° (as implemented by the tagging pulses in our sequence, shown in Figure 5.11) then $M_z(r)$ is:

$$M_z(r) = \frac{M_0}{2}\left[1 - \cos(kx)\right] \tag{5.10}$$

with $k \equiv \gamma G t = \frac{2\pi}{\lambda}$. By implementing 45° tagging pulses 100% modulation of magnetisation is achieved (Fig 5.12) while avoiding the ambiguity of sign reversal that occurs with magnitude imaging (Fig 5.13).
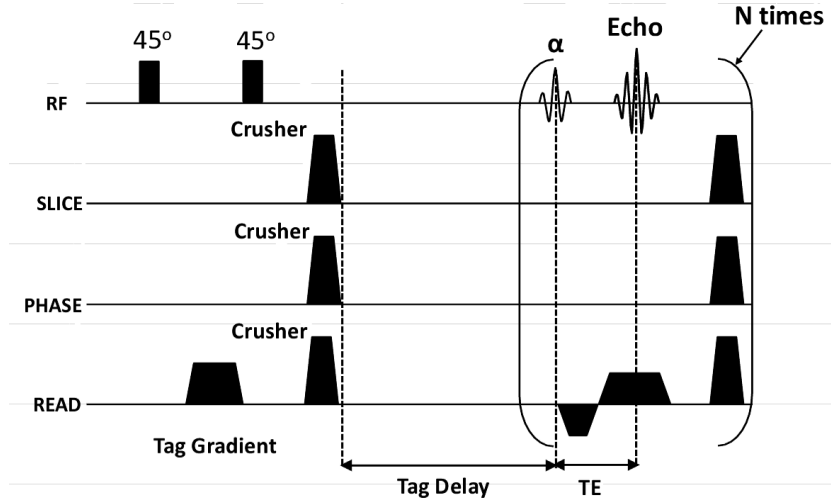

Figure 5.11: 1D FLASH tagging pulse sequence diagram. The two hard pulses and the tagging gradient (on the read axis) are shown clearly. Crusher gradients are shown on each axis after the tagging gradient ends. After sufficient evolution time of the tags, the imaging sequence is applied. Crushers are once again applied on all axes after each acquisition. TE = 6 ms.

After the tagging pulses have been applied the modulated magnetisation is attenuated by diffusion over times limited only by T_1 relaxation. Thus, values of ADC can be determined by $R = D_{sec}k^2$ where R is the decay rate constant of the modulation. The effect of both T_1 relaxation and RF attenuation (from the imaging pulses used to inspect the modulated magnetisation)
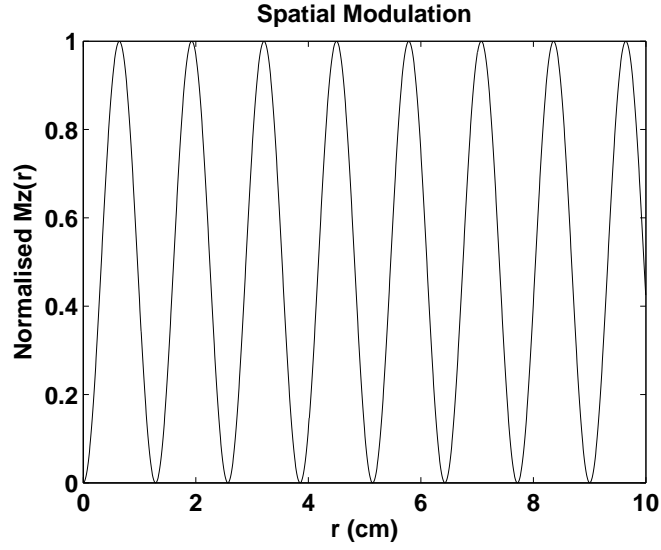
Figure 5.12: Spatial modulation resulting from 45° tagging pulses.

does not influence the decaying modulated magnetisation provided that both these effects remain uniform over λ [101].

The imaging sequence that was implemented to inspect the decaying tags was a 1D FLASH sequence. By disabling the phase encoding, each line of k-space represents the spatially modulated magnetisation at different times throughout the acquisition. A TR of 400 ms was used and 32 lines were acquired giving a total tag decay time of 12.8 s. A flip angle of 16° was selected to ensure good SNR for the ADC calculations and a wavelength of 1.6 cm was used in order to get several tags per lung which would be reasonably attenuated during the acquisition time. To have well defined tags 128 sample points were taken with a spectral bandwidth of 33.3 kHz (30 μs).
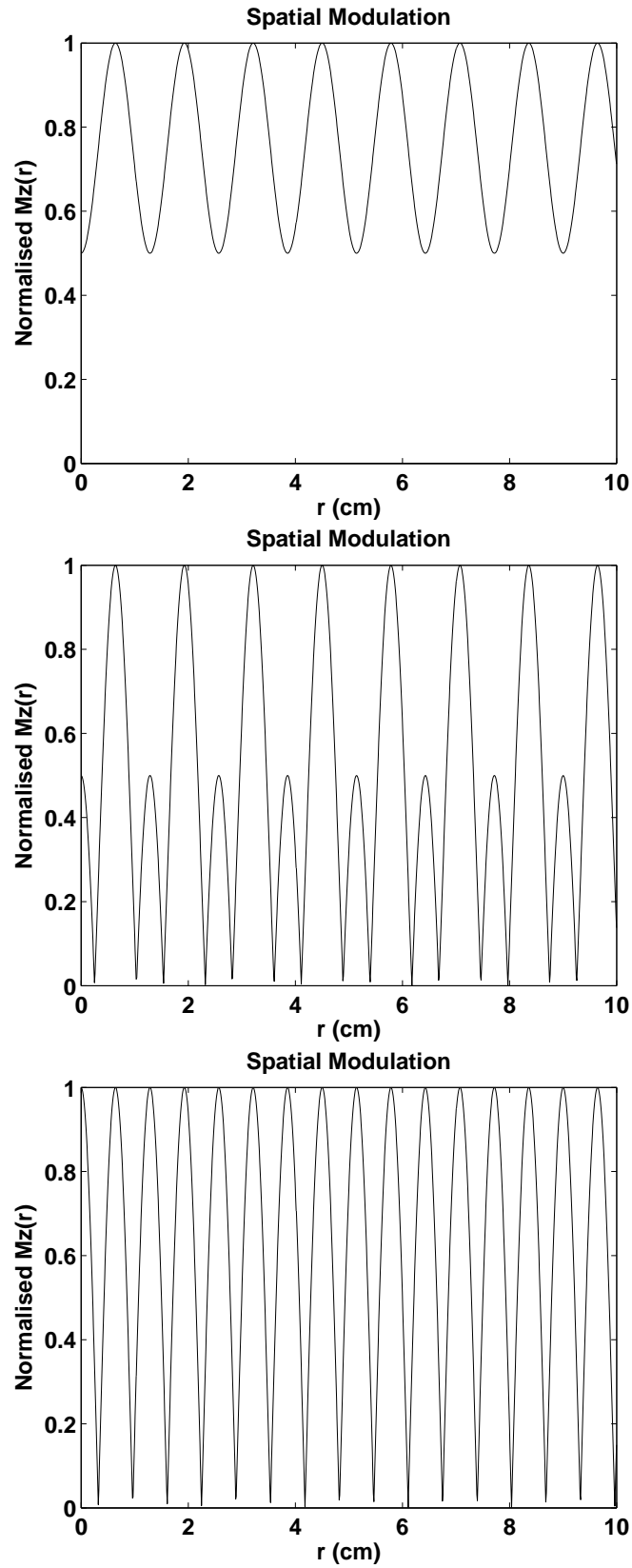
Figure 5.13: Spatial modulation resulting from $30°$(top),$60°$(middle),and $90°$ (bottom) tagging pulses.

5.4.3   Data Analysis

The acquired tag data is loaded into the `ADC_sec_RG_G.m` program for post processing and subsequent data output.

The raw data are DC offset corrected using the same method as previously mentioned. The data are then zero padded from 128 points to 256 and then extrapolated to 2048 sample points. This results in the tags being smooth and well defined.

The program then locates the peaks and troughs for each tag throughout the 32 acquired lines, the process of which has been made easier and more accurate from earlier smoothing. The distance between the peaks and troughs is then plotted against time and a straight line is fitted to the data points. The gradient of this line determines the decay rate R which is used to calculate the ADC. The program also calculates the standard error of the linear fit which is used to calculate the standard deviation.

The SNR starts to significantly fall after the 15th line and so no point after this is fitted to. In practice there is a rapid signal decay for the first 3 points which is attributed to diffusion through the large airways and so these are also excluded from the fit. Therefore for each tag there are 12 points that are fitted to from lines 4 to 15 over a time frame of 1.2 to 5.6 seconds.

The script automatically selects the best 3 tags for each lung based on signal and finds the mean D_{sec} as well as providing the standard deviation for each of the averaged D_{sec} values.

In some instances for which the spatial modulation of magnetisation deviates from that of 45° tagging pulses and the ambiguity of sign reversal is evident (as seen in the middle and bottom pictures of Fig 5.13), the program can discard the first line. In the few instances for which this has occurred the tagging pulses have never been more than 5° out.

Lastly, the program also generates a .jpg file of the data output when the script is run. This allows easy comparison between different datasets and also serves as a redundancy should the .MRD file ever be deleted or lost in some way. The output of the tag analysis software is shown in Figure 5.14.
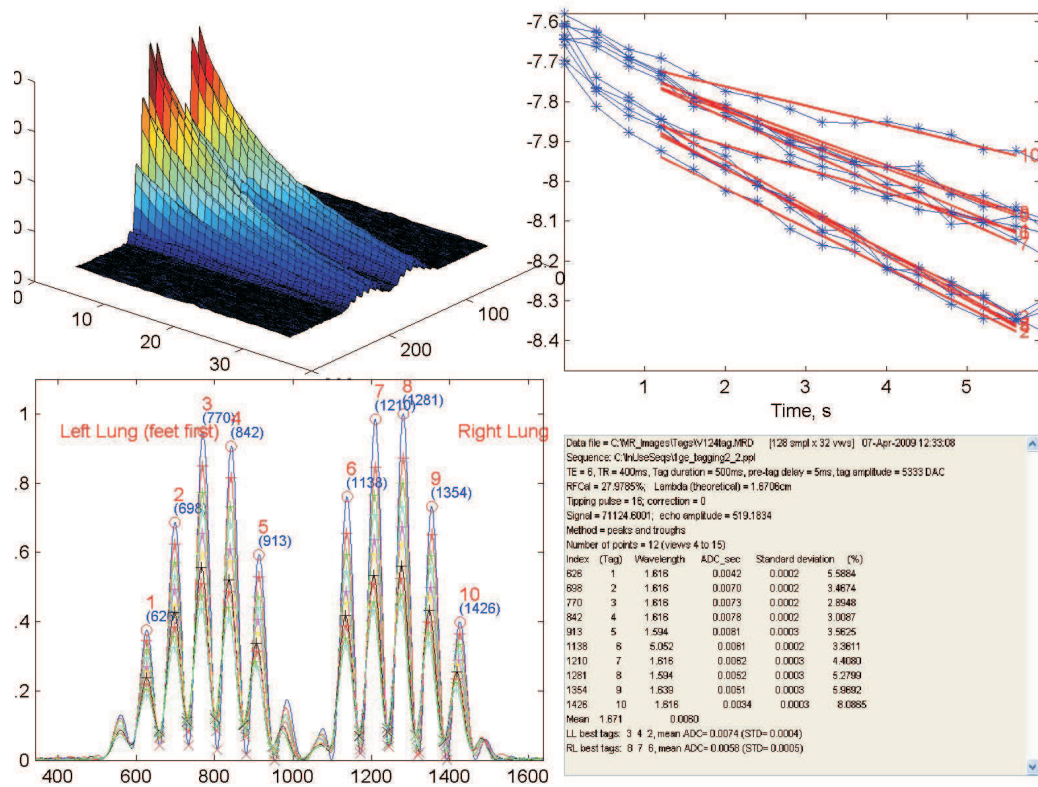

Figure 5.14: Tag output data.

5.5   Measurement Protocol

5.5.1   Subjects

During the course of this research diffusion measurements were performed on subjects from three different study groups utilising the previously described magnetic resonance (MR) sequences. The three study groups will hereon in be referred to as; the Leicester study group, the Asthmatic study group, and the Cystic Fibrosis (CF) study group.

Leicester Study Group

Children and young adults from 7 to 21 years of age were recruited for this study from community based databases in the Leicester area. Subjects over 11 years were recruited from the Leicestershire Respiratory Cohorts, a pre-existing stratified random sample of all children resident in the area originally recruited between the ages of 0 to 4 years. Information was available on pre-existing health problems and risk factors in this group of children as they had been followed up with questionnaires and had pulmonary function tests (PFTs) performed at Leicester General Infirmary (LGI) in the past.

Children less than 11 years old were recruited from a stratified random selection of all children resident in Leicestershire from the Leicester Specialist Community Child Health Services Database. Information on respiratory health and other risk factors was ascertained at the time of their visit to LGI.

The aim of the study was designed to look at normal alveolar development in children and so only children who were born at more than 36 weeks of gestation, who were never admitted to a neonatal unit and who had no current respiratory symptoms or chronic respiratory illnesses were included. The study had Research Ethics Committee approval with written informed

consent being obtained from all subjects and in the case of minors below 18 years, from their parents/legal guardians as well.

Asthmatic Study Group

The aim of the asthmatic study was to determine the alveolar structure in adult asthmatics with developed lungs compared with matched healthy control subjects (aged 22-70 years).

Asthmatic subjects were recruited from the difficult asthma cohort at Glenfield hospital (these patients must have severe asthma, eosinophillic asthma, be on maintenance dose prednisolone and have less than 10 pack year smoking history). Control subjects were recruited from staff and advertising at Glenfield hospital (no airways disease, negative PC20, negative skin prick test, and have less than 10 pack year smoking history). Diffusion measurements were performed on a total of 10 severe asthmatics and 7 controls.

CF Study Group

The aim of the CF study was to examine whether hyperpolarised ^{3}He MRI could provide any useful metrics for assessing CF severity.

Subjects were chosen from the Leicester paediatric Cystic Fibrosis Clinic. All children aged 6-11 years who attend this clinic were approached. A total of 10 subjects participated in the CF preliminary study.

5.5.2 Physiological Measurements

For each study group, PFTs were performed on subjects at their respective infirmaries to derive lung volumes and capacities. Pulmonary function was assessed using spirometry, body plethysmography, and multiple breath

washout (MBW) to provide a range of functional indices that were compared with the MR measurements. The basic principles behind each of the PFTs are well documented in the literature thus will not be re-iterated here. The derived functional indices include:

FEV1 The forced expiratory volume in 1 second is the volume of air that can be exhaled from the lungs in 1 second with maximal effort following a maximal inhalation.

FVC The forced vital capacity is the total volume of air that can be exhaled from the lungs with maximal effort following a maximal inhalation.

RV The residual volume is the volume of air remaining in the lungs at the end of maximal exhalation. The residual volume can never be expired because subatmospheric intrapleural pressure keeps the alveoli slightly inflated, and some air also remains in the noncollapsible airways.

FRC The functional residual capacity is the volume of air remaining in the lungs at the end of a normal expiration.

TLC The total lung capacity is the volume of air that is contained in the lungs at the end of maximal inhalation.

LCI The lung clearance index is derived from MBW tests and is used to quantify ventilation inhomogeneity. It is defined as the number of lung turnovers needed to lower the washout tracer to 2.5% of its starting concentration. It is a robust and sensitive index thereby making it ideal for assessing lung disease severity. Particularly, in CF there is a need for sensitive and repeatable clinical endpoints to aid therapeutic intervention.

V_a The alveolar volume is determined through MBW tests and represents the volume of the lung that is participating in gas exchange. In healthy subjects V_a is approximately equal to the TLC whereas for subjects with unevenly distributed ventilation (such as in asthma) there is a discrepancy.

The difference between TLC and V_a can therefore be used as a correction factor to assess the actual lung volume involved in gas exchange at FRC. The V_a and corrected FRC were then subsequently used for the scaling of MR measurements (see 5.6).

5.5.3   Hyperpolarised ^{3}He MRI Measurements

Measurements were undertaken in a 0.15 T permanent magnet system (Intermagnetics General Corporation, New York) with a Surrey Medical Imaging Systems console (Surrey, UK). The ^{3}He gas was hyperpolarised via metastable exchange optical pumping in a custom made polarisation system [102]. The stored hyperpolarised ^{3}He gas was then mixed with a buffer of ^{4}He to a particular volume and then transferred from the glass storage cell into a 1 litre tedlar bag (SKC Limited, Blandford Forum, UK). The subject, in a supine position inside the magnet with an appropriate ^{3}He receive coil around their chest, inhaled the gas mixture from FRC through a disposable one-way valve and then breath-held between 2-10 seconds depending on the nature of the measurement.

5.6   Scaling of Measurements

Depending on the study group, subjects were given either a ~ 350 ml bolus or a ~ 650 ml bolus of a ^{3}He $/^4$He gas mixture (comprising 15-30 ml hyperpolarised ^{3}He, depending on the sequence being used), for each measurement. Therefore the concentration of helium present in the lung, and the level of lung inflation differed for each individual. In order for measured values of ADC, X_{rms}, R, and h to be compared with one another, it is necessary to scale the measurements to account for the effects due to concentration and

inflation.

5.6.1 Effect of Concentration on X_{rms}, R, and h

X_{rms}, R, and h were measured in a healthy adult male (27 years) volunteer for a range of helium concentrations, at fixed lung volume, FRC. This was achieved by having the volunteer expire a controlled amount of air, from FRC, before inspiring the same amount of a hyperpolarised ^{3}He $/^4$He mixture. Figures 5.15 - 5.17 show that X_{rms}, R, and h remain constant across the range of helium concentrations (defined as the volume of helium inspired, divided by FRC).
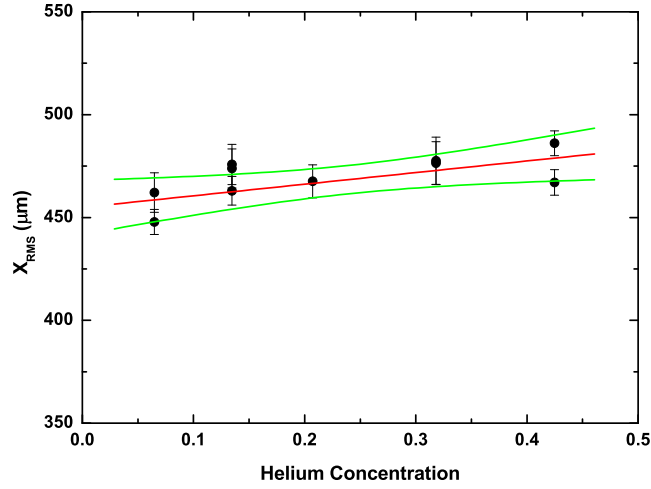
Figure 5.15: X_{rms} vs Helium Concentration. The line of best fit (red line) and 95% confidence intervals (green lines) are shown. Individual measurements for each concentration are shown.
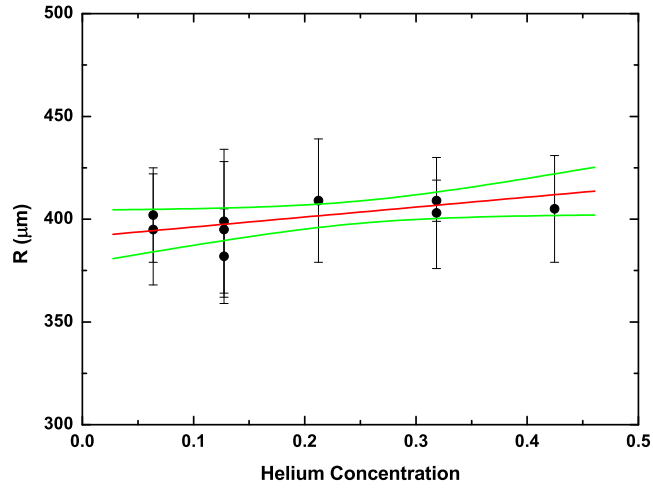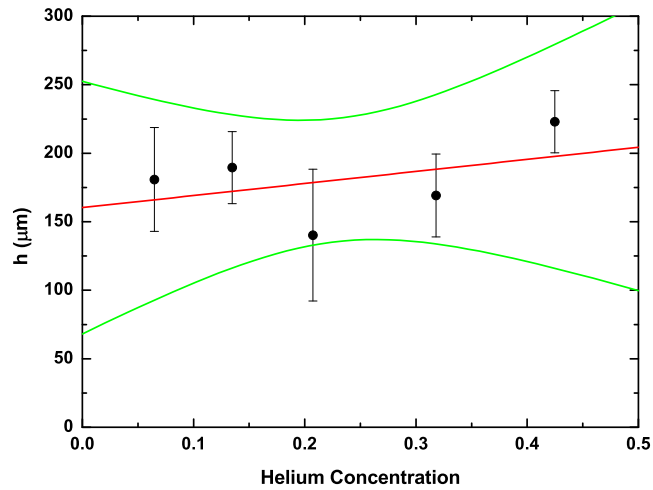
Figure 5.16: R vs Helium Concentration. The line of best fit (red line) and 95% confidence intervals (green lines) are shown. Individual measurements for each concentration are shown.

Figure 5.17: h vs Helium Concentration. The line of best fit (red line) and 95% confidence intervals (green lines) are shown. Each data point represents an average of 2-3 separate measurments

5.6.2   Effect of Concentration on D_{msec}

D_{msec} was measured at a fixed lung volume (i.e. FRC) in the same adult male volunteer, for a range of helium concentrations, and is presented in Figure 5.18. The concentration of helium in the lung was controlled using the method described in 5.6.1. D_{msec} appears to increase systematically with helium concentration and the data are well described by a second order polynomial expression.
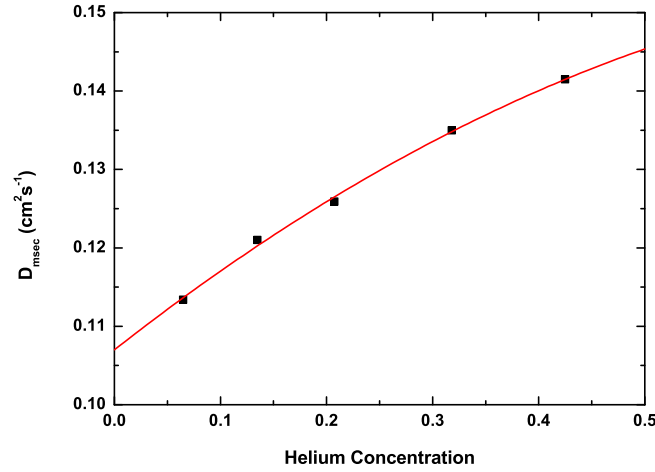

Figure 5.18: D_{msec} vs Helium Concentration. The solid red line is a fit to a second order polynomial expression, $D_{msec} = -0.059x^2 + 0.106x + 0.107$. Each data point represents an average of 4-6 separate measurments

The curve plotted in Figure 5.18 can be used as the basis for scaling all measurements of D_{msec} back to 'zero helium concentration' (i.e. the diffusion coefficient for one helium atom in the lungs, hereon referred to as D_0). This assumption was validated by conducting the following experiments on nine volunteers.

D_{msec} was measured in the routine manner described in 5.2, for two different boluses of helium gas, i.e. 350 ml and 650 ml. The two resultant

ADC values were scaled back to find D_0 and then compared. It was found that the scaling method gave values of D_0 that agreed with each other. By using the calibration curve, measurements that were carried out at different concentrations of helium can be compared with one another.

5.6.3 Effect of Lung Inflation on D_{msec}

The dependence of D_{msec} on the degree of lung inflation has been previously reported for measurements in adults; Waters *et al* [94] measured D_{msec} over a range of lung inflation levels and they found that D_{msec} increased linearly with inflation. Similar measurements were carried out on several subjects and also two adult volunteers.

Starting from FRC, the volunteers inspired a ^{3}He /^{4}He gas mixture, followed by a bolus of air, to inflate the lungs to the desired volume. The amount of helium was controlled so that the concentration remained the same for each level of expansion. D_{msec} was found to vary linearly with lung expansion (Fig 5.19). The lung volumes at various levels of inflation are presented in terms of normalised change from FRC, and similarly, D_{msec} is presented in terms of normalised change from D_{msec} at FRC (extrapolated from linear fit of D_{msec} vs lung inflation). The rate of change of the normalised D_{msec} with respect to normalised volume, denoted k, is found through the following expression;

$$\frac{D_{msec} - D_{msec}(FRC)}{D_{msec}(FRC)} = k\frac{V - V_{FRC}}{V_{FRC}} \tag{5.11}$$

this is the basis for scaling the D_{msec} values measured in the volunteers to D_{msec}(FRC).

While a linear relationship was inferred from the results of the 5 volun-

teers it is known biologically that the lungs do not inflate uniformly and that regions are recruited at different levels of inflation. The recruitment corresponds to collapsed and partially collapsed alveoli reopening as alveolar pressure increases. The different levels of lung inflation can thereby be seen as a combination of two processes: the first is the expansion of alveoli that are already open (i.e. already recruited), and the second is the recruitment and subsequent expansion of partially collapsed and collapsed alveoli. Further investigation of this relationship with more volunteers would be desirable as different individuals are expected to display recruitment at different levels of inflation.
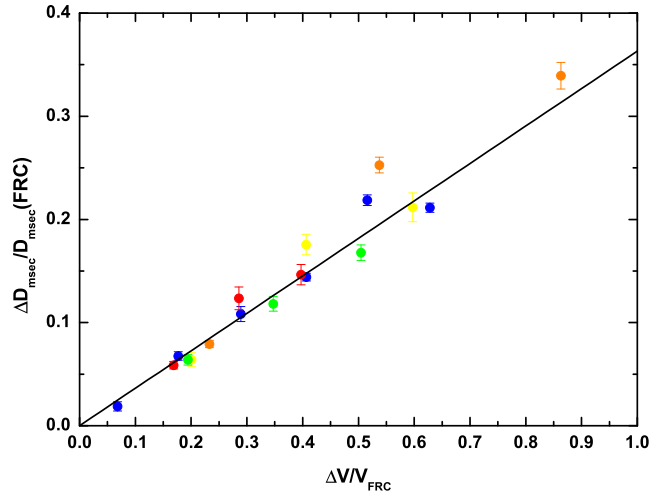

Figure 5.19: Variation of normalised D_{msec} with normalised lung volume in 5 volunteers. The constant of proportionality, k, was found to be 0.36±0.02

5.6.4   Effect of Lung Inflation on X_{rms}, R, and h

The data obtained from the global pulsed field gradient sequence as previously described in 5.3 can be analysed using two methods, namely q-space

analysis, and application of Yablonskiy's geometric model. A strong correlation between the fit parameters of the two analysis techniques, i.e. X_{rms} and R (the outer radius of the acinus) was found (see 6.1.2).

Yablonskiy has found it reasonable to assume that R (and h) scales with the cube root of lung inflation, an assumption supported by our own variable inflation measurements using the previously outlined protocol (see Figures 5.20 and 5.21). It is thus proposed that due to the strong agreement between X_{rms} and R, X_{rms} will scale in the same way. Therefore all measurements of X_{rms} and R have been scaled to 60% of total lung capacity (TLC).
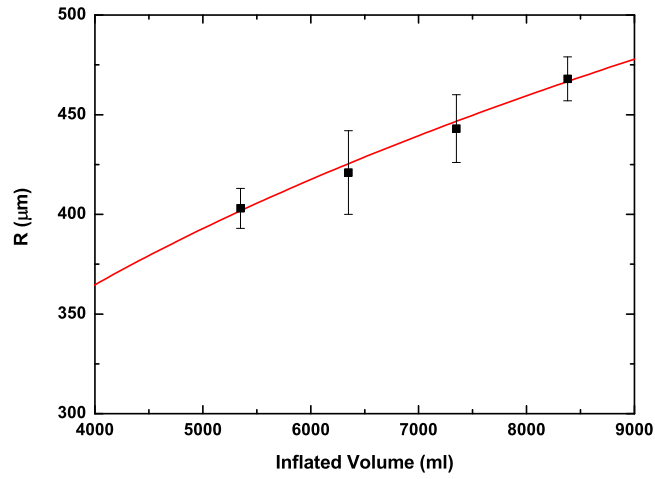
Figure 5.20: Variation of R with lung inflation. The solid red line represents a cube root fit. Each data point represents an average of 2-3 separate measurments.
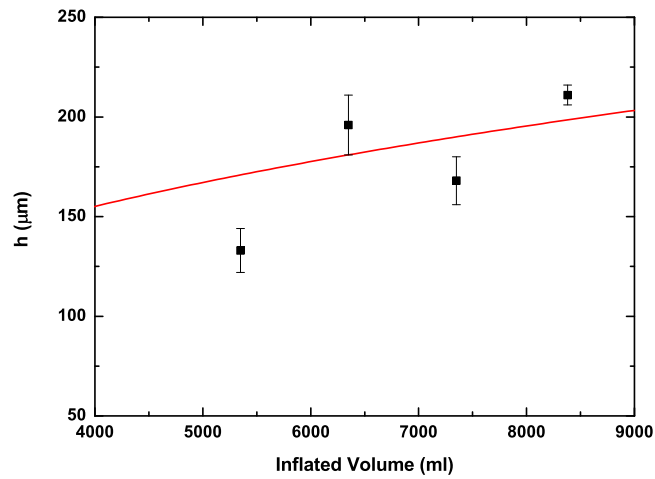

Figure 5.21: Variation of h with lung inflation. The solid red line represents a cube root fit. Each data point represents an average of 2-3 separate measurments.

Chapter 6

Results and Discussions

6.1 Leicester Study Results

6.1.1 Physiological and Lung Function Measurements

Physiological and lung function measurements were performed on 189 subjects (Table 6.1). There was a wide range and spread of measured parameters, as would be expected with a study population extending from 7 years of age to 21 years.

Age(Yrs)	12.5(2.60)
FRC(L)	1.88(0.64)
TLC(L)	4.06(1.38)
Height(cm)	154.7(14.9)
Weight(kg)	49.7(14.8)

Table 6.1: Mean and standard deviation of physiological and lung function measurements for all subjects in the Leicester study.

6.1.2 RARE Sequence Results

Three D_{msec} measurements were obtained in 189 subjects using a bolus size of 630 ml. The within subject coefficient of variation for these measurements is 4.9% and so for the purposes of analysis, the mean of these values are taken as the uncorrected ADC.

The mean (standard deviation - SD) volume and concentration corrected D_{msec} was 0.0932 (0.0119) cm^2s^{-1} and was similar in males and females (t-test, p = 0.80). The corrected ADC increased with measures of growth including age ($R^2 = 0.14$, p < 0.0001, Fig 6.1) and FRC ($R^2 = 0.34$, p < 0.0001, Fig 6.2). The change of D_{msec} with FRC remained significantly less than the predicted scenario of no neoalveolisation (p = 0.02).
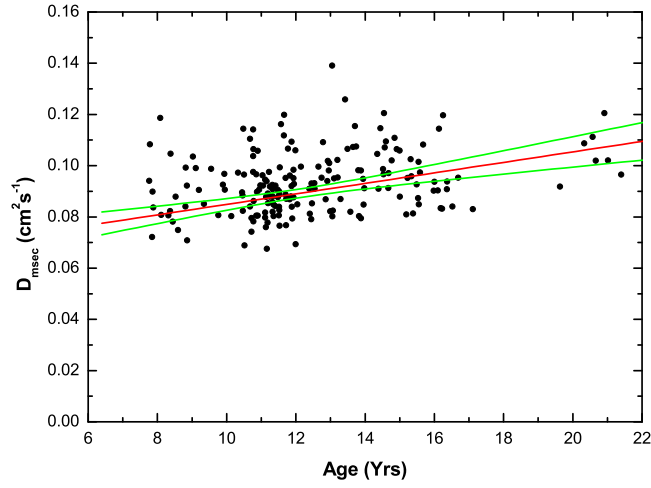
Figure 6.1: D_{msec} vs Age. The line of best fit (red line) and 95% confidence intervals (green lines) are shown. For the purposes of clarity, the error bars are not shown.
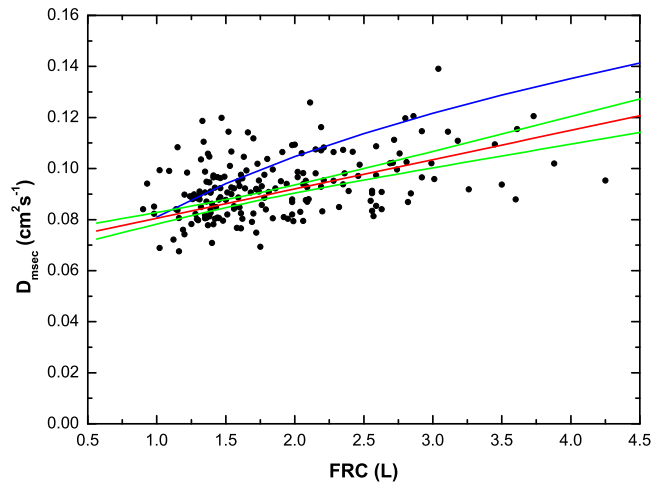

Figure 6.2: D_{msec} vs FRC. The line of best fit (red line) and 95% confidence intervals (green lines) are shown. The blue curve represents the predicted change if lung growth occured only by expansion of pre-existing alveoli. For the purposes of clarity, the error bars are not shown.

6.1.3 Global Pulsed Field Gradient Sequence Results

The mean peripheral airspace dimension obtained from q-space analysis (X_{rms}) was measured in 53 subjects. The within subject coefficient of variation for these measurements is 1.3%.

The mean (SD) volume and concentration corrected X_{rms} was 421 (37) μm and showed a statistically significant increase with age ($R^2 = 0.08$, p = 0.025, Fig 6.3). Similarly, a minor increase with FRC was observed which was shown to be statistically insignificant ($R^2 = 0.02$, p = 0.14, Fig 6.4).

The acinar radius (R) and alveolar sleeve depth (h) that were derived through application of the acinar model of Yablonskiy *et al* to our data were measured in the same 53 subjects. The within subject coefficient of variation for these parameters are 6.3% and 14% for R and h respectively.

The mean (SD) volume and concentration corrected R and h were 430 (41) μm and 243 (42) μm. These geometrical parameters also showed small increases with age (R, $R^2 = 0.166$, p = 0.0014, Fig 6.5) (h, $R^2 = 0.24$, p = 0.00014, Fig 6.7) and FRC (R, $R^2 = 0.197$, p = 0.0008, Fig 6.6) (h, $R^2 = 0.19$, p = 0.0009, Fig 6.8).

The values for X_{rms} and R were found to be closely related to each other (slope = 1.01, $R^2 = 0.58$, p < 0.0001, Fig 6.9).
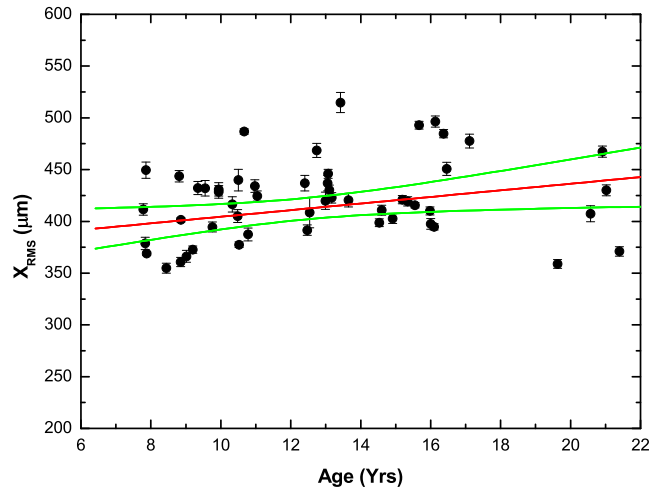
Figure 6.3: X_{rms} vs Age. The line of best fit (red line) and 95% confidence intervals (green lines) are shown.
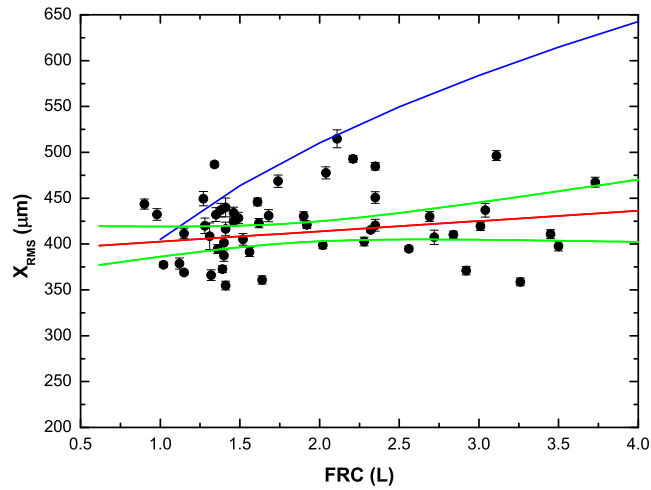

Figure 6.4: X_{rms} vs FRC. The line of best fit (red line) and 95% confidence intervals (green lines) are shown. The blue curve represents the predicted change if lung growth occured only by expansion of pre-existing alveoli
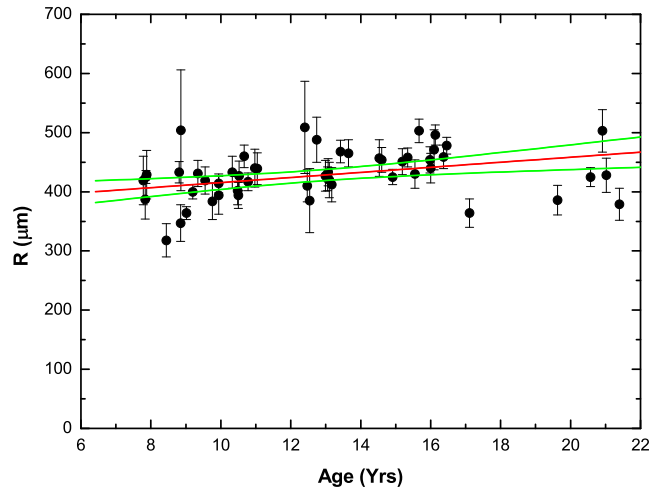
Figure 6.5: R vs Age. The line of best fit (red line) and 95% confidence intervals (green lines) are shown.
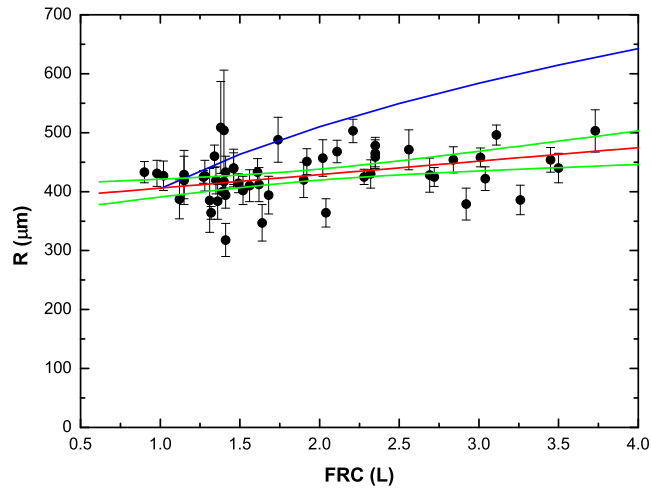

Figure 6.6: R vs FRC. The line of best fit (red line) and 95% confidence intervals (green lines) are shown. The blue curve represents the predicted change if lung growth occured only by expansion of pre-existing alveoli

Figure 6.7: h vs Age. The line of best fit (red line) and 95% confidence intervals (green lines) are shown.

Figure 6.8: h vs FRC. The line of best fit (red line) and 95% confidence intervals (green lines) are shown. The blue curve represents the predicted change if lung growth occured only by expansion of pre-existing alveoli
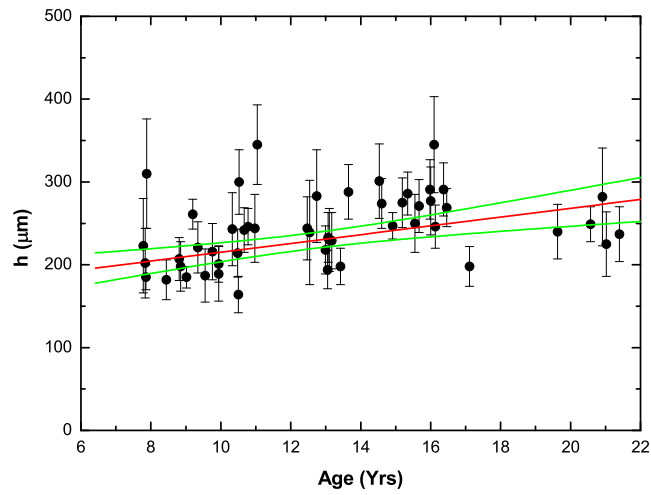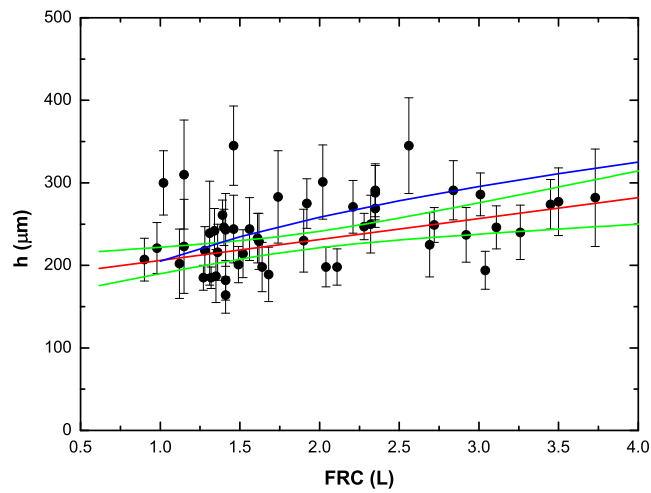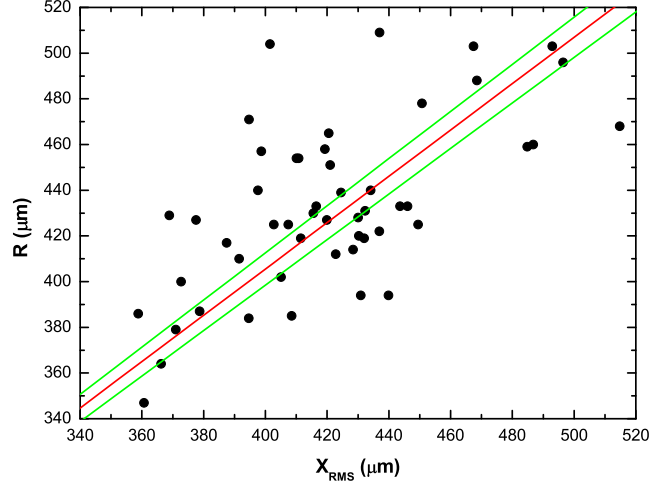
Figure 6.9: R vs X_{rms}. The line of best fit (red line) and 95% confidence intervals (green lines) are shown. For the purposes of clarity, the error bars are not displayed.

6.1.4   SPAMM Tagging Sequence Results

The long time scale apparent diffusion coefficient (D_{sec}) for both the left and right lungs was measured in 75 subjects. The within subject coefficient of variation for both these measurements is 5.4%.

The mean (SD) D_{sec} was 0.006 (0.0012) cm^2s^{-1} and 0.0063 (0.0012) cm^2s^{-1} for the left and right lung respectively. Both lungs showed statistically significant increases with age (left lung, $R^2 = 0.11$, p = 0.0019, Fig 6.10)(right lung, $R^2 = 0.12$, p = 0.0017, Fig 6.11) and FRC (left lung, $R^2 = 0.04$, p = 0.05, Fig 6.12)(right lung, $R^2 = 0.11$, p = 0.003, Fig 6.13).

The measured values of D_{sec} in each lung were found to closely correlate with each other (slope = 0.63, $R^2 = 0.43$, p < 0.0001, Fig 6.14).

Figure 6.10: Left lung D_{sec} vs Age. The line of best fit (red line) and 95% confidence intervals (green lines) are shown.

Figure 6.11: Right lung D_{sec} vs Age. The line of best fit (red line) and 95% confidence intervals (green lines) are shown.
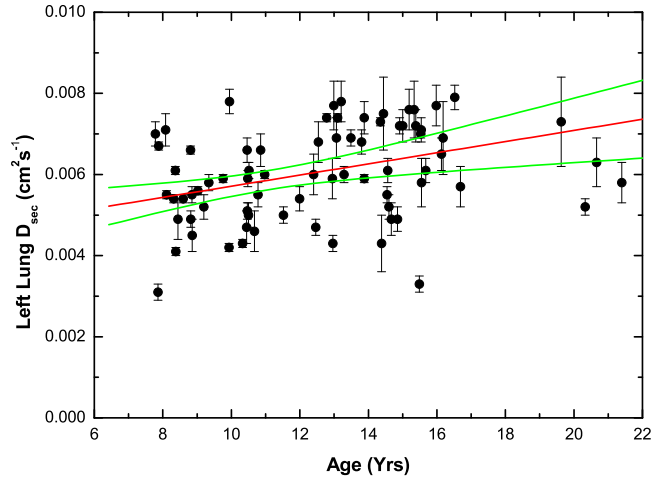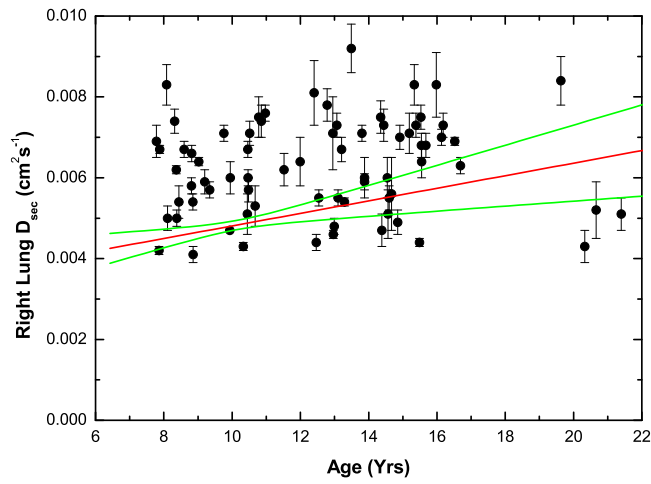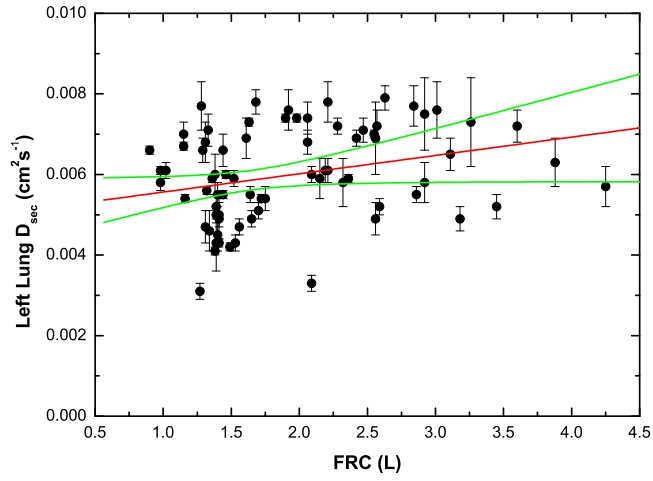
Figure 6.12: Left lung D_{sec} vs FRC. The line of best fit (red line) and 95% confidence intervals (green lines) are shown.
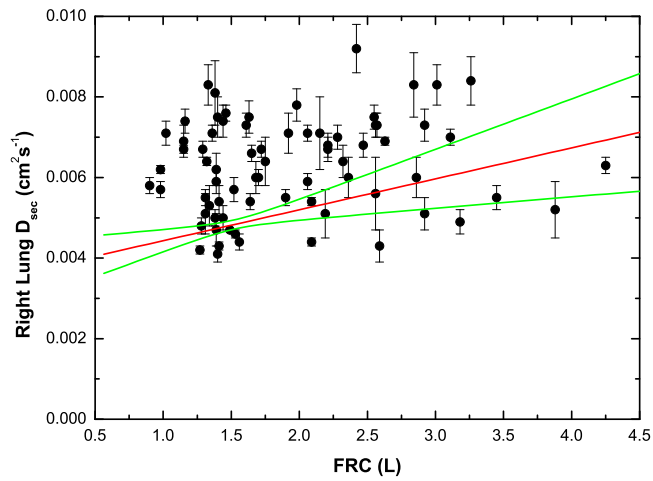

Figure 6.13: Right lung D_{sec} vs FRC. The line of best fit (red line) and 95% confidence intervals (green lines) are shown.
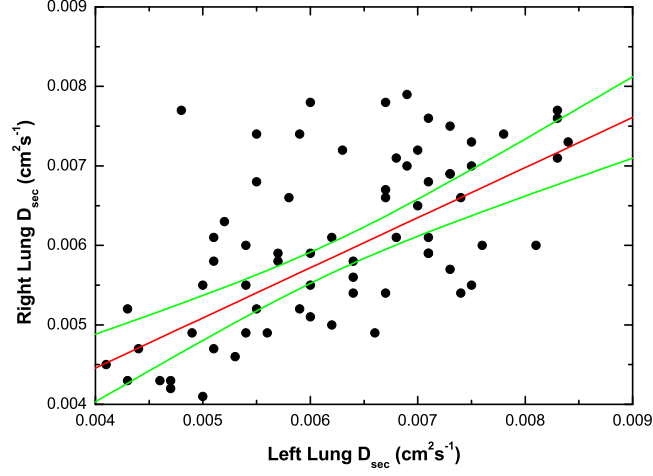
Figure 6.14: Right lung D_{sec} vs Left lung D_{sec}. The line of best fit (red line) and 95% confidence intervals (green lines) are shown. For the purposes of clarity, the error bars are not displayed.

6.2 Leicester Study Discussion

The results presented imply that the dimensions of the alveolar and acinar airspaces determined by three independent experimental methods increase with age and lung size during childhood and adolescence at a rate much less than expected if lung growth occurred only by expansion of pre-existing alveoli. One possible explanation for these observations is that neoalveolisation continues to occur throughout lung growth.

It is currently believed that pulmonary alveoli cease multiplying by 2-3 years of age in humans [103, 104]. This hypothesis is based on analysis of whole lung autopsies using older morphometric histological techniques. Available data on alveolisation [105, 106] shows a large disparity between studies and consequently a wide range of estimates of alveolar number. New

methods of measuring alveolar size and number have since been developed [107, 108], but not yet used to study alveolisation in humans, largely because ethical constraints preclude the acquisition of suitable post mortem tissue.

Recent studies using new morphometric techniques support continued alveolisation to adulthood in rabbits [109] and in rhesus monkeys [110]. Post pneumonectomy alveolisation is reported in mature dogs [111] and nutrition related alveolar loss and gain reported in adult mice [112]. Schittny *et al* [113] observed an increase in alveolar number after completion of microvascular maturation in rats using design based stereology. Using X-ray tomography, they showed local duplication of single capillary layers in areas of postmaturity alveolar septal growth, indicating a potential mechanism for post mature alveolisation. This dispelled the notion that the double capillary layer in alveolar walls is essential for new septation. There is indirect evidence that this occurs in humans as well. Brown *et al* [114] used electrical impedance tomography to determine an average alveolar number of 90 million at 2-3 years of age compared to 300 million in adults, implying that alveolisation continues to take place after 3 years of age.

Our study population had a large number of subjects from a wide age range spanning most of the period of growth in lung volume. This allowed us to test the hypothesis that human alveolisation stops by 3 years of age. Because resting lung volume increases four-fold between 7 and 21 years [115], the volume of individual alveoli should increase by the same extent over this period of growth if no more alveoli form. Other strengths of the study were: availability of prospectively collected data on exposures to risk factors and pre-existing lung disease (which enabled selection of healthy volunteers); repeated MRI measurements at varying inflation volumes in several subjects (see section 5.6) which enabled the hypothesis of no new alveolisation to

be statistically tested; independent measurement of lung size by plethys-
mography; and use of three different MR techniques to elucidate the lung
microstructure. One potential limitation of this study, in common with all
previous morphometric studies of alveolisation, is that the cross sectional
data acquired for each of the experimental methods was treated as if it had
been longitudinally measured.

The reliability of each of the techniques is critical to the proposed in-
terpretation of the results. The measurements were highly repeatable with
low coefficients of variation within subjects. Some scatter in the results is ex-
pected due to certain subjects being in different stages of puberty. The effect
of puberty results in enlargement of the alveoli through traction exercised by
the rib cage caused by the thorax growing faster than the lungs.

D_{msec} Measurements

The increase with age and lung size was significantly less than the predicted
scenario of no neoalveolisation, the possibility that these results could be
explained by changes in geometry of the lung acinus with growth was con-
sidered. However, the data obtained from the Global Pulsed Field Gradient
sequence, which is analysed using the Yablonskiy model and by q-Space anal-
ysis show that both acinar radius and alveolar sleeve depth along with mean
peripheral airspace dimension once again increase less than expected with age
and lung size. It is therefore unlikely that important changes in geometry
occur with growth.

In the only other report of D_{msec} in childhood, Altes *et al* [116] stud-
ied 29 healthy subjects aged 4 to 30 years old and showed that D_{msec} in-
creased with age. However, they did not measure lung size by independent
means and there was no attempt to determine an expected line for increase

of D_{msec} with age or lung size. Two subjects who were aged 27 and 30 (where physical growth must have ceased) had high values of ADC. Therefore their measured association between D_{msec} and age is probably spuriously stronger than would have been if only young growing subjects were included. The small population size was also another drawback of the study.

Yablonskiy Model Measurements

The quantification of the number of alveoli (accounting for height, as noted by [106]) from the Yablonskiy model would have been particularly useful to support the proposed hypothesis. However, the Yablonskiy geometrical model is semi-empirical, i.e. although it is based on an analytical expression for anisotropic diffusion in coaxial cylinders, linking the decay of the diffusion weighted MR signal to geometric parameters that describe the lung microstructure is only possible via Monte Carlo simulations. The values of certain coefficients and exponents in the resultant model are dependent on the experimental parameters, particularly those that determine the form of the bipolar gradient pulses. The diffusion time, Δ, must be selected appropriately - values of Δ that are too large will cause measurements to be increasingly distorted as a result of helium diffusing into adjoining airways [117]. In this study $\Delta = 5.2$ ms, which is more than three times larger than the diffusion time reported by Yablonskiy and colleagues [71].

Fitting our experimental data to this model results in values of the acinar radius and alveolar sleeve depth that are systematically larger than those reported [74], and can only be considered to be apparent values of the geometric parameters. The calculated parameters such as L_m, S/V, and N_a would therefore be distorted as a result of this. Extending the Yablonskiy model to account for longer diffusion times may be possible but is far from

trivial.

Nevertheless, comparing our measured R values to our q-space results we find excellent agreement between the two measurements. The strong correlation between the two techniques, one of which is model dependent and the other which is model independent adds weight to the Yablonskiy model being an accurate model of lung geometry.

Acknowledging that the acinar units are not completely closed and thus there being a fundamental problem with the lung being interpreted as a completely restricted geometry, it is reasonable to assume that the majority of the bolus that is inhaled resides in the acini, and for a short diffusion time, only a small amount of gas will be able to migrate into a neighbouring acinus. The measurements made using the RARE sequence and the Global Pulsed Field Gradient sequence can therefore still be interpreted as being representative of the ^{3}He gas confined in the acini even for a partially open geometry.

D_{sec} **Measurements**

The long diffusion length scale that is probed using the SPAMM tagging sequence (of the order $\lambda/2$) is much greater than the characteristic dimensions of the alveoli. In traversing this length, many alveoli within an acinus and perhaps even multiple acini will be visited. The associated D_{sec} values are therefore expected to reflect the connectivity and microstructural sizes of the lung airspaces.

The experimental values of D_{sec} obtained in this study are typically one order of magnitude smaller than D_{msec} and in agreement with the findings of other studies [99, 118]. There is evidence suggesting that D_{sec} could be more a sensitive metric than D_{msec} because of the order of magnitude difference

from the free diffusion coefficient thus leaving a greater range of values for grading stages of disease [98, 119].

The current understanding of values of D_{sec} being much smaller than those of D_{msec} is that the atoms of gas must negotiate the tortuous network of airways, having to find the node on the airway tree that connects to the required destination. However, computer simulations of long range diffusion which only take into account the canonical branching pathways yield D_{sec} values some 20 times smaller than those reported experimentally [120]. Two determinants of D_{sec} in healthy lungs have thus been proposed: collateral ventilation paths [120] and intra-acinar branching [118].

Collateral paths constitute additional routes that are available for gas motion that are not described by the canonical branching airway tree [121, 122]. These routes serve as more direct paths which avoid the tortuosity of the main airways. Reported collateral paths include interalveolar pores of Kohn [122] in the alveolar walls, bronchoalveolar channels of Lambert [123], and interbronchiolar channels of Martin [124]. The role of collateral paths in ventillating the healthy lung is believed to be unimportant and so invoking this mechanism to account for the discrepancy between theory and experiment seems contradictory.

The majority of the present knowledge on collateral paths has come from measurements of airflow resistance using the wedged catheter technique [125, 126]. These results show that resistance to collateral airflow is much greater than the resistance along the main airways. Bartel *et al* [120] counter these results by highlighting two important points concerned with the importance of collateral ventilation paths in a healthy lung. The first is that the collateral airflow resistances measured have been made at larger proximal airways and so are not representative of collateral paths at the diffusion length being

studied. The second point is that collateral flow and diffusion exhibit different scaling relationships when calculating their respective conductances. For a tube of radius r, flow conductance is proportional to r^4 whereas diffusive conductance scales as r^2. These scaling relations therefore demonstrate that a number of small radius holes through an airway wall offer a high resistance to flow but serve as an important path for diffusion.

Verbanck *et al* [118] performed computer simulations of long range diffusion within a single acinus modeled using three different internal branching patterns. The D_{sec} was found by observing how long it took for concentration differences in the acinus to equilibrate which in turn assesses how internal acinar structure influences the value. They reported values in agreement with experimental results (0.0085 cm^{2}s^{-1}) but at odds with the value deduced by Bartel *et al* (0.001 cm^{2}s^{-1}).

The differences in the values of D_{sec} deduced from each of the simulations can in part be reconciled in how the lungs were modelled in each of the studies. Bartel *et al* used a symmetric branching model where the airways are regarded as line segments, with subsequent branching generations between 5 and 14 being mimicked through 3D spatial orientation. In this model, any internal branching structure peripheral to generation 14 is suppressed, and each acinus (which cover generations 15-23) is treated as a single point object occupying a typical acinar volume. They then state that since the linear dimension of an acinus (about 6mm) is smaller than $\lambda = 2$ cm, intra-acinar branching alone cannot account for their simulated D_{sec} value. Verbanck *et al* acknowledge that their model simulations did not consider collateral ventilation or how connectivity between acini affects D_{sec}. Better knowledge of the number and distribution of collateral paths and on inter-acinar geometry is required to describe these effects in a quantitative way.

The results presented for D_{sec} display the same trends as those from the other quantities measured. Whilst there is a minor but statistically significant increase in D_{sec} with age and lung size, there is substantial variation of diffusivity between subjects. The values of D_{sec} within subjects appears consistent for both left and right lungs. It must be considered that some of the variation between subjects arises from artificially high measured values of D_{sec}. The attenuation of the tags should be a result of diffusive motion alone, however, any constant velocity motion will introduce potential sources of error into the measurements. This is because for the long time scale of this experiment, constant velocity motion results in a displacement which is linearly proportional to time and can become more important relative to diffusive motion which yields a root-mean-square displacement. The obvious sources of velocity motion are therefore lack of a complete breathold and cardiogenic mixing. Distinguishing between attenuation caused by diffusion and that caused by bulk motion of gas remains a challenge for all but the most obvious of individual cases.

The effects of concentration and lung inflation were not accounted for in these results. An initial rapid decay of signal is observed within all subjects in the first second of the experiment and is attributed to the much faster diffusion through the large airways. Once the bolus reaches the branching structure of the small airways diffusive equilibration is slowed down thus the measurement interval that D_{sec} is recorded becomes intrinsic to the structure being probed. Nevertheless, differences in the initial concentration between subjects will result in different rates of diffusive equilibration even within the branching structures that could bias the measurements. Larger concentration gradients between subjects could also result in increased collateral ventilation which would serve to artificially increase D_{sec}.

It is reasonable to assume that increased lung inflation results in a larger D_{sec} just as it does for D_{msec}. A possible explanation for this is that the collateral paths would become enlarged and thus facilitate diffusion through them just as what happens in disease [98,99]. In the context of the hypothesis of no neoalveolisation, the interalveolar pores of Kohn in the alveolar walls would become increasingly enlarged resulting in higher values of D_{sec} compared to the scenario of neoalveolisation. Further work needs to be conducted to see exactly how concentration and lung inflation influence the measured diffusivity.

Summary

There are important implications to the hypothesis that alveolisation is not confined to early life. Children who die following extremely preterm birth have been shown to have larger, simpler, and fewer alveoli [127], based on histological studies. There have been no studies of alveolisation in chronic lung disease survivors and it is possible that they show catch up of alveolisation. There may be recovery from diseases that result in diminished alveolar number at birth (such as pulmonary hypoplasia) or surgical lung resection. Adverse environmental exposures can affect alveolar structure. Systemic corticosteroids in early postnatal life can inhibit alveolisation [128, 129]. If alveolisation does extend beyond early life, it is possible that corticosteroids may be deleterious throughout childhood. Passive tobacco smoke exposure in childhood is linked to adult COPD [130], and the mechanism for this could be via an effect on alveolisation. Finally, the advent of potential alveolar therapy to restore damaged alveolar structure requires safe, non-invasive repeatable measurements to study the outcome of future therapeutic trials. Functional MRI of the lung using hyperpolarised ³He provides such a method.

This entire discussion has been themed around explaining the invariance in all the results through the process of neoalveolisation. However, another explanation can be implied from the invariances in the morphological parameters derived from the Yablonskiy model and q-space analysis. If these parameters truly are invariant over the four-fold increase in lung volume observed in this study, most if not all of the volume increase must be achieved by adding new units of constant size (the so called alveolar recruitment), otherwise one would have to allow for alveolar expansion which should increase these parameters but is refuted by the results. Determining whether the invariances in the results are due to neoalveolisation or in fact simple alveolar recruitment proves next to impossible.

6.3 Asthmatic Study Results

6.3.1 Spirometry Results

Spirometry was performed on all 10 severely asthmatic subjects and 8 healthy aged matched controls. Table 6.2 displays the values of the spirometric indices used to assess disease severity for all the subjects in the study.

A statistically significant correlation was found between the ratio of RV/TLC and LCI ($R^2 = 0.52$, p = 0.001, Fig 6.15), the ratio of FEV1/FVC ($R^2 = 0.36$, p = 0.009, Fig 6.16), and percentage of predicted FEV1 ($R^2 = 0.41$, p = 0.004, Fig 6.17). Statistically significant correlations were also found between LCI and percentage of predicted FEV1 ($R^2 = 0.42$, p = 0.005, Fig 6.18) as well as the ratio of FEV1/FVC ($R^2 = 0.25$, p = 0.043, Fig 6.19).

Subject	LCI	RV/TLC	FEV1/FVC	FEV1
A01	9.02	51.8	42.25	40.71
A02	10.02	53.2	76.96	112.84
A03	-	42.2	63.43	89.05
A04	6.02	42	82.89	104.69
A05	8.77	48.9	64.74	66.78
A06	7.88	34.3	80.79	71.31
A07	10.51	50	62.76	58.93
A08	6.79	38.8	75.27	94.1
A09	6.25	36.5	61.75	74.35
A10	9.61	50.2	59.62	66.35
C01	6.03	20.1	65.67	112.35
C02	6.28	31.7	83.46	93.54
C03	6.37	24.7	86.81	102.36
C04	5.93	15.1	78.8	106.33
C05	7.99	40	81.12	115.6
C06	8.97	32.68	74.68	62
C07	7.24	34.53	80.92	125
C08	6.2	27.15	91.54	114.68

Table 6.2: Spirometric indices for all subjects in the study.
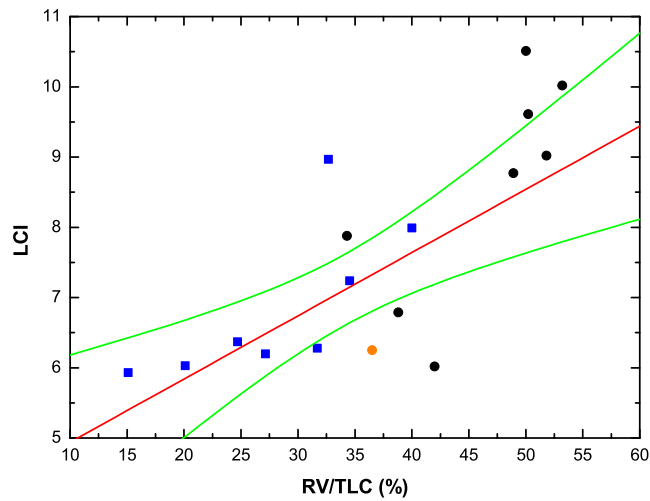

Figure 6.15: RV/TLC vs LCI. The line of best fit (red line) and 95% confidence intervals (green lines) are shown. Blue squares = controls, black circles = asthmatics, orange circle = outlier.
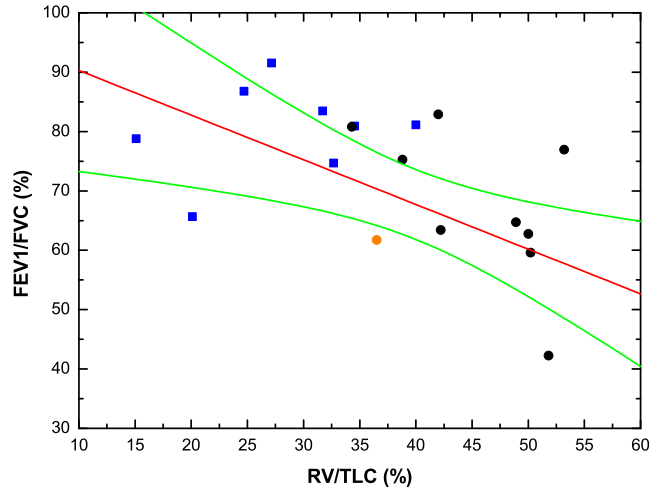
Figure 6.16: RV/TLC vs FEV1/FVC. The line of best fit (red line) and 95% confidence intervals (green lines) are shown. Blue squares = controls, black circles = asthmatics, orange circle = outlier.
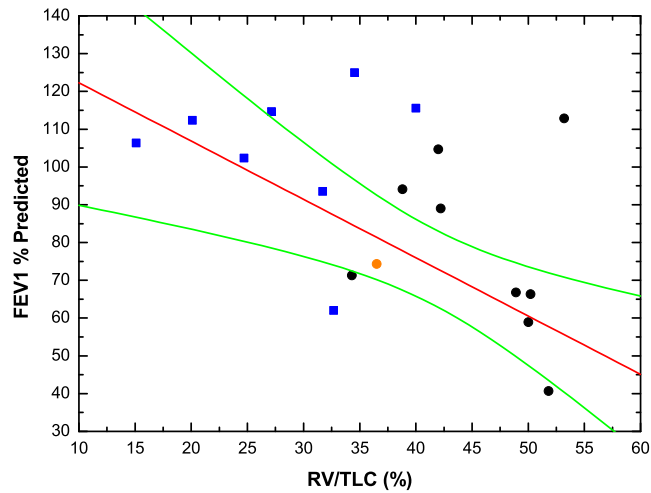

Figure 6.17: RV/TLC vs Percentage of predicted FEV1. The line of best fit (red line) and 95% confidence intervals (green lines) are shown. Blue squares = controls, black circles = asthmatics, orange circle = outlier.
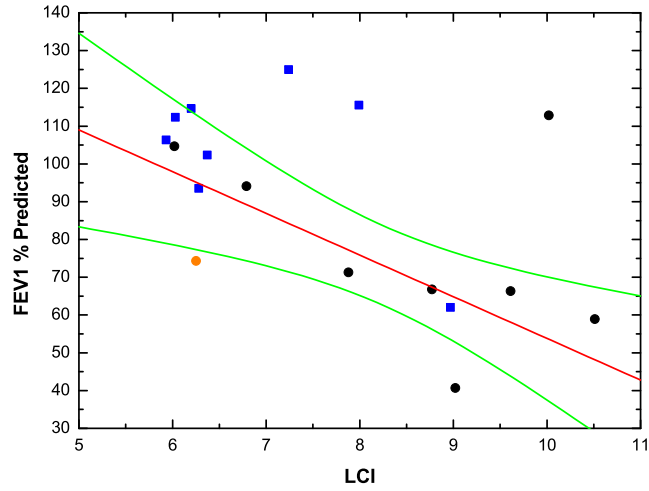
Figure 6.18: LCI vs Percentage of predicted FEV1. The line of best fit (red line) and 95% confidence intervals (green lines) are shown. Blue squares = controls, black circles = asthmatics, orange circle = outlier.
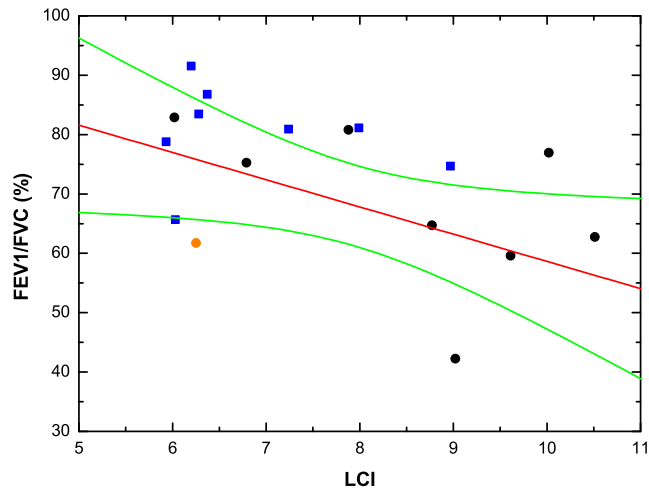

Figure 6.19: LCI vs FEV1/FVC. The line of best fit (red line) and 95% confidence intervals (green lines) are shown. Blue squares = controls, black circles = asthmatics, orange circle = outlier.

6.3.2 RARE Sequence Results

D_{msec} measurements were obtained in 10 severely asthmatic subjects and 5 healthy aged matched controls using an average bolus size of 350 ml. The mean (SD) volume and concentration corrected D_{msec} for the asthmatic subjects was 0.1095 (0.017) cm^2s^{-1} compared to 0.0940 (0.012) cm^2s^{-1} for the controls - a statistically insignificant increase (p = 0.086).

For all subjects, no statistically significant correlation was found between D_{msec} and the percentage of predicted FEV1 ($R^2 = 0.14$, p = 0.175, Fig 6.20), however, a statistically significant correlation was found with the ratio of FEV1 to FVC ($R^2 = 0.29$, p = 0.039, Fig 6.21), the LCI ($R^2 = 0.39$, p = 0.017, Fig 6.22), and the ratio of RV/TLC ($R^2 = 0.49$, p = 0.004, Fig 6.23).
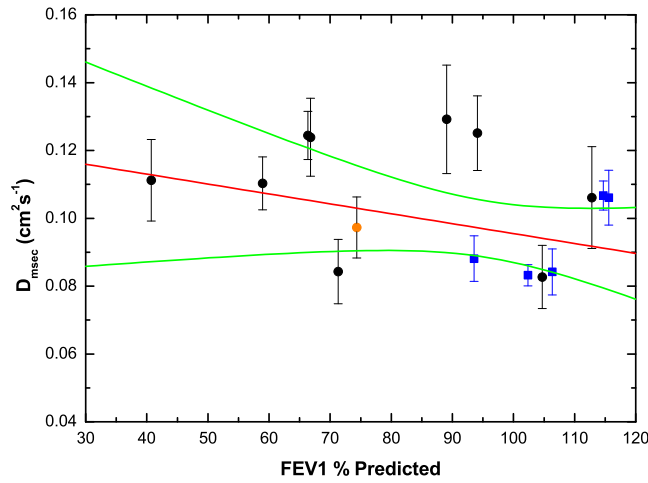

Figure 6.20: D_{msec} vs Percentage of predicted FEV1. The line of best fit (red line) and 95% confidence intervals (green lines) are shown. Blue squares = controls, black circles = asthmatics, orange circle = outlier.

Figure 6.21: D_{msec} vs FEV1/FVC. The line of best fit (red line) and 95% confidence intervals (green lines) are shown. Blue squares = controls, black circles = asthmatics, orange circle = outlier.

Figure 6.22: D_{msec} vs LCI. The line of best fit (red line) and 95% confidence intervals (green lines) are shown. Blue squares = controls, black circles = asthmatics, orange circle = outlier.
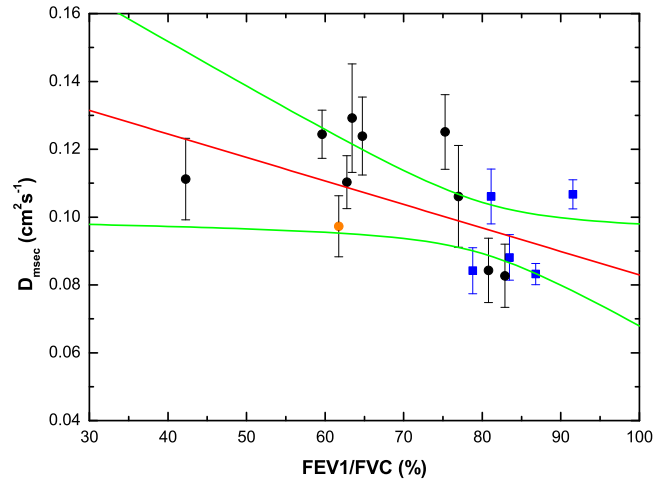
Figure 6.23: D_{msec} vs RV/TLC. The line of best fit (red line) and 95% confidence intervals (green lines) are shown. Blue squares = controls, black circles = asthmati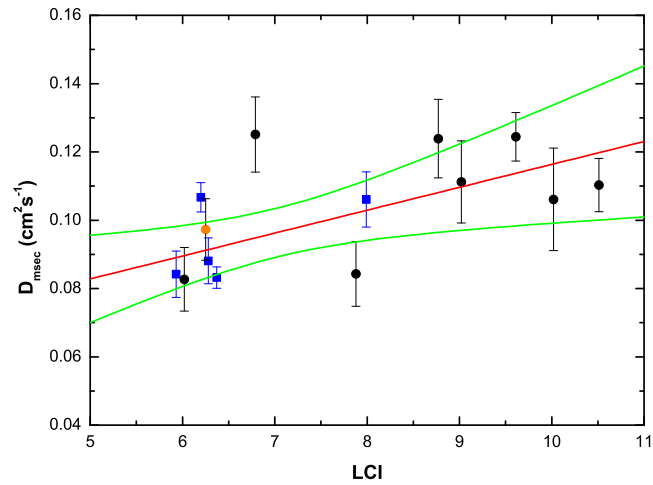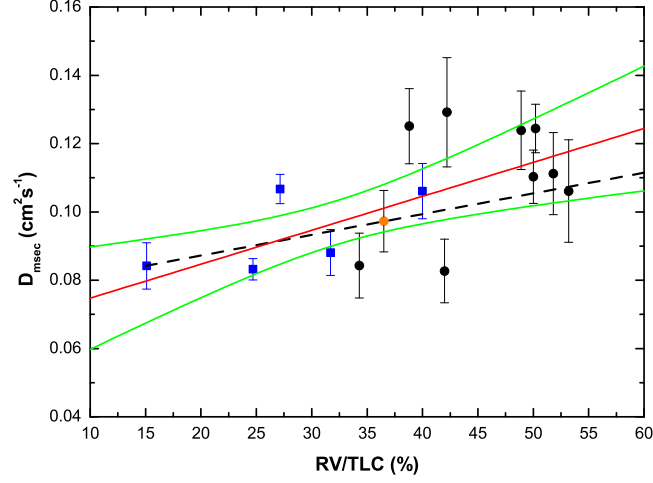cs, orange circle = outlier. The dashed line represents the predicted change of D_{msec} with increasing lung inflation.

The ADC histograms in control subjects demonstrated lower mean values and narrower distribution widths compared with those of the asthmatic subjects (Fig 6.24 and Fig 6.25). The distribution widths for the entire lung profile histograms and left lung histograms were significantly larger in asthmatics (p = 0.01 and p = 0.0001). However, for the right lung histograms no significant increase in distribution width was found (p = 0.5).
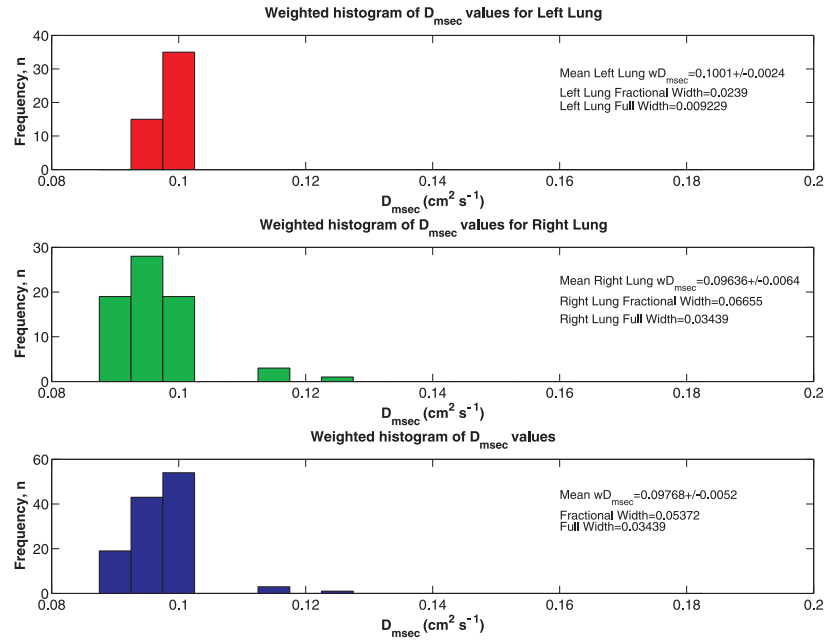
Figure 6.24: Control subject D_{msec} histogram.
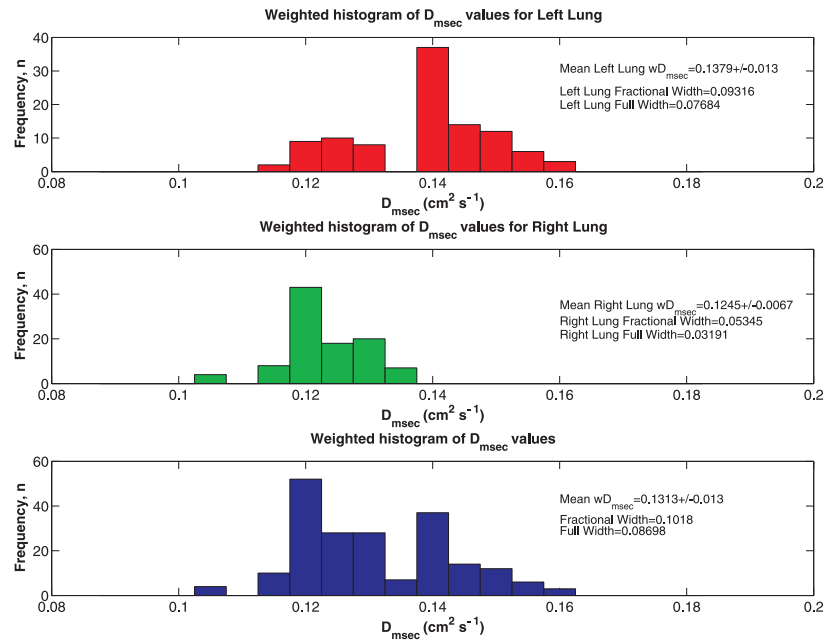
Figure 6.25: Asthmatic subject D_{msec} histogram.

6.3.3 Global Pulsed Field Gradient Sequence Results

The acinar radius (R) and alveolar sleeve depth (h) were measured in the same 10 asthmatic subjects and 7 healthy aged matched controls. The mean (SD) volume and concentration corrected R and h for the asthmatic subjects was significantly larger (p = 0.004 and p = 0.007 respectively) than those for the control subjects - 441 (36) μm compared to 383 (33) μm and 236 (40) μm compared to 183 (23) μm for R and h respectively.

For the asthmatic subjects a statistically significant correlation was found between R and the ratio of RV/TLC (R^2 = 0.6, p = 0.014, Fig 6.26), and LCI (R^2 = 0.87, p = 0.0007, Fig 6.27). However, no statistically significant correlation was found between R and the percentage of predicted FEV1 (R^2 = 0.07, p = 0.51, Fig 6.28) or the ratio of FEV1 to FVC (R^2 = 0.4, p = 0.07, Fig 6.29).

Figure 6.26: R vs RV/TLC. The line of best fit (red line) and 95% confidence intervals (green lines) are shown. Blue squares = controls, black circles = asthmatics, orange circle = outlier.

Figure 6.27: R vs LCI. The line of best fit (red line) and 95% confidence intervals (green lines) are shown. Blue squares = controls, black circles = asthmatics, orange circle = outlier.

Figure 6.28: R vs Percentage of predicted FEV1. The line of best fit (red line) and 95% confidence intervals (green lines) are shown. Blue squares = controls, black circles = asthmatics, orange circle = outlier.
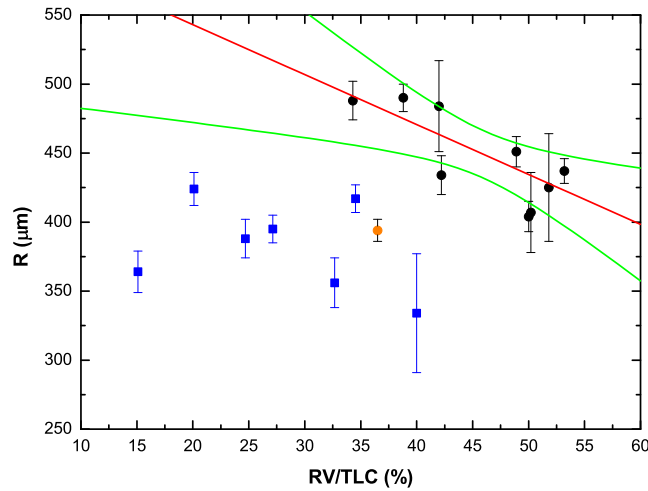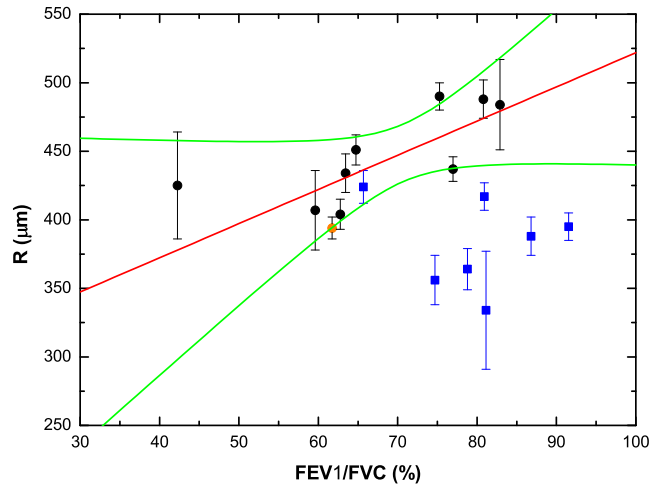
Figure 6.29: R vs FEV1/FVC. The line of best fit (red line) and 95% confidence intervals (green lines) are shown. Blue squares = controls, black circles = asthmatics, orange circle = outlier.

For the asthmatic subjects no statistically significant correlation was found between h and the percentage of predicted FEV1 ($R^2 = 0.02$, p = 0.69, Fig 6.30) or the ratio of FEV1 to FVC ($R^2 = 0.03$, p = 0.64, Fig 6.31). However, a statistically significant correlation was found between the LCI ($R^2 = 0.61$, p = 0.022, Fig 6.32), and the ratio of RV/TLC ($R^2 = 0.67$, p = 0.007, Fig 6.33).
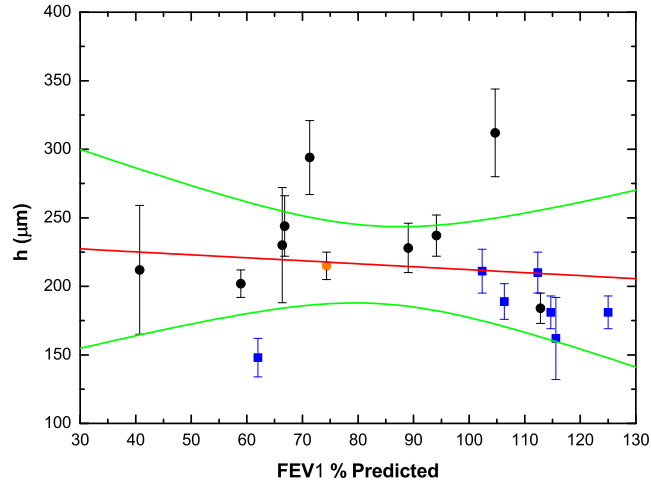
Figure 6.30: h vs Percentage of predicted FEV1. The line of best fit (red line) and 95% confidence intervals (green lines) are shown. Blue squares = controls, black circles = asthmatics, orange circle = outlier.
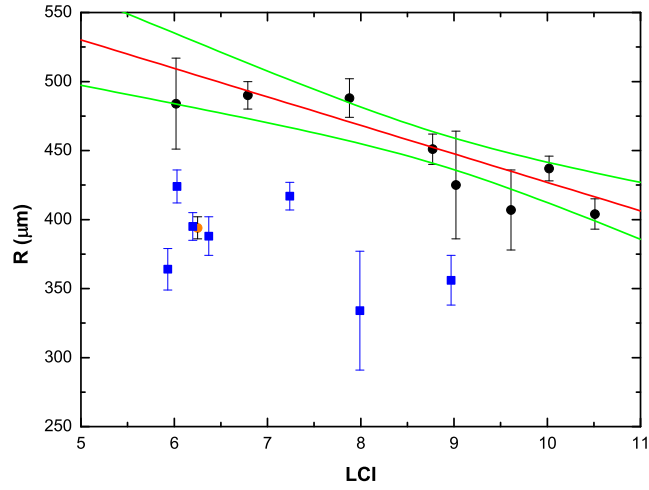

Figure 6.31: h vs FEV1/FVC. The line of best fit (red line) and 95% confidence intervals (green lines) are shown. Blue squares = controls, black circles = asthmatics, orange circle = outlier.
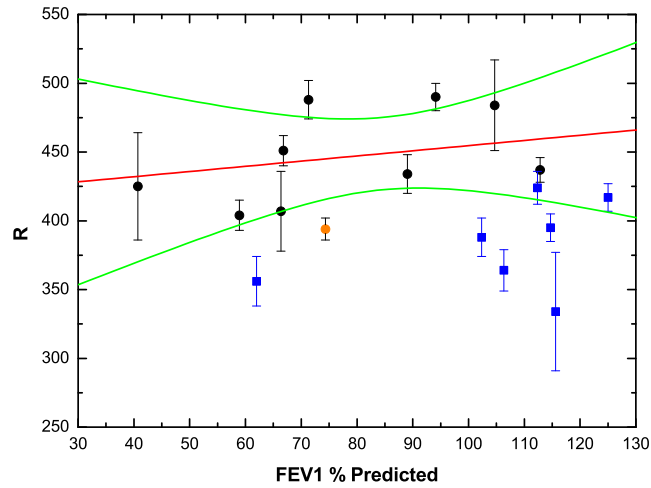
Figure 6.32: *h* vs LCI. The line of best fit (red line) and 95% confidence intervals (green lines) are shown. Blue squares = controls, black circles = asthmatics, orange circle = outlier.

Figure 6.33: *h* vs RV/TLC. The line of best fit (red line) and 95% confidence intervals (green lines) are shown. Blue squares = controls, black circles = asthmatics, orange circle = outlier.
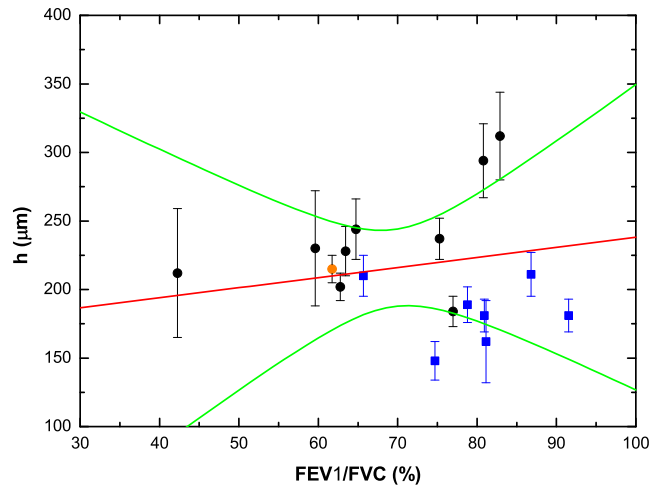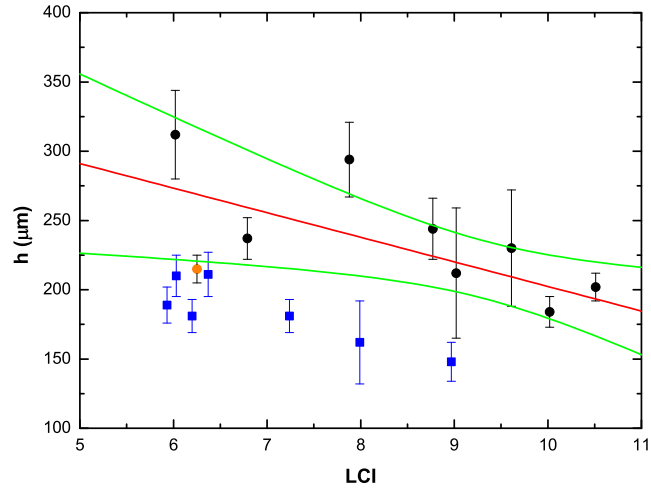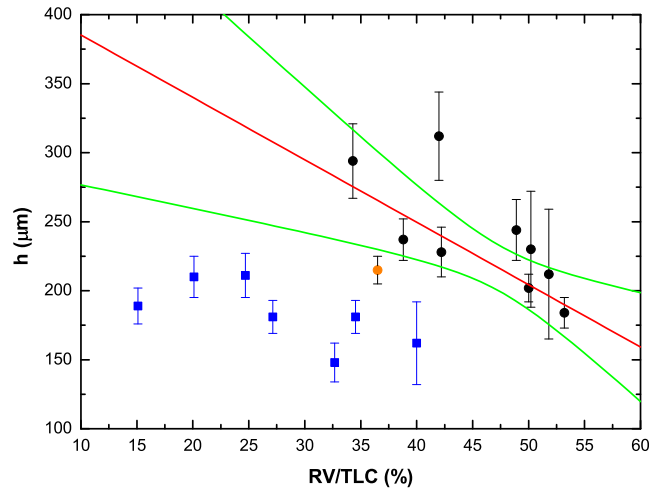
6.4 Asthmatic Study Discussion

The purpose of this study was to determine the relationships between D_{msec}, R, and h and clinical measures of asthma severity as gauged by spirometry.

The significant increase of R and h in asthmatics combined with their strong correlations to asthma severity indices such as LCI and RV/TLC are indicative of structural changes in the peripheral airways. These findings are consistent with experimental evidence [131] and recent theoretical modeling [132, 133] which implicate changes in small airway morphology being primarily responsible for functional defects.

In asthma, chronic recurrent inflammatory processes may lead to structural changes known as airway remodeling. Structural changes reported in asthmatic airways include epithelial denudation, goblet cell hyperplasia, enlargement of submucosal mucus glands, angiogenesis, increased thickness of the subepithelial layer (subepithelial fibrosis), increased airway smooth muscle (ASM) mass, wall thickening, and elastin abnormalities.

The impact on lung function caused by airway remodeling is believed to be greater in severe asthmatics or older asthmatics with longer duration of disease. This is a result of some structural changes being prominent only with increased severity or from longer duration [134].

Increased thickness of the subepithelial layer is not clearly related to the duration of disease but is related to the severity [135]. The thickness of this fibrotic layer has been found to correlate with wall thickness [136, 137] and is also believed to be a contributing factor to increases in ASM mass. Wall thickening increases both with severity [138, 139] and duration of disease [134]. In the latter report, the adventitia was found to be the primary site of wall thickening in the small airways with a three-fold increase

over controls while the inner wall showed only a minor increase. In studies where delineation between increased ASM mass and subepithelial fibrosis have been made [134], a four-fold increase in smooth muscle mass in small airways compared with age matched controls was found.

Airflow obstruction and airway hyperresponsiveness (AHR) are the functional consequences of airway remodeling which causes excessive airway narrowing. While airflow obstruction can be explained intuitively by constriction of airways through remodeling, the relationship between AHR and remodeling is not so simple. Earlier studies examining the consequences of structural changes on AHR came to the conclusion that increased ASM mass in the small airways could explain most of the changes in asthma [140]. Recent studies using computer modeling [141, 142] emphasize that alteration of smooth muscle dynamics (specifically the muscle contractility) may be a more likely mechanism for AHR. A combination of processes such as loss of mechanical plasticity, wall thickening, subepithelial fibrosis, and decreased elastic recoil serve to shorten the length of the smooth muscle thus increasing luminal constriction. The aforementioned studies hypothesised that the heterogeneous pattern of peripheral airway constriction rather than the mean level of constriction may be a more crucial determinant of increased AHR.

Mauad *et al* [143] reported remodeling involving loss of alveolar attachments is severe asthma. They found that reduction of tethering between the elastic alveolar attachments and the smooth muscle have significant effects on AHR and deep breath response.

Interpretation of the obtained experimental results in relation to degradation in lung function as a consequence of airway remodeling proves to be a challenge. While our results are indicative of remodeling in the small airways the mechanisms responsible for them or what structural change is occuring

cannot be elucidated. Nevertheless, the impaired lung function of the severe asthmatics in this study is evident in the results.

In this study, it was found that the R and h parameters showed strong correlation with the severity of the disease as determined by the spirometric indices LCI and the percentage of RV/TLC. It can be assumed that the decrease of R and h with increasing asthma severity reflects an increase in the number of constricted peripheral airways. Indeed, the decrease of alveolar sleeve depth, h, implies the alveoli become increasingly constricted leading to compromised gas exchange because the alveoli is operating as if it was functionally closed.

No significant correlation was found between percentage of predicted FEV1 and R and h. There was also no correlation of R and h with FEV1/FVC. In emphysema, these spirometric indices provide a sensitive measure of disease severity. In asthma, the absence of significant correlations with these indices may reflect their inadequacy to assess impaired peripheral airway function from remodeling changes occuring independently of the large airways.

This idea is further substantiated when comparing different spirometry indices to one another. Table 6.2 shows a comparisson of the different indices for the ten asthmatic subjects (A01 - A10) and the seven healthy controls (C01 - C07). The table and figures 6.15 - 6.19 highlight two asthmatic subjects, A02 and A09, who whilst having symptoms consistent with the disease exhibit associated lung function impairment from different mechanisms. The results of subject A02 are representative of the previously defined AHR. This subject has LCI and RV/TLC values indicitive of severe constriction of the small airways yet displays no evidence of airway obstruction in regard to their FEV1 and FEV1/FVC values. Subject A09 on the other hand

has percentage of predicted FEV1 and FEV1/FVC values indicating airway obstruction but low LCI and RV/TLC values. The results from this subject suggest airflow obstruction is predominantly occuring in the larger airways. The trends from figures 6.26 - 6.33 show that the peripheral airway constriction is interrelated with percentage of predicted FEV1 and FEV1/FVC and can thus be used as predictors of increased AHR. However, assessing the contribution of AHR independent of airflow measures remains difficult using these values as metrics of severity. The findings presented in the study therefore support the use of LCI and RV/TLC values for the evaluation of asthma phenotype. As such, the correlations of R and h with LCI and RV/TLC excluded those values of A09 (represented by an orange circle on the figures).

The statistical insignificance between the D_{msec} measurements of the asthmatic subjects and controls upon correcting for alveolar volume further supports the notion of airway remodeling. Measuring the ADC is limited by the virtue of only being able to obtain information from areas which are sufficiently ventillated with hyperpolarised ^{3}He. Regions that have airflow obstruction have a lower signal intensity which may be insufficient to properly determine the ADC and thereby introduce a bias in the mean. Correcting for alveolar volume and thereby accounting for airtrapping (to the best of our ability) demonstrates that diffusion is the same in ventilated regions of asthmatic lungs as it is for healthy lungs. Because ADCs provide an indirect measurement of the size of the peripheral airways, the invariance between the D_{msec} measurements of the asthmatic subjects and controls indicates that the size of the airways remains mostly unaltered especially in comparisson to emphysema where the airspaces are greatly enlarged through destruction of microstructure. Morphological alteration via airway remodeling processes can therefore be inferred as the cause of the symptomatic asthmatics.

The heterogeneity of ADCs in the asthmatic subjects represented by their broader D_{msec} histograms is further indirect evidence of airway remodeling. These findings are in agreement with recent evidence [141] which suggests that airway remodeling predisposes the lung to a more heterogeneous pattern of small airway constriction which in turn is an important determinant of increased airflow obstruction and AHR.

The significant correlations between D_{msec} and the spirometic indices RV/TLC and FEV1/FVC can be attributed with how D_{msec} is known to increase with increased inflation. A significant correlation was also found with LCI which is not suprising since these indices are interrelated to one another. Although a statistically significant correlation was not found with percentage of predicted FEV1, a clear trend was evident. Assuming that airtrapping has been accounted for and the measurement of ADC is coming purely from ventilated regions of the lung, it is expected that ADC will vary in regard to these indices using the expression in 5.6.3. The predicted line in Figure 6.23 is based on a modification of the expression in 5.6.3 which takes into account that the relative change in volume is now in regard to TLC instead of FRC. The line shows excellent agreement with the ADC values from the controls and for several asthmatics. The discrepancy between the line of best fit and the predicted line is attributed to loss of lung elastic recoil which is associated with increased age as well as longer duration of disease for the asthmatics.

Summary

The asthmatic preliminary study has demonstrated that hyperpolarised ^{3}He MRI can provide information about structural changes evident in asthma by assessing what size airways are closing. This information can then be

correlated with asthma severity and spirometry. The study has shown that
^{3}He MRI is more sensitive than spirometry for detecting changes in the small
airways as evidenced by asthmatic subjects with normal spirometry but ab-
normal R and h values as well as broader ADC histograms. In conjunction
with severity indices such as LCI and RV/TLC, it was demonstrated ^{3}He
MRI could be used to evaluate asthma phenotype which is especially useful
given the problematic nature of diagnosing the disease and the potential for
misclassification. The regional specificity of the MR techniques is also use-
ful for the assessment of treatment therapies targeted at the small airways
as larger airway treatments such as bronchial thermoplasty would not be
effective.

As this was only a preliminary study, the main limitation of the study is
the sample size. Another limitation is that of the Yablonskiy model itself.
The limitations of the Yablonskiy model have already been discussed (see
3.6.2 and 6.2) and caution should be expressed in overly interpreting the re-
sults in regard to true anatomical airway sizes. Lastly, since spirometry was
performed upright and ^{3}He MRI was performed with the subject supine, a
condition expected to reduce lung volume, an adjustment factor is warranted
even though it is doubtful that any correlations would be subsequently al-
tered.

Should the study be continued with a larger number of asthmatic subjects,
future work could focus on how D_{sec} measurements differ (if at all) between
controls and asthmatics to assess the role of collateral ventilation in severe
asthma.

6.5 Cystic Fibrosis Study Results

6.5.1 Spirometry Results

Spirometry was performed on 10 subjects with cystic fibrosis (CF) and 28 healthy aged matched controls (Table 6.3). For the CF subjects a statistically significant correlation was found between LCI and percentage of predicted FVC ($R^2 = 0.81$, p = 0.0004, Fig 6.34). Statistically significant correlations were also found between the ratio of RV/TLC and percentage of predicted FEV1 ($R^2 = 0.77$, p = 0.0008, Fig 6.35) and also percentage of predicted FVC ($R^2 = 0.39$, p = 0.05, Fig 6.36). However, no statistically significant correlation was found between LCI and the ratio of RV/TLC ($R^2 = 0.24$, p = 0.147, Fig 6.37), or percentage of predicted FEV1 ($R^2 = 0.19$, p = 0.21, Fig 6.38).

Measurement	CF value	Control value
Age(Yrs)	8.39(1.61)	9.27(1.04)
FRC(L)	1.33(0.42)	1.31(0.22)
TLC(L)	2.43(0.41)	2.83(0.46)
LCI	11.18(1.45)	6.66(0.81)
FEV1(L)	1.43(0.32)	1.82(0.31)
FVC(L)	1.75(0.44)	2.07(0.39)

Table 6.3: Mean and standard deviation of physiological and lung function measurements for all CF and control subjects in the CF study.

Figure 6.34: LCI vs Percentage of Predicted FVC. The line of best fit (red line) and 95% confidence intervals (green lines) are shown. The orange circle is the CF subject who displays anomalous MR results.
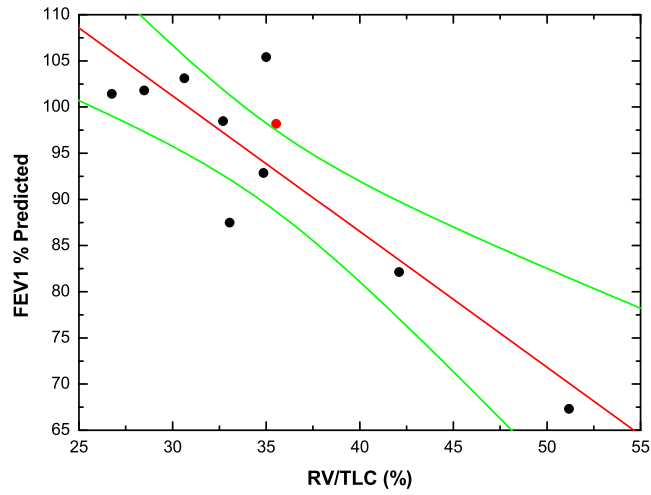
Figure 6.35: Percentage of Predicted FEV1 vs RV/TLC. The line of best fit (red line) and 95% confidence intervals (green lines) are shown. The orange circle is the CF subject who displays anomalous MR results.
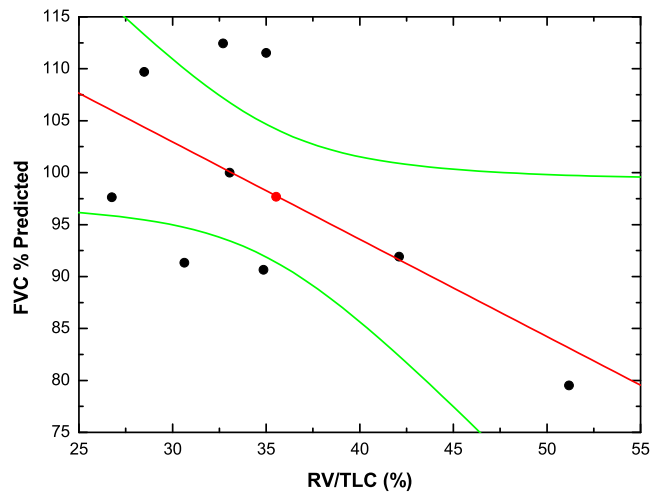
Figure 6.36: Percentage of Predicted FVC vs RV/TLC. The line of best fit (red line) and 95% confidence intervals (green lines) are shown. The orange circle is the CF subject who displays anomalous MR results.

Figure 6.37: LCI vs RV/TLC. The line of best fit (red line) and 95% confidence intervals (green lines) are shown. The orange circle is the CF subject who displays anomalous MR results.
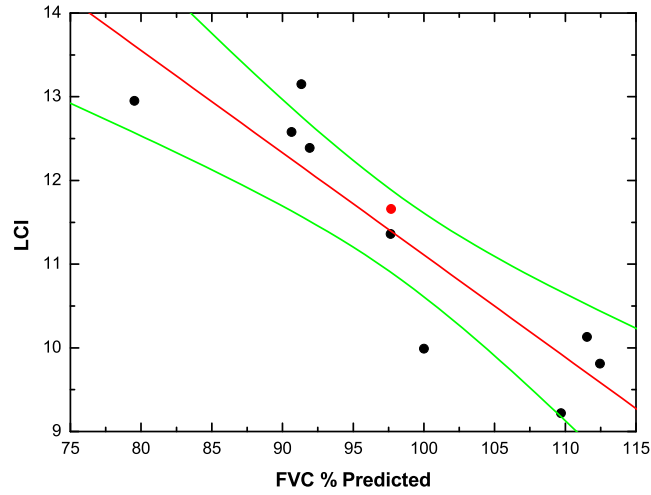

Figure 6.38: LCI vs Percentage of Predicted FEV1. The line of best fit (red line) and 95% confidence intervals (green lines) are shown. The orange circle is the CF subject who displays anomalous MR results.
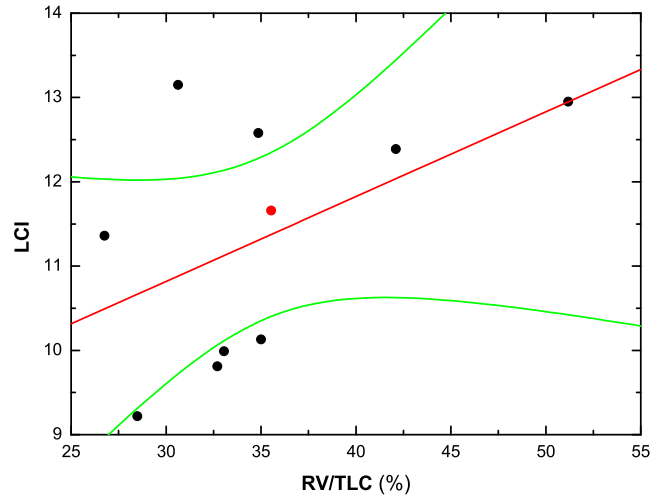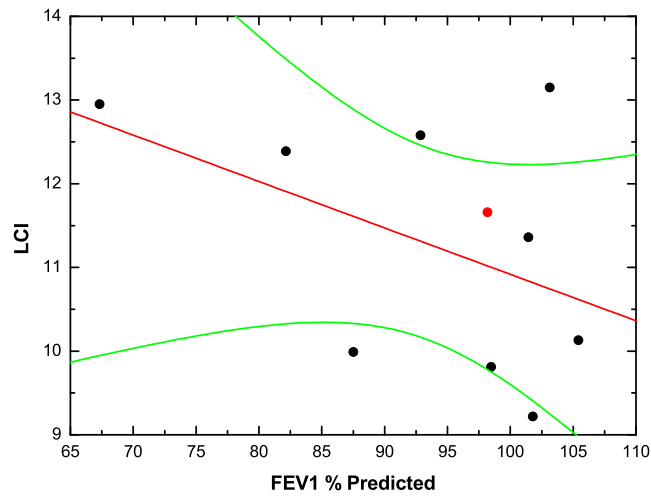
6.5.2 RARE Sequence Results

D_{msec} measurements were obtained for all 10 CF subjects and all 28 aged matched control subjects using an average helium gas bolus size of 350 ml. The mean (SD) volume and concentration corrected D_{msec} for the CF subjects was 0.083 (0.014) cm^2s^{-1} compared to 0.0912 (0.013) cm^2s^{-1} for the controls (Fig 6.39) - a statistically insignificant decrease (p = 0.097).
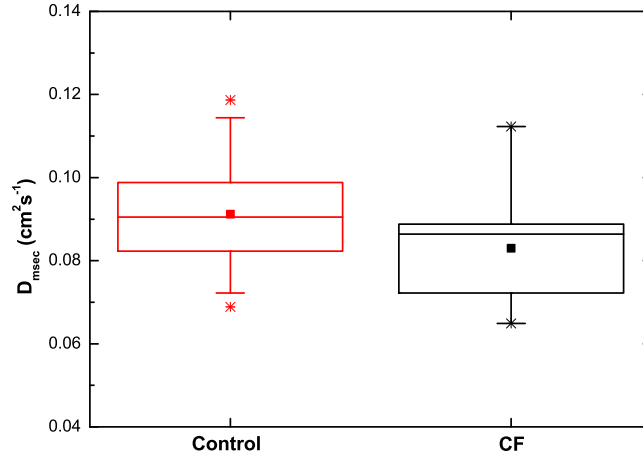
Figure 6.39: Box plot of D_{msec} values for control and CF subjects. The * marks the range of the results, the □ marks the mean, the bottom and top of the box are the lower and upper quartiles respectively, the solid line within the box is the median, and the ends of the bars represent the ±95% confidence interval.

For the CF subjects a statistically significant correlation was found between D_{msec} and LCI (R^2 = 0.46, p = 0.046, Fig 6.40) and percentage of predicted FVC (R^2 = 0.42, p = 0.042, Fig 6.41). However, no statistically significant correlation was found between D_{msec} and the ratio of RV/TLC (R^2 = 0.21, p = 0.18, Fig 6.42) or percentage of predicted FEV1 (R^2 = 0.0003, p = 0.96, Fig 6.43).

Figure 6.40: D_{msec} vs LCI. The line of best fit (red line) and 95% confidence intervals (green lines) are shown. The orange circle is the CF subject who displays anomalous MR results.
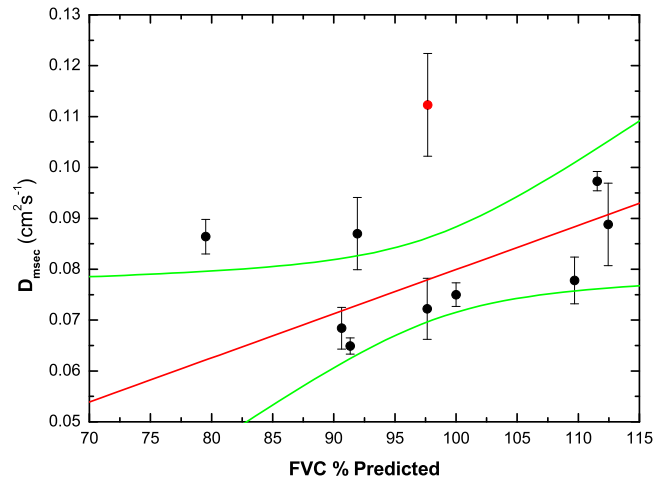
Figure 6.41: D_{msec} vs Percentage of predicted FVC. The line of best fit (red line) and 95% confidence intervals (green lines) are shown. The orange circle is the CF subject who displays anomalous MR results.
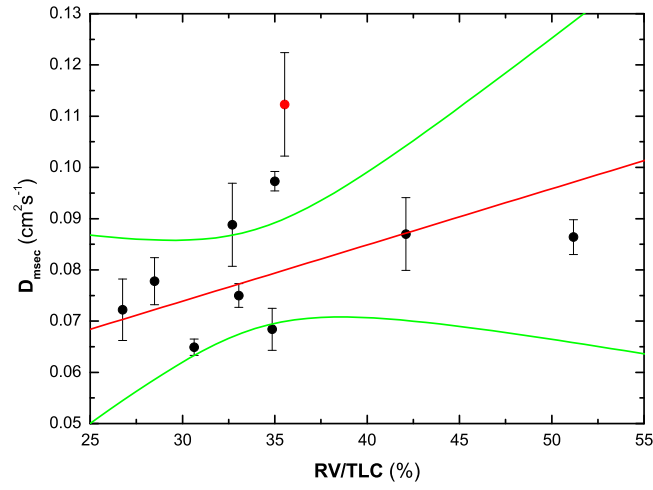
Figure 6.42: D_{msec} vs RV/TLC. The line of best fit (red line) and 95% confidence intervals (green lines) are shown. The orange circle is the CF subject who displays anomalous MR results.
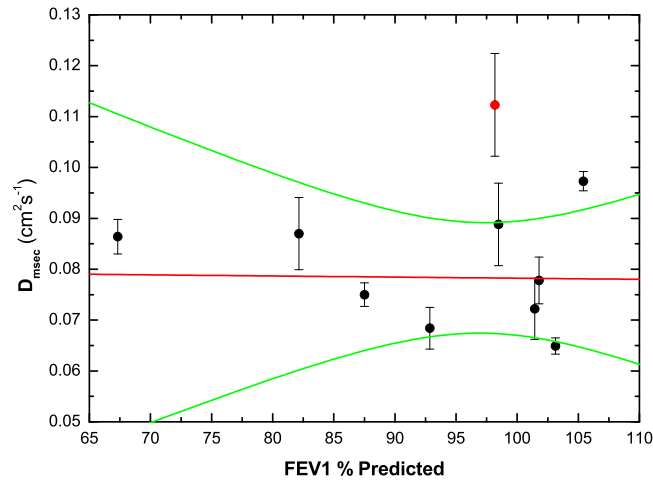
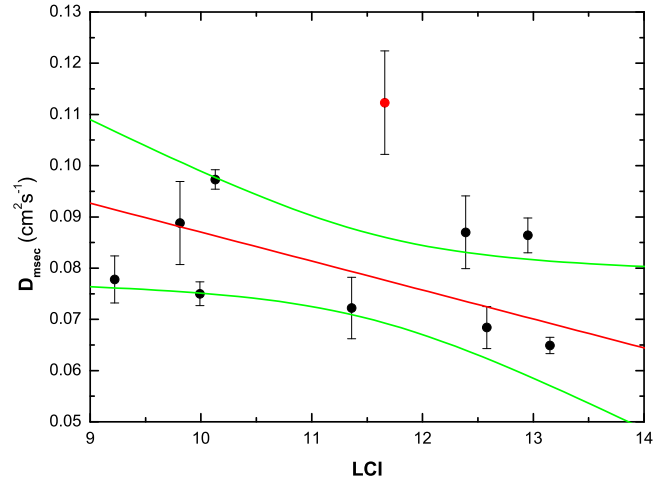Figure 6.43: D_{msec} vs Percentage of predicted FEV1. The line of best fit (red line) and 95% confidence intervals (green lines) are shown. The orange circle is the CF subject who displays anomalous MR results.

The D_{msec} histograms in the CF subjects demonstrated lower mean values compared with those of control subjects, however, no significant differences in distribution width were found between the groups for either the entire lung profile histograms and left lung histograms (p = 0.31 and p = 0.37 respectively). A statistically significant difference in distribution width was observed in the right lung histograms between CF and control subjects (p = 5.22×10^{-9}).

6.5.3 SPAMM Tagging Sequence Results

D_{sec} measurements were obtained for both the left and right lungs in 7 CF subjects and 24 controls using an average helium gas bolus size of 350 ml. The mean (SD) D_{sec} was 0.0067 (0.0039) cm^{2}s^{-1} compared with 0.0056 (0.0011) cm^{2}s^{-1} in the left lung of the CF and control subjects respectively. For the right lung, the mean (SD) D_{sec} was 0.0078 (0.004) cm^{2}s^{-1} for the CF subjects compared to 0.0061 (0.001) cm^{2}s^{-1} for the controls. Neither of these differences in D_{sec} between the groups were found to be statistically significant (p = 0.19 and p = 0.056 respectively). The results are displayed in figures 6.44 - 6.46.
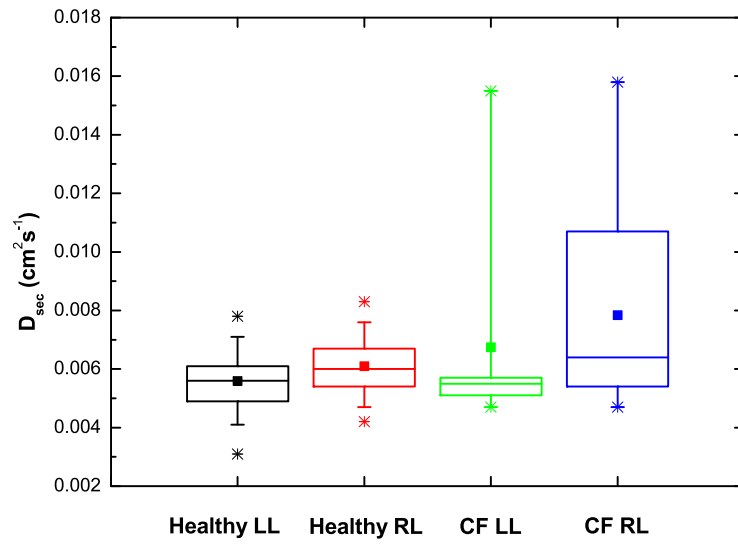
Figure 6.44: Box plot of D_{sec} values for the left and right lung (LL and RL) for healthy and CF subjects. The * marks the range of the results, the □ marks the mean, the bottom and top of the box are the lower and upper quartiles respectively, the solid line within the box is the median, and the ends of the bars represent the $\pm 95\%$ confidence interval. The large data range of the CF results is caused by the subject identified in the previous figures.
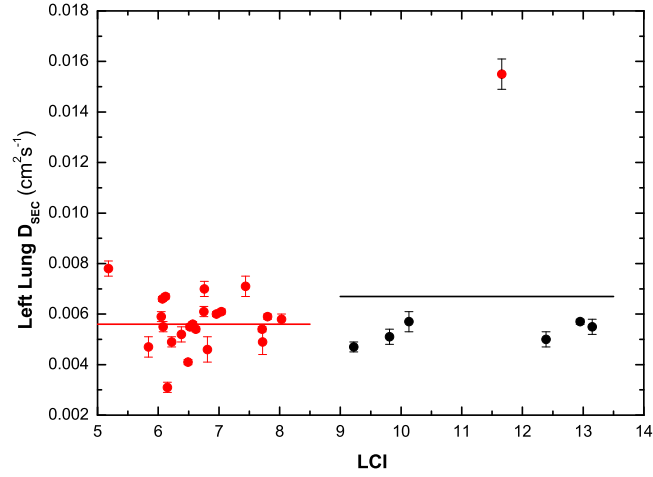
Figure 6.45: Left lung D_{sec} values for control (red circles) and CF (black circles) subjects. D_{sec} has been plotted against LCI to easily distinguish controls from CF subjects. The solid red and black lines represent the means. The orange circle is the CF subject who displays anomalous MR results.
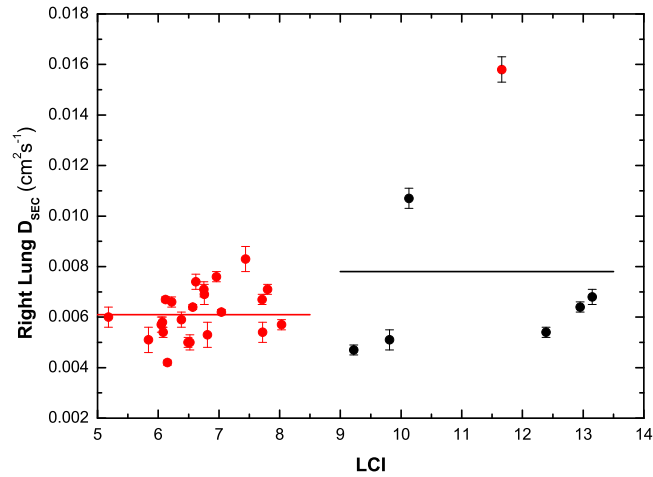
Figure 6.46: Right lung D_{sec} values for control (red circles) and CF (black circles) subjects. D_{sec} has been plotted against LCI to easily distinguish controls from CF subjects. The solid red and black lines represent the means. The orange circle is the CF subject who displays anomalous MR results.

6.5.4 Global Pulsed Field Gradient Sequence Results

The acinar radius (R) and alveolar sleeve depth (h) were measured in 9 CF subjects and 18 healthy aged matched controls using an average helium bolus size of 350 ml. The mean (SD) volume and concentration corrected R and h for the CF subjects were significantly larger (p = 0.01 and p = 0.0005 respectively) than those for the control subjects - 441 (23) μm compared to 405 (35) μm (Fig 6.47) and 295 (59) μm compared to 220 (38) μm (Fig 6.48) for R and h respectively.

For the CF subjects, no statistically significant correlation was found between R and LCI (R^2 = 0.08, p = 0.46, Fig 6.49), the ratio of RV/TLC (R^2 = 0.008, p = 0.82, Fig 6.50), percentage of predicted FEV1 (R^2 = 0.009, p = 0.82, Fig 6.51), or percentage of predicted FVC (R^2 = 0.05, p = 0.61, Fig 6.52).

Similarly, no statistically significant correlation was found between h and LCI (R^2 = 0.25, p = 0.17, Fig 6.53), the ratio of RV/TLC (R^2 = 0.03, p = 0.70, Fig 6.54), percentage of predicted FEV1 (R^2 = 0.07, p = 0.50, Fig 6.55), or percentage of predicted FVC (R^2 = 0.26, p = 0.16, Fig 6.56).
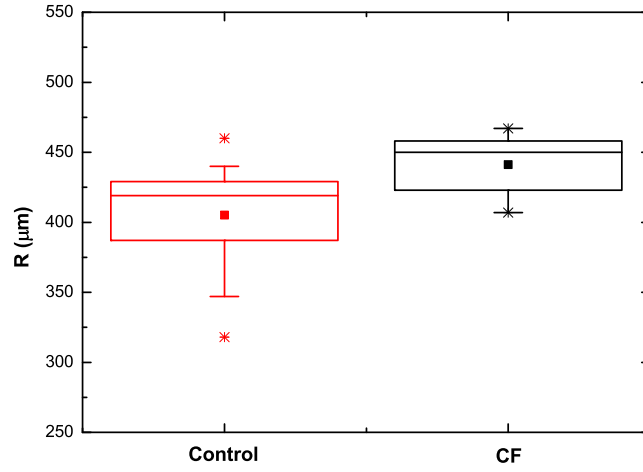
Figure 6.47: Box plot of R values for control and CF subjects. The * marks the range of the results, the □ marks the mean, the bottom and top of the box are the lower and upper quartiles respectively, the solid line within the box is the median, and the ends of the bars represent the ±95% confidence interval.
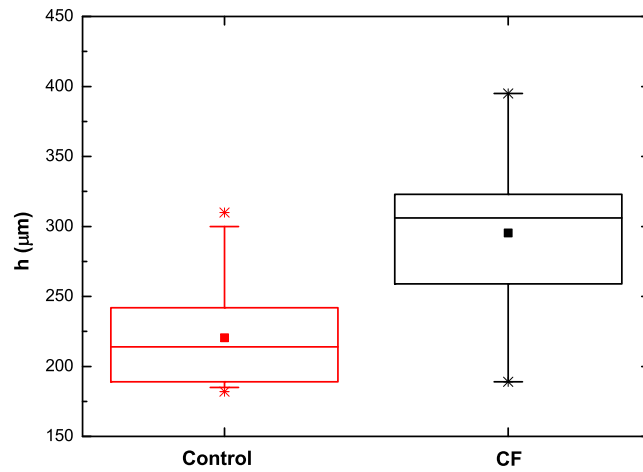
Figure 6.48: Box plot of h values for control and CF subjects. The * marks the range of the results, the □ marks the mean, the bottom and top of the box are the lower and upper quartiles respectively, the solid line within the box is the median, and the ends of the bars represent the ±95% confidence interval.
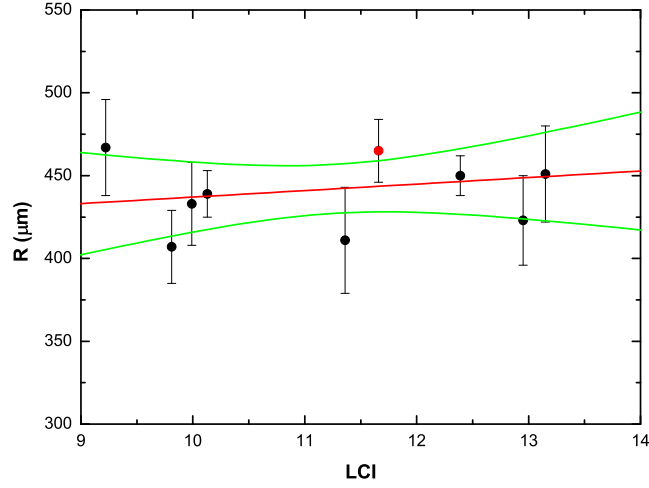
Figure 6.49: R vs LCI. The line of best fit (red line) and 95% confidence intervals (green lines) are shown. The orange circle is the CF subject who displays anomalous MR results.
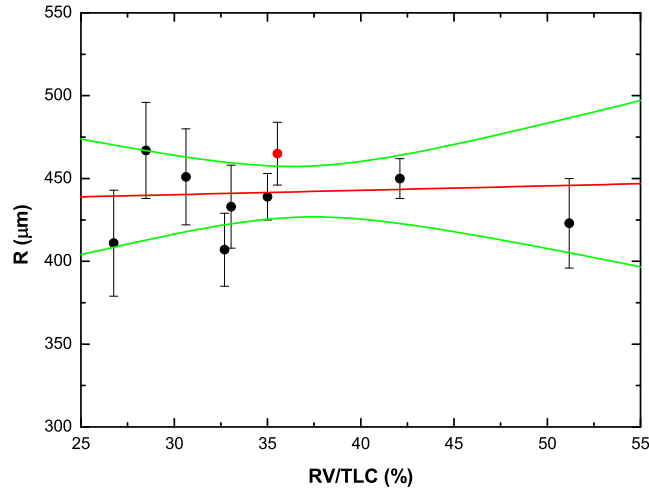
Figure 6.50: R vs RV/TLC. The line of best fit (red line) and 95% confidence intervals (green lines) are shown. The orange circle is the CF subject who displays anomalous MR results.
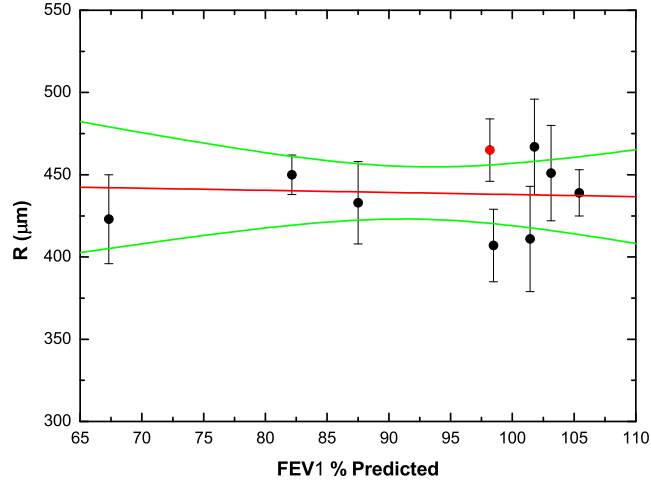
Figure 6.51: R vs Percentage of predicted FEV1. The line of best fit (red line) and 95% confidence intervals (green lines) are shown. The orange circle is the CF subject who displays anomalous MR results.
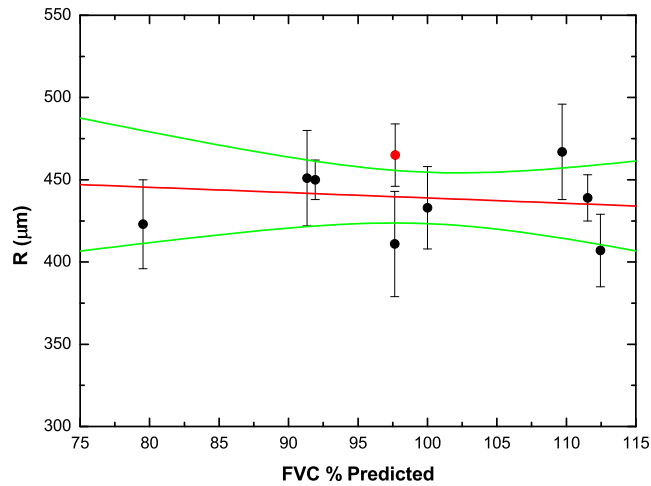
Figure 6.52: R vs Percentage of predicted FVC. The line of best fit (red line) and 95% confidence intervals (green lines) are shown. The orange circle is the CF subject who displays anomalous MR results.
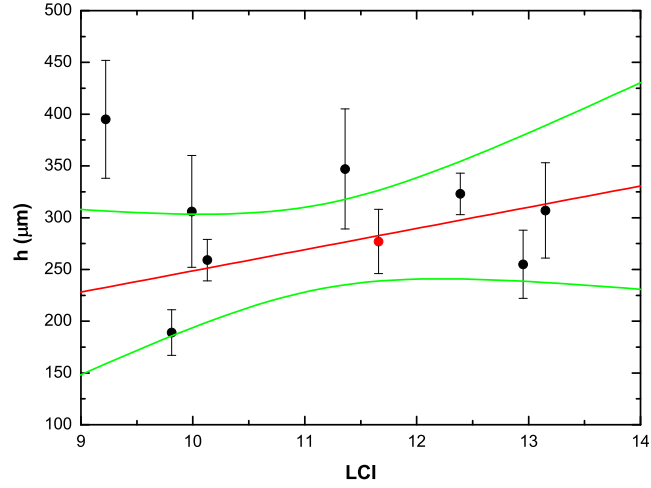
Figure 6.53: h vs LCI. The line of best fit (red line) and 95% confidence intervals (green lines) are shown. The orange circle is the CF subject who displays anomalous MR results.
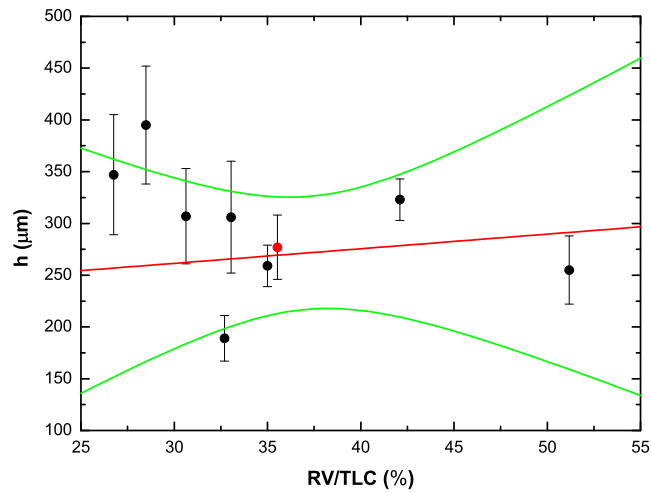
Figure 6.54: h vs RV/TLC. The line of best fit (red line) and 95% confidence intervals (green lines) are shown. The orange circle is the CF subject who displays anomalous MR results.
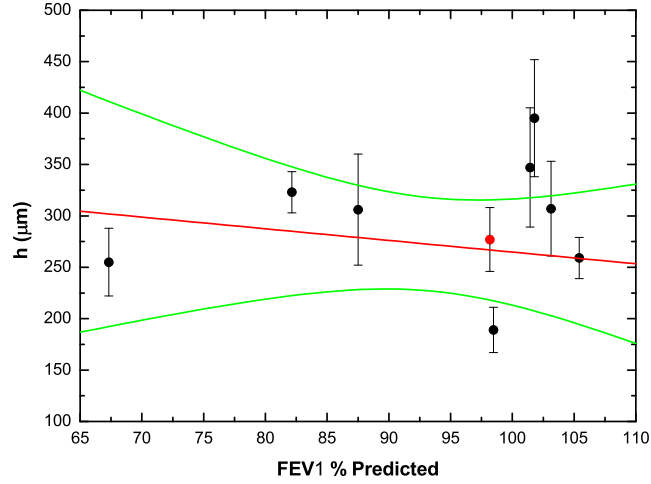
Figure 6.55: h vs Percentage of predicted FEV1. The line of best fit (red line) and 95% confidence intervals (green lines) are shown. The orange circle is the CF subject who displays anomalous MR results.
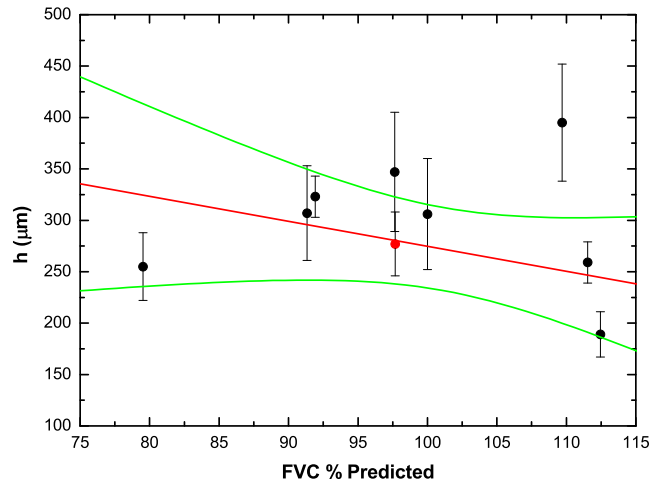
Figure 6.56: h vs Percentage of predicted FVC. The line of best fit (red line) and 95% confidence intervals (green lines) are shown. The orange circle is the CF subject who displays anomalous MR results.

6.6 Cystic Fibrosis Study Discussion

The purpose of this study was to determine the relationships between the three different MRI measurements and measurements of spirometry in subjects with CF and compare the results to those of healthy aged matched subjects.

The significantly elevated values of R and h in the CF subjects are consistent with the concept of intense neutrophilic inflammation occuring in the airways in response to bacterial infection. Both infection and inflammation occur early in the small airways [144] and are responsible for airway wall thickening, an increase in air trapping, and a reduction in FEV1.

High resolution computed tomography (HRCT) is recognised as being more sensitive for detecting early CF lung disease than standard chest X-rays [145]. Helbich *et al* [146] studied 117 patients with CF and divided them into three age groups: 0-5, 6-16, and $\geq$ 17 years old. The overall prevaling abnormalities found in this study were bronchiectasis, peribronchial wall thickening, air trapping, mucous plugging, and atelectasis. In the 6-16 years age group, the most prevalent abnormalities were bronchiectasis and air trapping. In a similar study by Brody *et al* [147], air trapping was found to be the most frequent abnormality in 60 subjects aged 6-10 years old, occuring in 63% of cases followed by 35% of subjects showing bronchiectasis.

The results obtained from this study are in agreement with the aforementioned studies that show air trapping as the most common abnormality found in younger and mildly affected subjects. Air trapping is a consequence of airway obstruction which impairs respiratory function. The strong correlation of LCI with percentage of predicted FVC as well the strong correlations between the ratio of RV/TLC with percentage of predicted FEV1 and FVC

highlight the use of these indices in assessing early stage CF before the disease no longer presents itself as merely an obstructive pattern.

The LCI is a particularly sensitive marker of peripheral airways obstruction because it is a measure of ventilation distribution inhomogeneity [148]. Because the measurement is performed at tidal breathing, reliable values on children can be routinely obtained since no forced manoeuvre, which is necessary for spirometry measurements, is required. This advantage in measurement technique was evident for several of the CF subjects in this study in which poor co-operation from the subject resulted in spirometric values being underestimated. The LCI and percentage of predicted FEV1 values of the CF subjects were found to be significantly different compared to those of the control subjects (p = 1.71×10^{-14} and p = 0.006 respectively) and consistent with the literature [149, 150]. In a report by Kraemer *et al* [151], it was shown that progression of CF was detected earliest by LCI which is in agreement with the results of the study.

It is recognised that treatment of CF should be focused on preventing structural damage and therefore the findings of LCI and percentage of predicted FVC being useful for measuring early disease progression could have applications on treatment therapies.

The lower D_{msec} of the CF subjects (except in one case) compared to those of the controls is further evidence of obstruction occuring in the peripheral airways. D_{msec} for the CF subjects correlated significantly with LCI and percentage of predicted FVC. A reduced ADC is indicative of smaller airway dimensions with airway narrowing caused by wall thickening a possible explanation. If airway narrowing was occuring it would be expected that R and h would decrease with increasing LCI and increase with increasing percentage of predicted FVC. However, no significant correlations were found

between R and LCI, percentage of predicted FEV1 or percentage of predicted FVC and neither were any found between h and those indices. In fact, R and h are found to marginally increase with LCI and slightly decrease with percentage of predicted FEV1 and FVC. A possible interpretation of this is wall thickening prior to eventual airway constriction although this explanation is far from conclusive. A more likely explanation for lower D_{msec} values and seemingly invariant microstructure values is mucopurulent plugging.

Ventilation distribution inhomogeneity was assessed further by measuring the distribution widths from the ADC histograms of each lung. The significantly broader right lung ADC histograms as compared to those of the controls suggests a greater amount of pulmonary function impairment. This finding is given further significance as it is known that pulmonary changes in CF often begin in the right upper lobe [152–154]. It has been hypothesised that CF affects the upper lobes more frequently because mucus is not as easily cleared as in the lower lobes where ventilatory excursion is much greater [155].

An anomalous result was found between D_{msec} and the ratio of RV/TLC. D_{msec} was seen to increase with increasing RV/TLC which is counter intuitive and at odds with the trend (albeit a weak one) found between LCI and RV/TLC which suggests that D_{msec} should correlate the same with RV/TLC as it does with LCI. This anomalous result was attributed as a spurious correlation caused by underestimation of spirometry measurements in several subjects due to their inability to expire to RV. As with LCI and percentage of predicted FEV1 and FVC, R and h remained invariant with RV/TLC, adding further support to mucous plugging being the predominant cause of air trapping in the CF subjects.

Although values of lung microstructure are seen to be invariant with sev-

eral indices, care should be taken when interpreting this result as evidence of no structural damage having yet occured. Structural changes such as airway dilation from bronchiectasis, airway narrowing from increased wall thickening, and complete loss of airways from obliterative fibrosing bronchiolitis occur to varying degrees between subjects. The observed invariance in R and h could therefore be a result of an apparent balance of forces and structural changes in the small airways. While pathological studies can highlight the prevaling disease processes [156–158], being able to define quantitatively the exact disease processes that are occuring in the peripheral airways of young and mildly affected subjects remains a challenge.

The statistical insignificance between the D_{sec} measurements of the CF and control subjects for each lung, taken in conjunction with their LCIs (6.45 - 6.46) and D_{msec} histogram distribution widths, seems to imply that in lungs with collateral pathways, peripheral airway obstruction has negligible impact on lung mechanics but has a drastic effect on ventilation distribution.

The results of one particular CF subject (highlighted orange in all the figures) in this study standout because of their large discrepancy compared with the other CF subjects. The subject has spirometry values indicative of normal airflow as evidenced from their percentage of predicted FEV1 and FVC but displays high D_{msec} and D_{sec} values. The high values of ADC imply larger peripheral airspace dimensions however the R and h values of the subject seem to be consistent with the other CF subjects. However, spirometry results in this subject were known to be variable and of poor quality, therefore the subject may in actuality have airflow obstruction. A possible interpretation of these results is that any airflow obstruction in this subject is found primarily in the larger airways. Because the total cross-sectional surface area from the large airways to the small airways increases

by several orders of magnitude, and recalling how flow conductance scales with area (D_{sec} Measurements, Section 6.2), obstruction in the larger airways has a much greater impact on airflow resistance. This explanation highlights the insensitivity of spirometry to localised structural change and thus as a truly direct measure of structural integrity of the peripheral airways.

If obstruction is indeed focused primarily in the larger airways then the high values of D_{msec} and D_{sec}, combined with the large level of ventilation inhomogeneity determined by their high LCI and broad ADC histograms could be suggestive of bronchiectasis being the dominant destructive process in this individual. The disease may have caused partial breakdown of the boundaries between the acini. The high D_{sec} value of this subject implies that ventilation has become impaired to the extent that ventilation through collateral paths has increased in order to maintain sufficient lung mechanical function. It is therefore surmised that this individual has the greatest disease severity and that their disease progression is now beyond the early obstructive pattern stages. As such, this subject is responsible for skewing several correlations and is the reason why no statistical significance was found between the D_{msec} measurements of the control and CF subjects.

Summary

The CF preliminary study has shown that hyperpolarised ^{3}He MRI in children with early CF lung disease can provide information on localised peripheral airway obstruction as well as airway inflammation. Because early stage CF presents itself as an obstructive pattern, D_{msec} measurements were found to correlate well with spirometry values such as FEV1, FVC, and LCI. The LCI was found to be a particularly useful biomarker of disease severity.

The higher values of R and h are characteristic of airway inflammation

but their invariance to spirometry was attributed to the variability of destructive processes occuring in the lungs of different CF subjects. Whilst these parameters are indicative of the disease, they are not sensitive enough to be used as biomarkers for disease severity or progression.

The information that ^{3}He MRI can provide about the peripheral airways of diseased lungs is important for early intervention strategies designed at preventing disease progression and thereby improving survival in CF patients. Lung MRI in CF is still in its infancy and so imaging based endpoints or scores of severity in CF are still being developed. A limitation of this study is therefore not just sample size but also the narrow spread of disease severity between subjects which can be attributed to their age range (6-11 years old). Should the study be continued then a greater sample size with a larger age range would provide better information on how MR measurements are influenced by disease progression.

The other limitations of this study are the same as those mentioned in the asthmatic study, with the addition that the D_{sec} measurements are once again subject to the effects of concentration and lung inflation (section 6.2). However, given that the subjects in each group were aged matched and the ^{3}He bolus administered was kept constant, any correction factor associated with these effects can be assumed to be negligible.

Chapter 7

Conclusions

The scope of this thesis is concentrated on two specific research aims.

The first was the development of three different MR sequences in assessing pulmonary function using hyperpolarised ^{3}He at low field (0.15 T). The RARE sequence had already been established and implemented previously by the research group. However, refinement of the SPAMM tagging sequence and the development of the Global Pulsed Field Gradient (GPFG) sequence were undertaken during this thesis and their sequence parameters have been subsequently optimised to the values presented in this work.

The three experimental sequences were designed with the deliberate intention of measuring the diffusion of hyperpolarised ^{3}He gas through the peripheral airspaces of lung over different timescales and therefore different length scales. The RARE sequence employed in this study measures the ADC at the acinar and alveolar level. However, any other information pertaining to lung microstructure cannot be elucidated when using only a single b-value. The GPFG sequence was designed to study the non-Gaussian effects on signal decay that arise from diffusion anisotropy which only become evident when imaging with higher and multiple b-values. By studying these effects struc-

tural information on lung morphometry can be obtained which provides an additional insight on the microstructure of the lung other than that from the ADC. The SPAMM tagging sequence is able to measure the ADC associated with length scales many times the characteristic dimensions of the alveoli. As such, the sequence provides an assessment of the interconnectivity of the peripheral airspaces.

The usefulness of an ADC measurement has been carefully considered throughout this research. While many studies successfully relate the ADC to both pathophysiological and histopathological measures, the understanding of many aspects of ADC behaviour in a complex medium such as the lung is still in its infancy. In addition to this, experimental parameters such as the mixture composition and volume of the administered bolus further complicate the interpretation of ADC measurements. A significant effort was made during this research to account for both of these experimental parameters and the subsequent effect they have on the level of helium concentration and inflation in the lungs of different individuals during MR diffusion measurements.

The second research aim was the implementation of these developed sequences on three separate subject study groups. The Leicester study group was the first and largest study group that these sequences were implemented on and thus forms the bulk of the results presented in the thesis. By contrast, the asthmatic and CF studies were preliminary ones whose aims were also different from the Leicester study.

All three MRI sequences were implemented on the subjects of the Leicester study. The aim of this study was to look at normal alveolar development in children and young adults in order to test the hypothesis that alveolisation continues beyond early life. The results obtained throughout the course

of this research demonstrated that the dimesions of the alveolar and acinar airspaces increase with age and lung size during childhood and adolescence at a rate much less than expected if lung growth occured only by expansion of pre-existing alveoli. Caution is advised however when interpreting this invariance as proof positive of the hypothesis. Invariance in morphological dimensions can also be explained by the process of alveolar recruitment. Thus, determining whether the invariances in the results are due to neoalveolisation or in fact simple alveolar recruitment proves to be a significant challenge.

The aim of the asthmatic study was to assess alveolar structure in severe asthmatic adult subjects compared with aged matched healthy controls. This assessment was accomplished by correlating MR diffusion measurements with clinical measurements of asthma severity determined through spirometry. Signal to noise issues precluded the use of the SPAMM tagging sequence in this preliminary study. Nevertheless, the acquired diffusion measurements demonstrated that hyperpolarised ^{3}He MRI can provide information about structural changes evident in asthma. The study showed that ^{3}He MRI is more sensitive than spirometry for detecting changes in the peripheral airways as evidenced by asthmatic subjects with normal spirometry but abnormal alveolar and acinar dimensions as well as broader ADC histograms. Lastly, the strong correlation of diffusion measurements with the asthma severity indices of LCI and RV/TLC demonstrated that ^{3}He MRI can provide an objective evaluation of asthma phenotype.

The CF study was conducted to examine whether hyperpolarised ^{3}He MRI could provide useful metrics for assessing CF severity. A thorough assessment was performed by comparing all three diffusion measurments in children with CF to aged matched healthy controls and also to measurements

of spirometry. The CF preliminary study demonstrated that hyperpolarised ^{3}He MRI in children with early CF lung disease can provide information on localised peripheral airway obstruction as well as airway inflammation. The larger acinar and alveolar dimensions found in CF subjects were characteristic of airway inflammation but their invariance to spirometry measurements was attributed to the variability of destructive processes occuring in the lungs of different CF subjects. As such, while these enlarged microstructure dimensions were indicative of the disease, the measurements were not sensitive enough to be used as biomarkers for disease severity or progression. ADC measurements in CF subjects obtained from the RARE sequence were found to correlate well with spirometry values such as percentage of predicted FVC and LCI. This finding was attributed to the obstructive nature of the disease in its early stages with airway obstruction also being responsible for the higher LCI values and broader ADC histograms of the CF subjects. An interesting observation was made when comparing the D_{sec} measurements from the SPAMM tagging sequence of the CF and control subjects. With evidence of airway obstruction occuring in CF subjects, the invariance of D_{sec} measurements between healthy and diseased groups seems to imply that in lungs with collateral pathways, there is negligible impact on lung mechanics but a drastic effect on ventilation distribution.

It is hoped that the findings presented in this thesis demonstrate the capability of hyperpolarised ^{3}He MRI in assessing lung development and pathophysiology. By using only a modest amount of ^{3}He (15-30 ml) for each diffusion measurement performed, regional information on both peripheral airspace morphology and function can be acquired. The information about the peripheral airways of diseased lungs is important for therapeutic intervention strategies designed at preventing disease progression and thereby

reducing mortality and morbidity.

Bibliography

[1] E.R. Weibel. *Morphometry of the Human Lung*. Springer Verlag, 1963.

[2] E.R. Weibel and R. Cristal. *Design of the Airways and Blood Vessel Considered as Branching Trees*. New York: Raven Press, 1991.

[3] B. Haefeli-Bleuer and E.R. Weibel. Morphometry of the Human Pulmonary Acinus. *Anat. Rec.*, 220:401–414, 1988.

[4] G.J. Tortora and B. Derrickson. *Principles of Anatomy and Physiology*. John Wiley & Sons, 11th edition, 2006.

[5] F. Bloch. Nuclear Induction. *Phys. Rev.*, 70:460–473, 1946.

[6] P.T Callaghan. *Principles of Nuclear Magnetic Resonance Microscopy*. Oxford University Press, 1993.

[7] R.S. Likes. Moving Gradient Zeugmatography. *U.S. Patent 4307343*, 1981.

[8] S. Ljunggren. A Simple Graphical Representation of Fourier Based Imaging Methods. *J. Magn. Reson.*, 54:338–343, 1983.

[9] M. A. Bouchiat, T. R. Carver, and C. M. Varnum. Nuclear Polarization in ^{3}He Gas Induced by Optical Pumping and Dipolar Exchange. *Phys. Rev. Lett.*, 5:373–375, 1960.

[10] F. D. Colegrove, L. D. Schearer, and G. K. Walters. Polarization of ^{3}He Gas by Optical Pumping. *Phys. Rev.*, 132:2561–2572, 1963.

[11] J. Brossel and A. Kastler. Detection of Magnetic Resonance in Excited Levels - an Effect of Resonance Radiation Depolarization. *Compt. Rend*, 229:1213–1215, 1949.

[12] A. Kastler. Some Suggestions for the Production and Detection of Unequal Population Levels. Application to the Stern-Gerlach Experiment and Magnetic Resonance. *J. Phys. Radium.*, 11:255–265, 1950.

[13] A. Kastler. Optical Methods of Atomic Orientation and of Magnetic Resonance. *J. Opt. Soc. Am.*, 47:460–465, 1957.

[14] M.S. Albert, G.D. Cates, B. Driehuys, and W. Happer. Biological Magnetic Resonance Imaging Using Laser Polarised ^{129}Xe. *Nature*, 370:199–201, 1994.

[15] J.R. MacFall, H.C. Charles, R.D. Black, H. Middleton, J.C. Swartz, B. Saam, B. Driehuys, C. Erickson, W. Happer, G.D. Cates, G.A. Johnson, and C.E. Ravin. Human Lung Air Spaces: Potential for MR Imaging with Hyperpolarized ^{3}He. *Radiology*, 200:553–558, 1996.

[16] H.U. Kauczor, D. Hoffman, K.F. Kreitner, H. Nilgens, R. Surkau, W. Heil, A. Potthast, M.V. Knopp, Otten E.W., and M. Thelen. Normal and Abnormal Pulmonary Ventilation: Visualisation at Hyperpolarised ^{3}He MR Imaging. *Radiology*, 201:564–568, 1996.

[17] M. Ebert, T. Grossmann, W. Heil, W.E. Otten, R. Surkau, M. Leduc, P. Bachert, M.V. Knopp, L.R. Schad, and Thelen M. Nuclear Magnetic Resonance Imaging on Humans Using Hyperpolarized ^{3}He. *Lancet*, 34:1297–1299, 1996.

[18] P. Bachert, L.R. Schad, M. Bock, M.V. Knopp, M. Ebert, T. Grossmann, W. Heil, D. Hoffman, R. Surkau, and W.E. Otten. Nuclear Magnetic Resonance Imaging of Airways in Humans with Use of Hyperpolarized ^{3}He. *Magn. Reson. Med.*, 36:192–196, 1996.

[19] N.D Bhaskar, W. Happer, and T. McClelland. Efficiency of Spin Exchange Between Rubidium Spins and ^{129}Xe Nuclei. *Phys. Rev. Lett.*, 49:25–28, 1982.

[20] W. Happer, E. Miron, S. Schaefer, D. Schreiber, W.A. van Wijngaarden, and X. Zeng. Polarisation of the Nuclear Spins of Noble Gas Atoms By Spin Exchange with Optically Pumped Alkali Metal Atoms. *Phys. Rev. A.*, 29:3092–3110, 1984.

[21] T.G. Walker and W. Happer. Spin-Exchange Optical Pumping of Noble-Gas Nuclei. *Rev. Mod. Phys.*, 69:629–642, 1997.

[22] G. Eckert, W. Heil, P. Meyerhoff, W.E. Otten, R. Surkau, M. Werner, M. Leduc, P.J. Nacher, and L.D. Schearer. A Dense Polarised ^{3}He Target Based On Compression of Optically Pumped Gas. *Nucl. Inst. Meth. Phys. Res. A.*, 320:53–65, 1992.

[23] E. Stoltz, M. Meyerhoff, N. Bigelow, M. Leduc, P.J Nacher, and G. Tastevin. High Nuclear Polarization in ^{3}He and ^{3}He-^{4}He Gas Mixtures By Optical Pumping With a Laser Diode. *Appl. Phys. B.*, 63:629–633, 1996.

[24] E. Brunner. Enhancement of Surface and Biological NMR Spectroscopy Using Laser-Polarized ^{129}Xe. *Concepts. Magn. Reson.*, 11:313–335, 1999.

[25] A. Ben-Amar Baranga, S. Appelt, M.V. Romalis, C.J. Erickson, A.R. Young, G.D. Cates, and W. Happer. Polarization of ^{3}He By Spin Exchange With Optically Pumped Rb and K Vapors. *Phys. Rev. Lett.*, 80:2801–2804, 1998.

[26] H.E. Moller, X.J. Chen, M.S. Chawla, B. Driehuys, L.W. Hedlund, and G.A. Johnson. Signal Dynamics in Magnetic Resonance Imaging of the Lung With Hyperpolarized Noble Gases. *J. Magn. Reson.*, 135:133–143, 1998.

[27] G.S. Sobering and Y. Shiferaw. Optimisation of Acquisition Parameters For Multi-Shot Hyperpolarised NMR: Variable Flip Angle Excitation. *In: Proc 3rd SMR Scientific Meeting*, page 687, 1995.

[28] L. Zhao, R. Mulkern, C.H. Tseng, D. Williamson, S. Patz, R. Kraft, R.L. Walsworth, F.A. Jolesz, and M.S. Albert. Gradient-Echo Imaging Considerations For Hyperpolarized ^{129}Xe MR. *J. Magn. Reson. B.*, 113:179–183, 1996.

[29] J.P. Mugler. Regional Measurement of the ^{3}He Diffusion Coefficient in the Human Lung. *In: Proc 6th ISMRM Scientific Meeting*, page 1904, 1998.

[30] E. Durand, G. Guillot, L. Darrasse, G. Tastevin, P.J. Nacher, A. Vignaud, D. Vatollo, and J. Bittoun. CPMG Measurments and Ultrafast Imaging in Human Lungs With Hyperpolarised ^{3}He at Low Field (0.1 T). *Magn. Reson. Med.*, 47:75–81, 2002.

[31] J. Hennig, A. Nauerth, and H. Friedburg. RARE Imaging: A Fast Imaging Method For Clinical MR. *Magn. Reson. Med.*, 3:823–833, 1986.

[32] M.E. Moseley, Y. Cohen, J. Mintorovitch, L. Chileuitt, H. Shimizu, J. Kucharczyk, M.F. Wendland, and P.R. Weinstein. Early Detection of Regional Ischaemia in Cats: Comparison of Diffusion and T_2-Weighted MRI and Spectroscopy. *Magn. Reson. Med.*, 14:330–346, 1990.

[33] X.J. Chen, H.E. Moller, M.S. Chawla, G.P. Cofer, B. Driehuys, L.W. Hedlund, and G.A. Johnson. Spatially Resolved Measurements of Hyperpolarized Gas Properties in the Lung in vivo. Part I: Diffusion Coefficient. *Magn. Reson. Med.*, 42:721–728, 1999.

[34] B. Saam, D.A. Yablonskiy, V.D. Kodibagkar, J.C. Leawoods, D.S. Gierada, J.D. Cooper, S.L. Lefrak, and M.S. Conradi. MR Imaging of Diffusion of ^{3}He Gas in Healthy and Diseased Lungs. *Magn. Reson. Med.*, 44:174–179, 2000.

[35] M. Salerno, E.E de Lange, T.A Altes, J.D. Truwit, J.R. Brookeman, and J.P. Mugler III. Emphysema: Hyperpolarized ^{3}He Diffusion MR Imaging of the Lungs Compared with Spirometric Indexes - Initial Experience. *Radiology*, 222:252–260, 2002.

[36] A.E. Morbach, K.K. Gast, J. Schmiedeskamp, A. Dahmen, A. Herweling, C.P. Heussel, H.U. Kauczor, and W.G. Schreiber. Diffusion Weighted MRI of the Lung With Hyperpolarised ^{3}He: A Study of Reproducibility. *J. Magn. Reson. Imag.*, 21:765–774, 2005.

[37] S. Fichele, N. Woodhouse, A.J. Swift, Z. Said, M.N.J. Paley, L. Kasuboski, G.H. Mills, E.J.R van Beek, and J.M. Wild. MRI of ^{3}He Gas in Healthy Lungs: Posture Related Variations of Alveolar Size. *J. Magn. Reson. Imag.*, 20:331–335, 2004.

[38] M. Bock. Simultaneous T_2^* and Diffusion Measurements With ^{3}He. *Magn. Reson. Med.*, 38:890–895, 1997.

[39] J. Liner and S. Weissman. Determination of the Temperature Dependence of Gaseous Diffusion Coefficients Using Gas Chromatographic Apparatus. *J. Chem. Phys.*, 56:2288–2290, 1972.

[40] J. Hirschfelder, C. Curtiss, and R. Bird. *Molecular Theory of Gases and Liquids.* Wiley, 1954.

[41] A.J. Deninger, B. Eberle, J. Bermuth, B. Escat, K. Markstaller, J. Schmiedeskamp, W.G. Schreiber, R. Surkau, E. Otten, and Kauczor H.U. Assessment of a Single Acquisition Imaging Sequence for Oxygen Sensitive ^{3}He MRI. *Magn. Reson. Med.*, 47:105–114, 2002.

[42] M. Salerno, J.R. Brookeman, E.E. deLange, J. Knight-Scottand, and J.P. Mugler III. Demonstration of an Alveolar Size Gradient in the Healthy Human Lung: A Study of the Reproducibility of Hyperpolarized ^{3}He Diffusion MRI. *In: Proc 8th ISMRM Scientific Meeting*, page 2195, 2000.

[43] E. Hahn. Spin Echoes. *Phys. Rev.*, 80:580–594, 1950.

[44] E. Carr and E. Purcell. Effects of Diffusion On Free Precession in Nuclear Magnetic Resonance Experiments. *Phys. Rev.*, 94:630–638, 1954.

[45] H.C. Torrey. Bloch Equations With Diffusion Terms. *Phys. Rev.*, 104:563–566, 1956.

[46] E.O. Stejskal and J.E. Tanner. Spin Diffusion Measurements: Spin Echoes in the Presence of a Time-Dependent Field Gradient. *J. Chem. Phys.*, 42:288–292, 1965.

[47] J.E. Tanner and E.O. Stejskal. Restricted Self-Diffusion of Protons in Colloidal Systems by the Pulsed-Gradient, Spin Echo Method. *J. Chem. Phys.*, 49:17681777, 1968.

[48] B. Balinov, B. Jonsson, P. Linse, and O. Soderman. The NMR Self Diffusion Method Applied to Restricted Diffusion: Simulation of Echo Attenuation from Molecules in Spheres and Between Planes. *J. Magn. Reson. A.*, 104:17–25, 1993.

[49] P. Linse and O. Soderman. The Validity of the Short Gradient Pulse Approximation in NMR Studies of Restricted Diffusion: Simulations of Molecules Diffusing Between Planes, in Cylinders and Spheres. *J. Magn. Reson. A.*, 116:77–86, 1995.

[50] M.E. Hayden, G. Archibald, K.M Gilbert, and C. Lei. Restricted Diffusion Within a Single Pore. *J. Magn. Reson.*, 169:313, 2004.

[51] J.S. Murday and R.M. Cotts. Self Diffusion Coefficient of Liquid Lithium. *J. Chem. Phys.*, 48:4938, 1968.

[52] T.M. de Swiet and P.N. Sen. Decay of Nuclear Magnetization by Bounded Diffusion in a Constant Field Gradient. *J. Chem. Phys.*, 100:5597–5604, 1994.

[53] S.D. Stoller, W. Happer, and F.J. Dyson. Transverse Spin Relaxation in Inhomogeneous Magnetic Fields. *Phys. Rev. A.*, 44:7459–7477, 1991.

[54] M.D. Hurlimann, K.G. Helmer, T.M. de Swiet, P.N. Sen, and C.H. Sotak. Spin Echoes in a Constant Gradient and in the Presence of Simple Restriction. *J. Magn. Reson. A.*, 113:260–264, 1995.

[55] J. Stepisnik. Validity Limits of Gaussian Approximation in Cumulant Expansion for Diffusion Attenuation of Spin Echo. *Physica. B.*, 270:110–117, 1999.

[56] W.G. Schreiber, A.E. Morbach, T. Stavngaard, K.K Gast, A. Herweling, L.V. Sgaard, M. Windirsch, J. Schmiedeskamp, C.P. Heussel, and H.U. Kauczor. Assessment of Lung Microstructure with Magnetic Resonance Imaging of Hyperpolarised ^{3}He. *Respir. Phys.*, 148:23–42, 1999.

[57] P.J. Basser, J. Mattiello, and D. LeBihan. MR Diffusion Tensor Spectroscopy and Imaging. *Biophys. J.*, 66:259–267, 1994.

[58] J.H. Jensen, J.A. Helpern, A. Ramani, H. Lu, and K. Kaczynski. Diffusional Kurtosis Imaging: The Quantification of non-Gaussian Water Diffusion by Means of Magnetic Resonance Imaging. *Magn. Reson. Med.*, 53:419–428, 2005.

[59] P.J. Basser, J. Mattiello, and D. LeBihan. Diffusional Kurtosis Imaging in the Lung Using Hyperpolarised ^{3}He. *Biophys. J.*, 56:733–737, 2006.

[60] R.E. Jacob, G. Laicher, and K.R. Minard. 3D MRI of non-Gaussian ^{3}He Diffusion in the Rat Lung. *J. Magn. Reson.*, 188:357–366, 2007.

[61] R.T. Callaghan, C.D. Eccles, and Y. Xia. NMR Microscopy of Dynamic Displacements: k-space and q-space Imaging. *J. Phys. E Sci. Instrum.*, 21:820–822, 1988.

[62] D.G. Cory and A.N. Garroway. Measurement of Translational Displacement Probabilities by NMR: An Indicator of Compartmentation. *Magn. Reson. Med.*, 14:435–444, 1990.

[63] R.T. Callaghan, D. MacGowan, K.J. Packer, and E.O. Zelaya. Diffraction Like Effects in NMR Diffusion Studies of Fluids in Porous Solids. *Nature*, 351:467–469, 1991.

[64] J.D. Seymour and R.T. Callaghan. Flow Diffraction Structural Characterisation and Measurements of Hydrodynamic Dispersion in Porous Media by PGSE NMR. *J. Magn. Reson. A.*, 22:90–93, 1996.

[65] Y. Assaf and Y. Cohen. Structural Information in Neuronal Tissue as Revealed by q-space diffusion NMR Spectroscopy of Metabolites in Bovine Optic Nerve. *NMR Biomed*, 12:335–344, 1999.

[66] A.M. Torres, A.T. Taurins, D.G. Regan, B.E. Chapman, and P.W Kuchel. Assignment of Coherence Features in NMR q-space Plots to Particular Diffusion Modes in Erythrocyte Suspensions. *J. Magn. Reson.*, 138:135–143, 1999.

[67] D.D. Shanbag, T.A. Altes, G.W. Miller, J.F. Mata, and J. Knight-Scott. q-Space Analysis of Lung Morphometry in vivo with Hyperpolarized ^{3}He Spectroscopy. *J. Magn. Reson. Imag.*, 24:84–94, 2006.

[68] N.F. Lori, T.E. Conturo, and D. LeBihan. Definition of Displacement Probability and Diffusion Time in q-space Magnetic Resonance Measurements That Use Finite Duration Diffusion Encoding Gradients. *J. Magn. Reson.*, 165:185–195, 2003.

[69] A. Caprihan, L.Z. Wang, and E. Fukushima. A Multiple Narrow Pulse Approximation for Restricted Diffusion in a Time Varying Field Gradient. *J. Magn. Reson. A.*, 118:94–102, 1996.

[70] L.Z. Wang, A. Caprihan, and E. Fukushima. The Narrow Pulse Criterion for Pulsed Gradient Spin-echo Diffusion Measurements. *J. Magn. Reson. A.*, 117:209–219, 1995.

[71] D.A. Yablonskiy, A.L. Sukstanskii, Leawoods J.C., Gierada D.S., Bretthorst G.L., Lefrak S.S., Cooper J.D., and Conradi M.S. Quantitative in vivo Assessment of Lung Microstructure at the Alveolar Level with Hyperpolarized ^{3}He Diffusion MRI. *Proc Natl Acad Sci*, 99:3111–3116, 2002.

[72] A.L. Sukstanskii and D.A. Yablonskiy. In vivo Lung Morphometry with Hyperpolarized ^{3}He Diffusion MRI: Theoretical Background. *J. Magn. Reson.*, 190:200–210, 2008.

[73] T.S. Tanoli, J.C. Woods, M.S. Conradi, K.T. Bae, D.S. Gierada, J.C. Hogg, J.D. Cooper, and D.A. Yablonskiy. In vivo Lung Morphometry with Hyperpolarized ^{3}He Diffusion MRI in Canines with Induced Emphysema: Disease Progression and Comparison with Computed Tomography. *J. Appl. Physiol.*, 102:477–484, 2007.

[74] D.A. Yablonskiy, A.L. Sukstanskii, J.C. Woods, D.S. Gierada, J.D. Quirk, J.C. Hogg, J.D. Cooper, and M.S. Conradi. Quantification of Lung Microstructure with Hyperpolarized ^{3}He Diffusion MRI. *J. Appl. Physiol.*, 107:1258–1265, 2009.

[75] W.S. Hartroft. Microscopic Diagnosis of Pulmonary Emphysema. *Am. J. Pathol.*, 21:889–903, 1945.

[76] J. Parra-Robles, S. Ajraoui, M.H. Deppe, S.R. Parnell, and J.M. Wild. Experimental Investigation and Numerical Simulation of ^{3}He Gas Diffusion in Simple Geometries: Implications for Analytical Models of ^{3}He MR Lung Morphometry. *J. Magn. Reson.*, 204:228–238, 2010.

[77] S. Fichele, M.N.J. Paley, N. Woodhouse, P.D. Griffiths, E.J. van Beek, and J.M. Wild. Finite-Difference Simulations of ^{3}He Diffusion in 3D Alveolar Ducts: Comparison with the Cylinder Model. *Magn. Reson. Med.*, 52:917–920, 2004.

[78] D.S. Grebenkov, G. Guillot, and B. Sapoval. Restricted Diffusion in a Model Acinar Labyrinth by NMR: Theoretical and Numerical Results. *J. Magn. Reson.*, 2007:143–156, 2007.

[79] K.S. Burrowes, M.H. Tawhai, and P.J. Hunter. Modeling RBC and Neutrophil Distribution Through an Anatomically Based Pulmonary Capillary Network. *Ann. Biomed. Eng.*, 32:585–595, 2004.

[80] S. Fichele, M.N.J. Paley, N. Woodhouse, P.D. Griffiths, E.J.R. van Beek, and J.M. Wild. Investigating ^{3}He Diffusion NMR in the Lungs Using Finite Difference Simulations and in vivo PGSE Experiments. *J. Magn. Reson.*, 167:1–11, 2004.

[81] H. Kitaoka, S. Tamura, and R. Takaki. A Three Dimensional Model of the Human Pulmonary Acinus. *J. Appl. Physiol.*, 88:2260–2268, 2000.

[82] T.G Reese, O. Heid, R.M. Weisskoff, and V.J. Wedeen. Reduction of Eddy Current Induced Distortion in Diffusion MRI Using a Twice Refocused Spin Echo. *Magn. Reson. Med.*, 49:177–182, 2006.

[83] X. Zhou. Quantitative Analysis of Eddy Current Effects on Echo Planar Images. *Proc. 4th. ISMRM*, page 1486, 1996.

[84] M.A. Bernstein, X.J. Zhou, J.A. Polzin, K.F. King, A. Ganin, N.J. Pelc, and G. Glover. Concomitant Gradient Terms in Phase Contrast MR: Analysis and Correction. *Magn. Reson. Med.*, 39:300–308, 1998.

[85] H.D.W. Hill. Limits of Measurement in Magnetic Resonance. *J. Phys. E. Sci. Instrum.*, 1:977–983, 1968.

[86] D.I. Hoult and P.C. Lauterbur. The Sensitivity of the Zeugmatographic Experiment Involving Human Samples. *J. Magn. Reson.*, 34:425–433, 1979.

[87] F.E. Terman. *Radio Engineers Handbook.* McGraw-Hill, 1943.

[88] F.D. Doty, G. Entzminger, C.D. Hauck, and J.P. Staab. Practical Aspects of Birdcage Coils. *J. Magn. Reson.*, 138:144–154, 1999.

[89] K.P. Pruessmann, M. Weiger, B. Scheidegger, and P. Boesiger. SENSE: Sensitivity Encoding for Fast MRI. *Magn. Reson. Med.*, 42:952–962, 1999.

[90] P. Kellman and E.R. McVeigh. Image Reconstruction in SNR Units: A General Method For SNR Measurement. *Magn. Reson. Med.*, 54:1439–1447, 2005.

[91] K.F. King and L. Angelos. SENSE Image Quality Improvement Using Matrix Regularisation. *In: Proc 9th ISMRM Scientific Meeting*, page 1771, 2001.

[92] F.H. Lin, K.K. Kwong, J.W. Belliveau, and L.L. Wald. Parallel Imaging Reconstruction Using Automatic Regularisation. *Magn. Reson. Med.*, 51:559–567, 2004.

[93] M. Weiger, K.P. Pruessmann, and P. Boesiger. Cardiac Real-Time Imaging Using SENSE. *Magn. Reson. Med.*, 43:177–184, 2000.

[94] B. Waters. *PhD Thesis*. University of Nottingham, 2006.

[95] P.B. Roemer, W.A. Edelstein, Hayes C.E., and S.P. Souza. The NMR Phased Array. *Magn. Reson. Med.*, 16:192–225, 1990.

[96] J. Wang, M. Qiu, Q.X. Yang, and M.B. Smith. Measurement and Correction of Transmitter and Receiver Induced Nonuniformities In Vivo. *Magn. Reson. Med.*, 53:408–417, 2005.

[97] D.D. Shanbag, T.A. Altes, G.W. Miller, J.F. Mata, and J. Knight-Scott. Global Assessment of Human Lung Microstructure in vivo with Hyperpolarised ^{3}He MR Diffusion Spectroscopy. *Unpublished*, 2008.

[98] J.C. Woods, D.A. Yablonskiy, K. Chino, T.S. Tanoli, J.D. Cooper, and M.S. Conradi. Magnetization Tagging Decay to Measure Long-range ^{3}He Diffusion in Healthy and Emphysematous Canine Lungs. *Magn. Reson. Med.*, 51:1002–1008, 2004.

[99] J.C. Woods, D.A. Yablonskiy, C.K. Choong, K. Chino, J.A. Pierce, J.C. Hogg, J. Bentley, J.D. Cooper, M.S. Conradi, and P.T. Macklem. Long-range Diffusion of Hyperpolarized ^{3}He in Explanted Normal and Emphysematous Human Lungs via Magnetization Tagging. *J. Appl. Physiol.*, 99:1992–1997, 2005.

[100] J. Owers-Bradley, F. Stanislao, A. Bennattayalah, C.J. Smith-McGloin, R.W. Bowtell, P.S. Morgan, and A.R. Moody. MR Tagging of Human Lungs Using Hyperpolarized ^{3}He Gas. *J. Magn. Reson. Imag.*, 17:142–146, 2003.

[101] M.S. Conradi, B.T. Saam, D.A. Yablonskiy, and J.C. Woods. Hyperpolarized ^{3}He and Perfluorocarbon Gas Diffusion MRI of Lungs. *Progress in Nuclear Magnetic Resonance Spectroscopy*, 48:63–83, 2006.

[102] S. Fichele. *PhD Thesis*. University of Nottingham, 2002.

[103] T.B. Zeltner and P.H. Burri. The Postnatal Development and Growth of the Human Lung II: Morphology. *Respir. Physiol.*, 67:269–282, 1987.

[104] E. Bancalari. *The Newborn Lung: Neonatology Questions and Controversies*. Saunders, 2008.

[105] A.A. Hislop, J.S. Wigglesworth, and R. Desai. Alveolar Development in the Human Fetus and Infant. *Early. Hum. Dev.*, 13:1–11, 1986.

[106] G.E. Angus and W.M. Thurlbeck. Number of Alveoli in the Human Lung. *J. Appl. Physiol.*, 32:483–485, 1972.

[107] D.M. Hyde, N.K. Tyler, L.F. Putney, P. Singh, and H.J. Gundersen. Total Number and Mean Size of Alveoli in Mammalian Lung Estimated Using Fractionator Sampling and Unbiased Estimates of the Euler Characteristic of Alveolar Openings. *Anat. Rec. A. Discov. Mol. Cell. Evol. Biol.*, 277:216–226, 2004.

[108] M. Ochs, J.R. Nyengaard, and A. Jung. The Number of Alveoli in the Human Lung. *Am. J. Respir. Crit. Care. Med.*, 169:120–124, 2004.

[109] J. Kovar, P.D. Sly, and K.E. Willet. Postnatal Alveolar Development of the Rabbit. *J. Appl. Physiol.*, 93:629–635, 2002.

[110] D.M. Hyde, S.A. Blozis, and M.V. Avdalovic. Alveoli Increase in Number but Not in Size from Birth to Adulthood in Rhesus Monkeys. *Am. J. Physiol. Lung. Cell. Mol. Physiol.*, 293:570–579, 2007.

[111] C.C. Hsia, L.F. Herazo, F. Fryder-Doffey, and E.R. Weibel. Compensatory Lung Growth Occurs in Adult Dogs After Right Pneumonectomy. *J. Clin. Invest.*, 94:405–412, 1994.

[112] D. Massaro, G.D. Massaro, A. Baras, E.P. Hoffman, and L.B. Clerch. Calorie-Related Rapid Onset of Alveolar Loss, Regeneration, and Changes in Mouse Lung Gene Expression. *Am. J. Physiol. Lung. Cell. Mol. Physiol.*, 286:896–906, 2004.

[113] J.C. Schittny, S.I. Mund, and M. Stampanoni. Evidence and Structural Mechanism for Late Lung Alveolarisation. *Am. J. Physiol. Lung. Cell. Mol. Physiol.*, 294:246–254, 2008.

[114] B.H. Brown, R.A. Primhak, R.H. Smallwood, P. Milnes, A.J. Narracott, and M.J. Jackson. Neonatal Lungs: Maturational Changes in Lung Resistivity Spectra. *Med. Biol. Eng. Comput.*, 40:506–511, 2002.

[115] M. Rosenthal, D. Cramer, S.H. Bain, D. Denison, A. Bush, and J.O. Warner. Lung Fuction in White Children Aged 4 to 19 Years: Single Breath Analysis and Plethysmography. *Thorax*, 48:803–808, 1993.

[116] T.A. Altes, J. Mata, E.E. de Lange, J.R. Brookeman, and J.P. Mugler III. Assessment of Lung Development Using Hyperpolarised ^{3}He Diffusion MRI. *J. Magn. Reson. Imag.*, 24:1277–1283, 2006.

[117] E. Osmanagic, A.L. Sukstanskii, J.D. Quirk, J.C. Woods, R.A. Pierce, M.S. Conradi, E.R. Weibel, and D.A. Yablonskiy. Quantitative Assessment of Lung Microstructure in Healthy Mice Using an MR Based ^{3}He Lung Morphometry Technique. *J. Appl. Physiol.*, 109:1592–1599, 2010.

[118] S. Verbanck and M. Paiva. Simulation of the Apparent Diffusion of ³He in the Human Acinus. *J. Appl. Physiol.*, 103:249–254, 2007.

[119] S. Verbanck and M. Paiva. Time Dependence of ³He Diffusion in the Human Lung: Measurement in the Long Time Scale Regime Using Stimulated Echoes. *Magn. Reson. Med.*, 56:296–309, 2006.

[120] S.E. Bartel, S.E. Haywood, J.C. Woods, Y.V. Chang, C. Menard, D.A. Yablonskiy, D.S. Gierada, and M.S. Conradi. The Role of Collateral Paths in Long Range Diffusion of ³He in Lungs. *Acad. Radiol.*, 15:675–682, 2008.

[121] J.B. West. *Resiratory Physiology*. Williams and Wilkins, 1995.

[122] H.A. Menkes and P.T. Macklem. *Handbook of Physiology*. Amer. Physiological. Society., 1977.

[123] M.W. Lambert. Accessory Bronchiole-Alveolar Communications. *J. Path. Bact.*, 70:311–314, 1955.

[124] H.B. Martin. Respiratory Bronchioles as the Pathway for Collateral Ventilation. *J. Appl. Physiol.*, 21:1443–1447, 1966.

[125] P.T. Macklem. Airway Obstruction and Collateral Ventilation. *Physiol. Rev.*, 51:368–436, 1971.

[126] C.R. Inners, P.B. Terry, R.J. Traystman, and H.A. Menkes. Effects of Lung Volume on Collateral and Airway Resistance in Man. *J. Appl. Physiol.*, 46:67–73, 1979.

[127] E. Baraldi and M. Filippone. Chronic Lung Disease After Premature Birth. *N. Engl. J. Med.*, 357:1946–1955, 2007.

[128] D. Massaro, N. Teich, S. Maxwell, G.D. Massaro, and P. Whitney. Post-natal Development of Alveoli: Regulation and Evidence for a Critical Period in Rats. *J. Clin. Invest.*, 76:1297–1305, 1985.

[129] D. Massaro and G.D. Massaro. Dexamethasone Accelerates Postnatal Alveolar Wall Thinning and Alters Wall Composition. *Am. J. Physiol.*, 251:218–224, 1986.

[130] C. Svanes, E. Omenaas, D. Jarvis, S. Chinn, A. Gulsvik, and P. Burney. Parental Smoking in Childhood and Obstructive Lung Disease: Results From the European Community Respiratory Health Survey. *Thorax*, 59:295–302, 2004.

[131] M. Yanai, K. Sekizawa, T. Ohrui, H. Sasaki, and T. Takishima. Site of Airway Obstruction in Pulmonary Disease: Direct Measurement of Intrabronchial Pressure. *J. Appl. Physiol.*, 72:1016–1023, 1992.

[132] K.R. Lutchen and H.L Gillis. Relatioship Between Heterogeneous Changes in Airway Morphometry and Lung Resistance and Elastance. *J. Appl. Physiol.*, 83:1192–1201, 1997.

[133] K.R. Lutchen, J.L. Greenstein, and B. Suki. How Inhomogeneities and Airway Walls Affect Frequency Dependence and Separation of Airway and Tissue Properties. *J. Appl. Physiol.*, 90:1696–1707, 1996.

[134] T.R. Bai, J. Cooper, T. Koelmeyer, Pare. P.D., and T. Weir. The Effect of Age and Duration of Disease on Airway Structure in Fatal Asthma. *Am. J. Respir. Crit. Care. Med.*, 162:663–669, 2000.

[135] A. Chetta, A. Foresi, M. Del Donno, G. Bertorelli, A. Pesci, and D. Olivieri. Airways Remodeling is a Distinctive Feature of Asthma and is Related to Severity of Disease. *Chest*, 111:852–857, 1997.

[136] M. Hoshino, Y. Nakamura, and J.J. Sim. Expression of Growth Factors and Remodelling of the Airway Wall in Bronchial Asthma. *Thorax*, 53:21–27, 1998.

[137] A.L. James, P.S. Maxwell, G. Pearce-Pinto, J.G. Elliot, and N.G. Carroll. The Relationship of Reticular Basement Membrane Thickness to Airway Wall Remodeling in Asthma. *Am. J. Respir. Crit. Care. Med.*, 166:1590–1595, 2002.

[138] K. Kuwano, C.H. Bosken, P.D. Pare, T.R. Bai, B.R. Wiggs, and J.C Hogg. Small Airways Dimensions in Asthma and in Chronic Obstructive Pulmonary Disease. *Am. Rev. Respir. Dis.*, 148:1220–1225, 1993.

[139] N. Carroll, J. Elliot, A. Morton, and A. James. The Structure of Large and Small Airways in Non Fatal and Fatal Asthma. *Am. Rev. Respir. Dis.*, 147:405–410, 1993.

[140] R.K. Lambert, B.R. Wiggs, K. Kuwano, J.C Hogg, and P.D. Pare. Functional Significance of Increased Airway Smooth Muscle in Asthma and COPD. *J. Appl. Physiol.*, 74:2771–2781, 1993.

[141] H.L. Gillis and K.R. Lutchen. Airway Remodeling in Asthma Amplifies Heterogeneities in Smooth Muscle Shortening Causing Hyperresonsiveness. *J. Appl. Physiol.*, 86:2001–2012, 1999.

[142] K.R. Lutchen, A. Jensen, and H. Atileh. Airway Constriction Pattern is a Central Component of Asthma Severity: The Role of Deep Inspirations. *Am. J. Respir. Crit. Care. Med.*, 164:207–215, 2001.

[143] T.R. Mauad, L.F. Silva, and M.A. Santos. Abnormal Alveolar Attachments with Decreased Elastic Fiber Content in Distal Lung in Fatal Asthma. *Am. J. Respir. Crit. Care. Med.*, 164:207–215, 2001.

[144] D.S. Armstrong, K. Grimwood, and R. Carizino. Lower Respiratory Infection and Inflammation in Infants with Newly Diagnosed Cystic Fibrosis. *BMJ*, 310:1571–1572, 1995.

[145] D.A. Lynch, R.C. Brasch, K.A. Hardy, and W.R. Webb. Pediatric Pulmonary Disease: Assessment with High Resolution Ultrafast CT. *Radiology*, 176:243–248, 1990.

[146] T.H. Helbich, G. Heinz-Peer, and I. Eichler. Cystic Fibrosis: CT Assessment of Lung Involvement in Children and Adults. *Radiology*, 213:537–544, 1999.

[147] A.S. Brody, J.S. Klein, P.L. Molina, J. Quanne, J.A. Bean, and R.W Wilmott. High Resolution Computed Tomography in Young Patients with Cystic Fibrosis: Distribution of Abnormalities and Correlation with Pulmonary Function Tests. *J. Pediatr*, 145:32–38, 2004.

[148] P.M. Gustafsson, P. Aurora, and A. Lindblad. Evaluation of Ventilation Maldistribution as an Early Indicator of Lung Disease in Children with Cystic Fibrosis. *Eur. Respir. J.*, 22:972–979, 2003.

[149] R.J. Knudson and M.D. Lebowitz. Maximal Mid-Expiratory Flow (FEF25-75%): Normal Limits and Assessment of Severity. *Am. Rev. Respir. Dis.*, 117:609–610, 1978.

[150] P. Aurora, A. Bush, and P.M. Gustafsson. Multiple Breath Washout As a Marker of Lung Disease in Preschool Children with Cystic Fibrosis. *Am. J. Respir. Crit. Care. Med.*, 171:249–256, 2005.

[151] R. Kraemer, A. Blum, A. Schibler, R.A. Ammann, and S. Gallati. Ventilation Inhomogeneities in Relation to Standard Lung Function

in Patients with Cystic Fibrosis. *Am. J. Respir. Crit. Care. Med.*, 171:371–378, 2005.

[152] J.F. Tomashefski, A.J. Christoforidis, and A.K. Abdullah. Cystic Fibrosis in Young Adults. *Chest*, 57:28, 1970.

[153] E.E. Schwartz and D.S. Holsclaw. Pulmonary Involvement in Adults with Cystic Fibrosis. *AJR*, 122:708, 1974.

[154] J.W. Reinig, F.W. Sanchez, D.W. Thomason, and R.P. Gobien. The Distinctly Visible Right Upper Lobe Bronchus on the Lateral Chest: A Clue to Adolescent Cystic Fibrosis. *Pediatr. Radiol*, 15:222–224, 1985.

[155] P.J. Friedman, J.R. Hardwood, and P.H. Ellenbogen. Pulmonary Cystic Fibrosis in the Adult: Early and Late Radiographic Findings with Pathologic Correlation. *AJR*, 136:1131, 1981.

[156] R. Hamatcu, J.M. Rowland, and M.V. Horn. Clinical Findings and Lung Pathology in Children with Cystic Fibrosis. *Am. J. Crit. Care. Med.*, 165:1172–1175, 2002.

[157] C.W.M. Bedrossian, S.D. Greenberg, D.B. Singer, J.J. Hansen, and H.S. Rosenberg. The Lung in Cystic Fibrosis: A Quantitative Study Including Prevalence of Pathological Findings Among Different Age Groups. *Human. Pathol*, 7:195–204, 1976.

[158] H.A.W.M. Tiddens, L.P. Koopman, and R.K. Lambert. Cartilaginous Airway Wall Dimensions and Airway Resistance in Cystic Fibrosis Lungs. *Eur. Respir. J.*, 15:732–742, 2000.